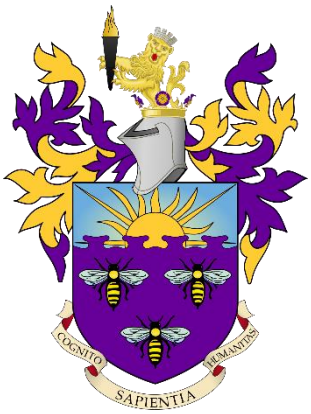

Evaporation of Graphene Droplets: from Fundamentals to the Crystallisation of Organic Molecules

A thesis submitted to The University of Manchester for the degree of Doctor of Philosophy in the Faculty of Science and Engineering.

Matthew Alexander Boyes

Department of Chemistry

2020

Contents

List of Figures

List of Tables

Abbreviations

2D	Two dimensional
3D	Three dimensional
AAO	Anodised aluminium oxide
AFM	Atomic Force Microscopy
at%	Atomic percentage
BPS	Bis-pyrene Stabiliser
BZ	Brillouin zone
CNT	Classical nucleation theory
CPG	Controlled pore glass
CVD	Chemical vapour deposition
ECE	Electrochemical exfoliation
FTIR	Fourier-transform Infrared spectroscopy
GO	Graphene oxide
hBN	Hexagonal boron nitride
HOPG	Highly orientated pyrolytic graphite
IPA	Isopropyl alcohol
LLC	Liquid-like cluster
LPE	Liquid phase exfoliation
PNC	Pre-nucleation clusters
rGO	Reduced graphene oxide
SAM	Self-assembled monolayer
SEM	Scanning Electron Microscopy
TEM	Transmission Electron Microscopy
WAXS	Wide Angle X-ray Scattering
wt%	Weight percentage
XPS	X-ray photoelectron spectroscopy
XRD	X-ray Diffraction

Abstract

Evaporation of liquids is a fundamental process to both nature and industry; thus, a great deal of research has gone into understanding this phenomenon. It is a key part to many fabrication techniques in technological applications which typically utilise a solvent based method to deposit a material of interest. Studies into the evaporation of droplets tend to be performed with supported droplets (*i.e.* on a substrate) where the support itself plays a vital role of the dynamics of evaporation. Therefore, a more fundamental understanding of evaporation requires the use of a contactless manipulation method, such as levitation.

Evaporation is also widely used in the crystallisation of organic molecules from solution. Controlling crystallisation and subsequently the properties of the resulting product is still a challenge due to a limited understanding of the early stages of crystallisation. The development of new techniques that enable us to gain insights into the nanoscale interactions between molecules is of great scientific interest. The application of templated crystallisation techniques readily allows for the investigation of these different nanoscale interactions and the use of graphene as a template would aid in furthering this area of research.

Graphene, the 2D carbon-based allotrope, has garnered a vast amount of scientific interest due to its unique combination of properties, such as exceptionally high electronic conductivity, high mechanical strength, transparency, and impermeability to gases. These properties make graphene an attractive material for a large variety of potential applications. To be effectively applied however, graphene must be produced through a large-scale process. Chemical exfoliation techniques, such as LPE and ECE, are promising routes to achieve this as they can generate large quantities of solution processed graphene with tuneable surface properties.

In this thesis, the evaporation process of graphene droplets is focussed upon. Specifically, two main studies are performed:

1) The evaporation of graphene droplets under acoustic levitation was investigated. We observed a distinct change in drying behaviours of graphene droplets when the concentration of graphene was varied, and the solvent system composed of equal parts water and IPA. At a low concentration of graphene, the droplets would reach a critical size and then stop evaporating, becoming stable for many hours in a form similar to a liquid marble. At higher concentrations, the droplets would buckle and produce a graphitic aggregate. In addition to graphene, aqueous glycine droplets were also levitated to allow for homogeneous

crystallisation conditions to be studied. It was found that under the influence of acoustic levitation, even with the addition of the anti-solvent IPA, glycine would exclusively form the α-polymorph despite changes in induction times and morphologies that suggested the presence of the less stable polymorph of glycine.

2) Heterogeneous crystallisation of glycine was investigated using graphene-based templates, which were used as either an additive or as the substrate for crystallisation. The preferential crystallisation of α-glycine was induced by graphene-templates, with a pronounced enhancement when additive-templated compared to substrate-templated. Computational modelling experiments highlighted the vital role of the oxygen-containing functional groups on graphene that stabilised the α-form to a greater degree than the β-form. The work revealed that the oxygen content must be carefully optimised to achieve preferential selectivity towards the α-form. These results demonstrate the possibility of using *ad hoc* designed graphene additives in crystal engineering for polymorph screening studies.

Finally, a different approach to produce graphene dispersions, Liquid Phase Exfoliation was utilised to produce stable dispersions in water. Bis-pyrene stabilisers, a new type of stabiliser, were synthesised and investigated for this study. Our results show that a higher concentration of exfoliated material as well as higher single layer content were achieved with these new stabilisers, when compared to traditional, water-soluble pyrene derivatives. The better exfoliation ability was attributed to the enhanced interaction of the stabiliser with graphene, due to the presence of two pyrene groups as opposed to the standard one, which made the stabiliser more hydrophobic and thus could be better adsorbed onto graphene. However, a higher toxicity towards living cells was also seen for the graphene dispersions produced.

In conclusion, this thesis reports novel results in the field of crystallisation, droplet evaporation, and graphene production, providing new insights into the use of 2D materials for crystallisation studies and the potential use of graphene dispersions for the production of liquid marbles, which could find practical applications as miniature chemical reaction vessels, gas sensors, and as liquid transport media.

Declaration

The University of Manchester

PhD by Published Work Candidate Declaration

Candidate Name: Matthew Alexander Boyes

Faculty: Engineering and Physical Sciences

Thesis Title: Evaporation of Graphene Droplets: from Fundamentals to the Crystallisation of Organic Molecules

Declaration to be completed by the candidate:

I declare that no portion of the work referred to in this thesis has been submitted in support of an application for another degree or qualification of this or any other university or other institute of learning.

Signed: **Date:**

Copyright Statement

[1] This excludes material already printed in academic journals, for which the copyright belongs to said journals and publishers. Pages for which the author does not own the copyright are numbered differently from the rest of the thesis.

Acknowledgements

I have known for a long time that I would end up doing a PhD, but what I did not realise was what a rollercoaster it would be. This has been one of the best decisions of my life, and this section is dedicated to the people who have helped make it possible.

I would like to express my gratitude to my supervisor, Cinzia Casiraghi, for her guidance, support, and overall, the opportunity to undertake this project in the first place. My thanks need to also go to my co-supervisor, Thomas Vetter, for the useful discussions and feedback he provided during the project.

There is a long list of fellow PhD students and PDRAs that I would like to thank, and I am certain I will forget a few. Starting off, thank you to all past and present members of the Casiraghi group, especially my project partner, Adriana Alieva, who has been a constant source of support, knowledge, and friendship. Additionally, thank you to Robyn Worsley, Vaiva Nagyte, Yuyoung Shin, Daryl McManus, Glenn Sunley, Josh Moore, Tom Raine, Venessa Tischler, Raymundo Marcial, and all members of OMIC for being there as well as going along with the wild ride that is a PhD.

Finally, I am ever grateful to my family and friends who have supported me through the ups and downs of the past 4 years and who will undoubtedly continue to support me through whatever life brings now.

Publications

1. Shin, Y.; Just-Baringo, X.; **Boyes, M.**; Panigrahi, A.; Zarattini, M.; Chen, Y.; Liu, X.; Morris, G.; Prestat, E.; Kostarelos, K.; Vranic, S.; Larrosa, I.; Casiraghi, C. Enhanced Liquid Phase Exfoliation of Graphene in Water using an Insoluble Bis-Pyrene Stabiliser, *Faraday Discussions*, accepted (2019), DOI: 10.1039/C9FD00114J
2. **Boyes, M.**; Alieva, A.; Tong, J. C.; Nagyte, V.; Vetter, T.; Franco, M. M.; Casiraghi, C. Exploiting the Surface Properties of Graphene for Polymorph Selectivity, *ACS Nano*, **14**, 10394-10401 (2020).
3. Alieva, A.; **Boyes, M.**; Vetter, T.; Casiraghi, C. Selective Polymorphism of α-glycine by Acoustic Levitation, *CrystEngComm*, accepted (2020) DOI: 10.1039/d0ce00856g
4. **Boyes, M.**; Alieva, A.; Vetter, T.; Casiraghi, C. Levitation of graphene – from droplet buckling to liquid marble formation, to be submitted.

Overview

The sp^2 hybridisation of carbon atoms allows them to produce allotropes of all dimensionalities: three-dimensional (*e.g.* graphite); two-dimensional (*e.g.* graphene); one-dimensional (*e.g.* carbon nanotubes); and zero-dimensional (*e.g.* fullerenes). The last allotrope to be isolated was the 2D form, graphene. This material can be viewed as the building block for the other graphitic materials: it can be stacked into graphite, rolled in carbon nanotubes, or folded into a fullerene. Graphene possesses many unique properties that have made it an appealing material for a wide range of applications in materials science and technological fields. Chemical exfoliation methods allow for the production of large amounts of graphene in solution, enabling its use in simple deposition methods, such as drop casting, spin and spray coating. However, all these methods are based on solvent evaporation. Currently, there are just a few studies focussing on the fundamentals of the evaporative process of graphene solutions and are mostly based on droplets that are supported by a substrate. Understanding the evaporation behaviour of liquids, and subsequently the graphene dispersions, is of crucial importance for the development of applications relying on solution-processed graphene.

Evaporation of liquids is a prominent method to achieve crystallisation from solution, which is a phase transformation process where solid crystalline structures form from liquid precursors. This process is heavily utilised as an isolation and purification technique of pharmaceuticals and chemical reagents as crystal formation and isolation occurs in a single step. However, control over the final crystalline product, thus the ability to obtain crystals with desired properties, remains a challenge because of a limited understanding of the first stages of molecular assembly, also known as nucleation.

One of the aims of this project is to study crystallisation by using a new approach to gain a better understanding of the interactions of crystallisation at play at the molecular level. This was achieved through the first reported use of the surface properties of graphene to template the crystallisation of organic molecules.

The second aim of this thesis is to study the drying behaviour of solution-processed graphene without any substrate interference.

The structure of this thesis is as follows:

- **Chapters 1-3** provide the required background and up-to-date literature reviews for the experiments performed.

Chapter 1 introduces graphene and gives an overview of its unique properties and how they can be related to crystallisation studies. There is a particular focus on the production methods of solution-processed graphene, mainly LPE and ECE, as they will be used to produce the graphene used in this study.

Chapter 2 provides details of the fundamental concepts of crystallisation from solution with relevant theory to establish a background understanding of the process. Both homogeneous and heterogeneous nucleation are described, and the concept of polymorphism is given as well as the introduction of glycine. The state-of-the-art understanding of the effect of substrates and impurities on crystallisation is provided with particular attention paid to tailored templates to drive selectivity of specific crystalline forms.

Chapter 3 contains a fundamental description of the process of acoustic levitation. The basic theory and some complications to levitation are detailed, followed by literature reviews of the application of acoustic levitation in the fields of droplet evaporation and crystallisation.

- **Chapters 4-7** detail the experimental results obtained in this project.

Chapter 4 provides the use of graphene to template the crystallisation of an organic molecule from supported microdroplets. Different types of graphene (*i.e.* with varying surface chemistry) were utilised and introduced to the crystallising system as either an additive or a substrate. Solution-processed graphene was directly added to glycine solutions to act as an additive template in the solutions, but graphene substrates were also produced by spray-coating the graphene dispersions onto bare silicon substrates. A comparison between the two types of templated crystallisation is given and the experimental results are corroborated with a theoretical model.

The second set of experimental results detailed in **Chapter 5** show the drying behaviour of graphene dispersions at a range of concentrations and solvent compositions. Our results show that under specific conditions (*i.e.* solvent compositions, temperature, and humidity), the droplets show two distinct drying behaviours depending on the concentration of graphene. At high concentrations, the droplet continuously evaporates whilst the graphene material starts to re-aggregate and causes instabilities within the droplet until no solvent remains and an aggregate forms. At low concentrations, the droplet's suddenly stop evaporating, allowing for stable levitation for several hours.

In **Chapter 6**, the evaporation and crystallisation behaviour of acoustically levitated glycine droplets was investigated. Different solvent systems were employed and their influence on

crystallisation were monitored. The crystalline agglomerates produced were precisely opened *via* laser cutting which permitted the investigation of the internal crystal structure as well as the external. The crystals appeared to grow with directionality towards the centre of the droplet, indicating that supersaturation of the solution was first reached at the liquid-air contact. Raman spectroscopy revealed that regardless of the solvent system used and the region analysed, all the crystals produced were a single polymorph of glycine.

The final set of results (**Chapter 7**) detail the use of an insoluble pyrene-based stabiliser to achieve efficient LPE of graphene in water. Previously thought to only be possible with soluble stabilisers, the work highlights the importance of the balance of interactions between graphene, the stabiliser, and water such that a new class of stabilisers could be explored in their use in graphene exfoliation.

Chapter 8 concludes the collective work presented in this thesis and lays out plans for future avenues of research.

Part I: Introduction

Chapter 1: Graphene

Nanomaterials are a class of materials that are principally defined as having at least one of their characteristic dimensions in the nanoscale range. A 2D material has a lateral size orders of magnitude larger than its thickness, therefore can be defined as a nanomaterial. Graphene, a single layer of graphite, having a thickness of only 1 carbon atom, thus belongs to the family of 2D materials.

Graphene was the first 2D material to be experimentally isolated,[1,2] and it has garnered significant research interest because of its remarkable properties,[3–5] which include: the highest electron mobility; high thermal conductivity and mechanical strength; and a chemical tuneability via covalent and non-covalent functionalisation routes. The combination of all these properties into one material has allowed graphene's research portfolio to cover many scientific fields,[6] hence graphene is expected have a huge impact on many aspects of our lives.[7]

This chapter will give a general overview of graphene's structure, properties and the synthesis methods used in this project.

1.1 Structure

Graphene is a monolayer of sp^2 hybridised carbon atoms tightly packed into a honeycomb lattice.[1,2,8–10] The sp^2 hybridisation allows each carbon to form three strong in-plane σ-bonds to neighbouring carbon atoms, giving rise to the hexagonal structure, and a π-orbital housing a free electron perpendicular to the plane. These π-orbitals cause extensive electronic delocalisation over the whole surface.[11,12] The filled σ- and π-orbitals each represent the low energy electron states, hence are called the bonding states, whilst the high energy antibonding states, denoted as the σ^*- and π^*-orbitals, are unfilled.[12]

The lattice structure of graphene is shown in Figure 1.1 (a). The carbon-carbon bond distance, $a_{c\text{-}c}$, is 1.42 Å and the real space lattice unit vectors $\mathbf{a_1}$ and $\mathbf{a_2}$ define the unit cell which contains two carbon atoms, A and B, and a lattice constant, a ($a = |\mathbf{a_1}| = |\mathbf{a_2}|$) of 2.46 Å.[9,11,13] The reciprocal lattice in Figure 1.1 (b) illustrates the Brillouin Zone (BZ), which also has a hexagonal shape and is defined by the vectors $\mathbf{b_1}$ and $\mathbf{b_2}$. The high symmetry points of the BZ are denoted as the K, K', M and Γ points. The Γ point is the centre of the BZ, and the two inequivalent points at the corners are the K and K' points. These two points can be repeated for the other four corners of the BZ. Finally, M denotes the halfway location between the points K and K'.[9,11]

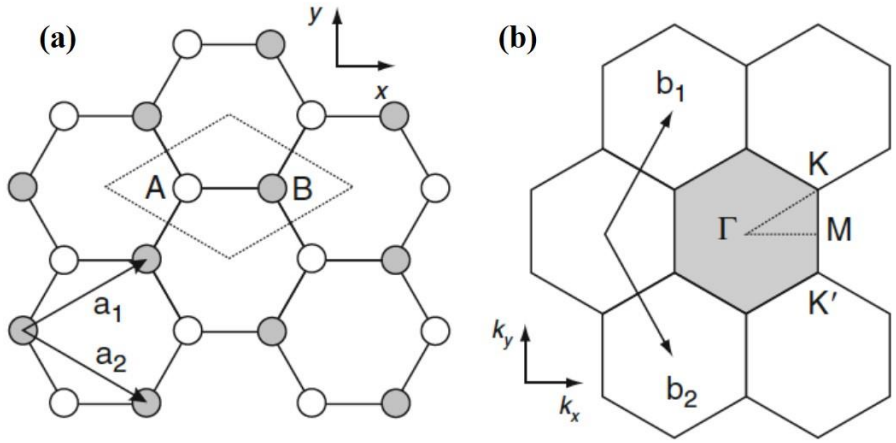

Figure 1.1 (a) Graphene's lattice structure and (b) its reciprocal lattice.[13]

1.2 Properties

Most of the outstanding properties that graphene displays arise from the unique symmetry of its atomic structure. There are other 2D crystals where the atoms are arranged in a honeycomb structure (*e.g.* hBN), but graphene is unique because all the atoms are equivalent, being all carbon atoms.

1.2.1 Electronic Properties

The electronic properties of graphene are defined only by the π- and π*-orbitals. Figure 1.2 (a) shows the 3D electron energy dispersion diagram of graphene: this is characterised by two surfaces, one at low energy (the conduction band) that is formed by the π-orbitals; and one at high energy (the valence band) that is formed by the π*-orbitals. The two surfaces touch at 6 points, called the Dirac points, and correspond to the K and K' points of the BZ (Figure 1.1 (b)). Because of the lack of a band gap between the two surfaces at the Dirac points, from an electronic point of view, graphene is classified as a zero-bandgap semiconductor or semimetal.[6,9]

Graphite is also a semimetal, so the unique properties of graphene must be related to another feature of the energy dispersion. This can be seen in the 2D energy dispersion diagram of Figure 1.2 (b) by focussing on the K and K' points; the energy dispersion is linear near these points. Graphene's unique electronic properties arise from the linear relation between the energy and the momentum of an electron, which is given by:[5]

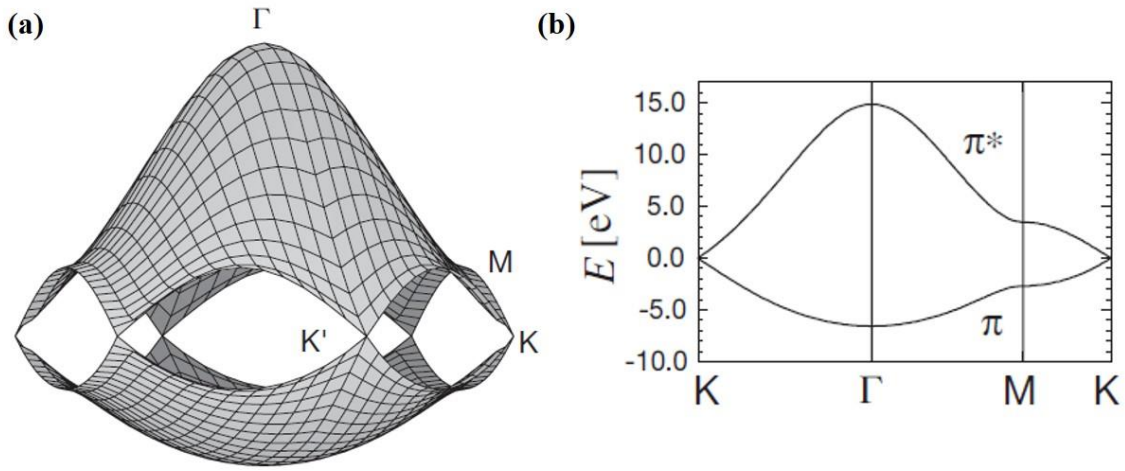

Figure 1.2 (a) 3D and (b) 2D energy dispersion diagrams of graphene detailing the points of high symmetry K, K', M and Γ.[12]

$$|E| = \frac{h}{2\pi} v_F |k| \qquad \textbf{(1.1)}$$

where v_F is the Fermi velocity (~10^6 m s^{-1}), h is Planck's constant (6.62 x 10^{-34} m^2 kg s^{-1}), and k is the wavevector or momentum. When plotted in 3D, this equation gives rise to a band structure where both the conduction and valence bands have a conical shape and touch at the Dirac points.

The linear dispersion between the energy and momentum implies that the speed of the electrons (the Fermi velocity) in graphene is constant and independent of the particle's mass. In other words, the electrons in graphene behave as massless Dirac fermions. This is very different to electrons in every other material, which are described by the Schrödinger equation, where the electron energy is dependent on the square of its wavevector (giving a parabolic energy dispersion) and its effective mass.[3,5] As a result, suspended (or encapsulated) graphene boasts the highest charge mobility ever reported (~200,000 cm^2 V^{-1} s^{-1}).[14]

1.2.2 Optical Properties

A pristine monolayer film of graphene shows high optical transparency, absorbing only ~2.3% of white light and has negligible reflectance (<0.1%).[15,16] The absorption of light is proportional to the number of layers, with each layer contributing to 2.3% more absorbance, as shown in Figure 1.3.

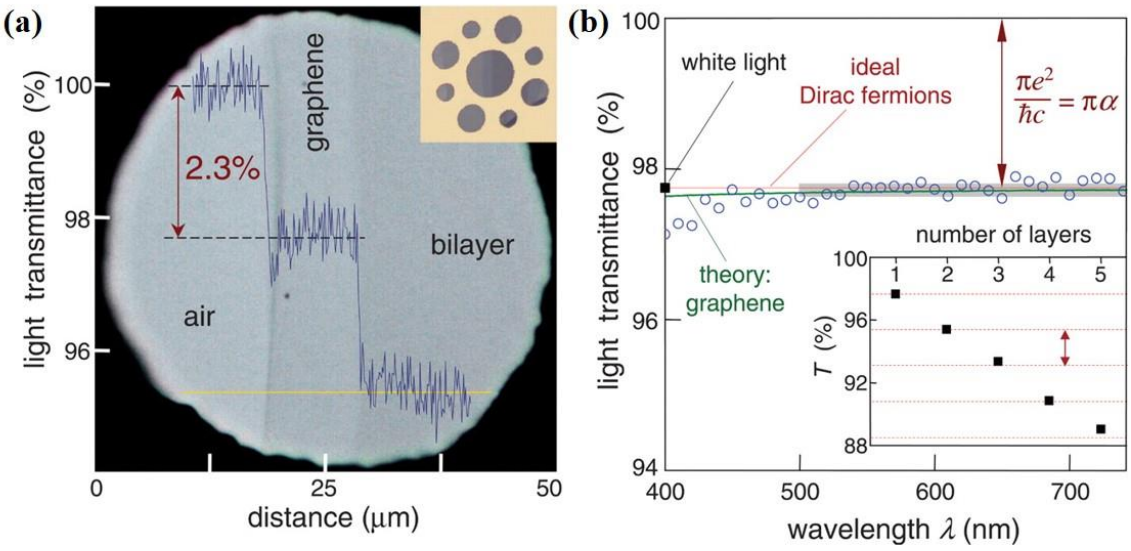

Figure 1.3 (a) Photograph of a 50 μm aperture covered by a single and bilayer of graphene. The line scan profile shows the intensity of transmitted light. Inset is the experiment setup. (b) Light transmittance spectrum of monolayer graphene (open circles) in comparison with the expected transmittance curve of Dirac fermions.[15]

1.2.3 Other Properties

The robustness of the covalent carbon-carbon bonds provides graphene with exceptional mechanical properties. Graphene has a Young's modulus higher than that of diamond (~1 TPa for graphene vs 900 GPa for diamond), making it the strongest material known.[17] It can also be stretched elastically up to 20% and is readily bent or folded.[3] The mechanical robustness of graphene makes it an attractive material for composite applications and considering its exceptional electronic and optical properties has made it an ideal material to be considered as a transparent electrode for flexible electronics and touch screen technologies.[18]

The thermal conductivity of graphene is also considerably high (> 3,000 W m K^{-1}), which obviously makes it a viable candidate for thermal management applications.[19] Graphene can also sustain extremely high current densities that are roughly a million times higher than that of copper.[20]

Finally, graphene membranes are impermeable to all gases, including helium.[21] This allows for the potential of graphene-based gas detectors.[22] One such detector could detect individual gas molecules as the resistivity of graphene would change when the gas molecules would adsorb to its surface. Being a 2D material, graphene's high surface area means that it is incredibly sensitive to very low gas concentrations.

1.3 Graphene Production

Graphene was isolated for the first time using micro-mechanical exfoliation, *i.e.* by physically peeling the layers of graphite apart until a single layer was isolated.[1] There are now several methods available to produce graphene, with the most important summarised in Figure 1.4.[6] Each method produces graphene with different properties (*e.g.* electronic quality, flake size and thickness, and surface chemistry).

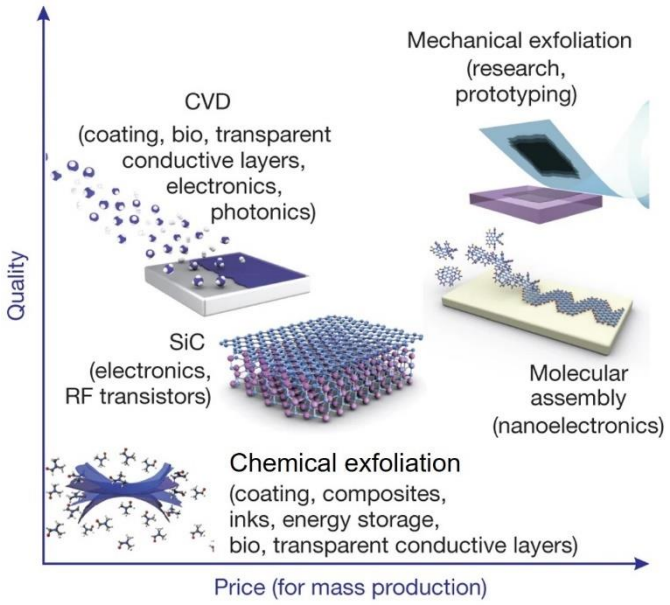

Figure 1.4 Schematic reporting the most used graphene production methods, classified based on the price and the electronic quality of graphene produced.[6]

Mechanical exfoliation is regarded as the production method of choice for generating graphene that is to be used in research because it can produce the highest quality graphene of reasonably large lateral sizes.[1,3] However, the process is time-consuming and delicate, thus has little application beyond proof-of-concept devices. Producing graphene from silicon carbide (SiC) sources provides a facile route to electronic applications as the substrate used for the growth is an insulator. There are two types of graphene that can be produced through the use of SiC: One where the graphene is grown on the Si-terminated face and another where the graphene is grown on the C-terminated face.[3,23] The former graphene is typically heavily doped by the substrate, leading to inferior quality, whilst the latter tends to produce 'multilayer epitaxial graphene'. CVD produces high crystalline quality graphene over a large area[3,24] by exposing metallic substrates (*e.g.* copper[24] or nickel[25]) to a gaseous mixture of methane and hydrogen at high temperatures (~1,000°C) which reacts at the surface to produce a polycrystalline monolayer of graphene with a substrate coverage greater than 95%. The main disadvantage of

CVD grown graphene it must be grown on a metallic substrate, thereby limiting the application potential as these substrates cannot be used for device fabrication.

In this work, graphene was produced in the group by chemical exfoliation routes, specifically by LPE of graphite and graphite oxide (to produce graphene oxide), and ECE (to produce slightly oxidised graphene). Thus, this section will focus on the production methods used in our studies. CVD graphene has also been used in our studies, but this was obtained by a commercial source.

1.3.1 Liquid Phase Exfoliation

LPE is a top-down production method where graphite is split into thinner and smaller 2D flakes with the assistance of a solvent and an input of energy, typically provided by sonication.[6,26–28] LPE was first applied to carbon nanotubes to break their bundles and disperse them individually into organic solvents.[29–32] The sonication inputs energy into the bulk crystal to physically peel the layers apart, while the solvent stabilises the forming nanomaterial. Hence, the solvent choice is the main factor governing the yield of LPE. After many years of extensive study, it has been established that in order to maximise the concentration of graphene, the surface energies of the solvent and graphene need to be as close as possible to minimise the energetic cost of the exfoliation.[26,33,34] Figure 1.5 shows the relationship between the surface tension, γ, of a range of solvents and the achievable concentration of graphene obtained under the same experimental conditions.

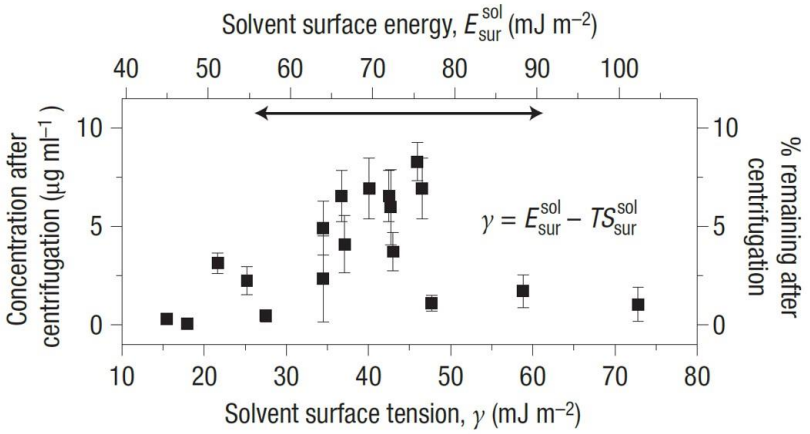

Figure 1.5 Graphene concentrations in a range of solvents plotted against the solvent surface tension and surface energy.[26]

The plot reveals a peak in concentration at a solvent surface tension of ~40 mJ m^{-2}, suggesting that organic solvents such as N-methyl-2-pyrrolidone (NMP), dimethyl sulfoxide (DMSO),

and dimethylformamide (DMF) are all efficient solvents for LPE. In contrast, water, which has a surface tension of ~72 mJ m^{-2}, cannot be used as a solvent to produce stable, concentrated graphene dispersions. Using water to produce graphene dispersions is desirable because water is cheap, clean, and safe, whereas the organic solvents are often expensive, toxic, and have high boiling points. To make water a viable solvent for LPE, two strategies can be employed: either the surface of graphene is altered (thus changing the surface energy),[7,35,36] or a stabiliser needs to be added to the water.

The first strategy is a production route for GO. This material is produced *via* the oxidation of and subsequent LPE of graphite oxide.[37–39] GO is readily dispersed in water due to the high oxygen content of the flakes, which can typically be ~40 at%, that randomly decorate the basal plane and edges of the flake in the form of epoxy (-O-), hydroxy (-OH), and carboxyl (-COOH) groups. The composition and structure of GO is still under debate due to the nonstoichiometric nature of the oxygen coverage of the flakes, but an estimation of the structure and an atomically resolved TEM image is shown in Figure 1.6. The oxygen content can be tuned within a range (from 60 wt% to 18 wt%) by using different reaction conditions, such as oxidiser concentration, and following the oxidation reaction with a reduction reaction to produce reduced graphene oxide (rGO).[36,40] GO is also a favoured platform for further functionalisation (when compared with pristine graphene) because the oxygen-containing functional groups allow for relatively simple chemistry to be performed on them.[41–43]

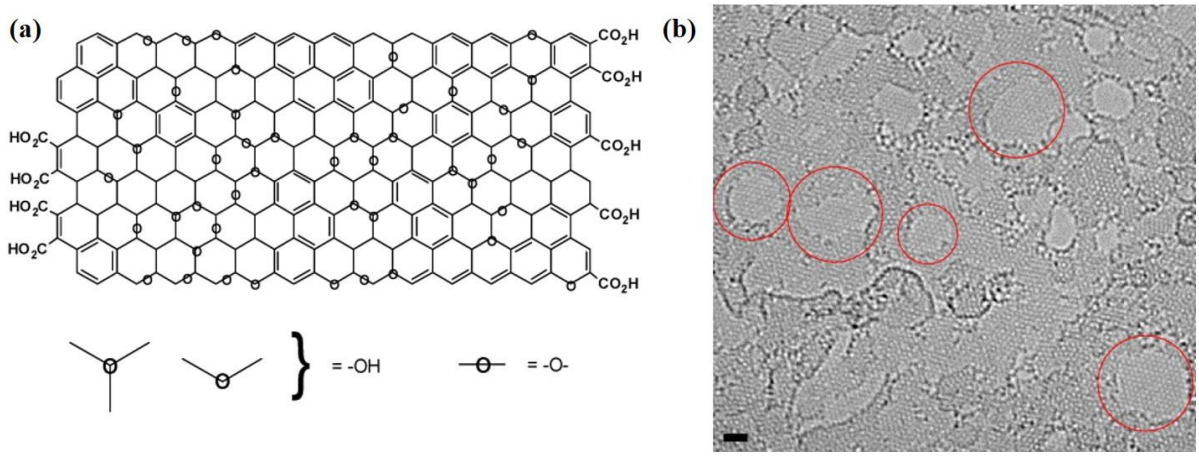

Figure 1.6 (a) An estimated chemical structure of GO, showing the potential oxygen-containing functional groups.[44,45] (b) Atomically resolved TEM image of a single-layer region of GO. The red circles indicate patches of pristine graphene whilst the majority of the area is covered by either adsorbates or functional groups.[46]

The second approach is based on the use of stabilisers, which non-covalently functionalise the graphene and facilitate favourable interactions with the water, as well as providing steric hinderance and electrostatic stabilisation to prevent re-stacking.[47,48] A wide range of stabilisers have been reported to produce stable graphene dispersions including surfactants,[49–51] polymers,[52,53] and polyaromatic molecules,[47,54,55] with pyrene derivatives being one of the more attractive stabilisers when compared to polymers and traditional surfactants.[47]

The design of the pyrene derivative is a key parameter in its effectiveness to stabilise graphene in water. A widely used derivative has sulfonyl groups (SO_3^-) bonded to the pyrene unit.[47,56–61] The pyrene unit would interact with the basal plane of the graphene flakes whilst the sulfonyl group would contribute to the stabilisation of the flakes *via* interactions with the water as well as electrostatic repulsion. However, it has been shown that too many sulfonyl groups bound to the pyrene unit has a detrimental impact on the yield of LPE, due to a very high solubility in water.[56] As well as sulfonyl groups, other charged functional groups, such as ammonium groups, pyridinium rings, and amino acid groups, have been shown to yield high concentrations of graphene in water.[59–63] It is clear from all the studies utilising pyrene derivatives that the yield of graphene in the final dispersion is determined by a balance of the interactions between the graphene, water, and the stabiliser. The current understanding of the mechanism of LPE in the presence of a stabiliser is that the stabiliser will intercalate between the layers during exfoliation,[63] however, this has not been experimentally confirmed.

1.3.2 Electrochemically Exfoliated Graphene

ECE of graphite consists of the structural deformation/delamination of a graphite electrode upon the application of a voltage between two electrodes in an electrolyte. Typical ECE experiments consist of a working electrode made of either a graphite rod, film/foil or highly orientated pyrolytic graphite (HOPG) sample and an organic, ionic or aqueous liquid as the electrolyte.[64] This electrochemical approach can either be performed *via* cathodic reduction or anodic oxidation, depending on the choice of electrolyte, which will lead to a graphene product with very different properties.

The mechanism by which the ECE of the working electrode occurs appears to be the same and it is the electrolyte that plays a crucial role in determining the exfoliation efficiency. The electrolyte should support the ions that induce the intercalation of the working electrode and generally controls the kinetics of this intercalation process. In the case of anodic oxidation, the intercalation process is coupled with an oxidation reaction between the graphite electrode and

the negative ions of the electrolyte. The mechanism of anodic ECE is shown in Figure 1.7 and can be described as a three part process: (i) application of the voltage bias causes a reduction of the water at the cathode, creating strong nucleophiles (the hydroxyl ions) in the electrolyte that attack and oxidise the graphite at the edges and grain boundaries of the electrode. (ii) The oxidation leads to expansion of the graphite layers due to electrostatic repulsion, which facilitates the intercalation of the negative ions of the electrolyte. (iii) The negative ions are reduced, and water is self-oxidised once intercalated and produce a variety of gaseous species which vigorously expand the graphite.[65,66] The expanded material can then be collected and processed further (typically with ultrasonication) to produce a high yield of graphene.

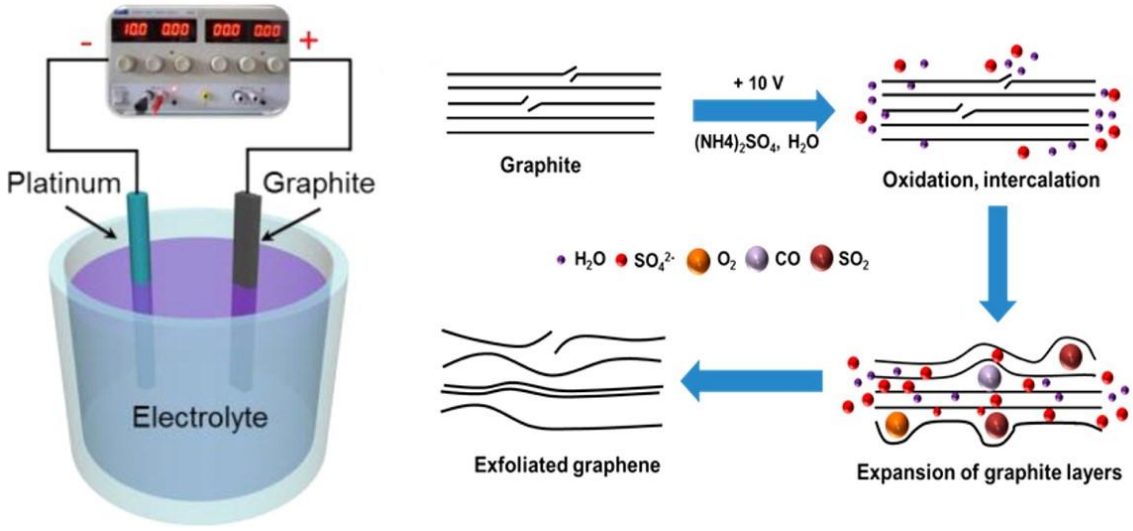

Figure 1.7 A schematic of an anodic ECE setup and the mechanism of exfoliation.[65]

Sulfate (SO_4^{2-}) based aqueous electrolytes are widely used in the anodic ECE of graphite as even before the isolation of graphene, sulfate ions were proven to be effective at generating graphite intercalated compounds,[64–68] and have been shown to produce higher yields when compared to sulfonates,[69] dodecyl sulphates,[70] and carboxylates.[71]

As the process name suggests, anodic oxidation produces oxygen-functionalised graphene, with a C/O ratio between 6.7 and 26.2, a ratio that is generally measured by X-ray photoelectron spectroscopy (XPS).[72,73] The oxygen content is heavily dependent on the experiment parameters, with the choice of electrolyte (specifically the choice of sulfate salt) greatly affecting the quality of the produced graphene.[74] The oxygen containing functional groups (*e.g.* hydroxyl groups -OH, carboxyl groups -COOH, and epoxy groups -O-) mean that ECE graphene is not only readily dispersible in organic solvents, such as NMP and DMF,[65] but also in aqueous solvents, such as water and mixed solvents.[75]

1.4 Summary

In this project, we are interested in studying the evaporation of droplets of graphene dispersions with and without organic molecules. While graphene has been widely investigated for many applications, graphene dispersions have rarely been used to conduct fundamental studies on the evaporative process of droplets (**Chapter 5**) and in particular has not been used in the framework of crystallisation of organic molecules (**Chapter 4)**. Being solution processable makes graphene an attractive material for templated crystallisation (see **Section 2.** for details on templated crystallisation) studies because it can be introduced into the crystallising system as either an additive or as a substrate, *e.g.* by depositing a thin film by drop casting or spray coating. CVD graphene can also be exploited as a substrate. Furthermore, because of its chemical tuneability, the surface properties can be readily varied (*i.e.* with different types and amounts of functional groups), which gives graphene a unique versatility that can be used to investigate the effect of the intermolecular interactions between the template and the growing crystal, as demonstrated in **Chapter 4**. The different types of graphene and their properties used throughout this thesis are summarised in Table 1.1.

Table 1.1 Comparison of the typical properties of the different types of graphene used in this thesis.

Type of Graphene	**Source**	**Lateral size**	**Thickness**	**Oxygen Content**
CVD graphene	Commercial	Wafer scale (cm)	Single layer	0 at%
LPE graphene	Produced in house	~100 *n*m	~50% single layer	0 at%
ECE graphene	Produced in house	5-10 μm	>85%, ≤3 layers	10-15 at%
GO	Commercial	<10 μm	<95% single layer	~40 at%

Chapter 2: Crystallisation from Solution

Crystallisation from solution is a phase separation and purification technique involving the molecular assembly of the solute in solution into a solid crystalline phase. Many organic molecules can crystallise with different molecular packing arrangements, generating different forms, called "polymorphs", of the same compound. The presence of these polymorphic forms can complicate the development of crystalline products because they tend to have different physical properties which could have considerable impact on the isolation of the product as well as its effectiveness. The ability to reproducibly grow crystals with the desired characteristics requires a thorough understanding of crystallisation, which is still limited, as detailed in this Chapter.

The following chapter aims to outline the known theory of nucleation and crystal growth, along with an introduction on the molecule of interest and relevant state-of-the-art for the project.

The chapter begins with an overview of some fundamental principles of crystallisation, before moving on to discuss glycine, the molecule of study during this project, and its polymorphs. The concept of heterogeneous nucleation via templated crystallisation is reviewed which lays the foundation for the work presented in **Chapter 4**.

2.1 Fundamentals of Crystallisation

The act of crystallisation is an important process in many industries and solid-state materials chemistry.[76,77] It can be separated into two main phases; the initial nucleation step followed by the crystal growth phase. Nucleation is the process by which molecules come together to form a cluster (or nucleus) of a sufficient size as to be able to drive the crystal growth.[77,78] Crystal growth is defined as the process where molecules add to a nucleus that is larger than a critical size, further increasing the size of the crystal.[77–79]

The thermodynamics of nucleation were described more than century ago by Gibbs[80] but the mechanisms governing the generation of a solid phase from solution is still limited due to the difficulty in observing the small number of molecules and short time scales involved. In this section, our current understanding on the main concepts of crystallisation are given which lays the foundation for the project.

2.1.1 Nucleation

Nucleation can be classified into either primary or secondary nucleation, where primary can be further divided into homogeneous or heterogeneous depending on the conditions, as illustrated in Figure 2.1. If primary nucleation is spontaneous in the absence of any foreign particles, then it is categorised as homogeneous. On the other hand, if it is induced in the presence of foreign particles, the process is heterogeneous.[77,78] Secondary nucleation occurs when crystals of the desired product are the cause of nucleation *via* a process known as "seeding". It has been shown that nucleation can be induced in a number of ways such as agitation, mechanical shock, friction and extreme pressures[81,82] but the main driving force behind nucleation is supersaturation of the solution.

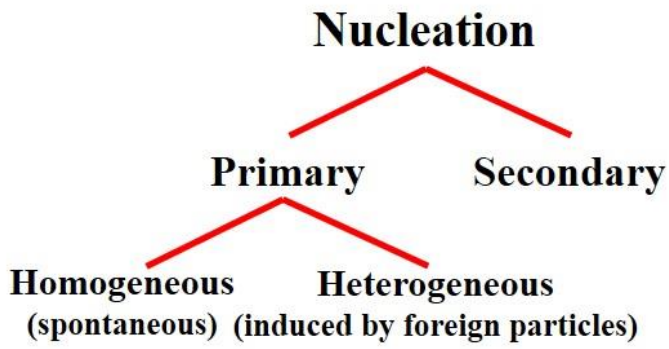

Figure 2.1 The classification cascade of nucleation.[78]

2.1.2 Supersaturation

For a non-ideal, binary solution containing a solvent and a solute, supersaturation can be related to the chemical potential difference, $\Delta\mu$, between the solute in solution, μ_s, and the solute in the bulk crystal, μ_c:[77–79,83,84]

$$\Delta\mu = \mu_s - \mu_c \qquad \textbf{(2.1)}$$

A chemical potential can be defined in terms of a standard potential, μ_0, and the activity of the solute, a:[78,79]

$$\mu = \mu_0 + k_B T \ln a \qquad \textbf{(2.2)}$$

Therefore, the chemical potential difference can be expressed as:

$$\Delta\mu = k_B T \ln \frac{a}{a^*} = k_B T \ln S \qquad \textbf{(2.3)}$$

where a^* is the equilibrium activity (*i.e.* the activity of the saturated solution) and S is the fundamental supersaturation ratio of the solution. For practical reasons however, it is common to express the supersaturation in terms of a solution concentration ratio:

$$S = \frac{c}{c^*} \tag{2.4}$$

Where c is the concentration of the solute in solution and c^* is the equilibrium saturation concentration at a given temperature. It is important to note that the fundamental supersaturation and the concentration-based supersaturation can be related using an activity coefficient, γ, ratio:

$$A = \frac{\gamma}{\gamma^*} \tag{2.5}$$

Figure 2.2 depicts a generic solubility diagram with respect to temperature. The blue solubility curve represents a concentration boundary between an undersaturated system and a supersaturated one. In the undersaturated system, solute molecules are stable with respect to crystallisation, meaning dissolution dominates and nucleation cannot occur. At low supersaturations, the system enters the "metastable zone" where nucleation becomes unfavourable whilst crystal growth occurs if seeds or nuclei are present. Continuing into the high supersaturated region means that spontaneous, and often uncontrolled, nucleation becomes favourable.

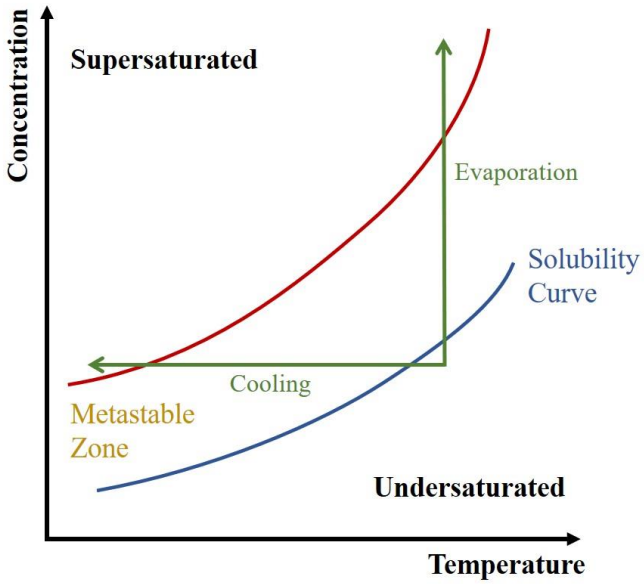

Figure 2.2 Solubility-supersaturation diagram showing the paths for evaporative and cooling crystallisation.[78,84]

There are two common methods to achieve supersaturation: evaporative crystallisation and cooling crystallisation. The former generates supersaturation by increasing the solute concentration through solvent evaporation, whilst the latter decreases the solubility of the solute, thereby decreasing the equilibrium concentration. Similarly to cooling crystallisation, adding an anti-solvent to the system, defined as a solvent that does not dissolve the given solute, will also decrease the equilibrium concentration and drive the system into supersaturation.[78,83,85,86]

2.1.3 Homogeneous Nucleation

Once enough solute molecules are in solution to constitute a supersaturated system, the molecules must form an agglomerate (the nucleus). The first model formulated for homogeneous nucleation, now referred to as classical nucleation theory (CNT), involves a first-order phase transition and was derived by Volmer and Weber[87] who based the model on the works of Gibbs.[80]

The model defines the overall change in free energy, ΔG, as a sum of the surface (interfacial) excess free energy, ΔG_S, and the volume excess energy, ΔG_V, as following:

$$\Delta G = \Delta G_S + \Delta G_V \qquad \textbf{(2.6)}$$

For a spherical nucleus of radius r, molecular volume v, and surface free energy γ, Equation 2.4 is expanded to give:[78,84,87]

$$\Delta G = 4\pi r^2 \gamma - \frac{4}{3}\pi \frac{r^3}{v} k_B T \ \ln S \qquad \textbf{(2.7)}$$

Due to the opposite signs and different dependencies on r of the right-hand terms, ΔG will pass over a maximum threshold, as illustrated in Figure 2.3. Physically, this illustrates the fact that the formation of nuclei is energetically unfavourable until a critical nucleus size, r_c, is reached where the free energy reaches a transition state, ΔG^*, and can proceed to crystal growth.

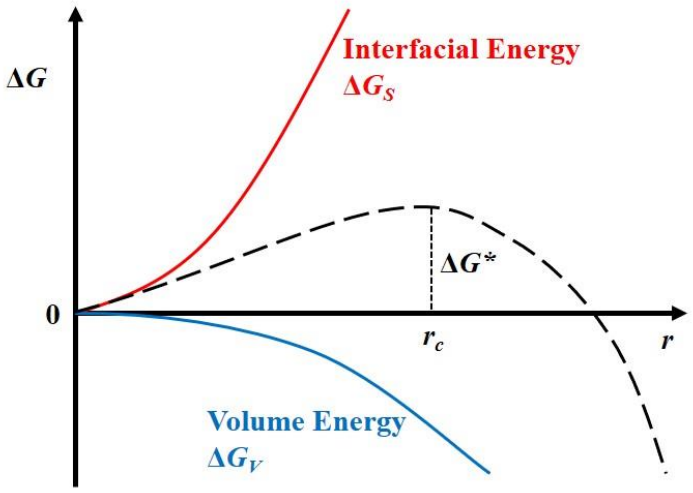

Figure 2.3 Free energy change with respect to nucleus size, with an indication of the critical nucleus size, r_c.[84]

The value of r_c can be determined by taking the derivative of the free energy since it occurs at a maximum:[78,84]

$$r_c = \frac{2\gamma v}{k_B T \ln S} \quad \textbf{(2.8)}$$

Substituting Equation 2.8 into 2.7 gives an expression for the Gibbs free energy of activation of nucleus formation, ΔG^*:[78,84]

$$\Delta G^* = \frac{16\pi v^2 \gamma^3}{3(k_B T \ln S)^2} \quad \textbf{(2.9)}$$

Equation 2.9 shows that the activation barrier to crystallisation is significantly impacted by both the interfacial energy of the crystal and the supersaturation of the system. By reducing the former or increasing the latter, the barrier can be drastically reduced. It is important to note at this stage that crystallisation is a dynamic process, therefore as it proceeds the supersaturation decreases in order to reach equilibrium, *i.e.* an S value of 1. By operating at higher supersaturations, nucleation is encouraged, hence promoting many smaller crystals. Conversely, by maintaining a supersaturation close to the metastable zone, nucleation can be restricted, resulting in the formation of fewer, but larger, crystals.[83]

2.1.4 Heterogeneous Nucleation

The model so far has described an ideal system where the solution is pure, containing only solvent and fully solvated solute molecules. Practically however, this is rarely the case as

solutions will frequently contain foreign entities such as impurities (*e.g.* dust, bubbles, contaminants *etc.*), solid surfaces (*e.g.* vessel walls) or, as mentioned in Section 2.1.1, seeds of the desired crystallisation product. Thus, it is generally accepted that true homogeneous nucleation is difficult to achieve,[77,84] so an insight into how the energetics are altered by surfaces will now be considered.

As shown in Equations 2.8 and 2.9, there is a heavy dependency on the surface free energy, γ, on the energetics of the system. Introducing foreign bodies into the system can modify this term and choosing a 'suitable' impurity will lower the barrier to nucleation, meaning heterogeneous nucleation becomes the favourable route to crystallisation. For this to be the case, the following expression must be true:

$$\Delta G^*_{HET} = \varphi \Delta G^*_{HOMO} \qquad \textbf{(2.10)}$$

Where ΔG^*_{HET} and ΔG^*_{HOMO} are the activation barriers under heterogeneous and homogeneous conditions, respectively, and φ is a correction factor that is less than unity.[78,84] As an example of how the correction factor can be calculated, let's consider a system that contains two solids and liquid, *i.e.* the crystalline solid (c), a foreign surface (s), and a liquid (l) and their associated surface free energies. Figure 2.4 (a) illustrates the system and how the surface free energies are connected, denoted as γ_{cl} (between the crystalline solid and the liquid), γ_{cs} (between the crystalline solid and the foreign surface), and γ_{sl} (between the foreign surface and the liquid).

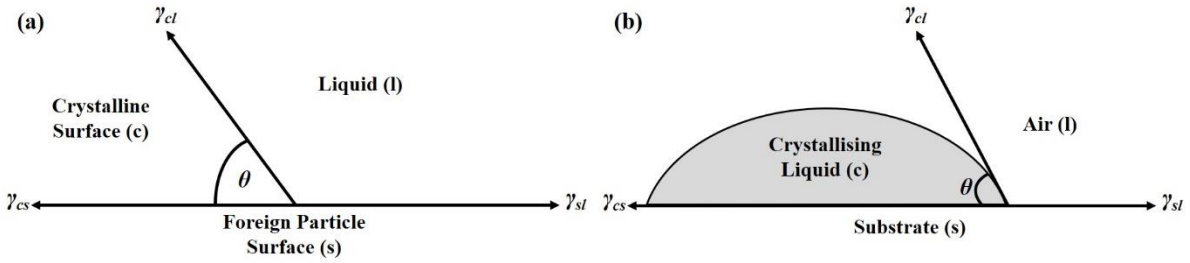

Figure 2.4 (a) Surface free energies at the boundaries between three phases (two solids and a liquid).[78] (b) Contact angle of a droplet on a substrate allowing for the derivation of the Young's equation.

By resolving the forces shown, the Young's equation can be established:[88]

$$\gamma_{sl} = \gamma_{cs} + \gamma_{cl} \cos\theta$$

$$\cos\theta = \frac{\gamma_{sl} - \gamma_{cs}}{\gamma_{cl}} \qquad \textbf{(2.11)}$$

The angle θ, the angle between the crystalline solid and the foreign surface, corresponds to the wetting angle (or contact angle, as shown in Figure 2.4 (b)) in solid-liquid systems.

The correction factor can then be expressed in terms of the contact angle by:[84,87,89]

$$\varphi = \frac{(2 + \cos\theta)(1 - \cos\theta)^2}{4} \quad \textbf{(2.12)}$$

Three cases are now established depending on the value of the angle θ and the wettability of the substrate with respect to the crystallising liquid. When $\theta = 180°$, there is no wetting of the substrate by the crystallising liquid ($\varphi = 1$), hence $\Delta G^*_{HET} = \Delta G^*_{HOMO}$ and no reduction in the activation barrier is observed. For angles $0° < \theta < 180°$, there is partial wetting substrate ($\varphi < 1$), resulting in a reduction in the activation barrier and favourability shift towards heterogeneous nucleation. The final case, when $\theta = 0°$, is for complete wetting of the substrate and results in a reduction of the activation barrier to zero. This is a unique case of heterogeneous nucleation and occurs when the foreign surface is a the desired crystalline solid, *i.e.* the system is seeded and proceeds *via* secondary nucleation.[77–79,83,84]

2.1.5 Nucleation Rate

The rate of nucleation, *J*, defined by CNT as the number of nuclei formed per unit time per unit volume, is dependent on the activation free energy and can be expressed by an Arrhenius equation:

$$J = A \exp\left(\frac{-\Delta G^*}{k_B T}\right) \quad \textbf{(2.13)}$$

Where the pre-exponential factor, *A*, also depends on the supersaturation and has a theoretical value of 10^{30} nuclei cm^{-3} s^{-1}.[90] Prior to a threshold of supersaturation, S_c, being reached, the nucleation rate is zero, but crossing the threshold causes the rate to increase exponentially, as shown in Figure 2.5. This threshold corresponds to the metastable zone width, *i.e.* the boundary between the undersaturated and high supersaturated regions of Figure 2.2.[77,84,91]

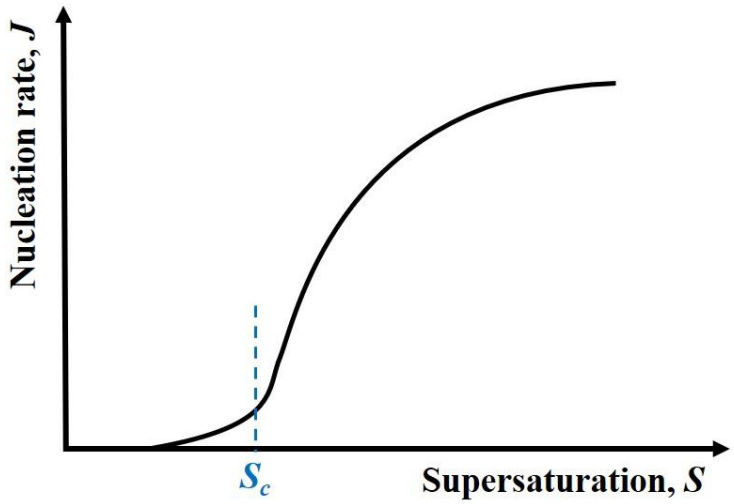

Figure 2.5 Nucleation rate, *J*, as a function of supersaturation, *S*.[77]

Whilst Equation 2.13 hints that the nucleation rate should continue to increase with increasing supersaturation without limit, Figure 2.5 shows that the rate does begin to level at sufficiently high supersaturations. This observation can be explained by considering the molecular freedom of solute molecules at varying supersaturations. At lower supersaturations, the solute molecules have a high degree of molecular movement, thus a positive relationship between supersaturation and nucleation rate exists. However, at very high supersaturations, the solution becomes viscous in terms of solute molecules. This viscosity restricts the molecular freedom of the solute molecules and will inhibit the formation of ordered crystal structures.[78]

2.1.6 Induction Time

Nucleation is an inherently stochastic process.[92] As the rate of nucleation is heavily dependent on the temperature, the supersaturation, and the surface free energy of the system, any slight variation of conditions can have a profound impact on the rate.[78,79] To overcome the potential randomness, a statistical approach is often taken to determine nucleation rates.[92–95] Additionally, direct measurement of nucleation rates is difficult which is typically overcome by inferring the rate from the observation of another kinetic parameter, the induction time, t_i. Induction times are defined as the elapsed time between achieving supersaturation and the detection of crystals and can be expressed as:[77,78]

$$t_i = t_r + t_n + t_g \qquad \textbf{(2.14)}$$

The three time periods seen in Equation 2.12 are defined as: the relaxation time, t_r, which is the time required for the system to reach a quasi-steady state distribution of molecular clusters;

the time required for the formation of a nucleus, t_n; and the time required for the nucleus to grow to a detectable size, t_g. The nucleation rate is then related to the induction times by the following:[77,78]

$$J \propto t_i^{-1} \quad \textbf{(2.15)}$$

2.2 Classical vs. Non-classical Nucleation

Since its conception, CNT has been a staple for researchers to explain their nucleation findings, but evidence exists showcasing its limitations, particularly between computational predictions and associated experimental results.[96–99] The discrepancies found for CNT have been attributed to the fact it was developed to describe the condensation of vapour to liquids, where local molecular density was the only order parameter that differs between the old and new phase.[100,101] This is not the case for solution-based crystallisation where periodic ordering is also necessary to distinguish between the two phases.[101,102] The equations detailed in Section 2.1 and Figure 2.3 hint at one of the more significant shortcomings of CNT; the only criterion for dictating whether an aggregate is defined as a nucleus is the size of the aggregate. CNT fails to give mechanistic information about how solute molecules arrange themselves into ordered arrays as it assumes that density and ordering occur simultaneously (*i.e.* molecules come together in ordered arrays), thereby inferring that the nuclei and the final crystal have the same structure, which has been shown to not be the case.[101,103,104]

An updated mechanism for nucleation has been proposed, which separates the processes of solute concentration and ordering into something called "Two-step Nucleation".[102,105–107] This model describes how a local increase in solute density (*i.e.* concentration) results in the formation of a dense liquid-like cluster (LLC), also commonly referred to as pre-nucleation clusters (PNC),[101,108,109] which leads on to a rate-determining step of molecular organisation into clusters that resemble the final crystal. An illustration of the process is provided in Figure 2.6. Figure 2.6 (a) and (b) are schematics of the formation and eventual ordering of a cluster into a nucleus.[107] A comparison of the free energies of nucleation between CNT and two-step is given in the profile shown in Figure 2.6 (c).[107,110] The profile also reveals that there are two possible paths for nucleation when considering two-step nucleation: if the LLC is unstable with respect to the solution, the free energy of formation of the LLC is $\Delta G^0_C > 0$ and nucleation occurs in the mesoscopic clusters; if the dense liquid is stable, the formation energy is $\Delta G^0_{L\text{-}L} < 0$ resulting in nucleation occurring inside macroscopic droplets. ΔG^*_1 is the energy barrier

for the formation of the LLC and ΔG^*_2 is the energy barrier for the structural rearrangement that leads to an ordered cluster.[107]

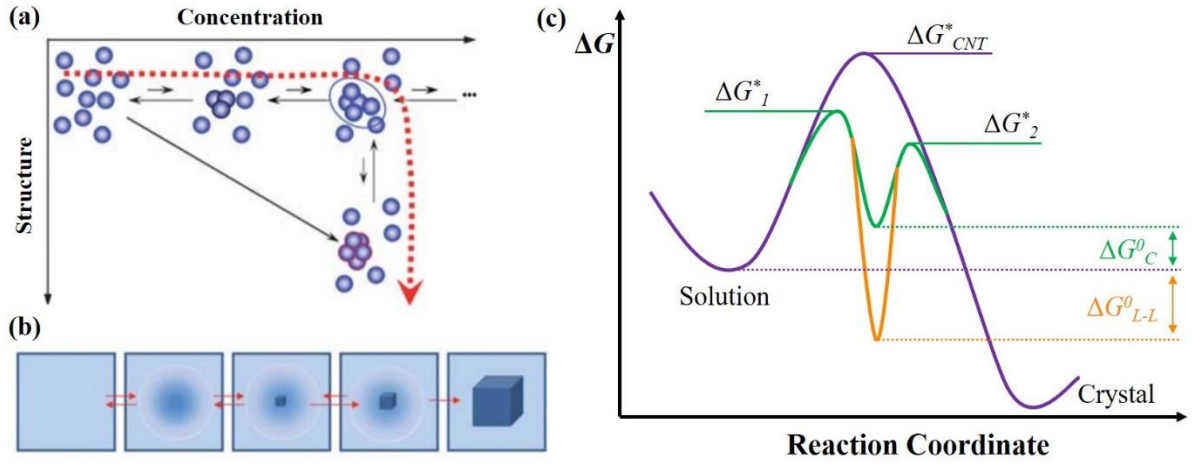

Figure 2.6 Schematic illustration of the two-step nucleation mechanism. (a) Microscopic viewpoint along the concentration-structure plane; (b) Macroscopic viewpoint of the events along the dashed line in (a). (c) Free energy diagram that compares the energies of CNT (purple) to two-step (green and orange) nucleation and shows the possibility of two pathways undertaken by two-step nucleation depending on the stability of the dense liquid phase.[107,110]

It is important to emphasise here that the formation of a dense LLC should not be confused with liquid-liquid phase separation (*i.e.* oiling out), which can be observed during the crystallisation of proteins and other small molecules.[104,111] Liquid-liquid phase separation leads to a dispersion of microscopically visible droplets of concentrated solution within a less concentrated continuous phase. This separation can arise because the initial liquid phase is metastable with respect to two liquid phases, a phenomenon known as a submerged liquid-liquid miscibility gap. Nucleation, either by classical or non-classical means, can occur in both phases as the act of separation only generates two different compositional environments, both being labelled as bulk phases.[104] So whilst nucleation looks to be proceeding in two-steps, oiling out is merely a potential pre-requisite to nucleation. The two-step theory has been successfully applied to many systems, predominantly proteins[105,107] and inorganic molecules[108,112–114] but has also started to be applied to organic molecules.[115–119]

2.3 Polymorphism

As well as growing with different morphologies, at varying sizes, and chemical purities, crystals can display a property known as polymorphism, which is the ability of a crystal to have more than one molecular packing arrangement, giving rise to multiple potential crystalline

structures.[120] The first example of polymorphism in an organic substance (benzamide) was found nearly 200 years ago by Liebig and Wohler in 1832.[121]

The different structures that are generated due to polymorphism can exhibit substantially different physical properties (*e.g.* solubility, density, heat capacity, melting point, and thermal conductivity), thus the study of polymorphism of molecular materials has become a very active area of research.[122–124] Despite many years invested into polymorphism control, obtaining a desired form of a crystal, particularly from solution, is still a challenge as the lattice energies of different polymorphs are generally only a few kJ mol^{-1} apart, therefore concomitant formation of various polymorphs from solution is often reported.[125–127]

It was observed in the 19th century that some salts would crystallise as a thermodynamically less stable polymorphic form when the solution was rapidly cooled. This led to the development of the "Ostwald's Rule" or "Ostwald's rule of stages" (from the name of the scientist, Wilhelm Ostwald), where the energy change going from a supersaturated solution to equilibrium involves a number of steps, where each step represents the lowest possible change in free energy.[128,129] Accordingly, the initial phase transformation produces the least stable form (or even an amorphous phase) of a crystal which then undergoes a series of irreversible transformations through progressively more stable forms until the thermodynamically stable form is generated, as illustrated in Figure 2.7. Whilst the rule ignores any effects of nucleation kinetics of the different forms and their relative growth rates, resulting in documented exceptions,[122,127] it has gone a long way in assisting in the understanding of polymorphism and the ability of crystals to actually grow in their thermodynamically unstable forms.[130–132]

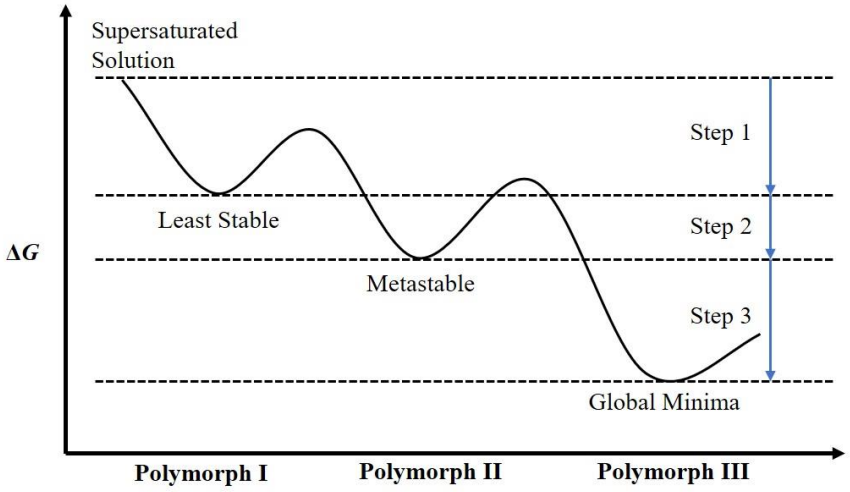

Figure 2.7 Hypothetical free energy diagram of successively more stable polymorphs of a crystal illustrating Ostwald's Rule.[133]

Polymorphs can have different stabilities with respect to temperature and solubility, and when a phase diagram is established between a polymorphic pair, a distinct relationship can be seen between the pair, as shown in Figure 2.8. If the solubility curves of the pair do not cross at any point on the diagram, it means the solubilities are independent of temperature, making the polymorphic pair monotropically related (Figure 2.8 (a)). This results in an inability of the polymorphs from transforming into the other. However, if the solubility curves do intersect at any point, the solubilities are temperature dependent, making the polymorphic pair enantiotropically related (Figure 2.8 (b)), enabling reversible transformation at a given transition temperature, $T_{transition}$.[83]

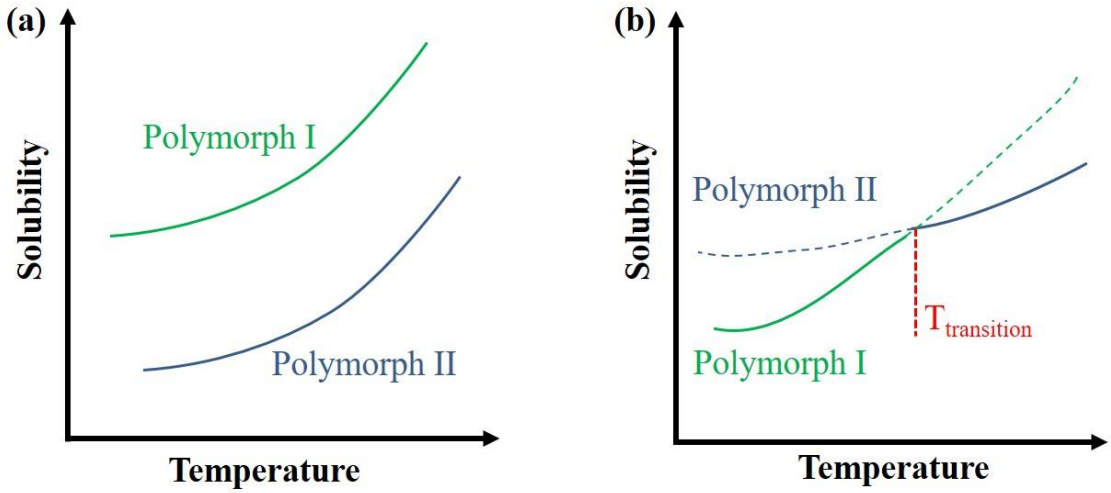

Figure 2.8 Solubility curves of a polymorphic pair that are either monotropically (a) and enantiotropically (b) related.[83]

2.4 Templated Crystallisation

As discussed in the previous section, there are many factors that can influence the polymorphic outcome of crystallisation. Temperature,[134] solvent choice,[135,136] solvent volume,[137,138] and even spatial confinement[132,139–141] have all been shown as effective ways of controlling polymorphism. An alternative approach is based on the use of templates. This is the method used in this work.

There are numerous ways to template and direct crystallisation towards obtaining crystals of specific polymorphs or morphologies. Typical strategies include designing specific substrates upon which the crystals grow, adding additives which can interact with the crystallising molecules in solution or even by confining the event in a small area. A short overview of some

these strategies is given in this section, whilst the next section will focus on the templated crystallisation of glycine, the model molecule of choice for this thesis.

As discussed in Section 2.1.4, the influence of foreign bodies (such as surfaces or additives) on nucleation depends on the affinity between the nucleus and the foreign body. This affinity is inferred to be related to the ability of the foreign element to effectively mimic the structure of the crystal.[78] In the case of low affinity, any solute molecules that adsorb onto the surface of the foreign body show no preferable orientation, *i.e.* they remain as free solute molecules. However, high affinities lead to epitaxial crystallisation where the solute molecules orientate themselves to the structure of the foreign body. Examples of epitaxial crystallisation have been reported for ice,[142,143] proteins,[144] and an assortment of inorganic and organic molecules[145–149] on specific substrates.

The influence of a foreign body on nucleation does not necessarily have to be a beneficially one. Whilst the affinity between the foreign species and nucleus could be strong, it could have an inhibiting effect on the developing nucleus.[150] In general, additives that hinder crystallisation have a strong influence on the crystal growth process as they attach to and block certain surfaces on the growing crystal.[104] It has been previously reported that some tailor made-made additives can stereo-selectively bind to faces of a crystal and alter the diffusion of the monomer molecules.[151–154]

The act of templating crystallisation through the use of additives has been, and continues to be, well documented.[154–163] Additives can have similar structures to the crystallising molecule but can also be made of a vastly different material. Examples of the latter of these two situations occur when inorganic salts are used to direct the crystallisations of proteins or organic molecules.[161–165] Sodium chloride has been used to stabilise the metastable form of flufenamic acid, which typically undergoes a rapid interface mediated polymorphic transformation.[161] The nucleation of glucose isomerase can be influenced through the use of ammonium sulfate, where increasing the concentration of the salt not only led to a polymorphic change from the I222 form to the $P2_12_12$ form, but also a change to the mechanism by which the crystal grows, as shown in Figure 2.9 (a).[163] When the additives have similar structures to the crystallising molecule, the major reason for any effect of the crystallising outcome is due to favourable (or competing) intermolecular interactions. As shown in Figure 2.9 (b), it was reported that the weak hydrogen bonds that can form between 3-nitrophenol (crystallising molecule) and 3-aminobenzoic acid (additive) hinder the kinetics of the crystallisation.[152]

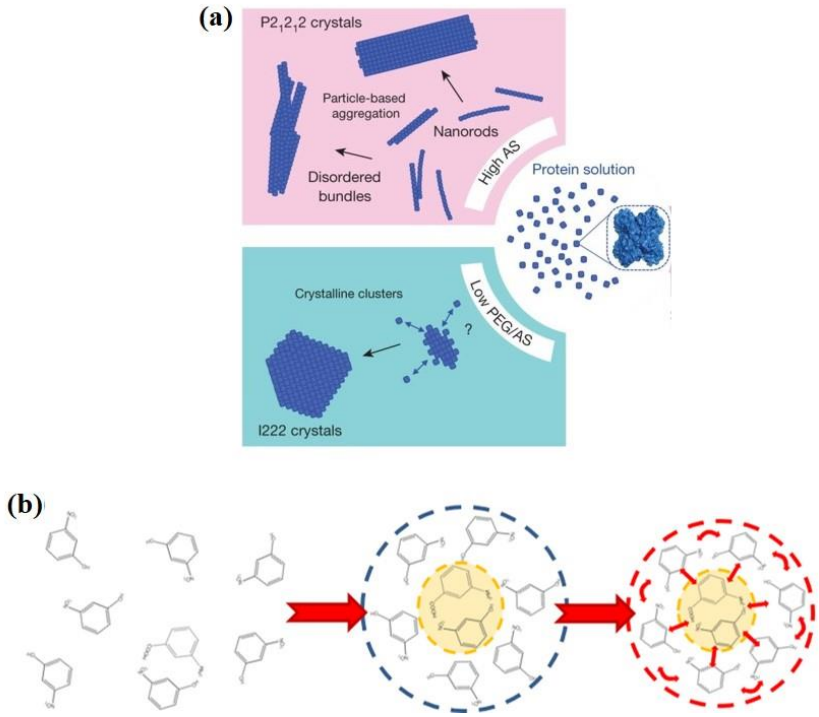

Figure 2.9 (a) Schematic representation of the crystallisation of glucose isomerase with respect to the concentration of ammonium sulfate. High concentrations led to a two-step type mechanism of nucleation, whilst low concentrations proceeded *via* a classical route.[163] (b) A scheme showing the ability of 3-aminobenzoic acid to inhibit the crystallisation of 3-nitrophenol through weak hydrogen bonding interactions.[152]

Substrate templating is readily employed to achieve control over crystallisation. One aspect of substrate templating is to utilise the physical structure of a substrate to direct crystallisation in a manner similar to epitaxial crystallisation.[166–173] A substrate selection process (Figure 2.10 (a)) was put in place and applied to the crystallisation of paracetamol. In the process, substrates must pass certain criteria such as matching unit cell parameters with the desired crystal, having certain functional groups, and being insoluble in the crystallising solvent in order to be eligible for testing.[171] One study rationalised the formation of the least stable polymorph of the salt $(DMTC^{+})(TMO^{-}).CHCl_3$ (DMTC = 3,3'-dimethylthiacarbocyanine; TMO = 3,3',5,5'-tetramthyltrime-thine oxonol) by explaining that there was a match between the dihedral angles of two-close packed planes of the single-crystalline succinic acid substrates and the pre-nucleation cluster of the salt.[166,167] Polymer substrates that had been imprinted with nanopillars angled to various degrees have been used to show that paracetamol's crystallisation can be angle-directed, schematically shown in Figure 2.10 (b). At angles of 40°, the nanopillars greatly enhanced the nucleation rate of paracetamol. This indicated a potential geometry match

between the growing crystalline phase and the pillars, which was later confirmed by molecular dynamic simulations that indicated that the intrinsic angle between the {001} and {011} faces of paracetamol is 34°.[168]

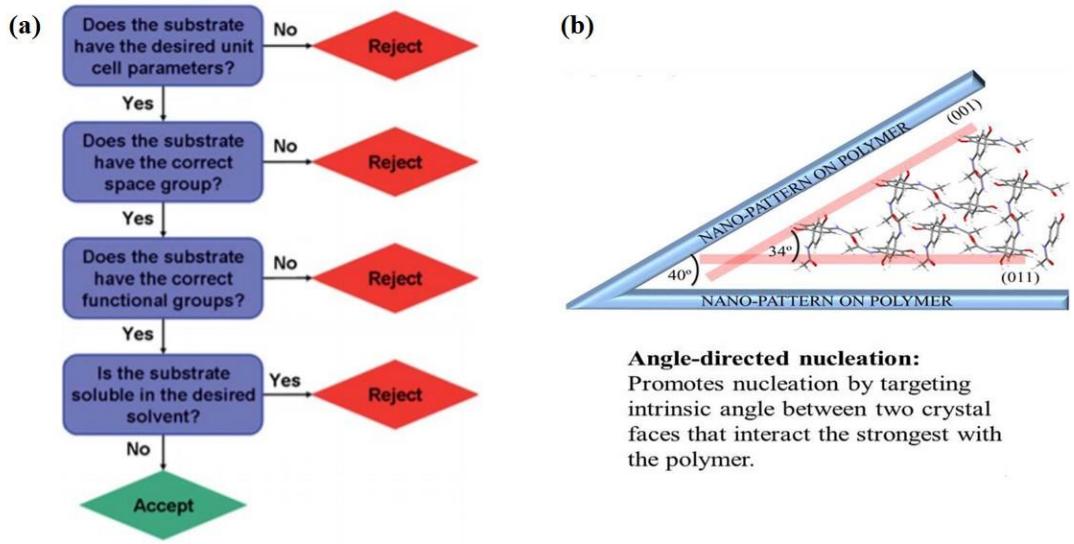

Figure 2.10 (a) Proposed substrate selection process.[171] (b) A representation of the angle-directed nucleation of paracetamol in 40° angled nanoimprinted polymer substrates.[168]

Self-assembled monolayers (SAMs) are a class of substrates that have been heavily utilised to template the crystallisation of a wide range of molecules because their surface properties can be easily tuned to suite a particular need.[174–179] A combination of geometric lattice matching and chemical interactions were proposed to be the governing mechanism behind the polymorphic selectivity of 1,3-bis(*m*-nitrophenyl) urea on 4-X-mercaptobiphenyls (X = H, I, and Br).[174] 11 different siloxane based SAMs and 3 different solvents were also used to selectively grow the metastable forms (*β*-, *δ*- and *γ*-) of 1,3-bis(*m*-nitrophenyl) urea due to a suppression of the stable *α*-form brought about by thermodynamic stabilisation at the SAM-crystal interface.[175] Siloxane-coated glass templates functionalised with different groups (*e.g.* isocyanate, acetate, bromine *etc.*) have further been exploited to crystallise the least stable form of diphenylurea. These crystals grew in a variety of morphologies (*e.g.* plates, needles, hollow tubes, or spirals) depending on the type of functional group on the SAMs.[176] The polymorphism of the nonsteroidal anti-inflammatory drug, indomethacin, has been examined on perfluoroalkyl-terminated siloxane SAMs where they were able to suppress the nucleation of the metastable *α*-form and selectively grow the more stable *γ*-form.[177] A phenylalanine derivative was used to fabricate a self-assembled multilayer substrate which was able to stabilise the metastable α-form of L-glutamic acid.[179]

Confining the space in which crystallisation occurs to the nanoscale is another approach taken to template crystallisation. A variety of nanoporous matrices (*e.g.* controlled pore glass (CPG), porous silica gel, anodised aluminium oxide (AAO), macroscopic polymeric matrices, and supramolecular gels) have been used to confine the crystallisation of different compounds.[132,140,180–187] Confinement is primarily a physical approach to templating, so the pore size and shape play a crucial role in the process, as evidenced by the confined crystallisation of aspirin and schematically shown in Figure 2.11 (a).[188] Multiple studies have shown that the least stable *β*-form of glycine could be formed when crystallised in nanoporous matrices of CPG and hydrophilic nanoporous poly(N,N-dimethylacrylamide)-block-polystyrene (PS-PDMA) monoliths.[132,140,184] These indicated that the relative stability of polymorphs may be connected to the size of the crystal, much like the stabilities are connected to each other by temperature as described in Section 2.3 and shown in Figure 2.11 (b).[189] Microemulsions can also confine the crystallisation and have been successfully applied to the polymorphic control of glycine, mefenamic acid and 5-methyl-2-[(2-nitrophenyl)amino]-3-thiophenecarbonitrile (also known as ROY due to the red, orange, and yellow crystals it can produce).[141,185,186,190]

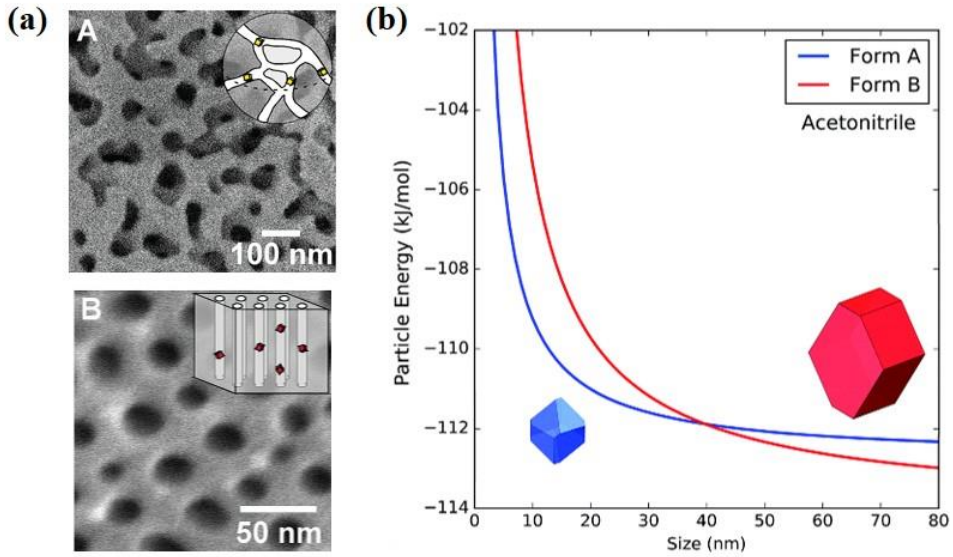

Figure 2.11 (a) Scanning electron micrographs of CPG with a pore diameter $d \approx 55$ nm (top) and porous monoliths with a hexagonal array of cylindrical pores with diameter $d \approx 30$ nm (bottom). Insets are schematic representations of nanocrystals being grown in the pores.[139] (b) Energy of crystals of an aromatic disulfide compound with two polymorphic forms A and B as a function of particle size in acetonitrile.[189]

2.4.1 Glycine

The molecule investigated in this thesis is glycine. It is the simplest of the amino acids, glycine and it is an important compound for biology as it serves as a basic building block for proteins. Its structure is shown in Figure 2.12. Glycine was chosen as the model molecule for our studies because of its already extensively researched ability to form different polymorphs.

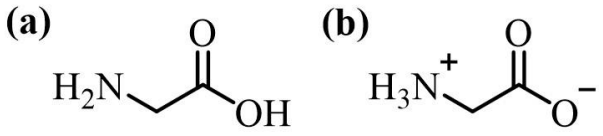

Figure 2.12 Molecular structure of glycine (a) and its zwitterionic form (b).

When glycine is dissolved in highly polar solvents, such as water, and even when it is in its crystalline form, it exists as a zwitterionic molecule (Figure 2.13 (b)).[191–193] Currently, there are six polymorphs of glycine known, denoted as: *α*-, *β*-, *γ*-, *δ*-, *ε*-, and *ζ*-glycine. The latter three polymorphs (*δ*-, *ε*-, and *ζ*-) are only known to exist under high pressures.[194–197] Given that our studies are all conducted at ambient conditions, only the former three polymorphs (*α*-, *β*-, and *γ*-) are considered relevant. Using calorimetry techniques, the relative thermodynamic stabilities of these three glycine forms at room temperature have been found to be $\gamma > \alpha > \beta$.[198,199] The crystal structures of the ambient polymorphs of glycine are shown in Figure 2.13. All three forms consist of head-to-tail robust chains of molecules held by NH···O hydrogen bonds.[200]

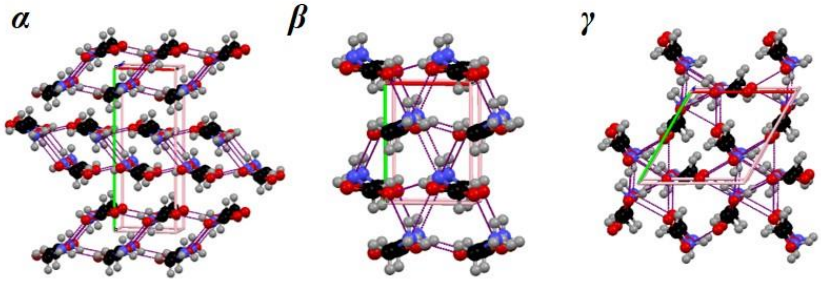

Figure 2.13 Crystal structures of the *α*-,[201] *β*-,[202] and *γ*-polymorphs[203] of glycine. The atoms are labelled as such; C: black, H: grey, N: blue, and O: red.

The metastable polymorph, the *α*-form, has a monoclinic crystal structure where the chains form into pairs of antiparallel layers. These layers are held together exclusively by van der Waals interactions.[198] It has a space group of $P2_1/n$ and unit cell dimensions of a = 5.102 Å, b = 11.970 Å, c = 5.447 Å, and β = 11.42°.[201,204] The unit cell consists of 4 molecules and as such is the densest of the three considered polymorphs.[205]

The least stable β-form also has a monoclinic crystal structure, where the layers are now linked by hydrogen bonds, in contrast to the α-form. The β-polymorph has no centre of symmetry and is actually a polar crystal, enabling it to display piezoelectricity.[206,207] It is part of the $P2_1$ space group, has a 2-fold screw along the polar b-axis, and has unit cell dimensions of a = 5.077 Å, b = 6.267 Å, c = 5.379 Å, and β = 113.12°.[206] This form is monotropically related to the other forms, thus will not transform as a result of temperature change.[193]

The most stable polymorph, γ-glycine, is composed of trigonal hemihedral units, where the zwitterionic chains form triple helixes, due to an out of plane nitrogen atom, that are linked by hydrogen bonds in a 3D network. It belongs to the $P3_1$ space group, has a 3-fold screw along the polar c-axis, and has unit cell dimensions of a = b = 7.037 Å, c = 5.483 Å, and β = 120°.[203] The α- and γ-forms of glycine are enantiotropically related, but the transition temperature between the two crystals is heavily dependent on the geometry and mechanical treatment of the crystals.[193]

In addition to distinguishable crystal structures, each polymorph has a typical crystal morphology when it grows, illustrated in Figure 2.14. The α-form typically grows with a bipyramidal shape (Figure 2.14 (a)).[208,209] The β-form normally has a needle-like morphology (Figure 2.14 (b))[210] but has been shown to form plate-like crystals when crystallised from aerosolised aqueous solutions.[211] γ-glycine can form in a variety of morphologies depending on the crystallisation parameters. The most notable ones are: the needle-like morphology (Figure 2.14 (c)),[212] which is the most common crystal habit to find; plate-like crystals through the solution-mediated transformation of the α- to the γ-form;[213] pyramidal crystals when crystallised under a strong direct current electric field;[214] and prismatic bipyramidal (Figure 2.14 (d)) which can be obtained through careful modulation of the supersaturation during crystal growth.[208]

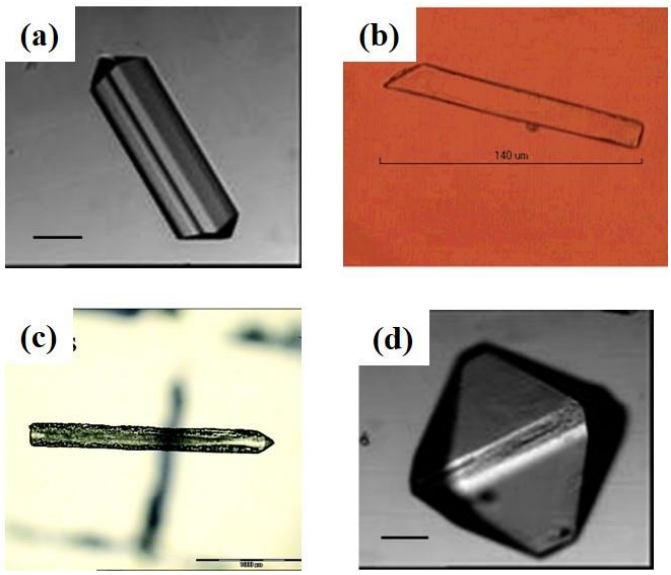

Figure 2.14 Examples of the typical morphologies obtained for the ambient polymorphs of glycine. (a) The bipyramidal crystal habit of α-glycine;[208] (b) the needle habit of β-glycine;[210] (c) the needle[212] and (d) prismatic bipyramidal habits of γ-glycine.[208]

Despite its molecular simplicity, glycine's polymorphism is relatively complex, with each polymorph being intrinsically linked. Being kinetically favoured, α-glycine is the major product from aqueous solution crystallisations.[201,215,216] The β-form is commonly yielded from anti-solvent cooling crystallisations, where alcohols such as ethanol or methanol are added to aqueous solutions to prohibit the nucleation of the α-form.[217] However, it readily transforms to α-glycine in the presence of water (*e.g.* in a humid environment), via a solvent-mediated phase transformation.[199,206,218] The stable γ-form can be crystallised from acidic or basic conditions,[155,203,219] but has also been shown to be the preferential product if crystallisation could proceed completely homogeneously.[220] Obtaining a single polymorph of glycine via evaporative crystallisation of small volumes of solution is challenging because all three polymorphs have the opportunity to crystallise concomitantly from supported microdroplets,[137,221] as also exemplified by our experiments (**Chapter 4**).

Raman spectroscopy is a non-invasive optical characterisation technique and is widely used for the structural analysis of molecules and crystals. It revolves around investigating the interaction of light with matter and specifically measures the energy of scattered photons produced when a molecule is irradiated with a high intensity laser.[222,223] The interaction of the light with a molecule induces a transition to a higher energy level. As Raman scattering is a non-direct excitation of molecular vibrations, a molecule is promoted to a virtual excited energy state which is highly unstable. A photon is then immediately re-emitted and detected. This photon

has been inelastically scattered through its interaction with a molecule, causing it to shift in frequency relative to the incident photons. The scattered photons carry specific information about a molecule's vibrational, rotational, and electronic states. For a molecular vibration to be Raman active there must be a change in polarisability (*i.e.* an induced dipole moment) upon photon absorption.[222,223] Therefore, any alteration to the polarisability and/or the vibrational energy states of a bond will result in a different Raman spectrum being generated. Consequently, Raman spectroscopy can be readily used to determine the polymorph of a crystal, as the different molecular packing of various polymorphs will change the polarisability of certain bonds. With a laser spot size typically around 0.5 μm, it is an ideal technique to measure crystals produced from microdroplet crystallisations where small crystals (often only ranging into the micrometre scale) are produced that can be difficult to individually measure using techniques such as XRD or FTIR. Another advantage that Raman spectroscopy has over IR is that water is a weak Raman scatterer, meaning any potential water residue will not show up in a Raman spectrum. However, an IR spectrum will show a very strong, broad peak if water is present. Thus, Raman spectroscopy can be used for aqueous based *in situ* studies.

The Raman spectrum of glycine can be described by two main regions. The region between 500 cm^{-1} and 1700 cm^{-1} contains many of the Raman bands used to identify a material, so is referred to as the fingerprint region. At the higher Raman shift frequencies (*i.e.* between 2850 cm^{-1} and 3000 cm^{-1}), there exists the CH stretching vibrations in region known as the CH region. For glycine, these vibrations represent the most prominent feature of the Raman spectrum and thus can be easily used to identify the polymorph. Each polymorph of glycine has a distinct Raman spectrum because of the different bonding arrangements in their structures. The CH region of the three ambient polymorphs of glycine are shown in Figure 2.15. It is clear to see how each polymorph can be distinguished from the others as the symmetric (at the lower shift value) and asymmetric (at the higher shift value) CH stretches of each polymorph is clearly defined. The symmetric and asymmetric CH stretching frequencies, respectively, for each polymorph are as follows: 2972 and 3008 cm^{-1} for the α-form; 2953 and 3009 cm^{-1} for the β-form; and 2964 and 3000 cm^{-1} for the γ-form.[224–226]

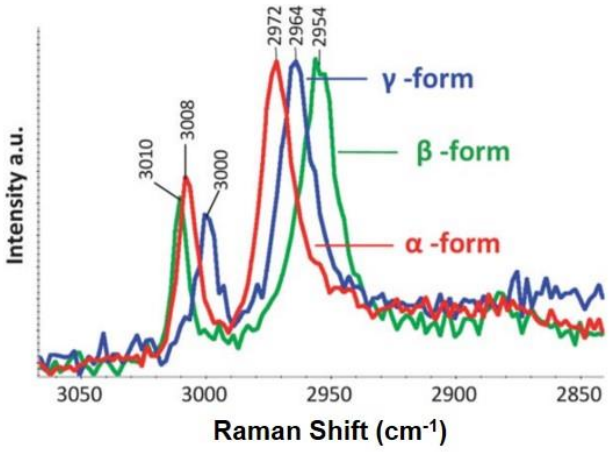

Figure 2.15 Raman spectrum of the CH region of the three ambient polymorphs of glycine.[224]

There are a few studies related to the templated crystallisation of glycine, which will be summarised here. Different additives have been used to template the crystallisation of glycine. One example is sodium chloride which was shown to exhibit some polymorphic control of glycine, where it was found to promote the formation of the γ-form over the α-form.[164] A wide range of carboxylic acid additives have also been investigated, where it was found that whilst small amounts of the additives promoted the most stable form, higher amounts resulted in the formation of glycine salts.[160] As well as carboxylic acids, other α-amino acids (such as phenylalanine, methionine, tryptophan, and napthylalanine) can be used to preferentially grow either the γ-form of glycine, in the case of phenylalanine and methionine, or the β-form, in the case of tryptophan and napthylalanine.[154] These preferences were attributed to the abilities of the additives to bind to the {010} surface of the glycine crystal. The less bulky amino acids could bind and block this surface, thus inhibiting the growth of the α- and β-forms.

SAM substrates have been designed to restrict the crystallisation of glycine to hydrophilic metallic islands to investigate the effect of feature sizes on the polymorphic outcome.[221] In this study, it was observed that the metastable α-form would crystallise exclusively on larger islands (725 μm) whilst the unstable β-form would grow on the smaller islands (25 μm). It was deduced that the selectivity of the smaller islands came from the higher supersaturation rate that was generated, which favoured and stabilised the β-form. This approach was later applied to the crystallisation of mefenamic acid, sulfathiazole,[227] and ROY.[228] Further reducing the size of the islands (to 1μm), and making the SAM material amphiphilic (Figure 2.16) resulted in the concomitant formation of the three ambient glycine polymorphs, revealing the competitive nature of the three forms within nanosized droplets.[224]

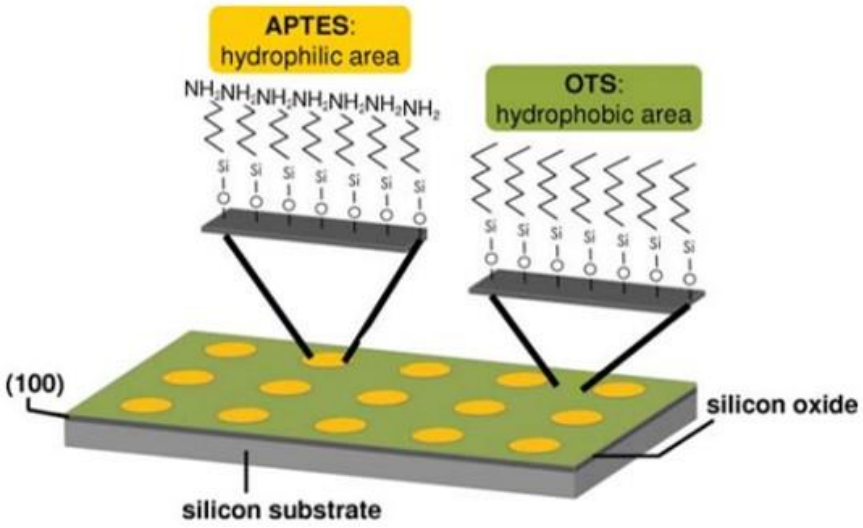

Figure 2.16 Schematic representation of the amphiphilic SAM substrate.[224]

2.5 Summary

In this chapter, the fundamentals of crystallisation have been provided. The reference molecule of the thesis (glycine) has been introduced and the recent advances on obtaining polymorphic control *via* templated crystallisation has been discussed.

Chapter 3: Acoustic Levitation

As discussed in **Chapter** 2, most crystallisation events involve surfaces, so in most cases, crystallisation occurs heterogeneously. To achieve homogeneous crystallisation, specialised setups are required. One setup is based on levitation, enabling contactless handling of a sample in a continuous fluid medium (air in our case) by balancing gravity with an upward force. This setup allows us to perform fundamental studies on the evaporative behaviour of droplets with no influence from a substrate, hence it has been applied in our studies on both graphene and glycine solutions (**Chapter 5** and **6,** respectively)

The following chapter will give details about the fundamentals of levitation, with particular emphasis on acoustic levitation, and how this technique has been used in crystallisation studies, as well as in the research of liquid evaporation.

3.1 Fundamentals of Levitation

Conceptually, levitation is based on a simple application of an upward contact-free force to an object that counters gravity. However, an issue encountered by early researchers on controllable levitation was the lack of stability of the levitated body upon horizontal or vertical perturbation, thereby claiming it to be impossible.[229] It has now been established that depending on the size and properties of the body to be levitated, a number of techniques can successfully achieve levitation.[230] These techniques, some of which are shown in Figure 3.1, include magnetic,[231–234] electrostatic,[235–239] aerodynamic,[240] optical,[241–243] and acoustic levitation.[244–249]

Each approach has its own advantages and disadvantages. Aerodynamic levitation (Figure 3 (a)) is based on the lifting of a spherical body with a fluid jet. The jet is offset from the centre of the body, which stabilises the body both vertically and horizontally by increasing the Bernoulli force at the side where the flow is faster, which produces a centering force.[230,240] Optical levitation (Figure 3 (b)) can be achieved by illuminating a sample with a high intensity laser that is focussed by a lens with a high numerical aperture. The laser imparts a scattering force on the sample which is pushed towards the energy flux of the laser. Due to the focus required, only small volumes (a few nL) of liquids have been optically levitated.[242,243,250] Electrostatic levitation (Figure 3 (c)) allows for the levitation of a conductive material by the application of an electrostatic field between two electrodes. However, this technique requires high voltages and frequencies to generate an electric field strong enough to overcome the

gravitational force on the sample.[230] A material that displays diamagnetic properties can be levitated magnetically (Figure 3 (d)). The most promising class of materials for magnetic levitation are superconductors, but with a strong enough magnetic field, even living frogs have been levitated.[230,233]

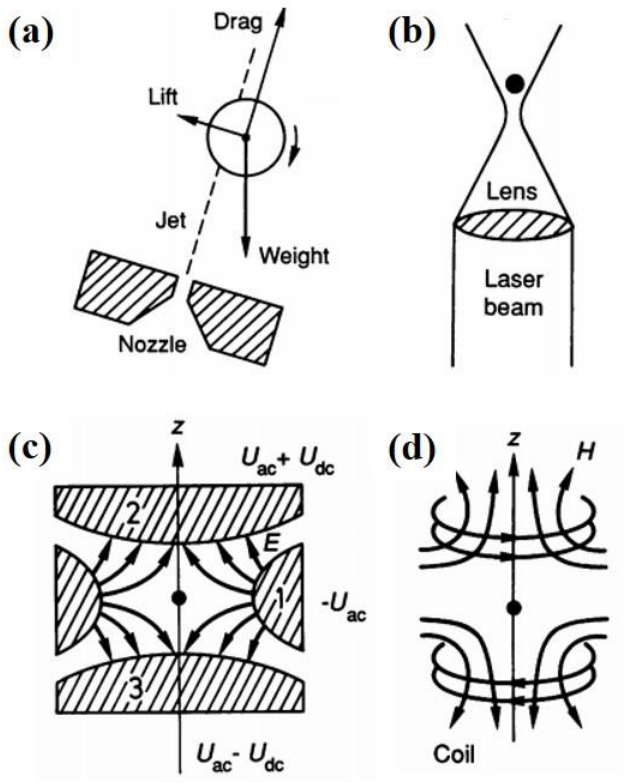

Figure 3.1 Schematic illustration of levitation techniques: (a) aerodynamically; (b) optically; (c) electrostatically; and (d) magnetically.[230]

Amongst all techniques, acoustic levitation stands out as the levitating body does not need to have any specific physical properties; potentially any sample can be levitated. Bücks and Müller first demonstrated that high frequency acoustic sound waves can be used to levitate small objects.[244] They noted that reflecting a sound wave back at itself generated a standing wave that consists of a set of equally spaced nodes. The waves transfer momentum to the object, which creates a force that can counter gravity, causing the object to levitate just below one of the nodes, as shown in Figure 3.2 (b). Further details will be discussed in the following sections.

3.1.1 Theory of Acoustic Levitation

Considerable effort has been made to theoretically understand the phenomenon of acoustic levitation.[230,245,251–256] The dominant force exerted on levitating particles is a radiation force. Gor'kov developed a general theory that described the acoustic radiation force on a rigid

spherical particle that is significantly smaller that the wavelength of the acoustic wave.[255–257] He derived an expression for the acoustic radiation potential, known as the Gor'kov potential *U*, which can be used to calculate the radiation force, $\boldsymbol{F}$, by taking the negative gradient as follows:

$$U = K_1(|p_c|^2) - K_2\left(|p_x|^2 + \left|p_y\right|^2 + |p_z|^2\right) \quad \textbf{(3.1)}$$

$$K_1 = \frac{1}{2}V\left(\frac{1}{c_0^2\rho_0} - \frac{1}{c_s^2\rho_s}\right) \quad \textbf{(3.2)}$$

$$K_2 = \frac{3}{2}V\left(\frac{\rho_0 - \rho_s}{\omega^2\rho_0(\rho_0 + 2\rho_s)}\right) \quad \textbf{(3.3)}$$

$$\boldsymbol{F} = -\nabla U \quad \textbf{(3.4)}$$

where V is the volume of the particle, ω is the frequency of acoustic waves, ρ is density and c is the speed of sound (the subscripts 0 and s refer to the propagation/fluid medium and the particle medium, respectively). The complex pressure is given as p_c and its spatial derivatives are given as p_x, p_y, and p_z. The complex pressure is a complex number and is dependent on the position in space and the emitting phase of the source. For a single axis levitator, it is possible to express Equation 3.1 as a function of the acoustic sound pressure, p, and particle velocity, v:[258,259]

$$U = \frac{3}{2}V\left(\frac{p^2}{3\rho_0 c_0^2} - \frac{\rho_0 v^2}{2}\right) \quad \textbf{(3.5)}$$

Plotting the Gor'kov potential and acoustic radiation force along a particular axis (*e.g.* *z*-axis), as shown in Figure 3.2 (a), reveals that the acoustic radiation force provides a restoring force towards the minimum of the Gor'kov potential. Figure 3.2 (b) is a schematic view of a single axis levitator and the associated sound pressure and acoustic force along the standing wave. It also shows how an object will be stabilised by the acoustic force close to a sound pressure node but will not rest directly in the node.[258]

The main components of a single axis acoustic levitator are a piezoelectric ultrasonic transducer and a reflector (Figure 3.2 (b)). Whilst both can be planar, it has been shown that there is a significant increase in the acoustic radiation force if the reflector is made to be concave.[253]

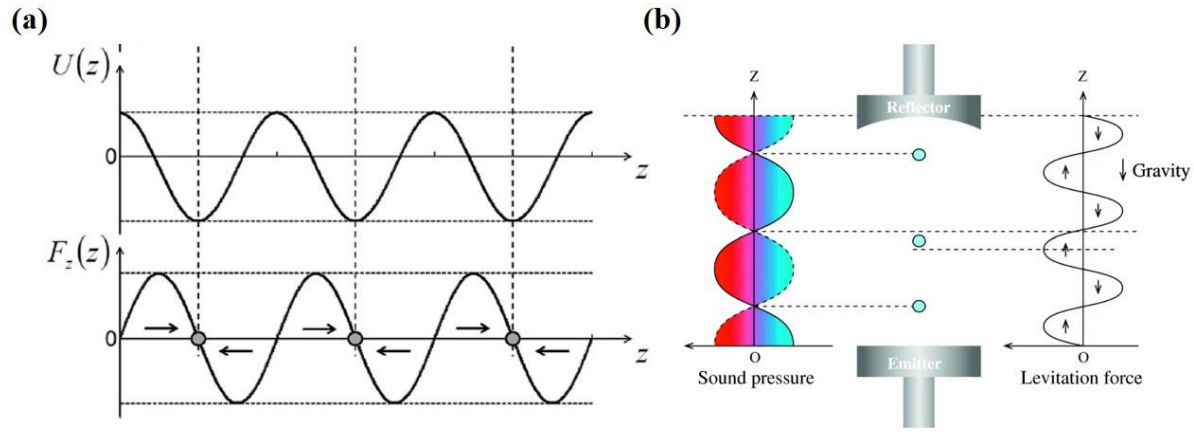

Figure 3.2 (a) The Gor'kov potential, *U*, and the corresponding radiation force, ***F***, on a small sphere subjected to an acoustic ultrasonic soundwave.[255] (b) Schematic view of a single axis levitator. The position of levitated bodies is shown with respect to the sound pressure and radiation force of the standing wave.[258]

This thesis focuses on liquid droplets (**Chapters 5** and **6**) and **t**here are issues that must be discussed to better understand the technique when the levitating object is not a rigid sphere. First, the acoustic radiation pressure on a liquid droplet is not uniform, typically positive at the polar area and negative at the equator, as shown in Figure 3.3. This results in compression (at the poles) and suction (at the equator) forces on the droplet which will cause the droplet to adjust its surface curvature to adapt to the radiation pressure. This will often cause a liquid droplet to adopt a non-spherical shape which can be described based on the droplets polar coordinates:[249,256,258,260,261]

$$R_s(\theta) = R_L\left[1 - \frac{3R_L P_A^2}{64\sigma\rho c_0^2}\left(1 + \frac{7}{5}(k_0 R_L)^2\right)(3\cos^2\theta - 1)\right] \qquad \textbf{(3.6)}$$

where $R_s(\theta)$ is the polar coordinate of the drop contour, R_L is the equatorial radius of the droplet, ρ is the density of the droplet, σ is the surface tension of the liquid, and k_0 is the wavenumber ($k_0 = \omega/c_0$). Second, introducing an acoustic field into a fluid medium often results in the generation of a non-linear acoustic field, which in turn can generate a type of flow known as acoustic streaming. This flow can influence both the internal and external dynamics of a droplet.[256,258,262–264] Externally, acoustic streaming can destabilise the levitating droplet by perturbing the force balance *via* the Bernoulli effect.[258,264] Internally, the streaming can have large implications on the heat and mass transfer within the levitating droplets.[256,259,262] The physical properties of the levitating droplet have a huge impact of the strength of acoustic streaming, where typically the more viscous the droplet, the weaker the streaming effect.[262–264]

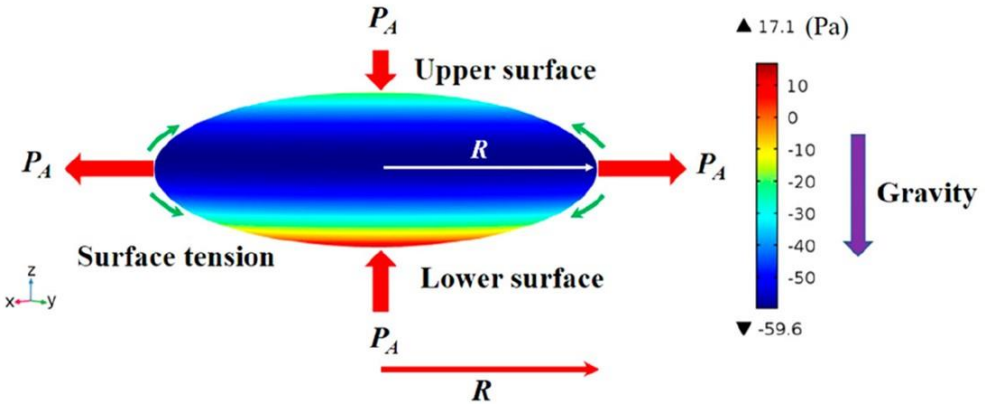

Figure 3.3 Schematic illustration of the non-uniform distribution of the acoustic radiation pressure, P_A, leading to distortion of the droplet shape from spherical to puddle-like.[265]

3.2 Applications of Acoustic Levitation

Even though it is a specialised technique, acoustic levitation has found some general applications in biomaterials research,[266–269] chemistry[249,270–273] and lab-on-a-drop procedures.[274] Levitation of liquids has also been employed to determine their dynamics,[275] surface tension,[276,277] and rheological properties.[278] Finally, for our purpose, acoustic levitation has also found uses in the study of droplet evaporation (**Chapter 5**) and the potential for homogeneous crystallisation of melts or solutes from solution (**Chapter 6**).

In this section, the current understanding of droplet evaporation and crystallisation from solution using acoustic levitation is given.

3.2.1 Evaporation *via* Acoustic Levitation

Droplet evaporation is a ubiquitous phenomenon in nature and industry alike, such as pharmaceutical manufacturing, inkjet printing, powder and food processing, and fuel combustion.[256] A great deal of theoretical and experimental research has understandably gone into the evaporation of sessile droplets on substrates.[279–286] Acoustic levitation of a single droplet is typically used as an analogue for spray drying, a well-established technique in both industry and research for the purpose of substrate preparation crystallisation.[287–290] However, due to the high intensity of droplets produced during spray drying, it is extremely difficult to study the behaviour of the droplets in detail. Thus, single droplet levitation is used to mimic the conditions of spray drying whilst allowing the investigation of the droplets. In recent years the drying characteristics of levitated droplets has started to be explored.[248,291–299]

For both sessile and levitated droplets, it is well established that the evaporation of pure droplets follows the 'd^2-law':[300]

$$\left(\frac{d}{d_0}\right)^2 = 1 - Kt \quad \textbf{(3.7)}$$

$$K = \frac{8\rho_g D}{\rho_l}\ln(1+B) \quad \textbf{(3.8)}$$

where d is the diameter of the droplet (the subscript 0 denotes initial diameter), t is time, ρ is the density (subscripts g and l denote the gas and liquid phases, respectively), and D and B are the mass and heat diffusion coefficients, respectively.[256] For levitated and multi-component droplets other factors must be considered in order to characterise their drying behaviours. For levitated droplets specifically, acoustic streaming has a complicated effect on the external and internal vortices of the droplet. The convection mode at the surface of the droplet is switched from a natural convection to a forced convection, which will enhance evaporation, but these same vortices may trap vapour, reducing the concentration gradient around the surface and thus inhibit evaporation. Multi-component droplets have the added complexity of varying densities, diffusion and mass coefficients, and composition over time that studies have tried to account for.[248,292–294,297] This section will give a more simplistic description of the evaporation process, with no additional effects from acoustic streaming.

Using the universal theory on the mass transfer rate at the surface of a suspended droplet,[291] the instantaneous evaporation rate for a multi-component system, $\dot{m}_v$, is written as the sum of each of the evaporating components, i:[248,293,297]

$$\dot{m}_v = \sum_i 2\pi\rho_{i,v}D_{i,v}R_i Sh_i^* \ln\left(1+\mathrm{B_{M,}}_i\right) \quad \textbf{(3.9)}$$

where $\rho_{i,v}$ and $D_{i,v}$ are the average density and vapour diffusivity of the ith component, respectively, R_i is the volume equivalent partial radius, Sh* is a modified Sherwood number, and B_M is the Spalding mass transfer number. Solving this equation takes a considerable theoretical effort, but its derivation and subsequent validation was a landmark achievement for evaporation studies.[248,293]

If the droplet contains non-volatile species, then their influence on the mass and heat transfer of the droplet needs to be accounted for. Manipulation of Equation 3.7 can yield the d^2-law for

single-component droplets in terms of partial pressures, temperature, and relative humidity, such that:[298,299]

$$\left(\frac{d}{d_0}\right)^2 = 1 - \frac{8DM}{\rho R}\left(\frac{p_s}{T_s} - \frac{p_\infty}{T_\infty}\cdot\frac{\mathrm{RH}}{100}\right)\frac{t}{{d_0}^2} \qquad \textbf{(3.10)}$$

where D is the diffusion coefficient in the gas phase, M and ρ are the molar mass and density of the evaporating species, respectively. R is the gas constant, p is the partial pressure, T is the temperature (subscripts s and ∞ denote at the surface of the droplet and in the ambient atmosphere, respectively), and RH is the relative humidity. Adding a non-volatile species into the droplet will affect the vapour pressure at the surface. Therefore, considering the molar fraction of the solute (x_u) and the degree of dissociation of the solute (given by the van't Hoff factor, i) Equation 3.10 can be written as:[298,299]

$$\left(\frac{d}{d_0}\right)^2 = 1 - \frac{8DM}{\rho R}\left(\frac{p_s(1-ix_u)}{T_s} - \frac{p_\infty}{T_\infty}\frac{\mathrm{RH}}{100}\right)\frac{t}{{d_0}^2} \qquad \textbf{(3.11)}$$

Whilst the above equations were shown to be in good agreement with the experimental observations of the studies (*i.e.* the evaporation of aqueous solutions of inorganic salts)[298,299] a number of assumptions had to be made (*e.g.* an ideal solution, no influence of acoustic streaming and does not seem to account for solute diffusion). A more comprehensive theoretical model for the drying behaviour of droplets containing non-volatile species has been recently presented that removes many of the assumptions made, but consequently increases the computational workload.[297]

A useful parameter to consider when analysing a drying droplet that contains non-volatile particles is the Peclet number, *Pe*.[297,301,302] This dimensionless number defines the ratio between the evaporation rate of the droplet, κ, and the diffusion rate of a species within the droplet, D_i, as:

$$Pe = \frac{\kappa}{8D_i} \qquad \textbf{(3.12)}$$

If the Peclet number is less than 1, it indicates that the diffusional mixing within the droplet is fast enough to replenish the surface with solvent and the droplet has a more-or-less homogeneous composition. However, a Peclet number greater than 1 means there is an enrichment at the surface of the solute molecules. This promotes the formation of crusts and can result in a variety of complex morphologies of the dried particle.[303,304]

3.2.2 Crystallisation *via* Acoustic Levitation

Acoustic levitation provides a good platform to investigate the crystallisation of molecules, the results of which can be compared with those obtained from sessile droplets, as crystallisation under the influence of levitation is a closer approximation of homogeneous nucleation. A breakdown of the crystallisation experiments performed so far is giving in Table S1 in Supporting Information of **Chapter 6**.

It has been reported that crystals obtained from acoustic levitation can exhibit higher growth rates, larger crystal sizes, more defined shapes with fewer defects when compared to control experiments that involve vessel walls.[305] Examples of crystals of NaCl grown with and without acoustic levitation are shown in Figure 3.4 (a) and (b), respectively. The crystals grown under the influence of acoustic soundwaves (Figure 3.4 (a)) grew larger and were more morphologically pure. Other inorganic systems have been crystallised from acoustic levitation, such as NH_4Cl,[305] $CaCO_3$,[306] $(NH_4)_2SO_4$, and Na_2SO_4,[267] where similar results to those for NaCl were found. Organic molecules have also been crystallised from acoustic levitation. Caffeine displays concomitant polymorphism of its α- and β-forms when it is crystallised on a variety of substrates, while only the α-form was obtained from levitated droplets.[307]

In the case of mannitol, the crystals produced from acoustic levitation presented a hollow morphology. This was assumed to be generated by the initial formation of a stable, but permeable crust at the surface of the droplet where eventually the crystal nucleated.[297,308] A recent study that took a theoretical approach to both the drying and crystallisation of aqueous mannitol droplets confirmed this shell/crust formation prior to crystallisation by taking into account heat and mass transfer as well as population balances that were used to describe the evolution of the particle size distribution within the droplet.[297]

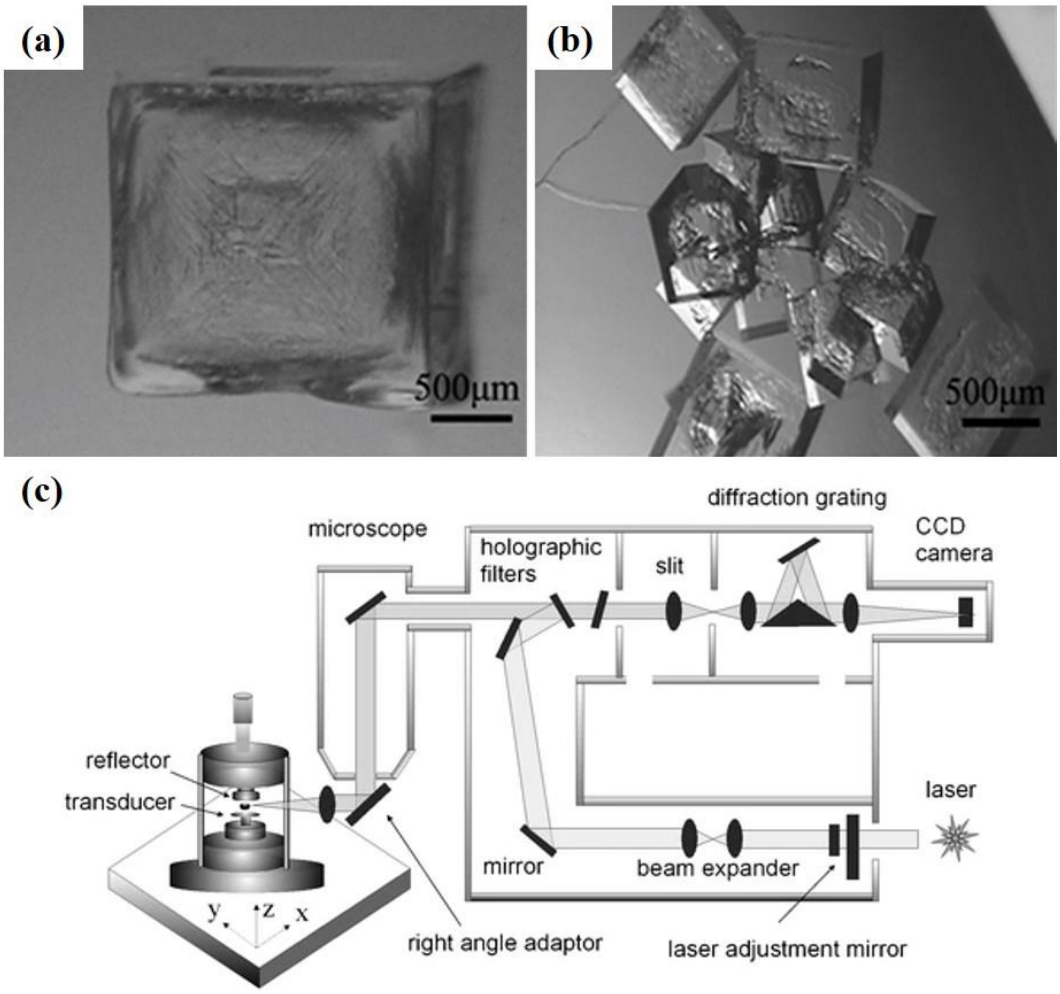

Figure 3.4 NaCl crystals grown (a) with and (b) without the influence of acoustic soundwaves.[305] (c) Schematic drawing of an example experiment setup for *in situ* Raman spectroscopy analysis of acoustically levitated droplets.[309]

Coupling acoustic levitation with analytical techniques (*e.g.* X-ray Diffraction (XRD), Raman Spectroscopy, Wide angle X-ray scattering (WAXS) *etc.*) enables fully isolated, *in situ* monitoring of the crystallisation process.[307–313] An experimental setup for *in situ* Raman spectroscopy of levitating droplets is shown in Figure 3.4 (c). Calcium carbonate was observed with WAXS to form amorphous LLC at the early stages of its crystallisation.[311] These preliminary particles were found to form homogeneously in solution and served as the templates for the subsequent crystallisation of calcite. Using a combination of *in situ* XRD and Raman spectroscopy, the solvent choice on the crystallisation of several compounds, such as ROY (5-methyl-2-[(2-nitrophenyl)amino]-3-thiophenecarbonitile),[310] nifepidine,[313] and paracetamol,[312] was investigated. The crystallisation of ROY was determined to proceed *via* different pathways which involved the formation of different intermediate phases leading to the production of alternative polymorphs. Generating specific polymorphs was then attributed

to the nearest neighbour interactions and intermolecular forces between solvent and solute.[310] For nifepidine, different intermediate phases (*e.g.* the metastable *β*-form and the glassy form) were detected depending on the solvent used, but both lead to the formation of the more stable *α*-form. Again, the formation of the different intermediates was attributed to solvent/solute intermolecular interactions.[313] Finally, paracetamol was shown to be heavily influenced by the choice of solvent as two different amorphous phases were identified that individually lead to the selective crystallisation of the two common forms of paracetamol (the monoclinic Form I and the metastable Form II).[312]

It should be noted however that although acoustic levitation allows for containerless study of crystallisation that is free of foreign substrates, it is unlikely to fully mimic homogeneous nucleation due to the non-linear properties induced by the sound waves that were discussed in Section 3.1.1. Therefore, these non-linear properties (*i.e.* acoustic streaming) that can affect the mass and heat transfer of the droplet cannot be disregarded when analysing levitation experiments.

3.3 Summary

This **Chapter** has introduced acoustic levitation and provided a short overview on its fundamentals and practical uses in the study of evaporation and crystallisation. It should be noted that to the best of the author's knowledge, no previous work has reported the levitation of glycine or graphene.

Part II: Experimental Results

Chapter 4: Exploiting the Surface Properties of Graphene for Polymorph Selectivity

My contribution: I produced the ECE graphene dispersions and optimised the spray coating parameters to produce the ECE graphene substrates. I conducted the crystallisation experiments except for the ones using CVD as a substrate (performed by A.A.) and performed the polymorph analysis of glycine after the crystallisation with graphene additives. I prepared all the figures related to the use of graphene as an additive. I wrote the first draft of the manuscript for the additive-templated crystallisation experiments and the related supporting information and continued to re-draft the manuscript until publication.

ACS NANO

www.acsnano.org

ARTICLE

Exploiting the Surface Properties of Graphene for Polymorph Selectivity

Matthew Boyes, Adriana Alieva, Jincheng Tong, Vaiva Nagyte, Manuel Melle-Franco, Thomas Vetter, and Cinzia Casiraghi*

Cite This: *ACS Nano* 2020, 14, 10394–10401

Read Online

ACCESS | Metrics & More | Article Recommendations | Supporting Information

ABSTRACT: **Producing crystals of the desired form (polymorph) is currently a challenge as nucleation is yet to be fully understood. Templated crystallization is an efficient approach to achieve polymorph selectivity; however, it is still unclear how to design the template to achieve selective crystallization of specific polymorphs. More insights into the nanoscale interactions happening during nucleation are needed. In this work, we investigate crystallization of glycine using graphene, with different surface chemistry, as a template. We show that graphene induces the preferential crystallization of the metastable α-polymorph compared to the unstable β-form at the contact region of an evaporating droplet. Computer modeling indicates the presence of a small amount of oxidized moieties on graphene to be responsible for the increased stabilization of the α-form. In conclusion, our work shows that graphene could become an attractive material for polymorph selectivity and screening by exploiting its tunable surface chemistry.**

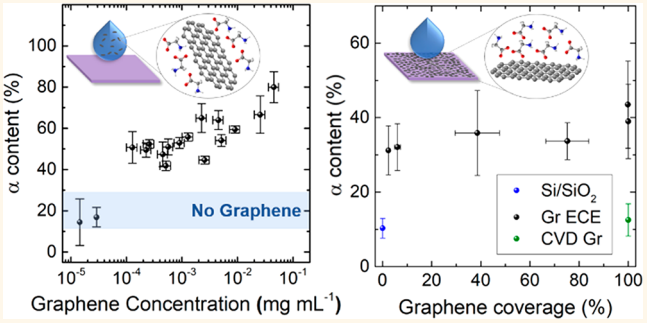

KEYWORDS: *graphene, surface chemistry, glycine, crystallization, polymorphism, computational modeling*

Crystallization from solution is one of the fundamental processes that can be experienced in our everyday lives. Despite this process being known since the early centuries[1] and its importance for numerous industries,[2] crystallization from solution is still not completely understood. This makes the production of crystals of a desired form (polymorph) challenging.[3,4] Therefore, establishing control over the crystallization process has been an area of active research for many decades.[5−9]

Surfaces play an important role in crystallization, as the interaction of the solute with a surface alters the energetics and kinetics of nucleation, giving rise to heterogeneous nucleation.[10,11] A surface can be introduced either as a substrate or as an impurity.[12−16] Although preferential nucleation has been achieved by utilizing a few selected surfaces, there is still no hard and fast rule for the design of smart templates for heterogeneous crystallization because of the lack of insights on the nanoscale mechanisms of crystallization. Hence, methodologies beyond traditional approaches need to be developed.

In this work, we propose an approach to study crystallization, which is based on the use of nanomaterials and the tools provided by nanotechnology. First, crystallization experiments are performed in microdroplets, in contrast to industrial crystallizers. Second, crystals are characterized by Raman spectroscopy, which can measure individual crystals, allowing the detection of minute changes in the polymorphic outcome, unlike X-ray diffraction, which is predominantly used for these studies. Finally, we use a particular type of nanomaterial as template: graphene, the most famous two-dimensional crystal, characterized by unique properties.[17,18] This material is very attractive to study crystallization because, being entirely a surface, its surface properties can be easily tuned *via* covalent functionalization[19−22] and electrostatic doping[23] and it is solution processable.[24,25] This allows us to perform two types of crystallization experiments: one where graphene is used as a substrate, and another where graphene is used as an additive. This is in contrast to previous works, where the template is tailored exclusively for being either a substrate[13] or an additive.[15] Furthermore, the tunable surface chemistry of graphene can be used to identify the specific intermolecular interactions responsible for the crystallization of a particular polymorph.

Received: May 19, 2020
Accepted: July 21, 2020
Published: July 21, 2020

https://dx.doi.org/10.1021/acsnano.0c04183
ACS Nano 2020, 14, 10394−10401

Glycine has been selected to investigate the use of graphene for templated crystallization because of its molecular simplicity and well-studied polymorphs, denoted as α, β, and γ.[26,27] In particular, we exploited the ability of glycine to produce both the α- and β-polymorphs after evaporation of a microdroplet on a silicon substrate covered with a thin oxide layer (Si/SiO_2), with the unstable β-form preferentially nucleating at the triple contact region. The γ-polymorph may crystallize from aqueous solutions, but very long induction times (several hours) are typically necessary.[28] Using different types of graphene and by performing Raman spectroscopy on individual crystals, we demonstrate that graphene can induce preferential crystallization of the metastable α-polymorph. Computer modeling indicates this selectivity to be related to the presence of hydroxyl groups allowing for hydrogen bonding interactions with the glycine molecules, thereby favoring the α-form more than the β-form once additional layers of the polymorphs are added during crystal growth.

This work shows that the surface chemistry tunability of graphene can be exploited to control polymorphism in small molecules. This allows for polymorph screening techniques using graphene and 2D materials to be implemented in drug manufacturing, where these techniques are strongly needed.

RESULTS AND DISCUSSION

Crystallization was obtained by solvent evaporation of a microdroplet of aqueous glycine solutions under controlled environmental conditions (see Methods and Supporting Information, section S1). Two types of crystallization experiments are performed: (i) additive-templated crystallization, in which solution-processed graphene was directly added into the droplet containing glycine, which is then drop-casted onto Si/SiO_2 (Figure 1a); and (ii) substrate-templated crystallization, where the droplet only contains glycine and is deposited onto a specific substrate (Figure 1b). In this experiment, two substrates were investigated: a film of solution-processed graphene spray-coated on Si/SiO_2 and also polycrystalline graphene, grown by chemical vapor deposition[29] (CVD Gr) on copper.

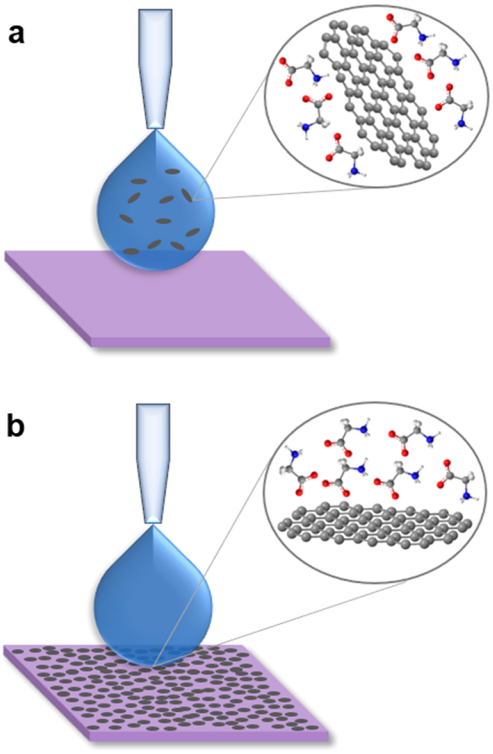

Figure 1. Schematics of the crystallization experiments using graphene as (a) additive and (b) substrate.

Solution-processed graphene was produced by electrochemical exfoliation (ECE) of graphite[30] using two different salts: $(NH_4)_2SO_4$ and $KHSO_4$ (see Methods), as this allows for the production of graphene with different surface chemistry: graphene produced with $(NH_4)_2SO_4$ (Gr ECE(NH_4)) contains, on average, a lower C/O ratio compared to that of graphene produced with $KHSO_4$ (Gr ECE(K)).[31] More details can be found in Supporting Information, section S3. The geometry of the droplet (contact angle, surface area, *etc.*) and induction time (*i.e.*, the amount of time required for the first crystal to be detected) were investigated. Raman spectroscopy was used to analyze the polymorph outcomes by considering each polymorph's characteristic C−H stretching frequency (see Supporting Information, section S2).[32] As the unstable polymorph (β) of glycine is known to appear at the contact region of the evaporating droplet,[33] Raman spectroscopy was performed on individual crystals both in the bulk and at the contact region of the droplets (the methodology followed for the Raman measurements is described in the Methods).

Additive-Templated Crystallization. We use ECE graphene suspended at varying concentrations in the aqueous glycine droplets. As pure water does not produce stable graphene dispersions due to the mismatch in surface energies between water and graphene,[24] a binary solvent mixture of H_2O/isopropyl alcohol (IPA) (3:1 v/v) was chosen to accommodate both a stable graphene dispersion[34] and complete dissolution of glycine (Figure S5.1). This approach avoids the use of stabilizers/surfactants,[35−37] the presence of which would further affect the crystallization process.

The geometric impact of the concentration of ECE graphene in the crystallizing droplet is shown by the surface area and volume ratio (SA/V) of the droplet in Figure 2a. This shows that there is no change to the geometry of the droplet when comparing the control experiments (*i.e.*, pure glycine solutions, indicated by the shaded area) to an increasing graphene concentration. This has significant implications as the SA/V is intrinsically related to the evaporation rate of the solvent, which, in turn, can influence the rate of nucleation through its impact on the evolution of the glycine solution concentration. As our results show no change in droplet geometry, then no change to the evaporation rate is expected when graphene is introduced into the mixture. Therefore, any change in induction time needs to be attributed to intermolecular interactions with graphene.

The kinetics of glycine's crystallization with graphene additives is displayed in Figure 2b. This figure shows that the two types of graphene crystals have different bearings on the crystallization kinetics. The Gr ECE(K) does not change the induction times, compared to the control droplets (shaded area in Figure 2b), whereas the presence of Gr ECE(NH_4) induces a marked increase in the induction times. This result could be attributed to the difference in defect concentration of the graphene flakes, in turn, affecting the interactions between graphene and the glycine molecules. At a glance, it seems that the more defective Gr ECE(NH_4) flakes allow for stronger interactions with the glycine molecules. However, we remark

https://dx.doi.org/10.1021/acsnano.0c04183
ACS Nano 2020, 14, 10394−10401

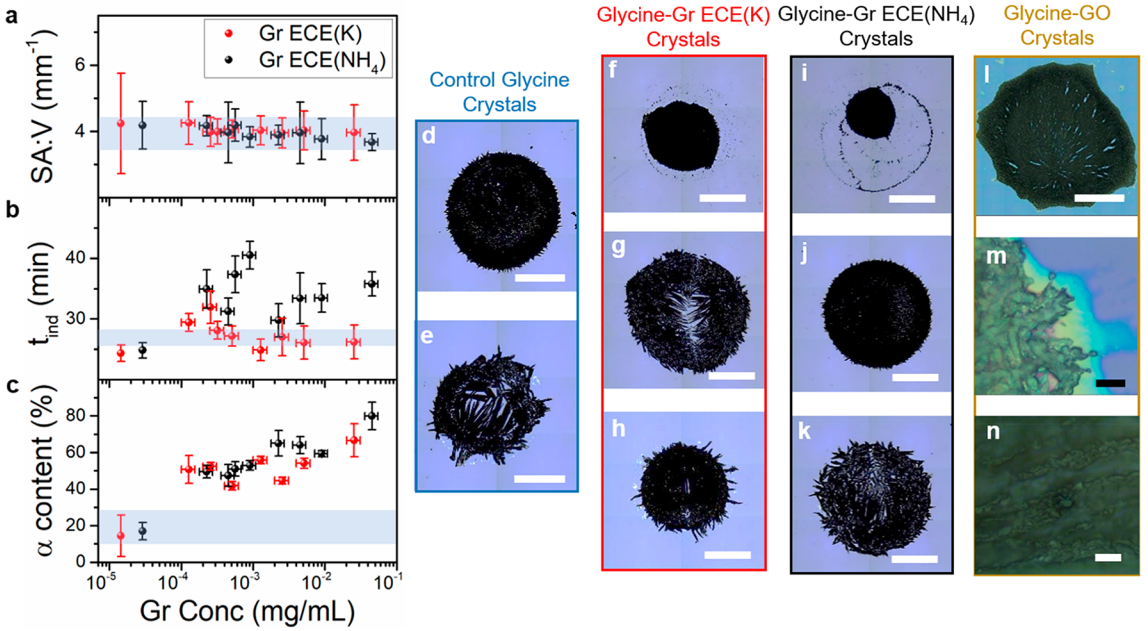

Figure 2. Crystallization of glycine with graphene additives. (a) Surface area and volume ratio (SA/V), (b) t_{ind}, and (c) average percentage of α-glycine edge crystals for varying graphene concentrations are reported. The blue areas represent the averages obtained for the control experiments (*i.e.*, droplet of 0.5 M glycine in 3:1 water/IPA). (d,e) Optical images of representative crystals from the control experiments of 0.5 M glycine in 3:1 water/IPA. (f–h) Optical images of representative crystals from the crystallizations of glycine with ECE(K) additives at 2.6×10^{-2} mg mL^{-1} (f), 1.3×10^{-3} mg mL^{-1} (g), and 2.6×10^{-4} mg mL^{-1} (h). (i–k) Optical images of representative crystals from the crystallization of glycine with ECE(NH_4) additives at 4.6×10^{-2} mg mL^{-1} (i), 2.3×10^{-3} mg mL^{-1} (j), and 4.5×10^{-4} mg mL^{-1} (k). (l–n) Optical images showing different regions of the crystals obtained from the crystallization of glycine with GO additives: whole droplet (l), droplet contact region (m), and droplet bulk region (n). Scale bars (d–l) ≈ 1 mm. Scale bars (m,n) ≈ 10 μm.

here that induction times are taken by visual inspection, hence, these measurements are only qualitative.

Figure 2d–l shows a collection of representative crystals obtained from some of the crystallization experiments. Magnified images are provided in the Supporting Information, section S5.3. The graphene-free crystals (Figure 2d,e) display two distinct morphologies: compact crystals made up of smaller grain-like crystals (Figure 2d) and spread out crystals made up of larger needle-like crystals (Figure 2e). The crystals obtained by the evaporation of the graphene mixtures (Figure 2f–k) also display this variation but only when exceptionally low concentrations of graphene (<2.6×10^{-4} mg mL^{-1}) were used. Above this concentration, the morphological outcome was exclusively compact. The occurrence of these morphologies is due to the competition between nucleation and crystal growth rates; that is, graphene alters this balance in favor of crystal nucleation over growth (a detailed explanation is given in the Supporting Information, section S5). Note that we never observed any graphene flake incorporated into the crystals, in agreement with Raman measurements performed on the glycine crystals, which do not show any of graphene's Raman features (Supporting Information, section S5.3).

Raman analysis of the crystals grown at the triple contact region (excluding the coffee-ring deposits, Supporting Information, section S5.4) was performed to determine the polymorph outcome. Figure 2c shows the percentage of α-glycine crystals measured as a function of graphene concentration. Both graphene crystals cause a sharp increase in the formation of the α-polymorph, with Gr ECE(NH_4) increasing the percentage up to 80%. With a decreasing graphene concentration there is an associated decrease in the α-form produced until a sufficiently low concentration brings the polymorph distribution back to the control level (shaded area in Figure 2c). This further confirms that intermolecular interactions between the graphene flakes and the glycine molecules during nucleation are responsible for the different polymorph outcomes observed for increasing graphene concentrations.

Note that the addition of IPA into the crystallizing system is expected to have its own impact on glycine's crystallization. However, IPA is known to be a weak antisolvent for the selective crystallization of β-glycine.[38] Compared to a pure aqueous solution of glycine, the addition of IPA causes the droplet surface area to slightly increase, thus causing a decrease in the induction time. This results in a slight increase in the α-form percentage at the contact region, compared to the pure aqueous systems.

Our results show that both types of graphene induce preferential nucleation of the metastable α-form. The selectivity seen for the Gr ECE(NH_4) flakes could be attributed to the kinetic effects, as a longer nucleation time could give rise to a higher α-form percentage.[39] However, as the induction times are only qualitative, and the selectivity found for the Gr ECE(K) flakes cannot be explained in the same way, this reinforces the hypothesis that the crystallization of glycine in the presence of graphene is driven by intermolecular interactions.

As graphene produced by ECE contains oxygen-containing functional groups,[40] these crystals are likely to interact with glycine through H-bonding. In order to investigate the effect of the surface chemistry of graphene, we then tested graphene containing the highest number of C–O groups, called graphene oxide (GO). Figure 2l–n shows that completely different types of crystals were observed when GO was used as

https://dx.doi.org/10.1021/acsnano.0c04183
ACS Nano 2020, 14, 10394–10401

an additive (mixture at a concentration of 5.0×10^{-2} mg mL^{-1}). The crystals no longer have well-defined crystal shapes. The difference in crystal outcome between GO and graphene produced by ECE is related to the large difference in oxygen content: GO is hydrophilic,[41] whereas graphene produced by ECE is hydrophobic.[40] This is confirmed by the measured SA/V of the GO mixture, which is ~5.2 mm^{-1}, noticeably larger than the SA/V measured for the Gr ECE solution (Figure 2a).

These experiments show that polymorph selectivity can be achieved only by carefully controlling the amount and type of functional groups on graphene, as selectivity is driven by the balance between the interactions of graphene with both the crystallizing molecule and the solvent. To further confirm the role of the oxygen groups on the polymorph selectivity, we performed substrate-templated crystallizations, where pristine (*i.e.*, oxygen-free) graphene is compared to graphene produced by ECE.

Substrate-Templated Crystallization. Graphene substrates were produced by spray-coating Si/SiO_2 wafers with ECE graphene (see Methods). For each dispersion, three different coverages were obtained by spraying different amounts of material on the substrates. Based on the coverage percentages, the samples were classified as low, moderate, and full coverage samples (see Supporting Information, section S6). The coverage of silicon with graphene changes the silicon's surface properties, and this is reflected in the SA/V ratios of Figure 3a. A steady decrease in the ratio is observed with an increase in graphene coverage, indicating a more hydrophobic surface is being generated.

Figure 3c shows representative optical images of crystals obtained on the substrates covered with different amounts of Gr ECE(NH_4) (images obtained with Gr ECE(K) are included in Supporting Information, section S6). An optical inspection of the crystals grown at the contact region reveal that their morphology has been altered by coating the silicon substrate with graphene: the quantity of elongated crystals protruding at the contact region decreases with increasing graphene coverage, suggesting a possible decrease in the number of β-polymorph crystals. A similar trend was observed for the Gr ECE(K)-coated substrates (see Supporting Information, section S6). Raman spectroscopy was used to identify the polymorph outcomes for different coverages. Figure 3b shows that the introduction of graphene increases the percentage of α-crystals by ~20%. Despite the large error bars, a clear change in the polymorph grown at the contact region is observed as soon as the substrate is covered with graphene. The promoting effect for the substrates is not as prominent as the one seen for graphene additives, possibly because the latter case allows for additional graphene−glycine interactions as well as the different solvent used.

A second type of substrate-templated experiment was performed using CVD Gr as a substrate. In contrast to graphene produced by ECE, this material is oxygen-free (more details in Supporting Information, section S6). Figure 3a,b shows that while the droplet geometry observed on the CVD Gr and the fully covered ECE substrates were similar, CVD Gr did not produce any enhancement in the α-polymorph percentage, as compared to the bare silicon substrate (Figure 3a,b). This further confirms the crucial role of the oxygen-containing functional groups on graphene in promoting the polymorph selectivity observed in both the substrate and additive-based crystallization experiments.

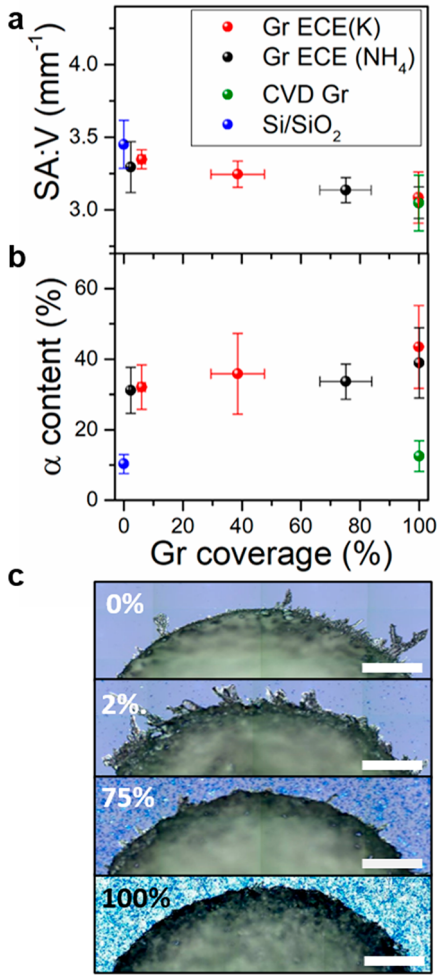

Figure 3. Crystallization of aqueous glycine solutions on Si/SiO_2 substrates with varying graphene coverages. (a) Surface area and volume ratio (SA/V) and (b) average percentage of α-glycine edge crystals are reported for increasing coverage. (c) Optical images of glycine crystallized on Si/SiO_2 substrates having 0, ~2, ~75, and 100% coverage of graphene (scale bar ≈ 250 μm).

Computer Modeling. In order to understand the effect of intermolecular interactions in the selective crystallization of glycine, we computed the energy of thin glycine crystals in α- and β-forms in three scenarios: (a) vacuum, (b) on pristine graphene (Gr), and (c) on oxygen-functionalized graphene. For the latter, an idealized system with 12.5% −OH groups, Gr−OH, was chosen after preliminary studies (not discussed here) precluded enhanced interactions with epoxide and alcohol functional groups. Figure 4 shows an overview of the results. Without a substrate, the surface energies for glycine crystals are endothermic and sizable, 1.25 eV per molecule for the monolayer (Table S3). For thicker crystallites, the β-form consistently shows lower surface energies than the α-form, which fits with the experimental observation that, although less stable, β-glycine should crystallize first. The interaction with Gr and Gr−OH stabilizes the monolayer for both polymorphs to the exothermic values of −0.35 and −0.83 eV, respectively. The energy difference is due to hydrogen bonding to the alcohol moieties, which is not possible on Gr (Figure 4b,c). Additionally, Gr−OH stabilizes the α-form more than the β-form, once additional layers of the polymorphs are added, further confirming the importance of the oxidized moieties in

https://dx.doi.org/10.1021/acsnano.0c04183
ACS Nano 2020, 14, 10394−10401

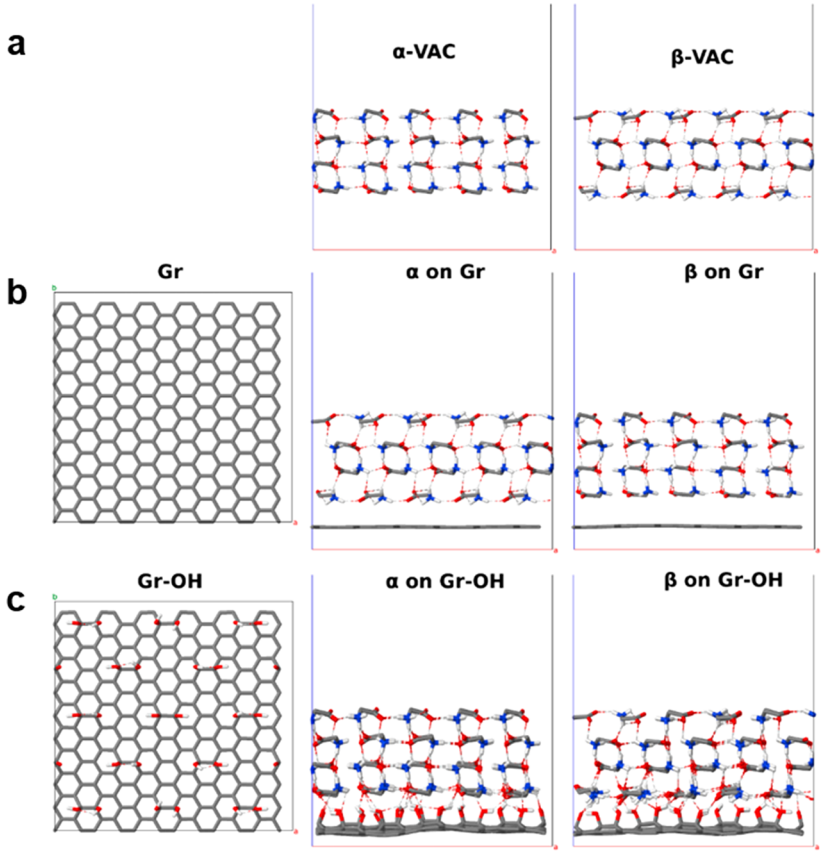

Figure 4. Computer models of four-layer slabs for the α-form and β-form of (010) glycine surfaces: (a) in vacuum, (b) adsorbed on a 2.6 × 2.5 nm^2 surface of pristine graphene (Gr), and (c) on 12.5% oxidized graphene (Gr−OH).

forming the α-form directly from solution. Additionally, these groups could act as spatially localized nucleation sites, which might explain why the induction times are lower when graphene produced by ECE is used in low concentrations.

CONCLUSIONS

Herein, we have shown that graphene preferentially favors the crystallization of the metastable α-glycine polymorph. Using different types of graphene with different surface chemistries allowed us to elucidate the importance of H-bonding interactions between graphene and glycine molecules in promoting polymorph selectivity. Computer modeling was used to get insights on such interactions, indicating that hydroxyl groups facilitated the hydrogen-bonding interactions with glycine, resulting in two effects: an enhancement of the intermolecular interactions of ∼0.5 eV per molecule with respect to oxygen-free graphene and a larger stabilization for the α-form compared to the β-form.

In conclusion, our results show that *ad hoc* designed graphene additives could be used in crystal engineering to achieve polymorphic selectivity and screening, which are of fundamental importance in many industrial processes.

METHODS

Materials. High-purity graphite foil (0.4 mm thick, 99.8%, metal basis), graphite rods (99.99% metal basis), and ammonium sulfate ($(NH_4)_2SO_4$, 98+%) were purchased from Alfa Aesar. Potassium hydrogen sulfate ($KHSO_4$, 99.8%), glycine powder (Reagent Plus ≥99%), and isopropyl alcohol (IPA, ≥99.5%) were purchased from Sigma-Aldrich. CVD Gr on Cu and GO in water were purchased from Graphenea. Silicon wafers (Si/SiO_2) with an oxide layer thickness of ∼300 nm were purchased from IDB Technologies Ltd. and were cleaned with acetone and IPA in an ultrasonic bath for 5 min for each solvent prior to any use. Plastic sample boxes with dimensions of 25 × 25 × 8 mm^3 were purchased from Agar Scientific. Deionized (DI) water (Millipore SIMPAK 1, 18.2 MΩ·cm) was used for all experiments requiring water. All chemicals and materials were used as received with the exception of IPA, which was filtered through a 0.45 μm pore sized membrane prior to use.

Graphene Preparation. Anodic electrochemical exfoliation[30] was carried out in a two-electrode configuration, using a piece of graphite foil (dimensions, 35 × 12 × 0.4 mm^3) as the anode and a graphite rod (dimensions, 35 × 3.05 mm^2) as the cathode. The electrodes were immersed in an aqueous solution (50 mL) of inorganic salts ($KHSO_4$ or $(NH_4)_2SO_4$) at a concentration of 0.5 M. A positive voltage of 10 V was then applied to the graphite anode for 5 min using a Tenma 72-2540 programmable power supply. The graphite rod was placed parallel to the graphite foil surface at a distance of about 2 cm. During this process, gas bubbles formed in both electrodes, with the graphite anode typically seen to expand and release graphitic fragments from its surface. After 5 min of electrolysis, the resulting exfoliated graphite was collected and washed with excess amount of DI water through vacuum filtration to remove residual salts as well as other products of the electrochemical reaction. Subsequently, the exfoliated material was sonicated (Sonorex RK 100, 35 kHz) in a given volume (100 mL) of H_2O/IPA mixture (1:1 ratio, v/v) for an hour; finally, the resulting dispersion was centrifuged using a Sigma 1-14k refrigerated centrifuge at 2000 rpm (295g) for 10 min to remove the unexfoliated material. The graphene dispersions prepared using $(NH_4)_2SO_4$ and $KHSO_4$ salts are denoted as Gr ECE(NH_4) and Gr ECE(K), respectively.

Preparation of Graphene-Coated Si/SiO_2 Substrates. A Spirit Air SP180K airbrush spray gun was used to coat 0.5 × 0.5 cm^2 squares of Si/SiO_2 with ECE graphene flakes. The Si/SiO_2 substrates were placed on a hot plate maintained at 100 °C, and the ECE graphene dispersions were sprayed from a fixed height of 20 cm above the

https://dx.doi.org/10.1021/acsnano.0c04183
ACS Nano 2020, 14, 10394−10401

substrates. For each dispersion, three different coverages (full, moderate, and low) were obtained by spraying a different amount of material on the substrates.

Preparation of Glycine + Graphene (Gly/Gr) Solutions. The ECE graphene dispersions were diluted with a 1:1 v/v mixture of H_2O/IPA to obtain dispersions of varying concentrations. An undersaturated glycine solution of 1.0 M was prepared by dissolving glycine in DI water with stirring at 50 °C for 1 h. An equal volume of an ECE graphene dispersion and the glycine solution were combined to produce a 0.5 M glycine solution in a 3:1 v/v mixture of H_2O/IPA plus graphene additives at a known concentration (see Supporting Information, section S5). GO dispersions first had to undergo a solvent exchange from pure water to a 1:1 v/v mixture of H_2O/IPA at the same concentration. The same procedure was then carried out with these dispersions as was performed with the ECE dispersions. All solutions were then agitated to ensure full dissolution of glycine.

Induction Time Measurements. For the crystallizations on graphene substrates, undersaturated glycine solution of 0.5 M was prepared by dissolving glycine in DI water. The solution was stirred for 1 h at 50 °C. The as-prepared Gly/Gr solutions were used for the graphene additive crystallizations. A fresh solution was used for every crystallization experiment to avoid any aging effects. All crystallizations were carried out in an incubator (My Temp Mini Benchmark), kept at 21 °C, in the following way: three substrates (either graphene substrates, CVD Gr, or cleaned pieces of silicon) were placed in a row in a plastic box equidistant from the front of the container; a 2 μL droplet of solution was deposited on the substrates, and then the box was covered by a clean glass slide (Figure S1). Values of t_{ind}, defined as the time taken for a crystal to be visible by eye after deposition, were measured for each crystallization experiment. Due to the stochastic nature of nucleation events, t_{ind} values were gathered for at least 12 samples for each coverage of graphene substrates and each dispersion of varying graphene concentration. We remark that t_{ind} was measured by eye, so the accuracy of such measurements is limited.

Optical Microscopy. A Nikon Eclipse LV100 microscope was used to observe the crystallization products and qualitatively ascertain the graphene coverage of the spray-coated substrates.

UV−Vis Spectroscopy. A Cary 5000 UV−vis−NIR spectrometer was used to assess the concentrations of the ECE graphene dispersions. The absorbance value at 660 nm was taken, and the Beer−Lambert law[42] was applied to calculate the concentrations using an absorption coefficient of 2460 L g^{-1} m^{-1}, as reported.[24] Sample spectra generated for Gr ECE(K) and Gr ECE(NH_4) are shown in the Supporting Information, Figure S3.1a.

Contact Angle Measurements. Contact angles were measured with an Attension Theta Lite optical tensiometer using the Young−Laplace equation[43] fitted to optical images as shown in Figure S4.

Surface Area to Volume Ratio Calculations. The surface areas of all droplets were calculated by applying the obtained contact angles as cap angles (θ) to the spherical cap model[44] (Figure S4), and the obtained values were divided to a fixed volume of 2 μL.

Raman Spectroscopy. A Renishaw inVia Raman spectrometer equipped with a 514.5 nm laser was used for (i) measuring the coverage of graphene on Si/SiO_2 substrates. This was calculated by taking Streamline maps on an area of 500 × 500 μm^2 on the samples associated with each coverage. The measurements were taken with a 20× objective, 1800 l/mm grating, and laser power well below 5 mW, with a step size of 3.2 × 3.2 μm^2. The graphene coverage was determined by generating Raman maps of the G peak intensity. Subsequently, the number of the pixels with no G peak signal was subtracted from the total number of pixels, and then the sum was divided by the total number of pixels and multiplied by 100 (see Supporting Information, section S6). Three samples were analyzed for each graphene dispersion and coverage: (ii) identification of the polymorphic distribution of glycine crystals, in particular, at the edge of the droplet. The measurements were performed with a 100× objective, 2400 l/mm grating, and the laser power well below 1.5 mW. At least 45 measurements of the crystals at the contact region were taken from each sample. For larger crystals, measurements were taken ~5−10 μm away from the end of the crystals, whereas for the smaller ones, the signal was collected from the contact region as their size is comparable to that of the laser spot. We also measured the polymorph distribution by taking a 2180 × 2530 μm^2 area Streamline map of glycine crystallized on Si/SiO_2 substrate (control sample) using the 20× objective, 1800 l/mm grating, and less than 5 mW laser power with a step size of 3.2 × 3.2 μm^2 (see Supporting Information, section S2). A large area (200 × 200 μm^2) Streamline map was also taken from the CVD Gr sample in order to confirm the full coverage of graphene on Cu and to investigate the homogeneity of the film. The measurements were taken with a 20× objective, 1800 l/mm grating, and laser power well below 5 mW, with a step size of 3.2 × 3.2 μm^2 (see Supporting Information, section S6).

Computer Models. Calculations were performed with the software DFTB+ version 18.2[45] at the DFTB3 level with the 3OB parameter set[46] augmented by empirical -D3 dispersion[47] and the H5 hydrogen bond correction.[48] As a reference, at this level, each molecule is 0.014 eV more stable in α-form than in β-form, in line with higher level plane-wave calculations at the PBE-D2 level.[49] Further details are available in the Supporting Information, section S7.

ASSOCIATED CONTENT

Supporting Information

The Supporting Information is available free of charge at https://pubs.acs.org/doi/10.1021/acsnano.0c04183.

Detailed information on the crystallization setup, Raman spectrum of glycine, characterization of the graphene dispersions, conversion of contact angles to surface areas, additional results from both the additive and surface-templated crystallizations, and computer modeling (PDF)

AUTHOR INFORMATION

Corresponding Author

Cinzia Casiraghi − *Department of Chemistry, University of Manchester, Manchester M13 9PL, United Kingdom;* orcid.org/0000-0001-7185-0377; Email: cinzia.casiraghi@manchester.ac.uk

Authors

Matthew Boyes − *Department of Chemistry, University of Manchester, Manchester M13 9PL, United Kingdom;* orcid.org/0000-0002-9489-6092

Adriana Alieva − *Department of Chemistry, University of Manchester, Manchester M13 9PL, United Kingdom*

Jincheng Tong − *Department of Chemistry, University of Manchester, Manchester M13 9PL, United Kingdom;* orcid.org/0000-0001-7762-1460

Vaiva Nagyte − *Department of Chemistry, University of Manchester, Manchester M13 9PL, United Kingdom;* orcid.org/0000-0003-0835-6039

Manuel Melle-Franco − *CICECO−Aveiro Institute of Materials, Department of Chemistry, University of Aveiro, Aveiro 3810-193, Portugal*

Thomas Vetter − *Department of Chemical Engineering and Analytical Science, University of Manchester, Manchester M13 9PL, United Kingdom*

Complete contact information is available at: https://pubs.acs.org/10.1021/acsnano.0c04183

Author Contributions

C.C. conceived the project. M.B. and A.A. contributed equally to the design of the crystallization experiments and related data analysis, under the supervision of C.C. and T.V., J.T., and V.N.

https://dx.doi.org/10.1021/acsnano.0c04183
ACS Nano 2020, 14, 10394−10401

performed some of the Raman spectroscopy measurements on the glycine crystals and graphene. M.M.F. performed the computational modeling. The paper was written by M.B., A.A., M.M.F., and C.C. in close consultation with all authors.

Notes

The authors declare no competing financial interest.

ACKNOWLEDGMENTS

This work is supported by the European Research Council (ERC) under the European Union's Horizon 2020 research and innovation programme under Grant Agreement No. 648417. V.N. acknowledges funding from the National Physical Lab in London and the EPSRC in the framework of the CDT Graphene NOWNANO. M.M.F. acknowledges support from the Portuguese Foundation for Science and Technology (FCT), under the projects PTDC/FIS-NAN/4662/2014, IF/00894/2015, and FCT ref. UID/CTM/50011/2019 for CICECO–Aveiro Institute of Materials. T.V. thanks the Royal Academy of Engineering for the support through an Engineering for Development research fellowship (Grant No. RF1516/15/22). The authors thank Aurora J. Cruz-Cabeza and Kostya Novoselov for useful discussions.

REFERENCES

(1) Schoen, H. M.; Grove, C. S.; Palermo, J. A. The Early History of Crystallization. *J. Chem. Educ.* **1956**, *33*, 373.
(2) Davey, R.; Garside, J. *From Molecules to Crystallizers*; Oxford University Press: New York, 2000.
(3) Bernstein, J. *Polymorphism in Molecular Crystals*; Oxford University Press: New York, 2010.
(4) Aitipamula, S.; Banerjee, R.; Bansal, A. K.; Biradha, K.; Cheney, M. L.; Choudhury, A. R.; Desiraju, G. R.; Dikundwar, A. G.; Dubey, R.; Duggirala, N.; Ghogale, P. P.; Ghosh, S.; Goswami, P. K.; Goud, N. R.; Jetti, R. R. K. R.; Karpinski, P.; Kaushik, P.; Kumar, D.; Kumar, V.; Moulton, B.; et al. Polymorphs, Salts, and Cocrystals: What's in a Name? *Cryst. Growth Des.* **2012**, *12*, 2147–2152.
(5) Erdemir, D.; Lee, A. Y.; Myerson, A. S. Nucleation of Crystals from Solution: Classical and Two-Step Models. *Acc. Chem. Res.* **2009**, *42*, 621–629.
(6) Rideal, E. K. How Crystals Grow. *Nature* **1949**, *164*, 303.
(7) Powers, H. E. C. Growth of Sucrose Crystals. *Nature* **1956**, *178*, 139.
(8) Aakeröy, C. B.; Seddon, K. R. The Hydrogen Bond and Crystal Engineering. *Chem. Soc. Rev.* **1993**, *22*, 397–407.
(9) Zhou, J.; Yang, Y.; Yang, Y.; Kim, D. S.; Yuan, A.; Tian, X.; Ophus, C.; Sun, F.; Schmid, A. K.; Nathanson, M.; Heinz, H.; An, Q.; Zeng, H.; Ercius, P.; Miao, J. Observing Crystal Nucleation in Four Dimensions Using Atomic Electron Tomography. *Nature* **2019**, *570*, 500–503.
(10) Hunter, M.; Davies, E. B. The Origin of Forms and Qualities. *The Works of Robert Boyle, Part I*; Routledge, 1999; Vol. 5.
(11) Mullin, J. W. *Crystallization*, 4th ed.; Butterworth-Heinemann: Oxford, UK, 2001.
(12) Aizenberg, J.; Black, A. J.; Whitesides, G. M. Control of Crystal Nucleation by Patterned Self-Assembled Monolayers. *Nature* **1999**, *398*, 495–498.
(13) Lee, A. Y.; Lee, I. S.; Dette, S. S.; Boerner, J.; Myerson, A. S. Crystallization on Confined Engineered Surfaces: A Method to Control Crystal Size and Generate Different Polymorphs. *J. Am. Chem. Soc.* **2005**, *127*, 14982–14983.
(14) Van Driessche, A. E. S.; Van Gerven, N.; Bomans, P. H. H.; Joosten, R. R. M.; Friedrich, H.; Gil-Carton, D.; Sommerdijk, N. A. J. M.; Sleutel, M. Molecular Nucleation Mechanisms and Control Strategies for Crystal Polymorph Selection. *Nature* **2018**, *556*, 89–94.
(15) Dobberschütz, S.; Nielsen, M. R.; Sand, K. K.; Civioc, R.; Bovet, N.; Stipp, S. L. S.; Andersson, M. P. The Mechanisms of Crystal Growth Inhibition by Organic and Inorganic Inhibitors. *Nat. Commun.* **2018**, *9*, 1578.
(16) Pons Siepermann, C. A.; Myerson, A. S. Inhibition of Nucleation Using a Dilute, Weakly Hydrogen-Bonding Molecular Additive. *Cryst. Growth Des.* **2018**, *18*, 3584–3595.
(17) Novoselov, K. S.; Fal'ko, V. I.; Colombo, L.; Gellert, P. R.; Schwab, M. G.; Kim, K. A Roadmap for Graphene. *Nature* **2012**, *490*, 192–200.
(18) Geim, A. K.; Grigorieva, I. V. Van Der Waals Heterostructures. *Nature* **2013**, *499*, 419–425.
(19) Criado, A.; Melchionna, M.; Marchesan, S.; Prato, M. The Covalent Functionalization of Graphene on Substrates. *Angew. Chem., Int. Ed.* **2015**, *54*, 10734–10750.
(20) Chua, C. K.; Pumera, M. Covalent Chemistry on Graphene. *Chem. Soc. Rev.* **2013**, *42*, 3222.
(21) Elias, D. C.; Nair, R. R.; Mohiuddin, T. M. G.; Morozov, S. V.; Blake, P.; Halsall, M. P.; Ferrari, A. C.; Boukhvalov, D. W.; Katsnelson, M. I.; Geim, A. K.; Novoselov, K. S. Control of Graphene's Properties by Reversible Hydrogenation: Evidence for Graphane. *Science* **2009**, *323*, 610–613.
(22) Felten, A.; Flavel, B. S.; Britnell, L.; Eckmann, A.; Louette, P.; Pireaux, J. J.; Hirtz, M.; Krupke, R.; Casiraghi, C. Single- and Double-Sided Chemical Functionalization of Bilayer Graphene. *Small* **2013**, *9*, 631–639.
(23) Novoselov, K. S. S.; Geim, A. K. K.; Morozov, S. V. V.; Jiang, D.; Zhang, Y.; Dubonos, S. V. V.; Grigorieva, I. V. V.; Firsov, A. A. A. Electric Field Effect in Atomically Thin Carbon Films. *Science* **2004**, *306*, 666–669.
(24) Hernandez, Y.; Nicolosi, V.; Lotya, M.; Blighe, F. M.; Sun, Z.; De, S.; McGovern, I. T.; Holland, B.; Byrne, M.; Gun'Ko, Y. K.; Boland, J. J.; Niraj, P.; Duesberg, G.; Krishnamurthy, S.; Goodhue, R.; Hutchison, J.; Scardaci, V.; Ferrari, A. C.; Coleman, J. N. High-Yield Production of Graphene by Liquid-Phase Exfoliation of Graphite. *Nat. Nanotechnol.* **2008**, *3*, 563–568.
(25) Ciesielski, A.; Samorì, P. Graphene via Sonication Assisted Liquid-Phase Exfoliation. *Chem. Soc. Rev.* **2014**, *43*, 381–398.
(26) Boldyreva, E. V.; Drebushchak, V. A.; Drebushchak, T. N.; Paukov, I. E.; Kovalevskaya, Y. A.; Shutova, E. S. Polymorphism of Glycine: Thermodynamic Aspects. Part I - Relative Stability of the Polymorphs. *J. Therm. Anal. Calorim.* **2003**, *73*, 409–418.
(27) Boldyreva, E. V.; Drebushchak, V. A.; Drebushchak, T. N.; Paukov, I. E.; Kovalevskaya, Y. A.; Shutova, E. S. Polymorphism of Glycine: Thermodynamic Aspects. Part II - Polymorphic Transitions. *J. Therm. Anal. Calorim.* **2003**, *73*, 419–428.
(28) Little, L. J.; Sear, R. P.; Keddie, J. L. Does the γ Polymorph of Glycine Nucleate Faster? A Quantitative Study of Nucleation from Aqueous Solution. *Cryst. Growth Des.* **2015**, *15*, 5345–5354.
(29) Li, X.; Cai, W.; An, J.; Kim, S.; Nah, J.; Yang, D.; Piner, R.; Velamakanni, A.; Jung, I.; Tutuc, E.; Banerjee, S. K.; Colombo, L.; Ruoff, R. S. Large Area Synthesis of High Quality and Uniform Graphene Films on Copper Foils. *Science* **2009**, *324*, 1312–1314.
(30) Parvez, K.; Wu, Z. S.; Li, R.; Liu, X.; Graf, R.; Feng, X.; Müllen, K. Exfoliation of Graphite into Graphene in Aqueous Solutions of Inorganic Salts. *J. Am. Chem. Soc.* **2014**, *136*, 6083–6091.
(31) Nagyte, V.; Kelly, D. J.; Felten, A.; Picardi, G.; Shin, Y.; Alieva, A.; Worsley, R. E.; Parvez, K.; Dehm, S.; Krupke, R.; Haigh, S. J.; Oikonomou, A.; Pollard, A. J.; Casiraghi, C. Raman Fingerprints of Graphene Produced by Anodic Electrochemical Exfoliation. *Nano Lett.* **2020**, *20*, 3411–3419.
(32) Kim, K.; Centrone, A.; Hatton, T. A.; Myerson, A. S. Polymorphism Control of Nanosized Glycine Crystals on Engineered Surfaces. *CrystEngComm* **2011**, *13*, 1127–1131.
(33) Poornachary, S. K.; Parambil, J. V.; Chow, P. S.; Tan, R. B. H.; Heng, J. Y. Y. Nucleation of Elusive Crystal Polymorphs at the Solution-Substrate Contact Line. *Cryst. Growth Des.* **2013**, *13*, 1180–1186.
(34) Zhou, K. G.; Mao, N. N.; Wang, H. X.; Peng, Y.; Zhang, H. L. A Mixed-Solvent Strategy for Efficient Exfoliation of Inorganic Graphene Analogues. *Angew. Chem., Int. Ed.* **2011**, *50*, 10839–10842.

https://dx.doi.org/10.1021/acsnano.0c04183
ACS Nano 2020, 14, 10394–10401

(35) Lotya, M.; Hernandez, Y.; King, P. J.; Smith, R. J.; Nicolosi, V.; Karlsson, L. S.; Blighe, F. M.; De, S.; Wang, Z.; McGovern, I. T.; Duesberg, G. S.; Coleman, J. N. Liquid Phase Production of Graphene by Exfoliation of Graphite in Surfactant/Water Solutions. *J. Am. Chem. Soc.* **2009**, *131*, 3611−3620.
(36) Lotya, M.; King, P. J.; Khan, U.; De, S.; Coleman, J. N. High-Concentration, Surfactant-Stabilized Graphene Dispersions. *ACS Nano* **2010**, *4*, 3155−3162.
(37) Parviz, D.; Das, S.; Ahmed, H. S. T.; Irin, F.; Bhattacharia, S.; Green, M. J. Dispersions of Non-Covalently Functionalized Graphene with Minimal Stabilizer. *ACS Nano* **2012**, *6*, 8857−8867.
(38) Bouchard, A.; Hofland, G. W.; Witkamp, G.-J. Solubility of Glycine Polymorphs and Recrystallization of *β*-Glycine. *J. Chem. Eng. Data* **2007**, *52*, 1626−1629.
(39) Seyedhosseini, E.; Ivanov, M.; Bystrov, V.; Bdikin, I.; Zelenovskiy, P.; Shur, V. Y.; Kudryavtsev, A.; Mishina, E. D.; Sigov, A. S.; Kholkin, A. L. Growth and Nonlinear Optical Properties of *β*-Glycine Crystals Grown on Pt Substrates. *Cryst. Growth Des.* **2014**, *14*, 2831−2837.
(40) Su, C.-Y.; Lu, A.-Y.; Xu, Y.; Chen, F.-R.; Khlobystov, A. N.; Li, L.-J. High-Quality Thin Graphene Films from Fast Electrochemical Exfoliation. *ACS Nano* **2011**, *5*, 2332−2339.
(41) Neklyudov, V. V.; Khafizov, N. R.; Sedov, I. A.; Dimiev, A. M. New Insights into the Solubility of Graphene Oxide in Water and Alcohols. *Phys. Chem. Chem. Phys.* **2017**, *19*, 17000−17008.
(42) Swinehart, D. F. The Beer-Lambert Law. *J. Chem. Educ.* **1962**, *39*, 333.
(43) Hansen, F. K.; Rødsrud, G. Surface Tension by Pendant Drop. I. A Fast Standard Instrument Using Computer Image Analysis. *J. Colloid Interface Sci.* **1991**, *141*, 1−9.
(44) Polianin, A. D.; Manzhirov, A. V. *Handbook of Mathematics for Engineers and Scientists*; Chapman & Hall/CRC, 2007.
(45) Aradi, B.; Hourahine, B.; Frauenheim, T. DFTB+, a Sparse Matrix-Based Implementation of the DFTB Method. *J. Phys. Chem. A* **2007**, *111*, 5678−5684.
(46) Gaus, M.; Goez, A.; Elstner, M. Parametrization and Benchmark of DFTB3 for Organic Molecules. *J. Chem. Theory Comput.* **2013**, *9*, 338−354.
(47) Grimme, S. Towards First Principles Calculation of Electron Impact Mass Spectra of Molecules. *Angew. Chem., Int. Ed.* **2013**, *52*, 6306−6312.
(48) Řezáč, J. Empirical Self-Consistent Correction for the Description of Hydrogen Bonds in DFTB3. *J. Chem. Theory Comput.* **2017**, *13*, 4804−4817.
(49) Lund, A. M.; Pagola, G. I.; Orendt, A. M.; Ferraro, M. B.; Facelli, J. C. Crystal Structure Prediction from First Principles: The Crystal Structures of Glycine. *Chem. Phys. Lett.* **2015**, *626*, 20−24.

https://dx.doi.org/10.1021/acsnano.0c04183
ACS Nano 2020, 14, 10394−10401

Exploiting the Surface Properties of Graphene for Polymorph Selectivity

Matthew Boyes[1], Adriana Alieva[1], Jincheng Tong[1], Vaiva Nagyte[1], Manuel Melle-Franco[2], Thomas Vetter[3], Cinzia Casiraghi[1*]

[1] Department of Chemistry, University of Manchester, Manchester, M13 9PL, UK

[2] CICECO – Aveiro Institute of Materials, Department of Chemistry, University of Aveiro, 3810-193 Aveiro, Portugal

[3] Department of Chemical Engineering and Analytical Science, University of Manchester, Manchester, M13 9PL, UK

* Corresponding author: cinzia.casiraghi@manchester.ac.uk

Supplementary Information

S1. Crystallisation set-up

Figure S1 shows the experimental set-up used for the crystallisation of glycine. Crystallisations were carried out in the following way: a substrate was placed in the centre of a plastic box, a 2 μL droplet of glycine solution was deposited on the substrate and then it was covered by a clean glass slide, without any contact between the droplet and the cover. The glass slide allowed a 1 mm gap to be present at the front of the sample box. All crystallisations were carried out in an incubator kept at 21 °C.

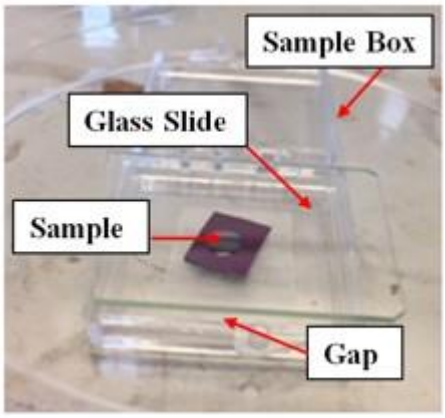

Figure S1 Image of the crystallisation set-up.

S2. Raman spectrum of glycine

Glycine crystallises in three distinct polymorphic forms at ambient conditions, denoted as α, β, and γ. The relative stabilities of these polymorphs are: $\gamma > \alpha > \beta$.[1,2] The most commonly obtained metastable α-form crystallises from aqueous solution;[3] the stable γ-form can be obtained from acidic or basic solutions;[4,5] while the unstable β-form crystallises from mixtures of ethanol or methanol with aqueous glycine solutions and it readily transforms to the α-form upon contact with humid air.[6] It has been shown that all three polymorphs of glycine crystallise simultaneously upon evaporation of aqueous solution microdroplets, which makes polymorphs of glycine classified as concomitant polymorphs.[7]

Figure S2.1 shows the distinct Raman spectra of the CH region (2900-3050 cm^{-1}) of the three polymorphs of glycine. These peaks represent the symmetric (lower shift) and asymmetric (higher shift) stretches of the C-H bonds. The positions of these modes are distinct for each polymorph, which were found to be at 2972 cm^{-1} and 3007 cm^{-1} for the α-form, at 2953 cm^{-1} and 3008 cm^{-1} for the β-form and at 2962 cm^{-1} and 3000 cm^{-1} for the γ-form. Only α- and β-forms were considered in our study as γ-form was not detected.

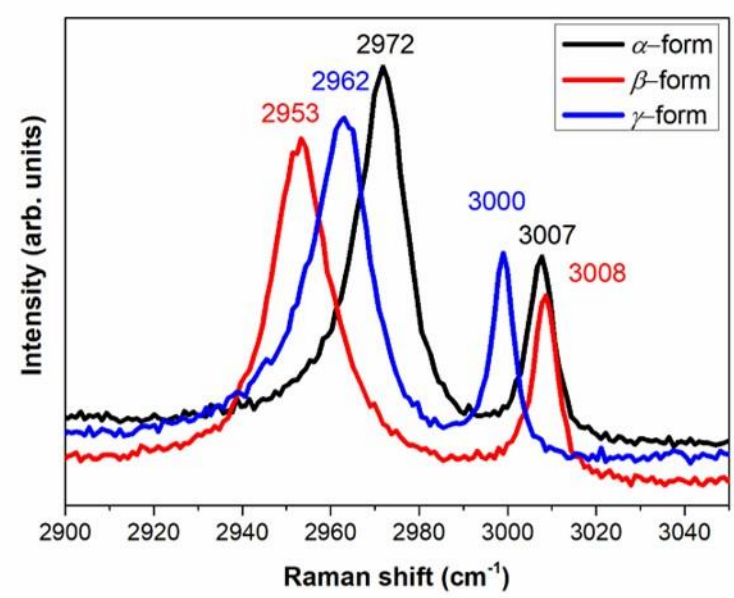

Figure S2.1 Raman spectra of glycine polymorphs.

A Raman map was obtained by scanning the whole area of a crystallised glycine droplet to ascertain the overall distribution of the polymorphs within the product crystal, as shown in Figure S2.2. This map shows the intensity ratio for the symmetric C-H stretch of the β-form (2953 cm^{-1}) to α-form (2972 cm^{-1}): a low ratio corresponds to α-form, while a high ratio corresponds to β-form. Raman spectroscopy confirms that the bulk of the droplet exclusively consists of the metastable α-form, while the unstable β-form preferentially nucleates at the edge of the droplet, as expected from literature.[8] To be more quantitative, ~10% of the crystals grown at the contact region are α- and ~90% are the β-form. This outcome has been attributed to the higher supersaturation rate generated at the droplet contact region, which should allow formation of a less stable polymorph.[8] Since Raman mapping on such a large scale is extremely time consuming, the analysis of the polymorphic outcome in this work has been performed by taking individual measurements of each crystal at the droplet contact region.

S3. Graphene dispersion characterisation

After the electrochemical exfoliation process (see Methods), the graphene dispersions were characterised with several techniques.

Figure S3.1a shows the typical UV-vis spectra of graphene dispersions. The concentration of the dispersions was calculated from the absorbance value taken at a wavelength of 660 nm and applying the Beer-Lambert Law.[9]

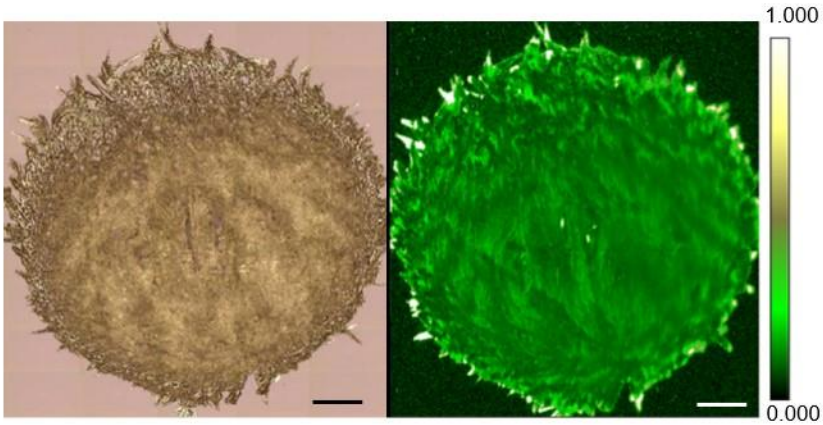

Figure S2.2 Optical image (left) and a StreamLine™ Raman map (right) of the intensity ratio between the symmetric C-H stretch of the β-form (2953 cm^{-1}) and the α-form (2972 cm^{-1}) of glycine crystallised on the Si/SiO_2 substrate: the green area corresponds to the α-form, while the white area corresponds to the β-form (Scale bar ≈ 500 μm; colour scale = intensity ratio, no units).

A detailed Raman characterisation of graphene produced by ECE has been recently provided by our group,[10] hence we only provide a brief overview of the results in this section. Figure S3.1b compares the Raman spectra taken from isolated flakes of ECE(NH_4) and ECE(K) samples. The Raman spectra show the characteristic peaks of solution processed graphene:[11] the G , D, D' and 2D peaks, which are observed at ~1580 cm^{-1}, ~1350 cm^{-1}, ~1620 cm^{-1} and ~2690 cm^{-1}, respectively, can be seen for both samples. The D peak, a defect activated feature,[12,13] is also observed in graphene produced by liquid phase exfoliation[11] as these flakes have a size smaller than the laser spot, so the edges act as defects.[14] However in our case, the average size of the flakes is a few micrometers,[15] so the D peak is likely to be activated by structural defects (*e.g.* formation of C-O bonds), which are known to form during the intercalation process, resulting in the partial oxidation of ECE graphene.[15,16]

The Raman spectrum of defective graphene can be described with a phenomenological three-stage amorphization trajectory.[12] In stage 1, starting from pristine graphene, the Raman spectrum evolves as follows: the D peak appears and the intensity ratio between the D and G peaks (I_D/I_G) increases; the D' appears; all the peaks broaden and G and D' begin to overlap. In this stage, I_D/I_G can be used to estimate the amount of defects,[12,17] while $I_D/I_{D'}$ can be used to distinguish between different type of defects.[13] At the end of Stage 1, the G and D' peaks are no longer distinguishable and I_D/I_G starts decreasing. As the number of defects keeps increasing, the Raman spectrum enters Stage 2, showing a marked decrease in the G peak position and increase broadening of the peaks; I_D/I_G sharply decreases towards zero and

second order peaks are no longer well defined. Stage 3 describes amorphous materials with increasing sp^3 content.[12]

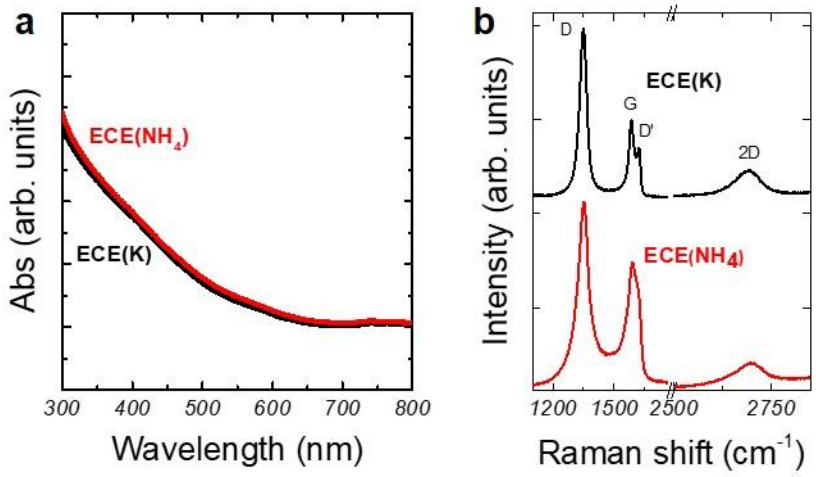

Figure S3.1 (**a**) UV-vis spectra of a 5x diluted ECE(K) dispersion (black) and a 10x diluted ECE(NH_4) dispersion (red). (**b**) Raman spectra of ECE(K) graphene and ECE(NH_4) graphene samples measured with a laser wavelength of 514.5 nm, 100x magnification and a 2400 l/mm grating.

Figure S3.2 shows representative fits of the Raman peaks, obtained by using a Lorentzian function. Table S1 shows the results of the fits. From the full width at half maximum (FWHM) of the peaks, we can conclude that the samples are defective and belong to Stage 2, so defects quantification is not possible. However, all the Raman peaks are broader for the ECE(NH_4) sample compared to the ECE(K) sample: in particular the FWHM of the G peak is ~35 cm^{-1} for ECE(K) and ~65 cm^{-1} for the ECE(NH_4) (Table S1). Furthermore, the G and D' peaks are still distinguishable for ECE(K), whereas they overlap considerably for the ECE(NH_4) sample. These observations indicate that both samples are highly defective, but ECE(NH_4) graphene contains, on average, a higher concentration of defects than the ECE(K) sample.[12] The defects are likely to be oxygen-containing functional groups which are formed during the ECE process.[16]

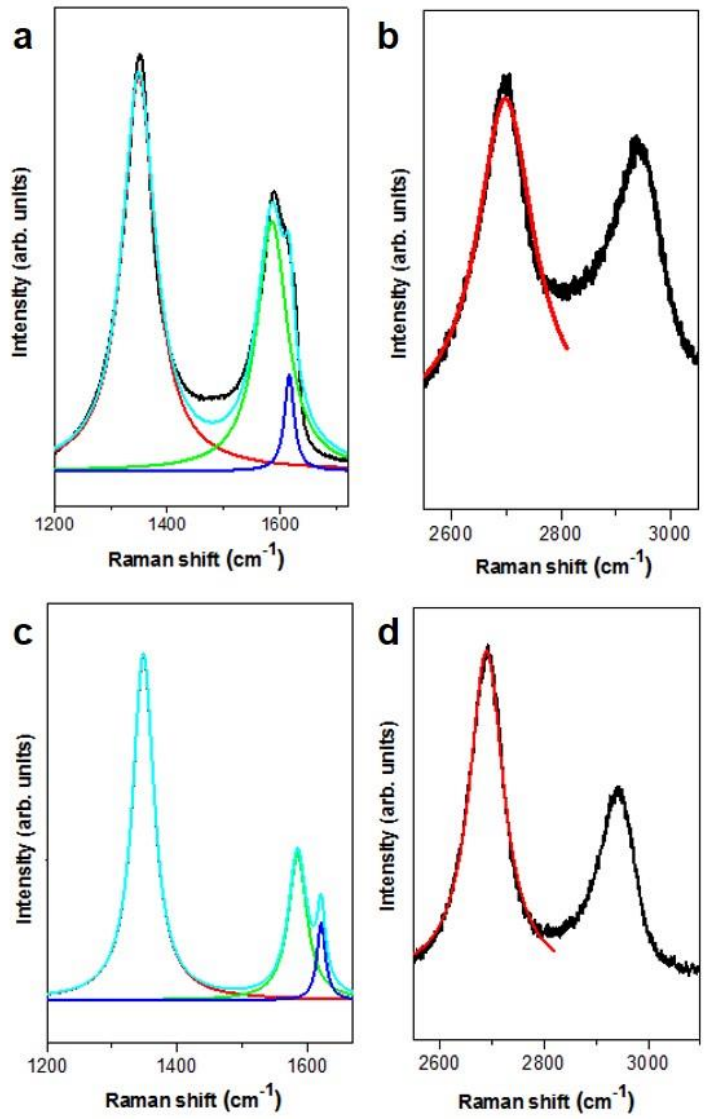

Figure S3.2 Raman spectra showing the fittings of (**a**) D, G and D' peaks and (**b**) 2D peak of ECE(NH_4) graphene sample. Raman spectra and related fittings of (**c**) D, G and D' peaks and (**d**) 2D peak of ECE(K) graphene sample.

Table S1 | Fitting results of Raman spectra of ECE(NH_4) and ECE(K) samples. The position and the fullwidth at half maximum (FWHM) of the peaks are reported.

Sample	Peak	Position / cm^{-1}	FWHM / cm^{-1}
ECE(NH_4)	**D**	1349.4	70.4
	G	1585.9	64.9
	D'	1616	20.7
	2D	2698.3	125
ECE(K)	**D**	1348.1	39.9
	G	1584.6	34.4
	D'	620.8	15.8
	2D	2689.4	79.4

S4. Surface area and volume ratio calculations

Figure S5 shows an example of a spherical cap. The surface areas of glycine droplets on different substrates were calculated by applying the obtained contact angles (see Section 5.2) as cap angles (θ) to the spherical cap model. The fixed volume (V) of 2 μL and the cap angles were applied to Equation 1 in order to obtain the radius (r) values:[18]

$$\boldsymbol{V = \frac{\pi}{3} r^3 (2 + cos\theta)(1 - cos\theta)^2} \quad \textbf{(1)}$$

Following, the surface areas (SA) were obtained using Equation 2:[18]

$$\boldsymbol{SA = 2\pi r^2 (1 - cos\theta)} \quad \textbf{(2)}$$

Finally, the surface area values were divided by a fixed volume of 2 μL in order to obtain Surface area and Volume ratios.

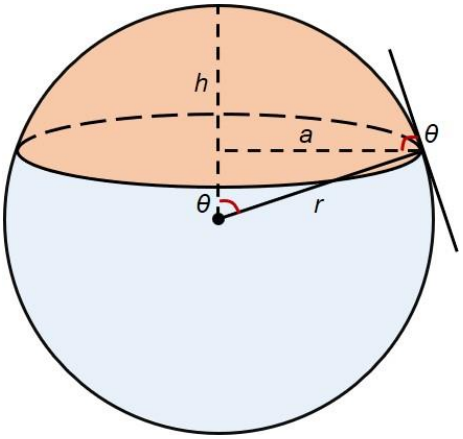

Figure S4 An example of a spherical cap (red).

S5. Additive-templated Crystallisation

S5.1 Samples

Figure S5.1 shows the final solutions used for the additive-templated crystallisation consisting of 0.5 M glycine in 3:1 v/v water/IPA with varying concentrations of ECE graphene.

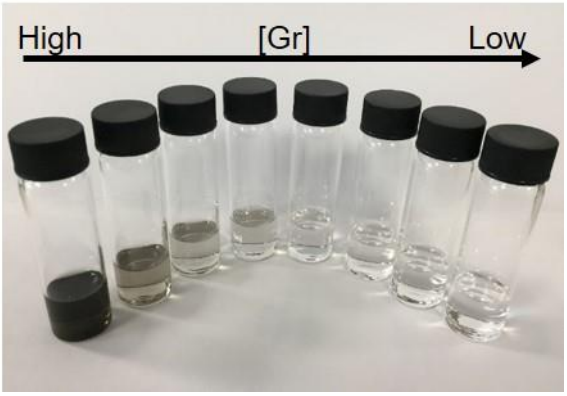

Figure S5.1 Photo of the range of graphene concentrations generated for the additive-templated crystallisation of glycine. The [Gr] ranged from 4.57 x 10^{-2} mg mL^{-1} to 2.63 x 10^{-4} mg mL^{-1}.

S5.2 Contact Angle Measurements

Figure S5.2 shows the contact angle measurements for a select few of the graphene/glycine dispersions. The contact angles were found to be ≈40°, ≈39° and ≈40° for the three concentrations of ECE(K) shown. For the ECE(NH_4) dispersions, contact angles of ≈47°, ≈36° and ≈40° were measured.

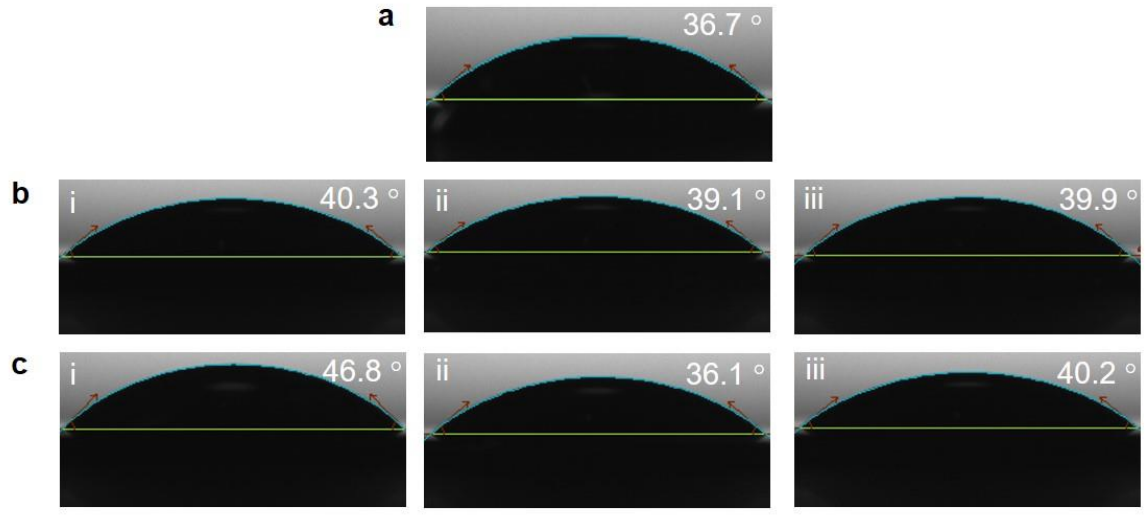

Figure S5.2 Contact angle measurements of various solutions used in the additive-templated crystallisation experiments. (**a**) 0.5 M glycine in 3:1 water/IPA; (**b**) mixtures containing ECE(K) Gr flakes at concentrations: i) 2.6 x 10^{-2} mg mL^{-1}; ii) 1.3 x 10^{-3} mg mL^{-1}, and iii) 2.6 x 10^{-4} mg mL^{-1}; (**c**) mixtures containing ECE(NH_4) Gr flakes at concentrations: i) 4.6 x 10^{-2} mg mL^{-1}; ii) 2.3 x 10^{-3} mg mL^{-1}, and iii) 4.5 x 10^{-4} mg mL^{-1}.

S5.3 Morphology

The observation noted in the main text regarding the distinct morphologies of the crystals can be rationalised by considering the solubility curve of glycine and relative growth and nucleation rates, k_G and J, respectively. Both k_G and J are dependent on the driving force for crystallization, which is typically expressed as the ratio of the actual liquid concentration to the equilibrium/solubility concentration. The solution begins undersaturated and via evaporation of the solvent crosses the supersaturation threshold into glycine's metastable zone (MSZ).[19] In this region, crystal growth dominates over nucleation (a low J/k_G ratio) so if the system were to crystallise, larger crystals would form. If the solvent continues to evaporate, the system will move past the MSZ into high supersaturation, where nucleation events dominate over crystal growth (a high J/k_G ratio).[20] It must be noted here that the crystals obtained from a pure water system (example shown in Figure S2.2) were always compact, thus implying that the addition of IPA, an antisolvent, causes a widening of the MSZ width, as already observed.[21,22]

The effect of graphene on the crystal morphology can be seen in Figure 2f-k. At the highest graphene concentrations, the system always crystallises with a compact morphology (Figures 2f and i). With a decreasing graphene concentration, the likelihood of obtaining the larger crystals increased (Figures 2g, h, j and k). We can infer from this result that graphene is narrowing the width of the MSZ meaning that nucleation is always dominant over crystal growth. This conclusion is reinforced by previous work on MSZ width measurements, where additives (such as sea salt and oxalic acid) could reduce the MSZ width with and produce smaller, more compact crystals.[23,24] Figure 2f and i also show coffee-ring deposits for the high graphene concentration samples.[25,26]

Figure S5.3 shows high magnification images of crystals formed at the contact region of some of the crystallising systems. They clearly show some graphene deposits underneath the crystals instead of being incorporated into them.

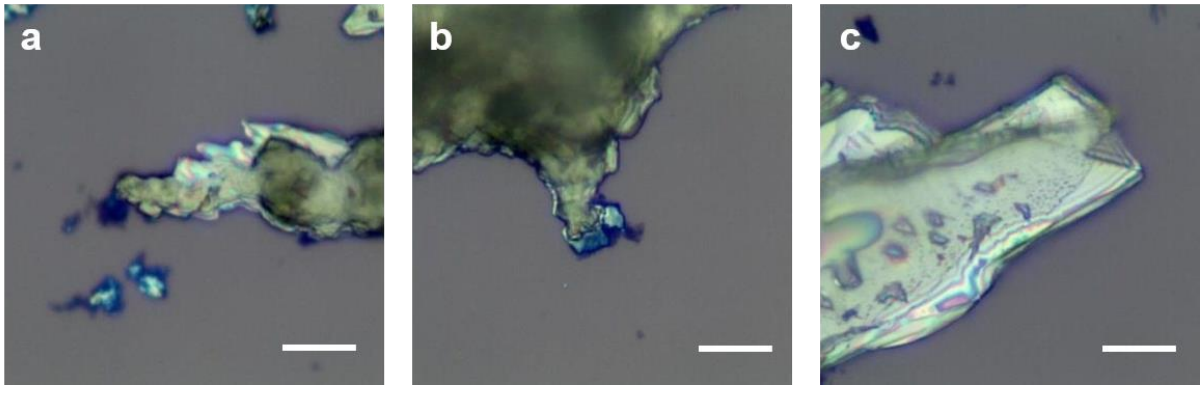

Figure S5.3 High magnification (100x) images of glycine crystals grown at the contact region of a crystallising system. (**a**-**b**) Glycine crystals from Gr ECE(NH_4) additive-templated

crystallisations and (**c**) glycine crystals from Gr ECE(NH_4) substrate-templated crystallisations. The dark blue spots that can be seen are the graphene deposits. Scale bars ≈ 10 μm.

Figure S5.4 shows a representative Raman spectrum of α-glycine generated from the crystallisation experiments undertaken. The lack of any of graphene's Raman features (*i.e.* a D or G peak) is further evidence that the graphene flakes do not incorporate themselves into the growing crystals.

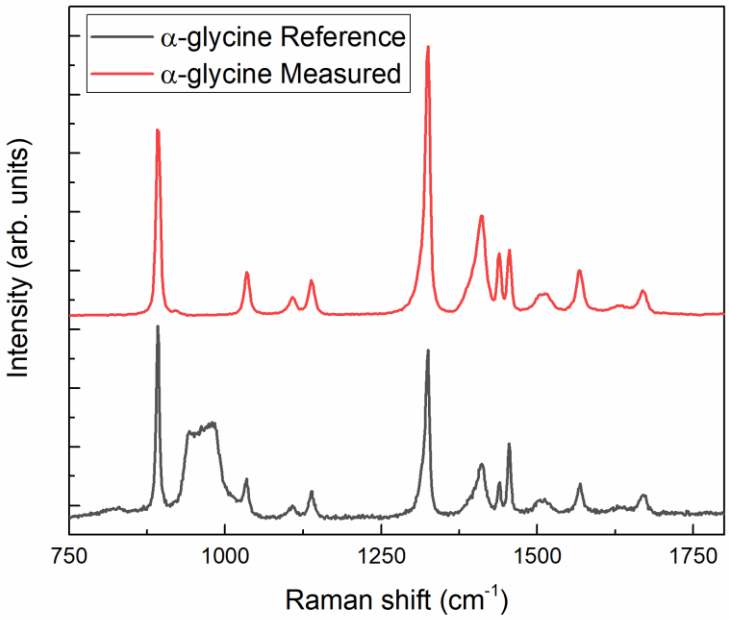

Figure S5.4 Raman spectra of glycine crystals in the Raman shift range of 750-1800 cm^{-1}. The broad peak at ~900 cm^{-1} is from the silicon substrate.

S5.4 Coffee-ring analysis

Figure S5.5 is a Raman spectrum of a deposit in the coffee-ring found after the crystallisation of an ECE(NH_4) solution at the highest graphene concentration available. These rings are formed during the evaporation process due to the shift from a pinned contact line to a constant contact angle.[27,28] During the former stage, the droplet has a constant base area allowing the Marangoni effect[25] to carry the graphene flakes to the first, outer edge which creates the first coffee-ring. Progressing through to the next stage of a constant contact angle, the droplet's base area decreases, therefore additional coffee-rings are generated at different stages as more graphene is deposited. The Raman retains the characteristic D, G, D' and 2D peaks found prior to crystallisation as well as the heavy overlapping of the G and D' peaks.

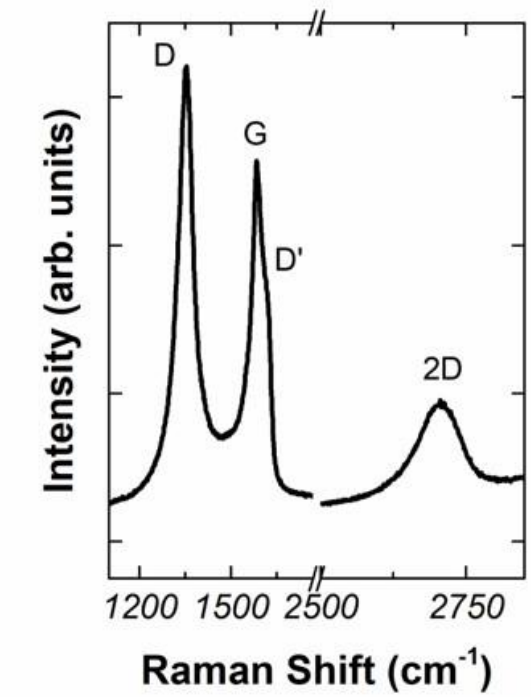

Figure S5.5 | Raman spectrum of a coffee-ring deposit from an ECE(NH_4) graphene crystallisation sample at a graphene concentration of 4.57 x 10^{-2} mg mL^{-1}.

S5.5 Use of GO

The concentration of GO used for this set of experiments were made comparable to those of the ECE graphene samples, ranging from 5 x 10^{-2} mg mL^{-1} to 5 x 10^{-4} mg mL^{-1}. All other experimental parameters were kept identical to the ECE graphene additive-templated crystallisations. The resulting crystals are vastly different, in size and morphology, to those obtained from the experiments with ECE graphene. This is attributed to the different geometries of the droplets between ECE graphene, which is hydrophobic, and GO, which is hydrophilic. Polymorph analysis was attempted by Raman spectroscopy, but the signal from GO made the determination of the glycine's polymorph impossible.

S6. Substrate-templated Crystallisation

S6.1 ECE Graphene

S6.1.1 Coverage Analysis

Figure S6.1 shows representative Raman spectra taken from different areas with no graphene coverage (area 1), as demonstrated by the absence of the G peak, and spectra with weak (area 2) and strong (area 3) G signal which indicates the presence of graphene on the substrate.

The coverages were calculated by subtracting the number of the pixels with no G peak signal from the total number of pixels and then the sum was divided by the total number of pixels and multiplied by one hundred. Table S2 shows the graphene coverage of the Si/SiO_2 substrates for both the ECE(K) and ECE(NH_4) samples.

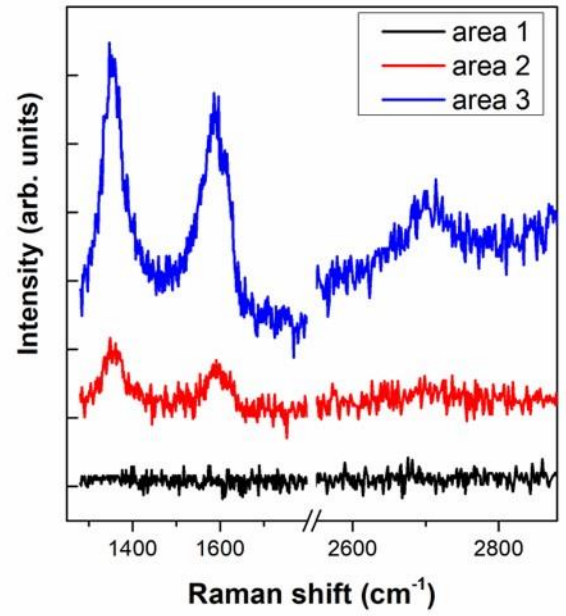

Figure S6.1 Representative spectra taken from areas covered with ECE(NH_4) graphene (area 2 and 3) and an area without graphene (area 1).

Table S2 | Graphene coverages on Si/SiO_2 substrates.

Coverage	ECE(NH_4) % covered	ECE(K) % covered
Low	~2	~6
Moderate	67-84	30-48
Full	100	100

Figure S6.2 shows the optical images and the Raman maps of the samples with different ECE(NH_4) graphene coverages. The coverage was extracted by analysing the areas

highlighted in the red rectangles. Figure S6.3 shows the optical images and the Raman maps of samples with different ECE(K) graphene coverages. The coverage was extracted by analysing the areas highlighted in the red rectangles.

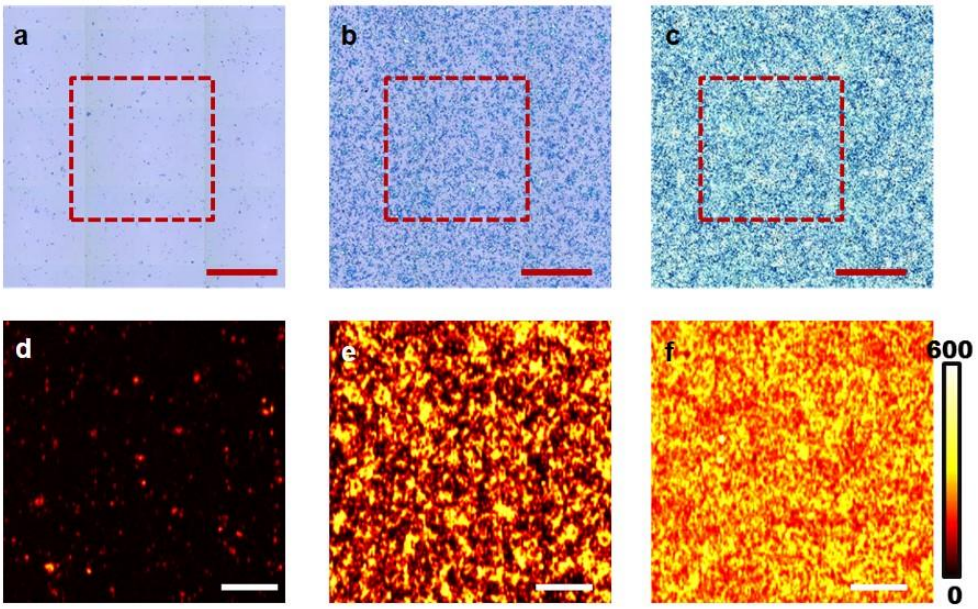

Figure S6.2 Optical images of (**a**) low, (**b**) moderate and (**c**) full coverages of ECE(NH_4) graphene on Si/SiO_2 substrates, scale bar ≈ 250 μm. Areas of mapping are marked by red dashed rectangles. (**d**), (**e**) and (**f**) are StreamLine™ Raman maps of the G peak intensity corresponding to samples in (**a**), (**b**) and (**c**), respectively (Scale bar ≈ 100 μm; colour bar= G peak intensity, in arb. units).

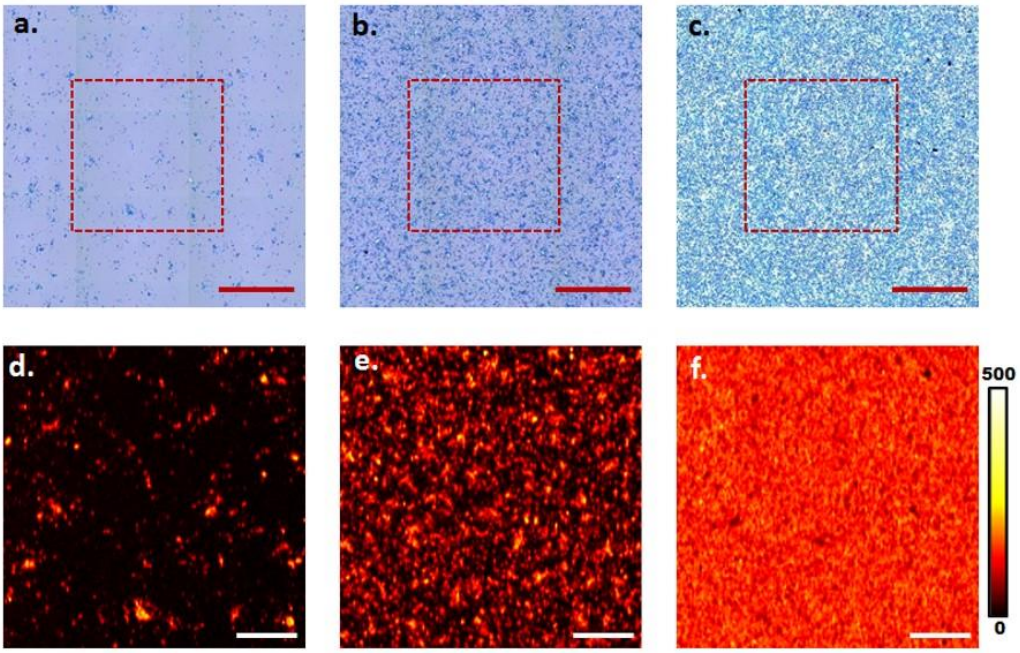

Figure S6.3 Optical images of (**a**) low (**b**) moderate (**c**) full coverages of ECE(K) graphene on Si/SiO_2 substrates, scale bar ≈ 250 μm. Areas of mapping are marked by red dashed rectangles. (**d**), (**e**) and (**f**) are StreamLine™ Raman maps of the G peak intensity corresponding to samples in (**a**), (**b**) and (**c**), respectively (Scale bar ≈ 100 μm; colour bar= G peak intensity, in arb. units).

S6.1.2 Contact Angle Measurements

Figure S6.4 shows the contact angle measurement results on different substrates. The contact angles were found to be ≈61°, ≈71° and ≈94° for the low, moderate and full ECE(NH_4) sample, respectively. For the ECE(K) sample, the contact angles were measured as: ≈58°, ≈64° and ≈77° for the low, moderate and full coverages, respectively. The contact angle for glycine solution on Si/SiO_2 (control sample) was measured as ≈54°.

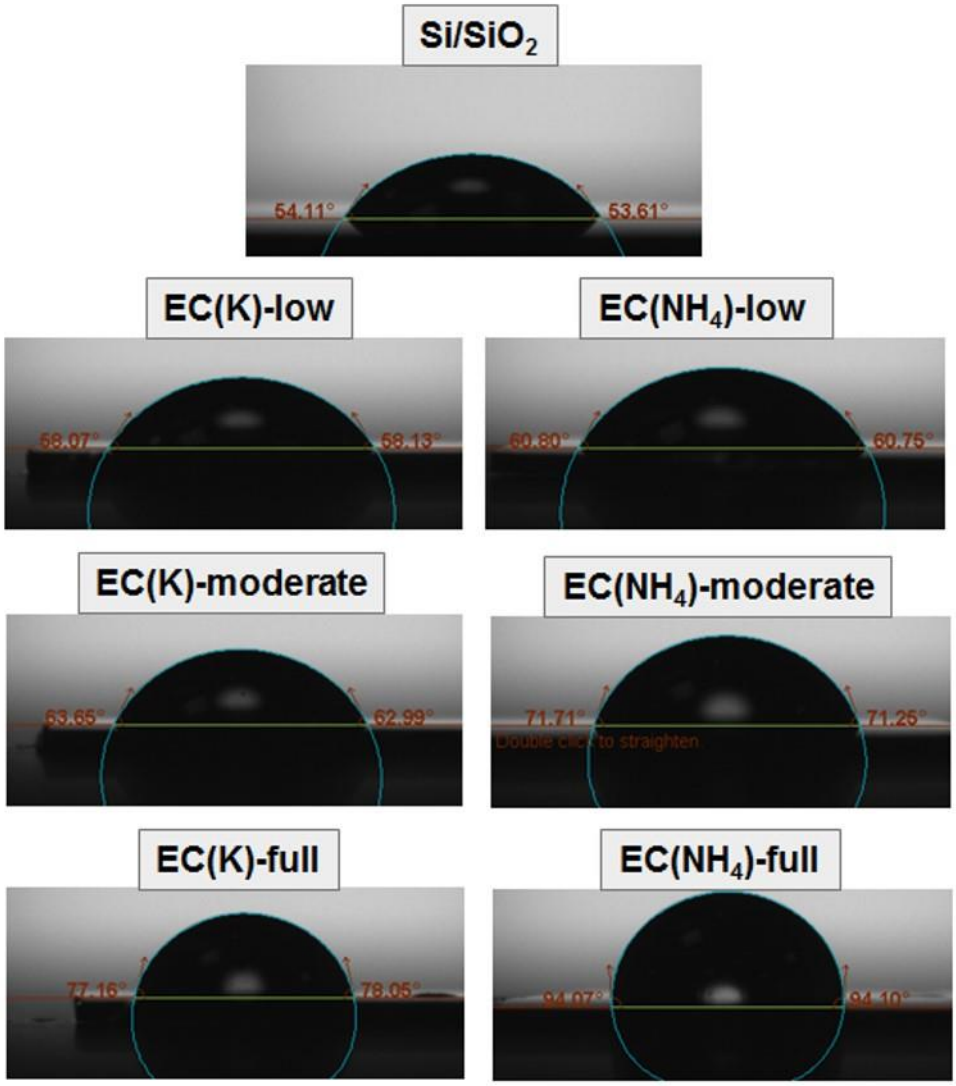

Figure S6.4 Contact angle measurements of glycine solution deposited on different substrates.

S6.1.3 Morphology

Figure S6.5 shows representative optical images of crystals obtained on substrates with different ECE(K) graphene coverages. It can be seen that the morphology of the crystals grown at the edge changes: the size of the crystals extending over the contact region decreases with an increasing graphene coverage, indicating a possible decrease of the β-form component.

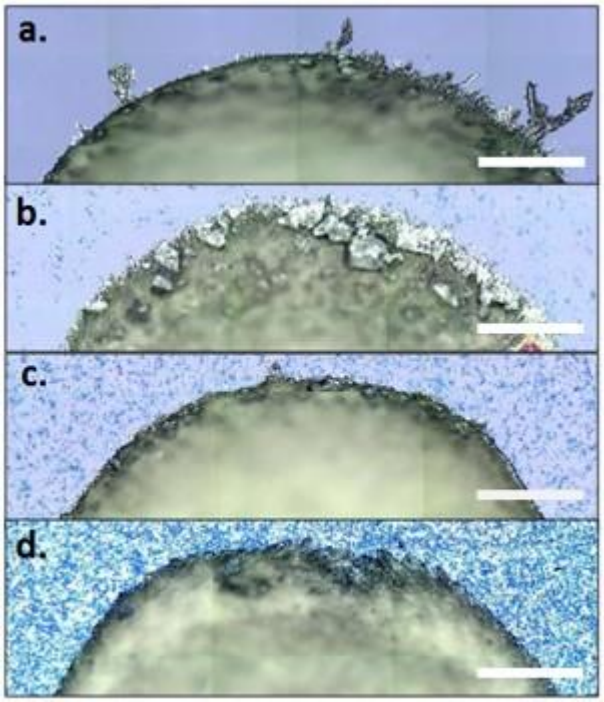

Figure S6.5 Optical images of glycine crystallised on Si/SiO_2 substrates having (**a**) 0%, (**b**) ~6%, (**c**) ~38% and (**d**) ~100% coverage of EC(K) graphene (Scale bar ≈ 250 μm).

S6.1.4 Kinetic Effects

Figure S6.6 shows the kinetic impact of graphene substrates on the crystallisation of glycine. As stated in the main text, the induction times do not follow the expected behaviour if the times were dictated by the geometry of the droplets. The implication from the geometry results of Figure 3a is that droplets should evaporate slower on the graphene substrates than on the bare silicon substrates, thus a longer induction time should be seen.[29] However, the graphene substrates had a promoting effect on the induction times, which furthers the hypothesis of H-bonding between graphene and glycine. It is unclear at this time why there is a reduction in the induction times for these substrate-templated experiments whilst there was an apparent increase in the times for the additive-templated ones, but it is likely due to the intricacies of the different solvent systems used. It is also important to remember that the induction times are all qualitative.

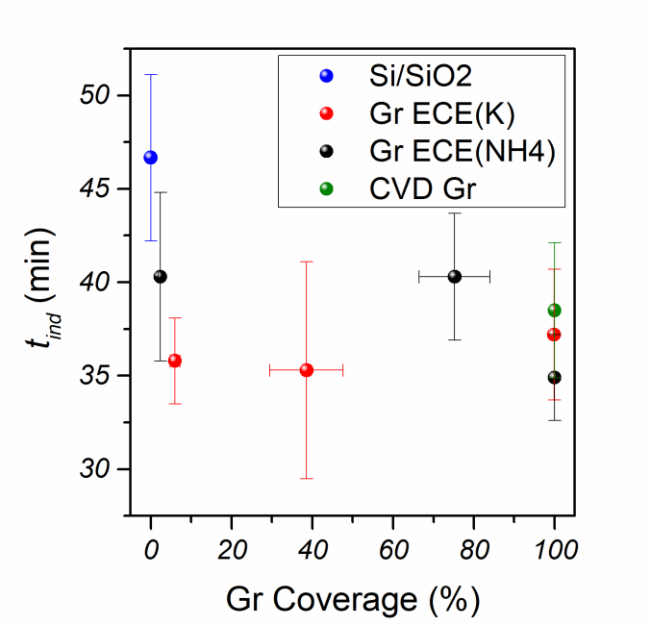

Figure S6.6 Induction times for all substrate-templated crystallisations of 0.5 M of aqueous glycine solution.

S6.2. CVD Graphene

S6.2.1 Coverage Analysis

To investigate the coverage of CVD graphene, we performed Raman mapping of a large area (200 x 200 μm^2). Figure S6.7 shows the 2D peak intensity Raman map (in blue) overlapped on an optical image of the same area. The presence of the 2D peak was detected from each point on the map, confirming the full coverage of graphene on Cu.

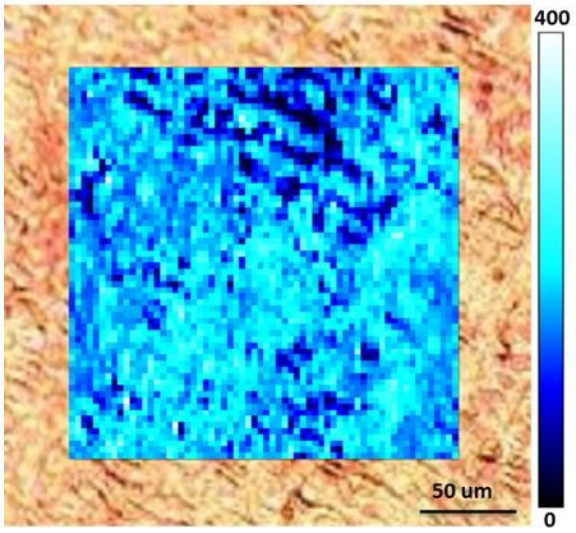

Figure S6.7 Large area (200 x 200 μm^2) Raman map (in blue) of the intensity of 2D peak of CVD Gr on Cu. Colour bar = G peak intensity, in arb. Units.

A representative Raman spectrum of CVD Gr on Cu can be seen in Figure S6.8, showing the characteristic G and 2D peaks of CVD Gr.[30] The high crystalline quality of the film is demonstrated by the absence of the D peak and the sharp G and 2D peaks.

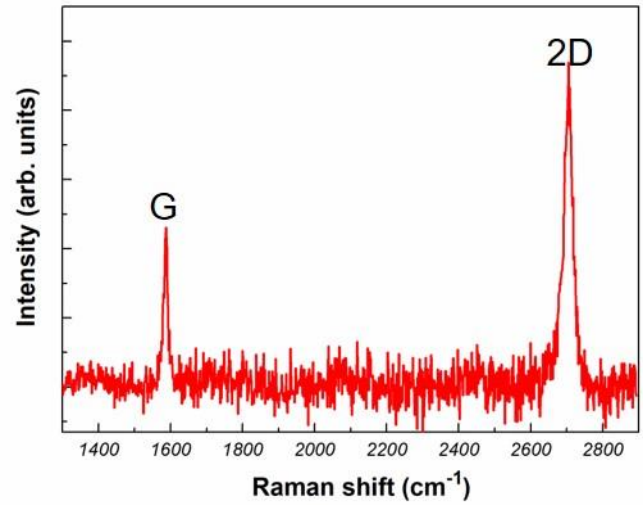

Figure S6.8 Representative Raman spectrum of CVD Gr on Cu.

S6.2.2 Morphology

Figure S6.9 shows a representative optical image of the crystals obtained on CVD Gr substrates. The crystals grown at the contact region are much smaller than that of the control samples (Figure 2d).

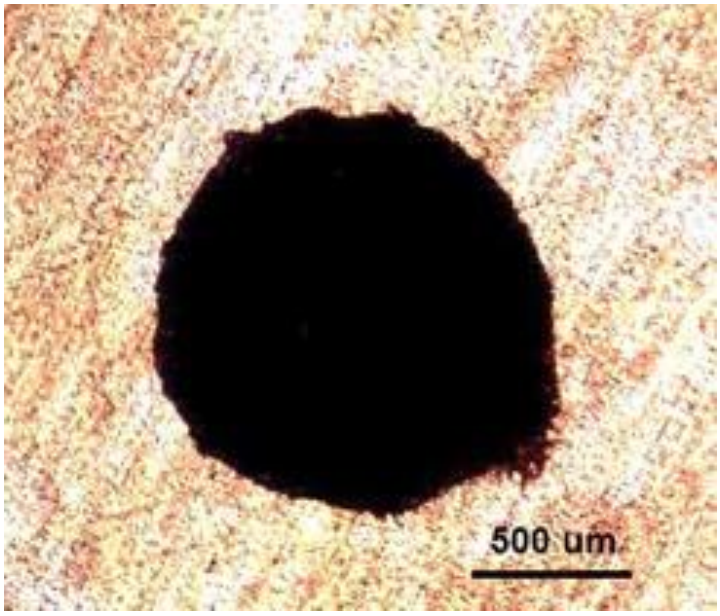

Figure S6.9 Representative optical image of crystals obtained on CVD Gr substrates.

S7. Computer modelling

We computed the interaction of surfaces of α- and β-glycine crystals modelled by slabs of increasing thickness, namely with 1, 2, 3 and 4 molecular layers in vacuo and interacting with pristine graphene and oxidised graphene. The oxidised graphene model had 12.5 % OH groups and was built by adding 30 OH groups in a 240 C atoms graphene surface of 2.6 nm x 2.5 nm in a highly regular fashion, Figure S7.1. The graphene periodic box was chosen as it is approximately square and has dimensions mostly commensurate with the most significant β-form surface: (010). In addition, the β-form (010) surface is highly commensurate with the α-form (010) surface which allows for their direct comparison. To ease this comparison and the comparison of graphene and oxidised graphene, the 2D periodic box dimensions were held fixed during the optimisations. In addition, the periodic dimension perpendicular to the surface was also fixed and set, in all cases, to 10 nm.

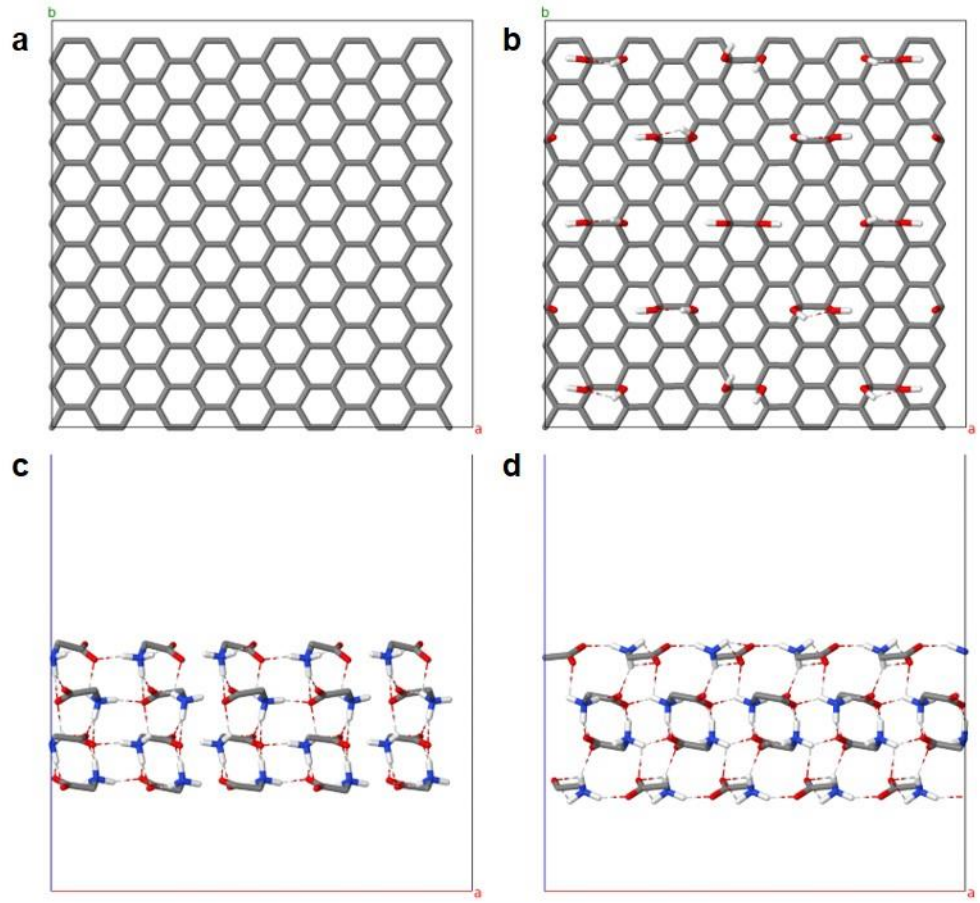

Figure S7.1 Optimised structures for a 2.6 x 2.5 nm^2 surface of (**a**) pristine graphene and (**b**) oxidised graphene (12.5 %) and commensurate 4 layers slabs of the (**c**) α-form and (**d**) β-form of the (010) glycine surfaces in vacuum.

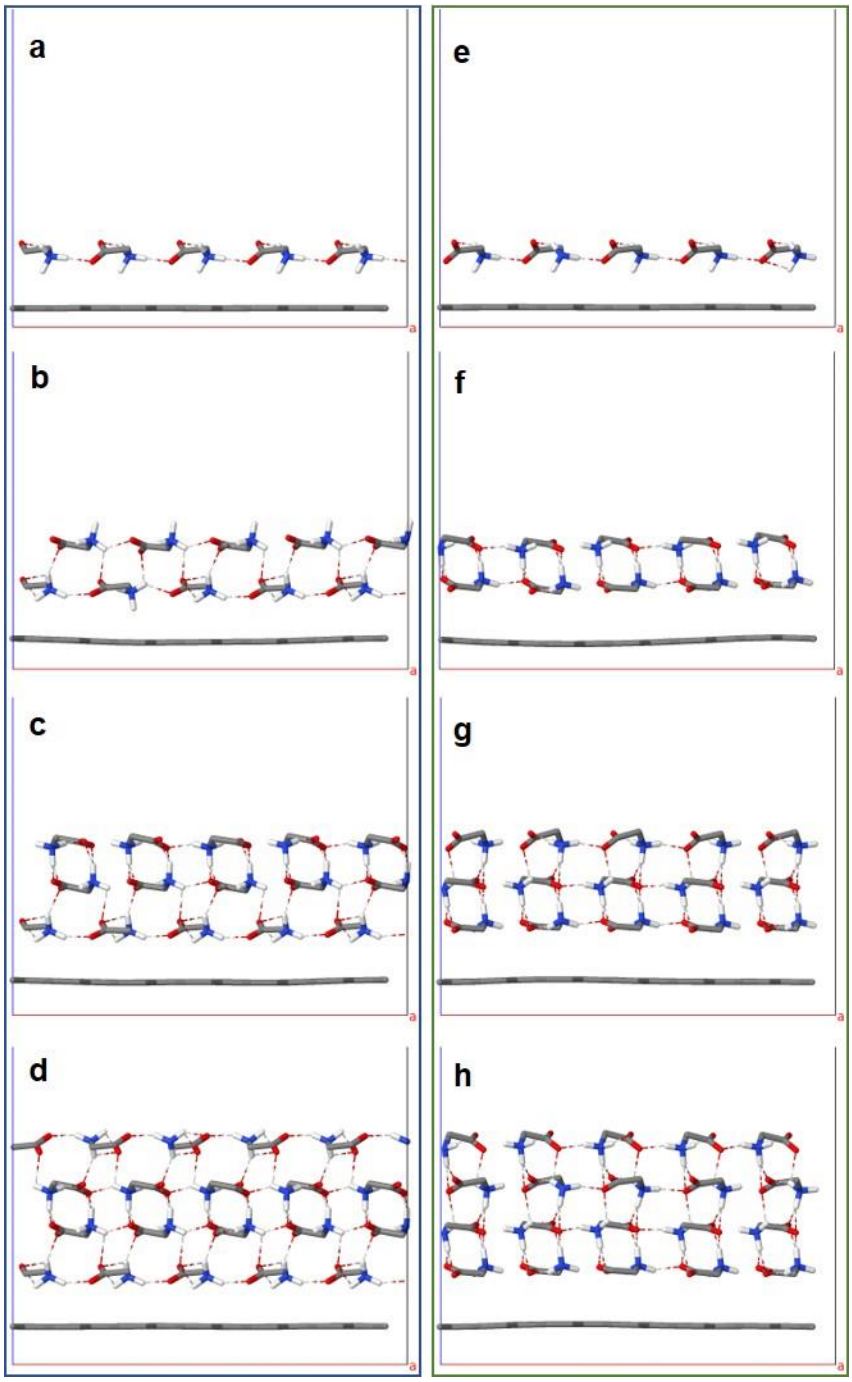

Figure S7.2 | Optimised structures for a 2.6 x 2.5 nm^2 surface of pristine graphene and, from top to bottom, 1, 2, 3 and 4 layers for the (**a-d**) α-form and (**e-h**) β-form of the (010) glycine surfaces.

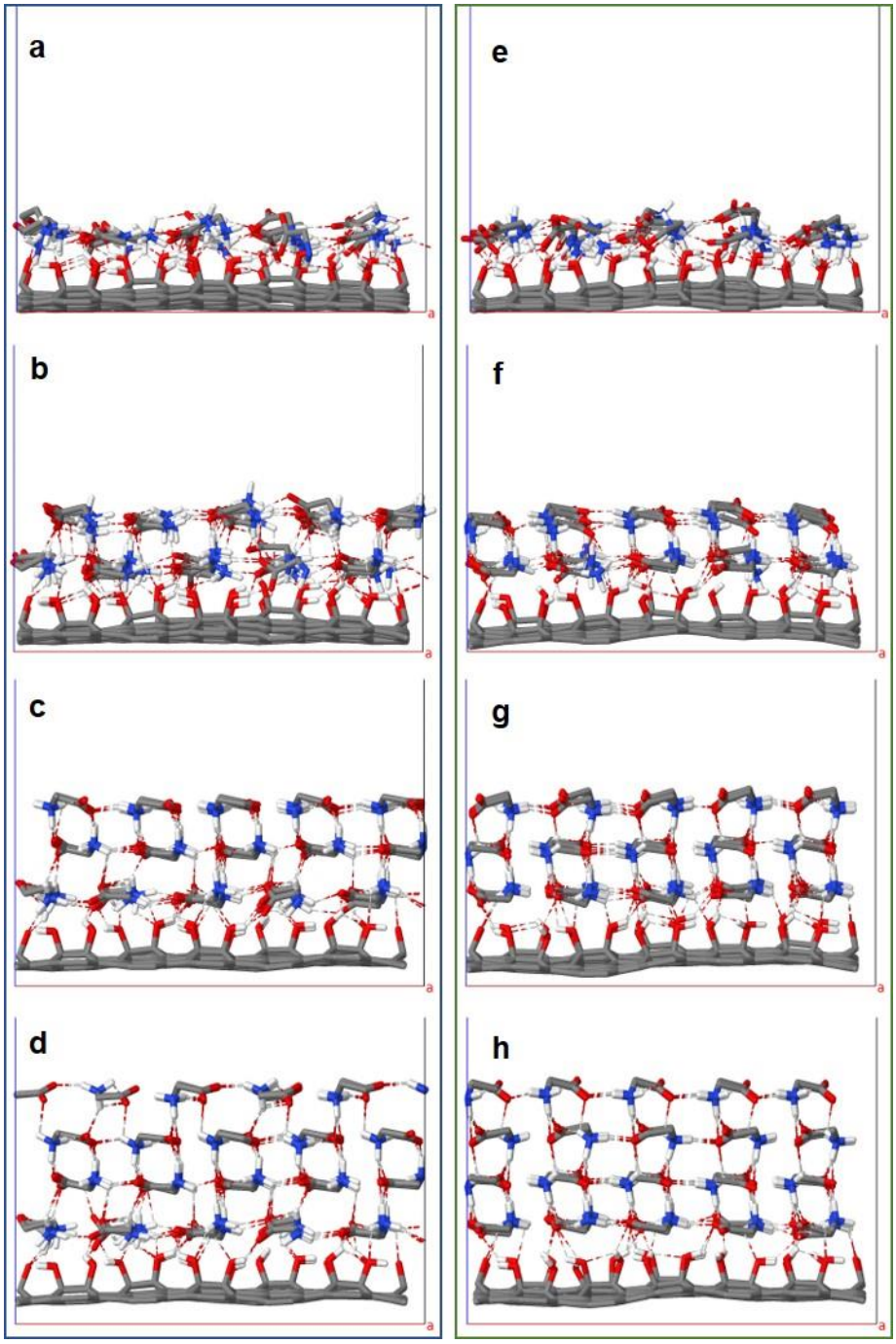

Figure S7.3 | Optimised structures for a 2.6 x 2.5 nm^2 surface of oxidised graphene and, from top to bottom, 1, 2, 3 and 4 layers of the (**a-d**) α-form and (**e-h**) β-form of the (010) glycine surfaces.

The surface energy was computed subtracting the energy of the slab against the energy of an infinite crystal. This value was normalized by the number of molecules on the surface, Table S3. The interface energy was computed subtracting the energy of the slab in vacuum against the energy of the same slab on contact with graphene and graphene hydroxyl normalized by the number of molecules at the interface. The interface energy quantifies how the presence of

graphene or oxidised graphene stabilises the crystalline surface, negative values indicate stabilising interfaces, Table S4.

Table S3 | Surface energy per molecule for α- and β- (010) glycine surfaces with 1,2, 3 and 4 molecular layers. **All energies in eV.**

Number of layers	**α-GLY**	**β-GLY**
1	1.25	1.24
2	1.58	0.96
3	1.25	1.05
4	1.47	1.11

Table S4 | Interface energy vs. graphene (Gr) and hydroxyl graphene (Gr-OH) per molecule for α- and β- (010) glycine surfaces with 1,2, 3 and 4 molecular layers. **All energies in eV.**

	Gr	**Gr-OH**	**Gr**	**Gr-OH**
Number of layers	**α-GLY**	**α-GLY**	**β-GLY**	**β-GLY**
1	-0.36	-0.83	-0.35	-0.83
2	-0.49	-0.93	-0.35	-0.50
3	-0.45	-0.70	-0.39	-0.52
4	-0.44	-0.78	-0.36	-0.50

Supplementary References

(1) Boldyreva, E. V.; Drebushchak, V. A.; Drebushchak, T. N.; Paukov, I. E.; Kovalevskaya, Y. A.; Shutova, E. S. Polymorphism of Glycine: Thermodynamic Aspects. Part I - Relative Stability of the Polymorphs. *J. Therm. Anal. Calorim.* **2003**, *73*, 409–418.

(2) Boldyreva, E. V.; Drebushchak, V. A.; Drebushchak, T. N.; Paukov, I. E.; Kovalevskaya, Y. A.; Shutova, E. S. Polymorphism of Glycine: Thermodynamic Aspects. Part II - Polymorphic Transitions. *J. Therm. Anal. Calorim.* **2003**, *73*, 419–428.

(3) Marsh, R. E. A Refinement of the Crystal Structure of Glycine. *Acta Crystallogr.* **1958**, *11*, 654–663.

(4) Iitaka, Y. The Crystal Structure of γ-Glycine. *Acta Crystallogr.* **1961**, *14*, 1–10.

(5) Tang, W.; Mo, H.; Zhang, M.; Gong, J.; Wang, J.; Li, T. Glycine's PH-Dependent Polymorphism: A Perspective from Self-Association in Solution. *Cryst. Growth Des.* **2017**, *17*, 5028–5033.

(6) Itaka, Y. The Crystal Structure of Beta-Glycine. *Acta. Cryst.* **1960**, *13*, 35–45.

(7) Lee, A. Y.; Lee, I. S.; Dette, S. S.; Boerner, J.; Myerson, A. S. Crystallization on Confined Engineered Surfaces: A Method to Control Crystal Size and Generate Different Polymorphs. *J. Am. Chem. Soc.* **2005**, *127*, 14982–14983.

(8) Poornachary, S. K.; Parambil, J. V.; Chow, P. S.; Tan, R. B. H.; Heng, J. Y. Y. Nucleation of Elusive Crystal Polymorphs at the Solution-Substrate Contact Line. *Cryst. Growth Des.* **2013**, *13*, 1180–1186.

(9) Swinehart, D. F. The Beer-Lambert Law. *J. Chem. Educ.* **1962**, *39*, 333.

(10) Nagyte, V.; Kelly, D. J.; Felten, A.; Picardi, G.; Shin, Y.; Alieva, A.; Worsley, R. E.; Parvez, K.; Dehm, S.; Krupke, R.; Haigh, S. J.; Oikonomou, A.; Pollard, A. J.; Casiraghi, C. Raman Fingerprints of Graphene Produced by Anodic Electrochemical Exfoliation. *Nano Lett.* **2020**.

(11) Hernandez, Y.; Nicolosi, V.; Lotya, M.; Blighe, F. M.; Sun, Z.; De, S.; McGovern, I. T.; Holland, B.; Byrne, M.; Gun'Ko, Y. K.; Boland, J. J.; Niraj, P.; Duesberg, G.; Krishnamurthy, S.; Goodhue, R.; Hutchison, J.; Scardaci, V.; Ferrari, A. C.; Coleman, J. N. High-Yield Production of Graphene by Liquid-Phase Exfoliation of Graphite. *Nat. Nanotechnol.* **2008**, *3*, 563–568.

(12) Cançado, L. G.; Jorio, A.; Ferreira, E. H. M.; Stavale, F.; Achete, C. A.; Capaz, R. B.; Moutinho, M. V. O.; Lombardo, A.; Kulmala, T. S.; Ferrari, A. C. Quantifying Defects in Graphene via Raman Spectroscopy at Different Excitation Energies. *Nano Lett.* **2011**, *11*, 3190–3196.

(13) Eckmann, A.; Felten, A.; Mishchenko, A.; Britnell, L.; Krupke, R.; Novoselov, K. S.; Casiraghi, C. Probing the Nature of Defects in Graphene by Raman Spectroscopy. *Nano Lett.* **2012**, *12*, 3925–3930.

(14) Casiraghi, C.; Hartschuh, A.; Qian, H.; Pliscanec, S.; Georgia, C.; Fasoli, A.; Novoselov, K. S.; Basko, D. M.; Ferrari, A. C. Raman Spectroscopy of Graphene Edges. *Nano Lett.* **2009**, *9*, 1433–1441.

(15) Parvez, K.; Wu, Z. S.; Li, R.; Liu, X.; Graf, R.; Feng, X.; Müllen, K. Exfoliation of Graphite into Graphene in Aqueous Solutions of Inorganic Salts. *J. Am. Chem. Soc.* **2014**, *136*, 6083–6091.

(16) Su, C.-Y.; Lu, A.-Y.; Xu, Y.; Chen, F.-R.; Khlobystov, A. N.; Li, L.-J. High-Quality Thin Graphene Films from Fast Electrochemical Exfoliation. *ACS Nano* **2011**, *5*, 2332–2339.

(17) Ferrari, A.; Robertson, J. Resonant Raman Spectroscopy of Disordered, Amorphous, and Diamond like Carbon. *Phys. Rev. B* **2001**, *64*, 440.

(18) Polianin, A. D.; Manzhirov, A. V. *Handbook of Mathematics for Engineers and Scientists*; Chapman & Hall/CRC, 2007.

(19) Mullin, J. W. *Crystallization*, 4th ed.; Butterworth-Heinemann: Oxford, Boston, 2001.

(20) Davey, R.; Garside, J. *From Molecules to Crystallizers*; Oxford University Press: New York, 2000.

(21) Bhamidi, V.; Lee, S. H.; He, G.; Chow, P. S.; Tan, R. B. H.; Zukoski, C. F.; Kenis, P. J. A. Antisolvent Crystallization and Polymorph Screening of Glycine in Microfluidic Channels Using Hydrodynamic Focusing. *Cryst. Growth Des.* **2015**, *15*, 3299–3306.

(22) El Bazi, W.; Porte, C.; Mabille, I.; Havet, J. L. Antisolvent Crystallization: Effect of Ethanol on Batch Crystallization of α Glycine. *J. Cryst. Growth* **2017**, *475*, 232–238.

(23) Titiz-Sargut, S.; Ulrich, J. Influence of Additives on the Width of the Metastable Zone. *Cryst. Growth Des.* **2002**, *2*, 371–374.

(24) Hrkovac, M.; Prlic Kardum, J.; Schuster, A.; Ulrich, J. Influence of Additives on Glycine Crystal Characteristics. *Chem. Eng. Technol.* **2011**, *34*, 611–618.

(25) Scriven, L. E.; Sternling, C. V. The Marangoni Effects. *Nature* **1960**, *187*, 186–188.

(26) Deegan, R. D.; Bakajin, O.; Dupont, T. F.; Huber, G.; Nagel, S. R.; Witten, T. A. Capillary Flow as the Cause of Ring Stains from Dried Liquid Drops. *Nature* **1997**, *389*, 827–829.

(27) Hu, H.; Larson, R. G. Evaporation of a Sessile Droplet on a Substrate. *J. Phys. Chem. B* **2002**, *106*, 1334–1344.

(28) Hu, H.; Larson, R. G. Marangoni Effect Reverses Coffee-Ring Depositions. *J. Phys. Chem. B* **2006**, *110*, 7090–7094.

(29) Djikaev, Y. S.; Ruckenstein, E. Free Energy of Formation of a Crystal Nucleus in Incongruent Solidification: Implication for Modeling the Crystallization of Aqueous Nitric Acid Droplets in Polar Stratospheric Clouds. *J. Chem. Phys.* **2017**, *146*, 1–34.

(30) Li, X.; Cai, W.; An, J.; Kim, S.; Nah, J.; Yang, D.; Piner, R.; Velamakanni, A.; Jung, I.; Tutuc, E.; Banerjee, S. K.; Colombo, L.; Ruoff, R. S. Large Area Synthesis of High Quality and Uniform Graphene Films on Copper Foils. *Science* **2009**, *324*, 1312–1314.

Chapter 5: Levitation of Graphene – from Droplet Buckling to Liquid Marble Formation

My contribution: I optimised and performed all the levitation experiments and conducted the evaporation profile analysis. I produced all the figures and prepared the first draft of the manuscript.

Levitation of graphene – from droplet buckling to liquid marble formation

Matthew Boyes[1], Adriana Alieva[1], Thomas Vetter[2], Cinzia Casiraghi[1]*

[1] Department of Chemistry, University of Manchester, Manchester, UK

[2] School of Chemical Engineering and Analytical Science, University of Manchester, Manchester, UK

* Corresponding author: cinzia.casiraghi@manchester.ac.uk

Abstract

Chemically exfoliated graphene, such as electro-chemically exfoliated (ECE), is typically produced as a dispersion of graphene flakes in a solvent medium. The application of this graphene requires the removal of the solvent through liquid evaporation to isolate the flakes. The evaporation of a liquid droplet on a substrate prevents a fundamental study of its drying behaviour as the properties of the substrate significantly impact the droplets characteristics. Suspending droplets *via* acoustic levitation provides an ideal container-less environment with which to study the evaporation of liquids.

We provide here an analysis of the evaporation profiles, under the influence of acoustic levitation, of graphene dispersions with varying solvent compositions and graphene concentrations. Two distinct profiles are observed: one where a high concentration of graphene causes the droplet to buckle and form a graphitic aggregate, and another where a low graphene concentration produces a shell around the liquid to prevent it form from evaporating for several hours. The latter set of droplets show that graphene could be used to produce liquid marbles: soft matter systems that have various applications.

Evaporation is an ubiquitous aspect of nature, driving significant research into understanding this everyday phenomenon (*1–6*), and a pivotal process used in many technological and biomedical applications, such as ink-jet printing (*7–9*), substrate coating (*10*), crystallisation (*11*,*12*), fuel combustion (*13*) and DNA microarrays (*14–16*). All of these processes often rely on the use of a substrate, where evaporation preferentially occurs at the triple liquid-solid-air interface and thus is heavily influenced by the surface's chemical and physical properties (*17–19*).

Levitation provides the ideal platform to completely remove the influence of solid-liquid interfaces, thus allowing to get insights on the fundamentals of evaporation (*20*). There are several ways to achieve levitation; such as electrostatic (*21*,*22*), magnetic (*23*,*24*), and acoustic levitation (*25–27*). In particular, magnetic levitation has been widely used to levitate a large variety of materials and objects (*28*,*29*), including a living frog (*30*). However, acoustic levitation is also attractive as it benefits from the advantage that it can be used to levitate virtually anything, as there are no restrictions associated to the electronic and magnetic properties of the material. As such, it has already been applied to the studies of droplet evaporation (*27*,*31*,*32*), nucleation (*33–35*) and fluid manipulation (*36*,*37*).

In this study we investigate the evaporation of a graphene microdroplet by acoustic levitation. Graphene, the most famous 2-dimensional (2D) material has attracted strong research interest, due to its outstanding properties that make it suitable for a wide range of applications (*38–40*). Graphene can be easily solution processed through several methods, from liquid-phase exfoliation to electro-chemical exfoliation (ECE) (*41–44*), making it suitable to perform levitation experiments. Our results indicate the presence of two evaporation regimes, depending on the ratio between the binary solvent mixture (of water and isopropyl alcohol (IPA)) and the concentration of graphene. At low concentrations of graphene, for a given solvent, a threshold is reached during evaporation where the rate of evaporation slows considerably compared to the graphene-free solvent. For example, at an initial solvent composition of 50 vol% IPA and a graphene concentration below 0.006 mg mL^{-1}, evaporation of the droplet virtually stops, suggesting the formation of a liquid marble. At higher graphene concentrations, buckling of the droplet occurs and a graphene nanoassembly is produced.

To evaluate the evaporation behaviour of graphene dispersions under the influence of acoustic levitation, a microdroplet of a dispersion was injected into the temperature and humidity-controlled levitation chamber and its progress was tracked via a CCD camera capturing at 0.5 frames per second. The schematic and details of the acoustic levitator can be found in the Supporting Information, Section S1. During evaporation, the temperature was stabilised at 21 ± 0.5 °C and the relative humidity was 0% (due to the absence of any liquid vapour flow into the chamber). This was achieved from a series of calibration runs of the system to ensure these conditions are held for the time needed to gather the evaporation data. Prior to the use of graphene dispersions, control runs of pure water, IPA and mixtures of the two at different volume ratios were performed to assess the properties of the solvents. Note that

careful control of the environmental conditions is mandatory as small variations in temperature and relative humidity will induce drastic changes in the evaporation characteristics, making the experiments not reproducible. In our case, we repeated the experiment at least 6 times for each solvent control and graphene dispersion.

The evaporation profiles of the solutions, obtained from the recorded videos from the CCD, are shown in Figure 1. As expected, an increase in the ratio of water in the starting droplet causes a retardation in the evaporation rate, visualised by the decrease in the slope of the line at short time. Figure 1 also shows the presence of long tails in the profiles of the 50 vol% and 75 vol% IPA samples starting at about 500 s. Considering the very small volume of the droplets during this period of very slow evaporation, the long tail is attributed to some form of non-volatile residual impurity in the IPA solvent.

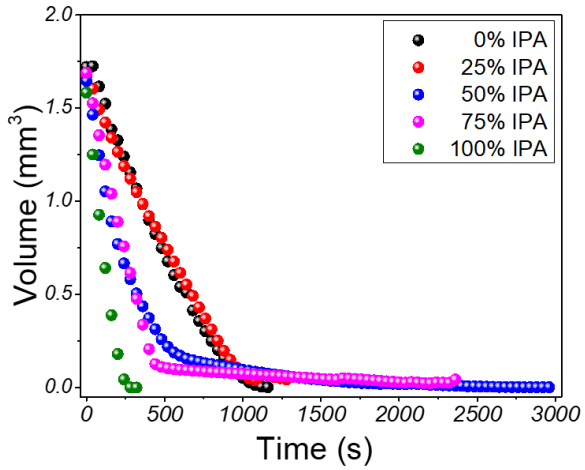

Figure 1. Evaporation profiles for levitating microdroplets of varying water/IPA composition.

Solution-processed graphene was produced by ECE (experimental details in Methods), as this method allows the facile dispersion of graphene in IPA/water mixtures, thus direct comparison of the results in Figure 1 can be drawn. The nanosheets have been fully characterized in previous works (*45*,*46*): the graphene flakes have an average surface area of 13.2 ± 3.6 μm^2, are between 1-3 layers thick and contain approximately 15% oxygen-containing functional groups.

Figure 2 shows the evaporation profiles of graphene dispersions in a 1:1 vol/vol mix of water and IPA at different graphene concentration. This figure shows a distinctive change in the evaporation profile with the graphene concentration. For concentrations above 0.012 mg mL^{-1}, a steady evaporation rate for their entire lifetime is observed, comparable to those measured for the control solution, Figure 1, i.e. the volume rapidly decreases until the solvent is completely evaporated. The evaporation profile is not strongly affected by the graphene concentration in the range investigated. The solvent evaporation gives rise to a collectable clump of material with a lateral size of ~200 μm (see Figure 2C).

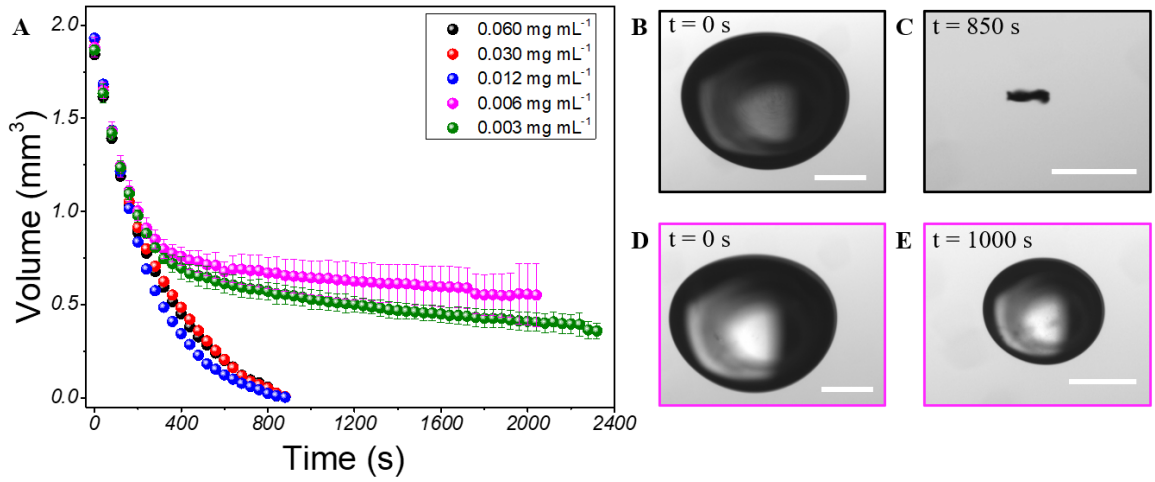

Figure 2. Evaporation profiles for graphene dispersions of varying graphene concentration in 1:1 v/v mixtures of water/IPA (**A**). Optical images of an example levitating droplet (**B**) and resulting nanoassembly (**C**), with a graphene concentration of 0.060 mg mL^{-1} at specific times. Optical images of an example levitating droplet (**D**) and resulting liquid marble (**E**), with a graphene concentration of 0.006 mg mL^{-1} at specific times. All scale bars ≈ 500 μm.

Raman spectroscopy, typically used to characterize graphene and its derivatives (*47*,*48*), was used to further investigate the structure of the residual clump. Figure 3 compares the Raman spectra of a membrane produced by vacuum filtration of the same graphene dispersion tested for levitation (see Methods), and of the residual obtained from the levitation experiment at 0.060 mg mL^{-1}. A membrane was chosen as a comparison model due to the likely stacked nature of the graphene flakes within the post-levitated samples. Figure 3 shows no remarkable changes in the Raman spectra, indicating that the structure of graphene has not been affected by the levitation process and the clump is indeed an agglomerate of graphene nanosheets (further details on the Raman analysis are shown in Supplementary Information, Section S4).

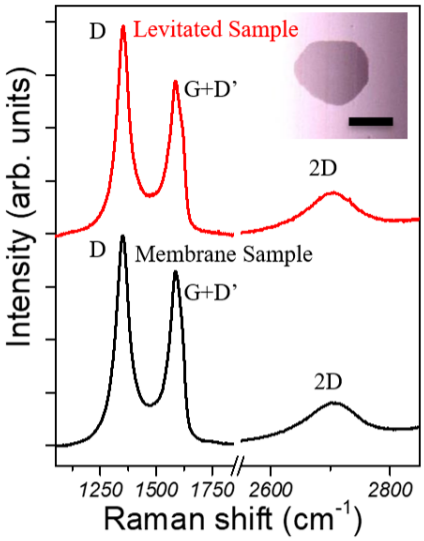

Figure 3. Raman spectra of an ECE graphene membrane and post-levitated graphene material. Inset: Optical picture of a graphene clump caught after the levitation of a dispersion with graphene concentration of 0.06 mg mL^{-1}. The scale bar = 200 μm.

Remarkably, a close look at the images recorded by the CCD camera indicates that close to the end of the evaporation, the droplet becomes unstable (i.e. it buckles) and evaporation continues till the formation of the clump, shown in Figure 4.

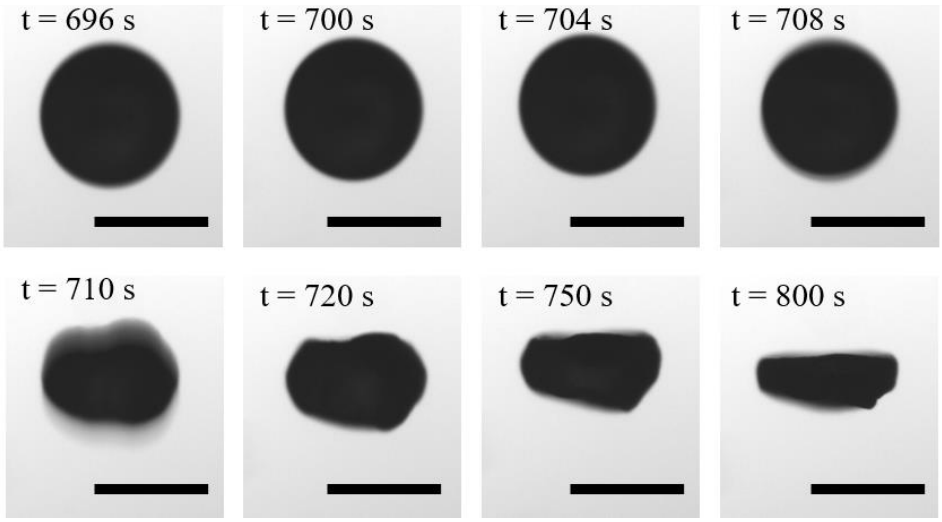

Figure 4. An example of a levitated droplet with a graphene concentration of 0.060 mg mL^{-1} buckling after a specified time, which goes on to form a nanoassembly.

For concentrations below 0.006 mg mL^{-1}, a completely different behaviour is seen: the evaporation rate initially is quite high, but at ~300 s a relatively large droplet is formed and remains stable for at least 2 hours, see Figure 2E. Evaporation is hence strongly hindered. This effect is attributed to the presence of graphene: as IPA starts evaporating, the droplet gets enriched in water. However, graphene is

hydrophobic, so the nanosheets will move towards the surface of the droplet and form a sort of coating, which slows down evaporation. This behaviour is typical of a class of materials known as liquid marbles (*49*). Liquid marbles are typically obtained by rolling a small amount of liquid on a very hydrophobic powder (*50–53*). The grains spontaneously coat the drop and encapsulate the liquid, giving rise to unique properties, such as non-wettability and high compressibility. Thus, our results indicate that by changing the graphene concentration of a levitating microdroplet in a 1:1 v/v mixture of water and IPA, it is possible to observe a sharp phase change from liquid to a soft solid, associated to the formation of a liquid marble. Previous experiments have demonstrated liquid marbles consisting of graphite particles led to slow down of evaporation (*54*,*55*). The graphene droplets seen in our study show similar lifetime extension properties to those of the graphite liquid marbles but require no additional surfactant to stabilise them.

An assessment can be made about whether there is enough graphene in the droplet to cover its surface. Assuming a certain single layer content within the dispersion; as well as a lack of restacking during the levitation process; and that all the graphene migrates to the surface of the droplet, Eq. 1 can be used to determine the percentage of the droplet's surface that is covered by graphene (further details of the derivation, assumptions and values used can be found in the Supplementary Information, Section S5):

$$Percentage\ of\ Droplet\ Covered = \frac{c_0 V_0 \sigma_{uc}}{\sigma_d (2m_C + 0.3m_O)} \times 100\% \quad (1)$$

Where c_0 is the initial concentration of the dispersion; V_0 is the initial volume of the droplet; σ_{uc} is the area of the unit cell of graphene; σ_d is the surface area of the droplet at a given time; m_C is the mass of a carbon atom; and m_O is the mass of an oxygen atom. From this, with an initial concentration of 0.006 mg mL^{-1} and taking the surface area of the droplet after 300 s of levitation, a droplet coverage of ~300% can be calculated. This means that there is more than enough graphene to create a thin shell around the droplet's surface.

Finally, levitating liquid droplets typically have an internal flow associated to them, which is greater towards the liquid-air contact and effectively null in the centre (*56*). The internal flow of the graphene dispersions is clearly seen in the levitating droplets showcased here (see Supplementary Videos 1 & 2), but there is again a distinct difference determined by the graphene concentration. The high concentration dispersions are shown to have a relatively fast internal flow throughout the evaporation process. On the other hand, the low graphene concentration displays a very slow and seemingly random flow on the liquid's surface, suggesting that a steady state within the droplet is reached, compatible with the formation of a liquid marble.

Based on our results, we expect the solvent ratio to play an important role, together with the graphene concentration, in the delicate balance between a buckling droplet and the liquid marble formation. Under our experimental conditions, we observed that only when the initial solvent ratio was equal parts

water and IPA did the concentration of graphene influence the evaporation behaviour of the droplet, as already discussed. When the initial solvent ratio is non-equal, we do not observe the formation of a liquid marble (see Supplementary Information, Section S3). Figure S3 details the evaporation profiles of levitated droplets with varying graphene concentrations where the initial solvent composition is either 25% IPA or 75% IPA (Figure S3a and b, respectively). These sets of dispersions behave identically to their graphene-free counterparts, regardless of the concentration of graphene in the dispersion. This has been attributed to the relative stabilities of the graphene dispersions at the different solvent compositions. It has been shown that dispersions of graphene in a mixed solvent system of water and IPA is most stable when the mixture is close to equal parts of both solvents (*57*). It can be assumed then that the dispersions with non-equal solvent ratios have less graphene in them, due to rapid restacking, preventing the possible formation of a liquid marble. Thus, the initial stability of the dispersion, which is directly correlated to the solvent composition, plays a major role in the evaporation behaviour of the graphene dispersions.

Conclusions

Acoustic levitation has been used to analyse the evaporation behaviours of microdroplets of graphene dispersions that varied in solvent composition and graphene concentration. Our results show that when the initial solvent is composed of equal parts water and IPA, two distinct drying behaviours are observed depending on the concentration of graphene. For concentrations above 0.012 mg mL^{-1}, the liquid evaporated enough to cause the droplet to buckle due to an excess of graphene at the surface. For concentrations below 0.006 mg mL^{-1}, the graphene appeared to form a shell around the liquid which prevented further evaporation for several hours, in a behaviour similar to liquid marbles. The evaporation profile dependence on graphene concentration was also revealed to be exclusive to a specific solvent composition. Liquid marble formation was only found to be possible when the initial ratio of water/IPA was equal. Non-equal solvent compositions always led to droplet buckling, irrespective of the graphene concentration used, which can be attributed to the stability of the graphene in the dispersion.

Acknowledgements

This work is supported by the European Research Council (ERC) under the European Union's Horizon 2020 research and innovation programme under grant agreement No 648417. T.V. thanks the Royal Academy of Engineering for the support through an Engineering for Development research fellowship. The authors thank Anne Juel for the constructive discussions.

Materials and Methods

Materials High purity graphite foil (0.4 mm thick, 99.8%, metal basis), graphite rods (99.99%, metal basis) and ammonium sulfate ($(NH_4)_2SO_4$, 98+%) were purchased from Alfa Aesar. Isopropyl alcohol (IPA, ≥99.5%) was purchased from Sigma-Aldrich. Deionised (DI) water (Millipore SIMPAK® 1, 18.2 MΩ.cm) was used for all experiments requiring water.

Graphene Dispersion Production Anodic electrochemical exfoliation (*42*) was carried out in a two-electrode configuration, using a piece of graphite foil (dimensions, 35 x 12 x 0.4 mm^3) as the anode and a graphite rod (dimensions, 35 x 3.05 mm^2) as the cathode. The electrodes were immersed in an aqueous solution (50 mL) of $(NH_4)_2SO_4$ at a concentration of 0.5 M. A positive voltage of 10 V was then applied across the electrodes using a Tenma 72-2540 programmable power supply. The graphite rod was placed parallel to the graphite foil surface at a distance of about 2 cm. During this process, gas bubbles formed in both electrodes, with the graphite anode typically seen to expand and release graphitic fragments from its surface. After 5 minutes of electrolysis, the resulting exfoliated graphite was collected and washed with excess amount of DI water through vacuum filtration to remove residual salts as well as other products of the electrochemical reaction. Subsequently, the exfoliated material was sonicated (Sonorex RK 100, 35 kHz) in a given volume (100 mL) of H_2O/IPA mixture (1:1 ratio, v/v) for an hour; finally, the dispersion was centrifuged using a Sigma 1-14k refrigerated centrifuge at 2000 rpm (295 xg) for 10 min to remove the unexfoliated material. The concentrations of the graphene dispersions were determined from their UV-vis spectra (acquired using a Cary 5000 UV-vis NIR spectrometer), calculating the concentration from the absorbance at 660 nm and a reported absorption coefficient of 2,460 L g^{-1} m^{-1} (*41*), (see Supplementary Information, Section S2 for details).

Acoustic Levitation The instrument setup can be seen in Supplementary Information, Figure S1. A microdroplet of a solution is suspended in the standing wave of the ultrasonic levitator (tec5 AG, Oberursel, Germany) and allowed to stabilise, determined by a lack of vibration of the droplet. The levitator operated at 100 kHz and generated several equally spaced nodes and antinodes between the transducer and the reflector. For each levitation run, the microdroplet was placed under the same node for consistency and to maintain droplet stability throughout the evaporation, the distance between the emitter and reflector was adjusted. Each result set was repeated at least 6 times to generate average evaporation profiles. To eliminate potential batch-to-batch inaccuracies of the graphene dispersions, at least 2 separate batches were used for each levitation set. Additionally, the order in which the dispersions were levitated was randomised. A Manta G-505 CCD camera (Allied Division, Stadtroda, Germany) was used to capture the levitation process with a backlight illuminating the droplet. Image and video processing was achieved with MATLAB© and the videos were sped up by a factor of 20.

Raman Spectroscopy A Renishaw inVia Raman spectrometer equipped with a 514.5 nm laser was used to acquire all spectra regarding the quality control of the graphene dispersions. All measurements were

acquired using a 100x objective lens, 2400 l/mm grating and laser power less than 1.3 mW. 30 measurements were taken for each sample found in this study and the spectra shown are averages generated from those measurements. The membrane was produced from an ECE graphene dispersion by vacuum filtration of the dispersion through a filter with pore size 0.2 μm (Anodisc 25, Whatman, Germany) until a free-standing membrane was produced. Due to the small size of the post-levitated samples and to minimise the potential of loss of the samples, they were kept in the sample vials they were collected in during measurements. The difficulty of catching such small samples meant that only a handful from all the levitated samples could be analysed.

References

1. Maxwell, J. C. The scientific papers of Clerk Maxwell. (1890).
2. Picknett, R. G. & Bexon, R. The evaporation of sessile or pendant drops in still air. *J. Colloid Interface Sci.* **61**, 336–350 (1977).
3. Dixit, S., Crain, J., Poon, W. C. K., Finney, J. L. & Soper, A. K. Molecular segregation observed in a concentrated alcohol-water solution. *Nature* **416**, 826–832 (2002).
4. Hu, H. & Larson, R. G. Evaporation of a sessile droplet on a substrate. *J. Phys. Chem. B* **106**, 1334–1344 (2002).
5. Fang, X. *et al.* Factors Controlling the Drop Evaporation Constant. *J. Phys. Chem. B* **109**, 20554–20557 (2005).
6. Christy, J. R. E., Hamamoto, Y. & Sefiane, K. Flow Transition within an Evaporating Binary Mixture Sessile Drop. *Phys. Rev. Lett.* **106**, 205701 (2011).
7. Sirringhaus, H. *et al.* High-Resolution Inkjet Printing of All-Polymer Transistor Circuits. *Science* **290**, 2123 LP – 2126 (2000).
8. Kawase, T., Sirringhaus, H., Friend, R. H. & Shimoda, T. Inkjet Printed Via-Hole Interconnections and Resistors for All-Polymer Transistor Circuits. *Adv. Mater.* **13**, 1601–1605 (2001).
9. Layani, M. *et al.* Transparent Conductive Coatings by Printing Coffee Ring Arrays Obtained at Room Temperature. *ACS Nano* **3**, 3537–3542 (2009).
10. Kim, H. *et al.* Controlled Uniform Coating from the Interplay of Marangoni Flows and Surface-Adsorbed Macromolecules. *Phys. Rev. Lett.* **116**, 124501 (2016).
11. Erdemir, D., Lee, A. Y. & Myerson, A. S. Nucleation of Crystals from Solution: Classical and Two-Step Models. *Acc. Chem. Res.* **42**, 621–629 (2009).
12. Poornachary, S. K., Parambil, J. V., Chow, P. S., Tan, R. B. H. & Heng, J. Y. Y. Nucleation of Elusive Crystal Polymorphs at the Solution–Substrate Contact Line. *Cryst. Growth Des.* **13**, 1180–1186 (2013).
13. Birouk, M. & Gökalp, I. Current status of droplet evaporation in turbulent flows. *Prog. Energy Combust. Sci.* **32**, 408–423 (2006).
14. Schena, M., Shalon, D., Davis, R. W. & Brown, P. O. Quantitative Monitoring of Gene Expression Patterns with a Complementary DNA Microarray. *Science* **270**, 467 LP – 470 (1995).
15. Bensimon, D., Simon, A. J., Croquette, V. & Bensimon, A. Stretching DNA with a Receding

Meniscus: Experiments and Models. *Phys. Rev. Lett.* **74**, 4754–4757 (1995).

16. Dugas, V., Broutin, J. & Souteyrand, E. Droplet Evaporation Study Applied to DNA Chip Manufacturing. *Langmuir* **21**, 9130–9136 (2005).

17. Chainani, E. T., Ngo, K. T. & Scheeline, A. Electrochemistry in an Acoustically Levitated Drop. *Anal. Chem.* **85**, 2500–2506 (2013).

18. Deegan, R. D. *et al.* Capillary flow as the cause of ring stains from dried liquid drops. *Nature* **389**, 827–829 (1997).

19. Sefiane, K., Tadrist, L. & Douglas, M. Experimental study of evaporating water-ethanol mixture sessile drop: Influence of concentration. *Int. J. Heat Mass Transf.* **46**, 4527–4534 (2003).

20. Brandt, E. H. Levitation in Physics. *Science* **243**, 349–355 (1989).

21. Okress, E. C., Wroughton, D. M., Comenetz, G., Brace, P. H. & Kelly, J. C. R. Electromagnetic Levitation of Solid and Molten Metals. *J. Appl. Phys.* **23**, 545–552 (1952).

22. Kelton, K. F. *et al.* First X-Ray Scattering Studies on Electrostatically Levitated Metallic Liquids: Demonstrated Influence of Local Icosahedral Order on the Nucleation Barrier. *Phys. Rev. Lett.* **90**, 195504 (2003).

23. Braunbeck, W. Free diamagnetic levitation of bodies in the magnetic field. *Z. Phys.* **112**, 753–763 (1939).

24. Mirica, K. A., Shevkoplyas, S. S., Phillips, S. T., Gupta, M. & Whitesides, G. M. Measuring densities of solids and liquids using magnetic levitation: fundamentals. *J. Am. Chem. Soc.* **131**, 10049–10058 (2009).

25. Apfel, R. E. A Novel Technique for Measuring the Strength of Liquids. *J. Acoust. Soc. Am.* **49**, 145–155 (1971).

26. Trinh, E. H. Compact acoustic levitation device for studies in fluid dynamics and material science in the laboratory and microgravity. *Rev. Sci. Instrum.* **56**, 2059–2065 (1985).

27. Brenn, G., Deviprasath, L. J., Durst, F. & Fink, C. Evaporation of acoustically levitated multi-component liquid droplets. *Int. J. Heat Mass Transf.* **50**, 5073–5086 (2007).

28. Catherall, A. T., Eaves, L., King, P. J. & Booth, S. R. Floating gold in cryogenic oxygen. *Nature* **422**, 579 (2003).

29. Hill, R. J. A. & Eaves, L. Nonaxisymmetric Shapes of a Magnetically Levitated and Spinning Water Droplet. *Phys. Rev. Lett.* **101**, 234501 (2008).

30. Berry, M. V & Geim, A. K. Of flying frogs and levitrons. *Eur. J. Phys.* **18**, 307–313 (1997).

31. Yarin, A. L., Brenn, G., Kastner, O. & Tropea, C. Drying of acoustically levitated droplets of liquid – solid suspensions : Evaporation and crust formation Drying of acoustically levitated droplets of liquid – solid suspensions : Evaporation and crust formation. *Phys. Fluids* **14**, 2289 (2002).

32. Kolwas, M. & Jakubczyk, D. Soft Matter Evaporation of a free microdroplet of a binary mixture of liquids with different volatilities. *Soft Matter* **15**, 1825–1832 (2019).

33. Chung, S. K. & Trinh, E. H. Containerless protein crystal growth in rotating levitated drops. *J. Cryst. Growth* **194**, 384–397 (1998).

34. Santesson, S. *et al.* Screening of Nucleation Conditions Using Levitated Drops for Protein Crystallization. *Anal. Chem.* **75**, 1733–1740 (2003).

35. Wolf, S. E., Leiterer, J., Kappl, M., Emmerling, F. & Tremel, W. Early Homogenous Amorphous Precursor Stages of Calcium Carbonate and Subsequent Crystal Growth in Levitated Droplets. *J. Am. Chem. Soc.* **130**, 12342–12347 (2008).

36. Zang, D. *et al.* Inducing drop to bubble transformation via resonance in ultrasound. *Nat. Commun.* **9**, 3546 (2018).

37. Watanabe, A., Hasegawa, K. & Abe, Y. Contactless Fluid Manipulation in Air : Droplet Coalescence and Active Mixing by Acoustic Levitation. *Sci. Rep.* **8**, 10221 (2018).

38. Novoselov, K. S. *et al.* A roadmap for graphene. *Nature* **490**, 192–200 (2012).

39. Geim, A. K. & Grigorieva, I. V. Van der Waals heterostructures. *Nature* **499**, 419–425 (2013).

40. Geim, A. K. Status and Prospects. *Science* **324**, 1530–1534 (2009).

41. Hernandez, Y. *et al.* High-yield production of graphene by liquid-phase exfoliation of graphite. *Nat. Nanotechnol.* **3**, 563–568 (2008).

42. Parvez, K. *et al.* Exfoliation of graphite into graphene in aqueous solutions of inorganic salts. *J. Am. Chem. Soc.* **136**, 6083–6091 (2014).

43. Halim, U. *et al.* A rational design of cosolvent exfoliation of layered materials by directly probing liquid-solid interaction. *Nat. Commun.* **4**, (2013).

44. Neklyudov, V. V., Khafizov, N. R., Sedov, I. A. & Dimiev, A. M. New insights into the solubility of graphene oxide in water and alcohols. *Phys. Chem. Chem. Phys.* **19**, 17000–17008 (2017).

45. Parvez, K., Worsley, R., Alieva, A., Felten, A. & Casiraghi, C. Water-based and inkjet printable inks made by electrochemically exfoliated graphene. *Carbon N. Y.* **149**, 213–221 (2019).

46. Nagyte, V. *et al.* Raman Fingerprints of Graphene Produced by Anodic Electrochemical Exfoliation. *Nano Lett.* **20**, 3411–3419 (2020).

47. Ferrari, A. C. *et al.* Raman spectrum of graphene and graphene layers. *Phys. Rev. Lett.* **97**, 187401–187404 (2006).

48. Eckmann, A., Felten, A., Verzhbitskiy, I., Davey, R. & Casiraghi, C. Raman study on defective graphene: Effect of the excitation energy, type, and amount of defects. *Phys. Rev. B - Condens. Matter Mater. Phys.* **88**, 034526 (2013).

49. Aussillous, P. & Quéré, D. Liquid marbles. *Nature* **411**, 924 (2001).

50. Binks, B. P. & Murakami, R. Phase inversion of particle-stabilized materials from foams to dry water. *Nat. Mater.* **5**, 865–869 (2006).

51. Xue, Y. *et al.* Magnetic Liquid Marbles: A "Precise" Miniature Reactor. *Adv. Mater.* **22**, 4814–4818 (2010).

52. Vadivelu, R. K., Kamble, H., Munaz, A. & Nguyen, N.-T. Liquid Marble as Bioreactor for Engineering Three-Dimensional Toroid Tissues. *Sci. Rep.* **7**, 12388 (2017).

53. Rong, X. *et al.* Liquid marble-derived solid-liquid hybrid superparticles for CO2 capture. *Nat. Commun.* **10**, 1854 (2019).

54. Dandan, M. & Erbil, H. Y. Evaporation Rate of Graphite Liquid Marbles: Comparison with Water Droplets. *Langmuir* **25**, 8362–8367 (2009).

55. Doganci, M. D., Sesli, B. U., Erbil, H. Y., Binks, B. P. & Salama, I. E. Liquid marbles stabilized by graphite particles from aqueous surfactant solutions. *Colloids Surfaces A Physicochem. Eng. Asp.* **384**, 417–426 (2011).

56. Yan, Z. L., Xie, W. J. & Wei, B. Vortex flow in acoustically levitated drops. *Phys. Lett. A* **375**, 3306–3309 (2011).

57. Yi, M., Shen, Z., Ma, S. & Zhang, X. A mixed-solvent strategy for facile and green preparation of graphene by liquid-phase exfoliation of graphite. *J. Nanoparticle Res.* **14**, 1003 (2012).

Levitation of graphene – from droplet buckling to liquid marble formation

Matthew Boyes[1], Adriana Alieva[1], Thomas Vetter[2], Cinzia Casiraghi[1*]

[1] Department of Chemistry, University of Manchester, Manchester, UK

[2] School of Chemical Engineering and Analytical Science, University of Manchester, Manchester, UK

* Corresponding author: cinzia.casiraghi@manchester.ac.uk

Supporting Information

S1. Acoustic Levitation Setup

Figure S1 shows a schematic of the acoustic levitation instrument setup. Environmental control is achieved in two ways. First, the acoustic emitter and reflector are encased in a double walled, glass chamber. The chamber is connected to a digitally controlled water bath (Ministat 230, Huber, Germany) that flows temperature regulated water around the outside of the levitation chamber. Secondly, dry N_2 gas is passed through the chamber at a controlled flow rate (Bronkhorst, Netherlands). Not only is the N_2 gas temperature controlled but it reduces the relative humidity to 0 %RH due to a lack of any additional water flow. The temperature and relative humidity within the levitation chamber were confirmed with the use of an iButton temperature and humidity sensor (Thermochron). The flow rate of N_2 gas was set low enough so as not to agitate the levitating droplet, but sufficiently high enough to maintain the environmental control within the chamber. All levitation experiments were captured with a Manta G-505 CCD camera (Allied Division, Stadtroda, Germany).

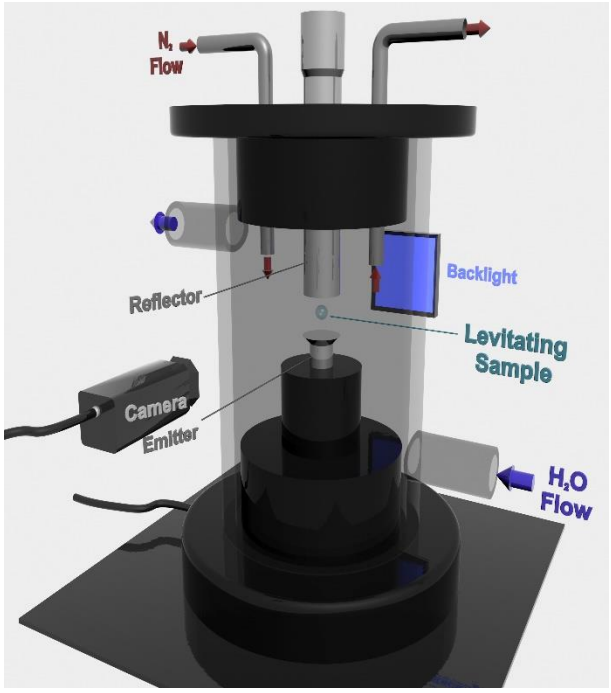

Figure S1 | Schematic representation of the acoustic levitation instrument setup.

S2. Graphene dispersion characterisation

Once the graphene is produced via electrochemical exfoliation (see Methods in the main text), the dispersions were characterised prior to their levitation.

Figure S2 shows the typical UV-vis spectrum of the ECE graphene dispersion that was diluted by a factor of 10. The concentration of a dispersion was calculated by applying the Beer-Lambert Law (*1*) at the absorbance value at 660 nm and a reported absorption coefficient of 2,460 L g^{-1} m-^{1} (*2*). The highest concentration of graphene used for this study was found to be 0.0597 ± 0.0037 mg mL^{-1}. Additional analysis of the produced ECE dispersions have been previously carried out in other works (*3*).

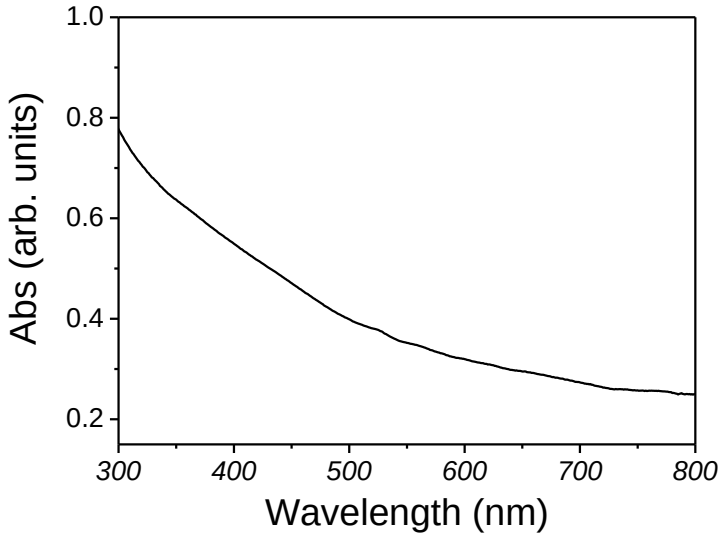

Figure S2 | UV-vis spectrum of a 10x diluted ECE graphene dispersion.

S3. Other graphene dispersions

Figure S3 contains the evaporation profiles of the levitated graphene dispersions that initially had nonequal volume ratios of water and IPA. Unlike the dispersions in the main text, which initially have a 1:1 v/v ratio of water and IPA, neither of the sets of dispersions shown in Figure S3 display liquid marble-like behaviour. Both have similar evaporation profiles as their respective graphene-free solutions (see Figure 1 in the main text), irrespective of the concentration of graphene used. All these dispersions completely evaporated, and some left behind graphene clumps, provided the concentration of graphene was ≥ 0.012 mg mL^{-1}.

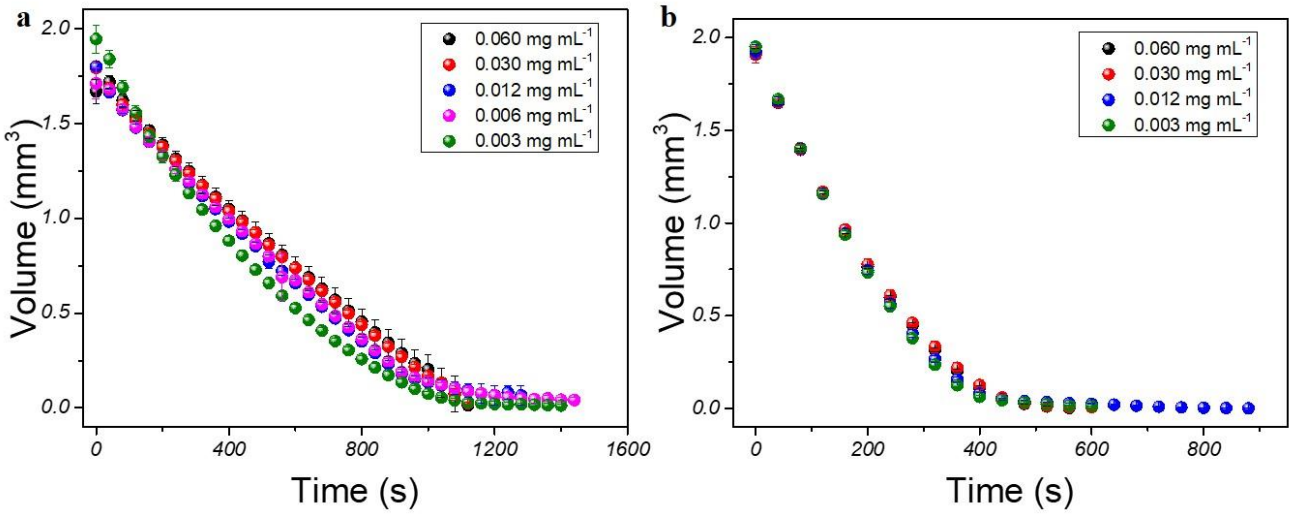

Figure S3 | Evaporation profiles of graphene dispersions with varying graphene concentrations in water/IPA solvent ratios of (**a**) 3:1 and (**b**) 1:3.

S4. Raman characterisation

Table S1 details the peak fitting results of the major peaks found in the spectra of the graphene membranes and levitated samples, *i.e.* the D, G and 2D peak. An additional peak also arises (the D' peak) due to the heavily defective nature of ECE graphene (*4*,*5*). As can be seen by the results, both the position and the full-width at half maximum (FWHM) do not change a significant amount between the membrane and the post-levitated samples. This shows, coupled with the spectra in Figure 3 of the main text, that whilst both sets of samples are defective, there is little-to-no change in the defect density after the graphene dispersion has been acoustically levitated.

Table S1 | Fitting results of the Raman spectra of an ECE graphene membrane and a post-levitated graphene clump.

Sample	Peak	Position / cm^{-1}	FWHM / cm^{-1}
ECE Membrane	**D**	1351	78
	G+D'	1587	69
	2D	2703	128
Post-levitated nanoassembly	**D**	1353	74
	G+D'	1587	74
	2D	2703	116

S5. Surface Area Coverage Calculations

Finding the percentage of the droplet's surface that is covered by graphene means solving Eq. S1:

$$Percentage\ of\ Droplet\ Covered = \frac{\sigma_{Gr}}{\sigma_d} \times 100\% \quad \text{(S1)}$$

Where σ_{Gr} is the total area that can be covered by the total amount of graphene that is in the droplet and σ_d is the surface area of the droplet at a given time. σ_d can be obtained from the images captured during the levitation. Assuming that the graphene flakes do not overlap one another, σ_{Gr} can be roughly calculated by knowing the surface area of one graphene flake, σ_{gr}, and the number of flakes in the droplet, N_{Gr}, according to Eq. S2:

$$\sigma_{Gr} = \sigma_{gr} \times N_{Gr} \quad \text{(S2)}$$

N_{Gr} can be found from the relationship shown in Eq. S3:

$$N_{Gr} = \frac{m_{Gr}}{m_{gr}} \quad \text{(S3)}$$

Where m_{Gr} is the total mass of graphene in the droplet and m_{gr} is the mass of one flake. The number of flakes can only be justified under the following assumptions; all the graphene present in the

dispersion is single layer; and there is no restacking of the flakes during the levitation process. The total mass can be calculated from the initial concentration, c_0, and the initial droplet volume, V_0, according to Eq. S4. The mass of one flake can be found by the sum of the mass of the carbon and oxygen atoms that make up the flake, shown in Eq. S5:

$$m_{Gr} = c_0 V_0 \quad \text{(S4)}$$

$$m_{gr} = N_C m_C + N_O m_O \quad \text{(S5)}$$

Where N_X is the number of the given atom and m_X is the mass of the given atom. The hydrogen atoms have been excluded for ease. The defects that are present on the flakes are assumed to only be due to the presence of the oxygen containing functional groups, i.e. there are no hole defects within the flakes. To obtain the number of carbon atoms, the number of unit cells per flake needs to be calculated and then doubled since each unit cell contains 2 carbon atoms. This can be achieved from knowing the surface area of a flake and the area of the unit cell, σ_{uc}. The number of oxygen atoms can then be derived as it is known that a flake produced by ECE in the manner described in this study contains an average of 15% oxygen content. Thus, the number of carbon atoms and the number of oxygen atoms are given by Eq. S6 and S7, respectively:

$$N_C = \frac{2\sigma_{gr}}{\sigma_{uc}} \quad \text{(S6)}$$

$$N_O = \frac{0.3\sigma_{gr}}{\sigma_{uc}} \quad \text{(S7)}$$

Substituting Eq. S2 – S7 into Eq. S1 yields Eq. 1 in the main text. Table S2 details the values used for the calculation described in the main text.

Table S2 | Example values used in Eq. 1 to calculate the percentage of the droplet's surface that is covered by the graphene at a known concentration.

Parameter / units	**Value**
c_0 / mg mL^{-1}	0.006
V_0 / mL	0.002
σ_{uc} / mm^2	5.10 x 10^{-14}
σ_d / mm^2	4.27
m_C / mg	1.99 x 10^{-20}
m_O / mg	2.66 x 10^{-20}

References

1. Swinehart, D. F. The Beer-Lambert Law. *J. Chem. Educ.* **39**, 333 (1962).

2. Hernandez, Y. *et al.* High-yield production of graphene by liquid-phase exfoliation of graphite. *Nat. Nanotechnol.* **3**, 563–568 (2008).

3. Parvez, K., Worsley, R., Alieva, A., Felten, A. & Casiraghi, C. Water-based and inkjet printable inks made by electrochemically exfoliated graphene. *Carbon N. Y.* **149**, 213–221 (2019).

4. Parvez, K. *et al.* Exfoliation of graphite into graphene in aqueous solutions of inorganic salts. *J. Am. Chem. Soc.* **136**, 6083–6091 (2014).

5. Su, C. Y. *et al.* High-quality thin graphene films from fast electrochemical exfoliation. *ACS Nano* **5**, 2332–2339 (2011).

Chapter 6: Selective Polymorphism of α-Glycine by Acoustic Levitation

My contribution: I optimised and performed all the levitation experiments and conducted the evaporation profile and induction time analysis. I prepared the levitation set up figure and assisted A.A. in the preparation of the manuscript.

CrystEngComm

PAPER

View Article Online
View Journal

Cite this: DOI: 10.1039/d0ce00856g

Selective polymorphism of α-glycine by acoustic levitation†

Adriana Alieva, [a] Matthew Boyes,[a] Thomas Vetter [b] and Cinzia Casiraghi *[a]

Received 13th June 2020,
Accepted 4th October 2020

DOI: 10.1039/d0ce00856g

rsc.li/crystengcomm

In this work we investigate the crystallisation behaviour of glycine in water and in a binary solvent mixture in an acoustic levitator under controlled environmental conditions. High speed video microscopy was used to monitor the changes in the microdroplet volume upon evaporation of the solvent. The glycine crystals obtained from levitation form an agglomerate, whose exact morphology depends on the solvent system used. The agglomerates have been collected and precisely opened *via* laser cutting, allowing further investigation of the morphology and structure of the internal crystals. The crystals appear to grow from the external region towards the centre of the sphere, indicating the formation of a solid shell, whose formation depends on the solvent used. The polymorphic outcome was thoroughly investigated by Raman spectroscopy: all of the crystals measured, regardless of the region or the solvent used, were found to be exclusively of the α-form, despite the addition of IPA inducing changes in the induction time and morphology.

Introduction

Crystallisation from solution is at the heart of various phenomena occurring in nature[1,2] and also the most widely applied approach for the isolation and purification of compounds in the chemical process industries.[3] Although thermodynamic principles describing this phenomenon have been established more than a century ago,[4] a full understanding of the underlying mechanism of nucleation is still not attained. This makes the production of organic crystals of desired size, shape and polymorph very challenging.

It is well known that surfaces play an important role in crystallisation: the interaction of solute molecules with foreign surfaces, such as container walls, can change the energetics and kinetics of nucleation.[5] A simple way to avoid the use of containers and other foreign elements affecting crystallisation is provided by levitation. A number of different levitation techniques are available, including magnetic,[6] electric,[7–9] optical,[10,11] aerodynamic,[12] and acoustic[13–16] to mention a few. In particular, acoustic levitation is very attractive because it does not require the sample to have any specific properties, *i.e.* any material can be levitated. This versatility has made acoustic levitation a promising tool to investigate density,[15,17] evaporation,[18,19] and drying[19,20] behaviour of droplets. Acoustic levitation has been also applied to study crystallisation, although only a very limited number of studies have been conducted up to now (see state-of-the-art table in ESI,† Section S1).[19,21–30] To the best of our knowledge, there are no acoustic levitation studies conducted on glycine, the simplest amino acid, despite its wide use in crystallisation studies,[31–35] due to its simple molecular structure and well-known polymorphism. Glycine crystallises in three distinct polymorphic forms at ambient conditions, denoted as α, β and γ, with relative stabilities: γ > α > β at room temperature.[36] The α- and β-forms both have monoclinic structure with a space group symmetry of $P2_1/n$ and $P2_1$, respectively.[37,38] The most stable form, γ, has a trigonal crystal structure belonging to the $P3_1$ or $P3_2$ groups.[39] Crystallisation from aqueous solutions typically yields the metastable α-form, as it is kinetically favoured.[40] The least stable, β-form of glycine, is commonly obtained from cooling crystallisation by the addition of alcohol such as ethanol or methanol as an anti-solvent to aqueous solution and readily transforms to the α-form in the presence of water or upon heating;[37,41] while the stable γ-form can be crystallised from acidic or basic solutions.[39,42]

Herein, we report an *ex situ* polymorph analysis of glycine crystals obtained from levitation experiments, in pure water and with isopropanol (IPA) as a co-solvent, by using Raman spectroscopy. Our results show that selective crystallisation of the α-form of glycine is obtained by acoustic levitation, regardless of the solvent investigated. The presence of the co-

[a] Department of Chemistry, University of Manchester, Manchester, UK. E-mail: cinzia.casiraghi@manchester.ac.uk
[b] Department of Chemical Engineering and Analytical Science, University of Manchester, Manchester, UK

† Electronic supplementary information (ESI) available. See DOI: 10.1039/d0ce00856g

solvent in the crystallising solution influences the kinetics of the crystallisation of glycine and the morphology of the obtained crystals, but does not affect the polymorphic outcome from evaporative crystallisation. This polymorph outcome is very different from the one observed on evaporative droplets of glycine on a substrate, where both α- and β-forms are detected and the unstable β-form of glycine is exclusively located at the contact region of the droplet with the substrate, as a result of the higher supersaturation rate. Based on the same effect, one would expect to see the β-form of glycine on the surface of the crystallised droplet, while we find that all crystals are of the α-form. The selective crystallisation of the α-form of glycine under acoustic levitation could be attributed to several concomitant effects, such as geometric effects and the presence of the ultrasonic field, as selective crystallisation of the α-form over the β-form of glycine was also obtained in sono-crystallisation experiments.[43–45] More experiments, such as a detailed comparison between crystallisation in an acoustic levitator and in a sonicator, under similar conditions, may help to elucidate the origin of the selectivity of the α-form observed in our work.

Results and discussion

The experimental set up of the acoustic levitator used in our studies is shown schematically in Fig. S2† (more details in Methods and Section S2). A conditioned gas is introduced with controlled gas flow rate, temperature and humidity around the droplet, allowing performing the crystallisation experiments at constant temperature (21 ± 0.5 °C) and dry conditions (RH = 0%). The setup consists of a 100 kHz ultrasonic droplet levitator, equipped with a CCD camera, backlight illumination and a controlled evaporator unit. The levitating droplets were monitored *in situ* during solvent evaporation using a CCD camera, the projected area of the droplet over the time is then analysed with a home-made automated images processing software. A representative video is included in the ESI,† Video S1. Full details of the levitator setup are provided in ref. 22.

In a typical crystallisation experiment, a 2 μL droplet of 0.5 M undersaturated glycine solution, in either pure water or water/IPA (starting concentration, 3 : 1 v : v) mixture, was injected and levitated in one of the wave nodes of the acoustic levitator equipped with an environmentally

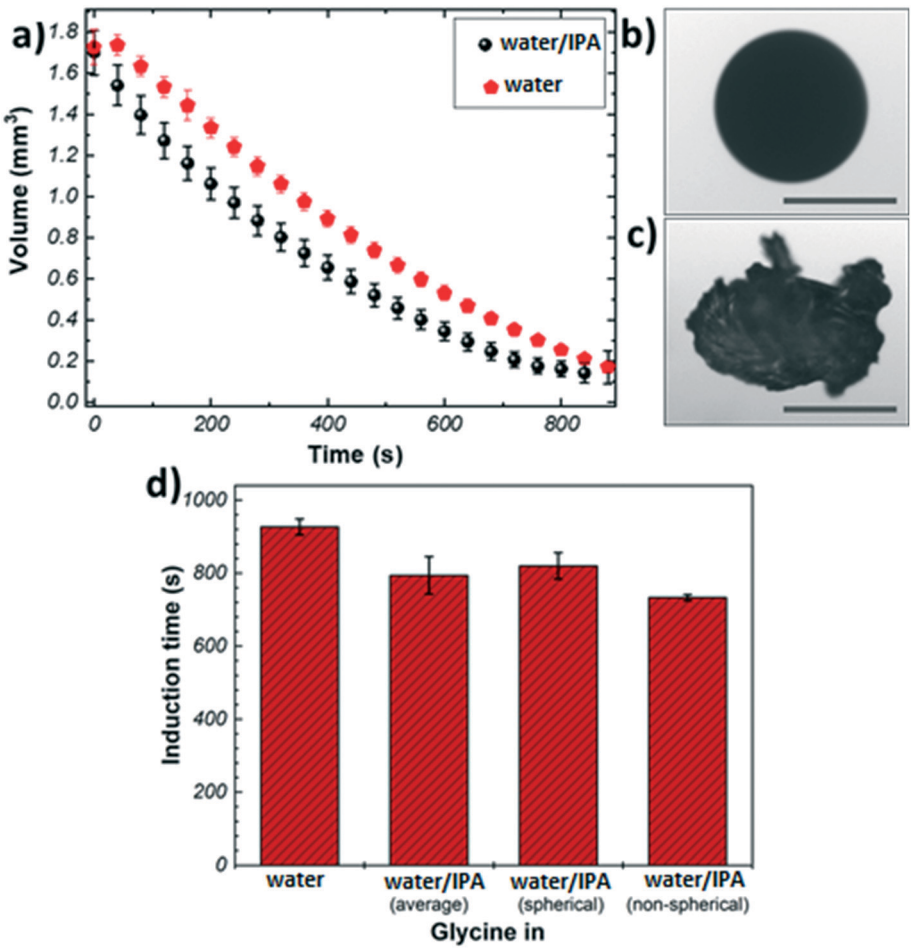

Fig. 1 (a) Evaporation profiles of glycine microdroplets from different solvents (b) image of a spherical agglomerate of glycine crystals obtained from pure water; (c) image of a non-spherical agglomerate of glycine crystals obtained from water/IPA mixed solvent (d) induction time of glycine from different solvent systems. Scale bars ≈ 0.5 mm.

controlled chamber. Note that this mixture ratio was selected as higher ratios of IPA result in the precipitation of glycine for the selected conditions.

Fig. 1(a) shows the evaporation profiles of glycine microdroplets for different solvents. As expected, regardless of the type of the solvent used the droplet volume is found to decrease continuously till complete solvent removal. The evaporation rate of pure water shows a steady evolution with time. In the case of the binary solvent mixture, different stages can be seen: the initial slope of volume *vs.* time, Fig. 1(a), for the bi-component solvent system is higher compared to that of pure water. This is due to the preferential evaporation of the more volatile component (*i.e.*, IPA) in the first stage of evaporation. The slope decreases over time indicating that the composition of the remaining liquid phase gets richer in water causing retardation in the evaporation rate.

Fig. 1(b) and (c) show representative images of crystals obtained from the levitation experiments. Typically, two distinct morphologies were observed: spherical agglomerates composed of small crystallites (Fig. 1(b)), and non-spherical agglomerates composed of large needle-like crystals (Fig. 1(c)). Only agglomerates with spherical morphology were obtained from pure water, whereas the addition of IPA resulted in a split in the morphology (7 : 3 split of spherical *vs.* non-spherical). This outcome could be attributed to the presence of IPA as an anti-solvent causing a widening of the metastable zone (MSZ) width in which crystal growth dominates over nucleation.[46,47] Therefore, the probability of obtaining larger crystals increases in the presence of IPA. The evaporation profiles of the spherical and non-spherical agglomerates obtained from the binary solvent mixture exhibit a similar trend (Fig. S3†).

The crystallisation kinetics was determined by measuring the induction time of crystallisation (see details in Materials and methods), Fig. 1(d). It can be clearly seen than the addition of IPA to the crystallising solution has a promoting effect on the nucleation of glycine, as compared to the case of pure water: the presence of IPA increases the evaporation rate of the droplets generating higher supersaturation rate, hence inducing nucleation sooner. The induction times for the non-spherical glycine agglomerate obtained from the binary mixture (733 ± 8 s) were found to be slightly shorter than the spherical samples (820 ± 36 s)- this can be rationalised by considering the solubility curve of glycine and relative growth and nucleation rates. The solution begins well below the saturation concentration and it crosses the supersaturation threshold into glycine's MSZ with the evaporation of the solvent.[5] In this region, crystal growth dominates over nucleation leading to the formation of larger crystals. If the solvent continues to evaporate, the system moves past the MSZ into high supersaturation, where nucleation events dominate over crystal growth.[3]

Further morphological characterisation was conducted on the spherical glycine agglomerates obtained from either water or the mixed solvent system by scanning electron microscopy (SEM). Fig. 2 shows SEM images of a broken glycine sphere crystallised from pure aqueous solution. These images show the morphology of the crystals in both the inner and outer parts of the sphere – the crystals seem to grow following the radial direction. Considering that the solvent evaporates from the surface of the droplet, one might infer that nucleation has been induced heterogeneously at the air–water interface due to the generation of higher supersaturation rate at the droplet surface. This is in agreement with previous studies, for example with mannitol[22] and calcite crystals.[26] This outcome can be explained by taking into account the mechanisms involved in drying of droplets containing solutes, where there are two types of drying processes happening: the first is driven by surface evaporation, and the second is driven by internal moisture migration.[22,48,49] Initially, the solvent migrates towards the surface and the solute towards the centre due to solvent evaporation at the surface, which causes shrinking of the droplet diameter; at a critical point, the droplet stops shrinking, hence the molecules start diffusing on the surface, where supersaturation is reached first. Nucleation and crystallisation lead to a strong increase of the total solid fraction within the droplet, which ultimately produces a stable but permeable crust at the droplet surface.[22] The exact morphology of the shell depends on the evaporation rate: a slow evaporative process will allow to produce a solid porous structure as molecules have enough time to diffuse.[50] This description matches very well with the obtained morphology of the crystal agglomerate surface, as shown in Fig. 2, *i.e.* a rigid structure with holes of about 10–20 μm in size.

The shell is expected to form at a critical point, where the solid particles are unable to move sufficiently relative to each other.[22] Since the induction time is measured by looking at the changes in shape of the droplet due to solid formation and the images only show the droplet surface, in first approximation one can assume the induction time as the time at which the critical solid fraction is reached first on the surface. Hence, the shell formation is expected at around 900 s for pure water, and at around 733 s and 820 s for the mixed solvent system, depending on the final morphology of the crystals aggregate. The time of shell formation reduces when IPA is used as co-solvent because the higher evaporation rate results in faster and higher enrichment at the droplet boundary. It is interesting to note the difference in induction times (~90 s) between the two morphologies obtained in the mixed solvent: this seems to indicate that the addition of IPA may lead to the formation of regions within the droplet with very high initial solute concentration, which in turn will produce particles with larger size (*i.e.*, non-spherical agglomerates), making shell formation more difficult to achieve.

Let us now move to the polymorph characterisation. Raman spectroscopy is a simple and fast technique that allows taking individual measurements on crystals with spatial resolution of ~300–500 nm. In contrast to powder X-ray diffraction (XRD), where the samples have to be ground

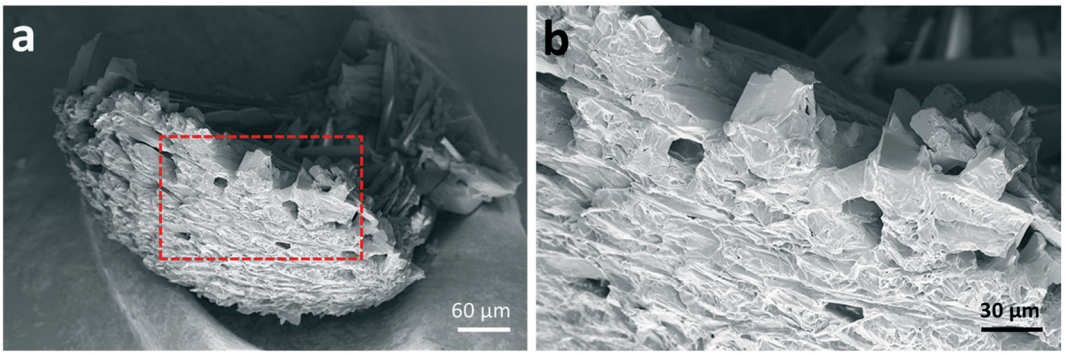

Fig. 2 (a) SEM image of a broken spherical agglomerate of glycine crystals, revealing the morphologies of both inner and outer parts of the sample (b) magnified view of the area marked with a red-dashed rectangle in (a).

and fair amount of material is required, little or no sample preparation and a small amount of material is sufficient for Raman spectroscopy measurements. In addition, it has been shown that Raman spectroscopy is able to easily identify glycine polymorphs: each crystal structure show Raman peaks in distinct positions due to the variations in the intermolecular hydrogen bonding interactions.[51] In this work, the characteristic C–H stretching modes, representing the symmetric (lower shift) and asymmetric (higher shift) stretches of the C–H bonds of glycine were used for the identification of glycine polymorphs.[32] The positions of these modes were found to be at 2972 and 3007 cm^{-1} for α-form; at 2953 and 3008 cm^{-1} for β-form, and at 2962 and 3000 cm^{-1} for γ-form (see representative Raman spectra of the three polymorphs in Fig. S5†).

Raman measurements have been taken first from the agglomerates obtained directly after levitation, *i.e.* the measurements are performed on the outer part. The samples were then cut in half with high precision using a laser cutter (Materials and methods). This allowed us to get access also to the inner region of the samples in a controlled way. Raman measurements were collected from at least 50 crystals

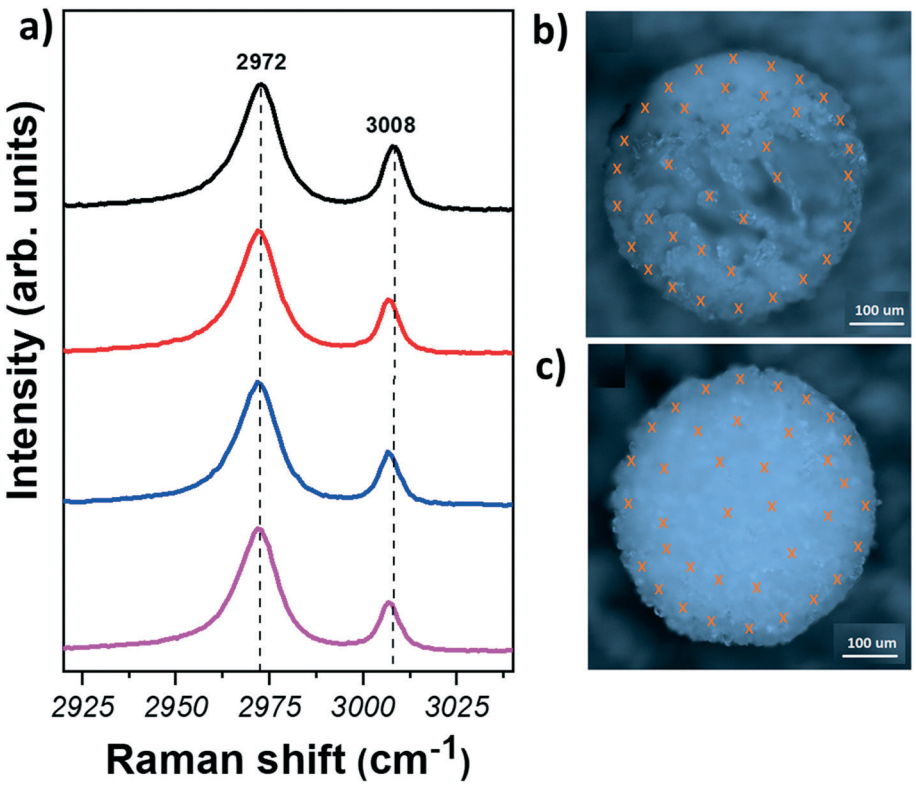

Fig. 3 (a) Raman spectra of the CH region measured on glycine crystals from the spherical agglomerates, obtained from different solvent systems (*from top to bottom: outer region, solvent = pure water; inner region, solvent = pure water; outer region, solvent = water/IPA; inner region, solvent = water/IPA*). Optical microscopy images of glycine spherical agglomerates after laser cutting (b) crystallised from pure water (c) crystallised from water/IPA solvent system. Crosses represent different points where the Raman measurements were taken.

for each sample in order to obtain statistically significant results.

Fig. 3 shows representative Raman spectra obtained from different regions of glycine samples and optical images of the spherical agglomerates after laser cutting. The crosses in Fig. 3(b) and (c) indicate the points where measurements were taken. Fig. 3(a) (see also Section S6†) shows that the Raman spectra of glycine crystals do not show any significant variation amongst different crystals. Furthermore, C–H stretching mode positions are found at ~2972 and ~3008 cm^{-1}, indicating that the crystals are of α-form. Hence, our results show that the α-form is found for all crystals, regardless of the region or the solvent used.

It is interesting to compare our results with those obtained from evaporating droplets of glycine placed on a substrate. In this case, concomitant polymorph formation was observed: both α- and β-form have been identified, with the β-form detected only at the contact region of the droplet with the substrate and air, due to the higher supersaturation rate generated in this region.[31,35,51–53] In contrast, under acoustic levitation, the α-form is observed even in the region of higher supersaturation. Similarly, polymorph selectivity of caffeine under acoustic levitation has been also demonstrated: both α- and β-forms were obtained when caffeine was crystallised on different substrates while only pure α-form was obtained from the levitated droplets.[27] There are several explanations to elucidate our results. First, one could assume that the β-form is indeed formed on the outer surface and it transforms to the α-form once the droplet is removed from the levitator and exposed to humid air. This would be especially relevant for the mixed solvent system, as the addition of alcohol as an anti-solvent to aqueous solution has been observed to yield the unstable β-form, which transforms to the α-form in the presence of water or upon heating.[37,41] However, we did not observe any difference in the polymorphic outcome between the crystals obtained from water and the mixed solvent. Furthermore, the β-crystals obtained from crystallisation of microdroplets on a surface have shown to be very stable in ambient conditions, hence we tend to rule out the possibility of polymorph transformation. The second explanation is related to a pure geometric effect: the droplet has a different shape when levitated and when deposited on a substrate. In surface-assisted crystallisation, the contact angle is known to determine the energy barrier of nucleation.[5] In the case of a levitating droplet, from a geometric effect, the crystallisation is expected to be homogeneous, so the energy barrier of nucleation is the highest. It is however unclear how this would reflect on the polymorph outcome. Therefore, an interesting comparison to elucidate the difference in the polymorph outcome can be drawn by determining the nucleation rates.[54] Although levitation is considered as a method to achieve homogenous nucleation, currently there are discussion on the effect of mass transport and rotation induced by the acoustic pressure on crystallisation, hence the theory developed for homogeneous nucleation may not be directly applicable to crystallisation in an acoustic levitator.[55–57] Finally, exclusive nucleation of the α-form in water or mixed solvent has been also observed in sono-crystallisation experiments using bath or tip sonication:[43–45] it has been shown that ultrasound promotes the α-form by inhibiting the formation of the β-form. The presence of ultrasonic waves also narrows down the size distribution and enhances the growth rate of the crystals. Hence, the exclusive formation of the α-form in a levitated droplet of glycine could be attributed to the effect of the acoustic waves, which results in the formation of the metastable α-form, even in the regions of higher supersaturation. As the processes of levitation and sono-crystallisation are not exactly the same, some differences, for example in size distribution of the crystals, may arise between the two methods, but this would require further investigation, which is beyond the scope of this work.

Summary and conclusions

An acoustic levitator has been used to study the evaporation of microdroplets of glycine in pure water and in water/IPA solutions. The resulting crystals were analysed by scanning electron microscopy and Raman spectroscopy. The changes in the shape of the droplet and the formation of solid on the surface were monitored with a CCD camera during evaporation. Our results show that selective crystallisation of the α-form of glycine is achieved by crystallisation under acoustic levitation, even in the presence of an anti-solvent. The morphology of the spherical agglomerate obtained from water suggests the formation of small and high density crystals growing from the outer part of the droplet towards the centre, due to the higher supersaturation rate generated in the region in contact with air. Despite the higher supersaturation rate, the crystals at the outer region have been found to be of the α-form, in contrast to crystallisation of glycine on substrates, where the β-form is formed at the highest supersaturation region. The selective crystallisation of the α-form of glycine under acoustic levitation could be attributed to several concomitant effects, such as geometric effects and the presence of an ultrasonic field.

Materials and methods

Materials

Glycine powder (Reagent Plus ≥99%) and isopropyl alcohol (IPA, ≥99.5%) were purchased from Sigma-Aldrich. Deionised (DI) water (Millipore SIMPAK® 1, 18.2 MΩ cm) was used for all experiments requiring water.

Acoustic levitation

The experimental set up of the acoustic levitator used in our studies is shown schematically in Fig. S2.† In a typical crystallisation experiment, 2 μL of a 0.5 M undersaturated glycine solution (either in pure water or water/IPA (3 : 1 v : v) mixture) was injected in an acoustic levitator (tec5 AG, Oberursel, Germany). The levitator operated at a frequency of

100 kHz generating several nodes and antinodes between the emitter and the reflector. For each levitation experiment, the microdroplet was injected under the same node and the distance between the emitter and the reflector was adjusted to stabilise the droplet throughout the evaporation. Each set was repeated minimum 6 times for the generation of the average evaporation profiles of the solvents. A Manta G-505 CCD camera (Allied Division, Stadtroda, Germany) was used to monitor the levitation process with a backlight illumination of the droplet. MATLAB© was used for video processing.

In order to make sure that experiments performed during different days are reproducible, a 2 μL droplet of pure water was introduced first in the levitator and its evaporation monitored. Although the evaporation rate was not exactly the same in all experiments, the deviations were typically within ±6.9%.The samples obtained from the levitation experiments were carefully collected using a fine mesh net after the solvent evaporation was completed.

Volumes of the droplets were calculated using MATLAB© by determining the width, a, and the height, b, of the ellipsoid droplet and then applying the formula $V = 4\pi/3a^2b$ to find the volume of an ellipsoid.

Induction times were extracted by analysing the collected images and determined by the change in the shape of the droplets when a solid is present.

Laser cutting

The spherical glycine samples were cut in half using a laser based sample preparation system (microPREP) equipped with a 532 nm laser. In order to avoid any heating effects generated by the laser the power was kept at 0.1 W. 30 line cuts with a distance of 2.5 μm from each other were performed for each cut.

Raman spectroscopy

A Renishaw inVia Raman spectrometer equipped with a 514.5 nm laser was employed to acquire all spectra for the polymorph assignment of glycine crystals. All measurements were taken using a 100× (NA = 0.85) objective lens, 2400 l mm^{-1} grating and laser power less than 1.3 mW. 50 measurements were taken from each sample prior to laser cutting in half for the identification of the crystals grown outside of the spheres. After cutting, the crystals grown in the centre of the spheres were also extensively characterised by taking 50 point measurements from different crystals. Minimum 2 spherical samples of glycine crystals grown from each solvent system were characterised.

Scanning electron microscopy (SEM)

ZEISS Sigma field emission SEM with an acceleration voltage of 5 kV was used to obtain images from glycine agglomerate coated with ~15 nm Pt layer.

Conflicts of interest

There are no conflicts of interest to declare.

Acknowledgements

This work is supported by the European Research Council (ERC) under the European Union's Horizon 2020 Research and Innovation Programme under grant agreement No 648417. T. V. thanks the Royal Academy of Engineering for the support through an Engineering for Development research fellowship (Grant No. RF1516/15/22).

References

1 A. Sigel, H. Sigel and R. K. O. Sigel, *Biomineralization: from nature to application*, 2008.
2 S. K. Haldar and J. Tišljar, *Introduction to Mineralogy and Petrology*, Elsevier Inc., 2013.
3 R. Davey and J. Garside, *From molecules to crystallizers*, Oxford University Press, New York, 2000.
4 J. W. Gibbs, *Am. J. Sci.*, 1878, **s3–16**, 441–458.
5 J. W. Mullin, *Crystallization*, Butterworth-Heinemann, Oxford, Boston, 4th edn, 2001.
6 M. V. Berry and A. K. Geim, Of flying frogs and levitrons, *Eur. J. Phys*, 1997, **18**, 307.
7 M. D. Barnes, K. C. Ng, W. B. Whitten and J. M. Ramsey, *Anal. Chem.*, 1993, **65**, 2360–2365.
8 W. B. Whitten, J. Michael Ramsey, S. Arnold and B. V. Bronk, *Anal. Chem.*, 1991, **63**, 1027–1031.
9 K. C. Ng, W. B. Whitten, S. Arnold and J. M. Ramsey, *Anal. Chem.*, 1992, **64**, 2914–2919.
10 G. G. Hoffmann, E. Lentz and B. Schrader, *Rev. Sci. Instrum.*, 1993, **64**, 823–824.
11 A. Ashkin, *Phys. Rev. Lett.*, 1970, **24**, 156–159.
12 E. G. Lierke, *Forsch. Ingenieurwes.*, 1995, **61**, 201–216.
13 A. R. Hanson, E. G. Domich and H. S. Adams, *Rev. Sci. Instrum.*, 1964, **35**, 1031–1034.
14 E. H. Trinh, *Rev. Sci. Instrum.*, 1985, **56**, 2059–2065.
15 C. J. Hsu, *J. Acoust. Soc. Am.*, 1986, **79**, 1335–1338.
16 E. Welter and B. Neidhart, *Fresenius' J. Anal. Chem.*, 1997, **357**, 345–350.
17 E. H. Trinh and C. J. Hsu, *J. Acoust. Soc. Am.*, 1986, **80**, 1757–1761.
18 E. H. Trinh, P. L. Marston and J. L. Robey, *J. Colloid Interface Sci.*, 1988, **124**, 95–103.
19 Y. Maruyama and K. Hasegawa, *RSC Adv.*, 2020, **10**, 1870–1877.
20 A. L. Yarin, G. Brenn, O. Kastner and C. Tropea, *Phys. Fluids*, 2002, **14**, 2289–2298.
21 H. Schiffter and G. Lee, *J. Pharm. Sci.*, 2007, **96**, 2284–2295.
22 H. Abdullahi, C. L. Burcham and T. Vetter, *Chem. Eng. Sci.*, 2020, **224**, 115713.
23 H.-L. Cao, D.-C. Yin, Y.-Z. Guo, X.-L. Ma, J. He, W.-H. Guo, X.-Z. Xie and B.-R. Zhou, *J. Acoust. Soc. Am.*, 2012, **131**, 3164–3172.

24 J. Leiterer, W. Leitenberger, F. Emmerling, A. F. Thünemann and U. Panne, *J. Appl. Crystallogr.*, 2006, **39**, 771–773.
25 J. Leiterer, F. Delißen, F. Emmerling, A. F. Thünemann and U. Panne, *Anal. Bioanal. Chem.*, 2008, **391**, 1221–1228.
26 S. E. Wolf, J. Leiterer, M. Kappl, F. Emmerling and W. Tremel, *J. Am. Chem. Soc.*, 2008, **130**, 12342–12347.
27 J. Leiterer, F. Emmerling, U. Panne, W. Christen and K. Rademann, *Langmuir*, 2008, **24**, 7970–7978.
28 M. Klimakow, J. Leiterer, J. Kneipp, E. Rössler, U. Panne, K. Rademann and F. Emmerling, *Langmuir*, 2010, **26**, 11233–11237.
29 T. Gnutzmann, Y. Nguyen Thi, K. Rademann and F. Emmerling, *Cryst. Growth Des.*, 2014, **14**, 6445–6450.
30 Y. Nguyen Thi, K. Rademann and F. Emmerling, *CrystEngComm*, 2015, **17**, 9029–9036.
31 A. Y. Lee, I. S. Lee, S. S. Dette, J. Boerner and A. S. Myerson, *J. Am. Chem. Soc.*, 2005, **127**, 14982–14983.
32 K. Kim, A. Centrone, T. A. Hatton and A. S. Myerson, *CrystEngComm*, 2011, **13**, 1127–1131.
33 B. D. Hamilton, M. A. Hillmyer and M. D. Ward, *Cryst. Growth Des.*, 2008, **8**, 3368–3375.
34 X. Yang and A. S. Myerson, *CrystEngComm*, 2015, **17**, 723–728.
35 A. B. M. Buanz and S. Gaisford, *Cryst. Growth Des.*, 2017, **17**, 1245–1250.
36 G. L. Perlovich, L. K. Hansen and A. Bauer-Brandl, *J. Therm. Anal. Calorim.*, 2001, **66**, 699–715.
37 Y. Iitaka and IUCr, *Acta Crystallogr.*, 1960, **13**, 35–45.
38 G. Albrecht and R. B. Corey, *J. Am. Chem. Soc.*, 1939, **61**, 1087–1103.
39 Y. Iitaka, *Acta Crystallogr.*, 1961, **14**, 1–10.
40 G. Albrecht and R. B. Corey, The Crystal Structure of Glycine, *J. Am. Chem. Soc.*, 1939, **61**, 1087.
41 I. Weissbuch, V. Y. Torbeev, L. Leiserowitz and M. Lahav, *Angew. Chem., Int. Ed.*, 2005, **44**, 3226–3229.
42 W. Tang, H. Mo, M. Zhang, J. Gong, J. Wang and T. Li, *Cryst. Growth Des.*, 2017, **17**, 5028–5033.
43 K. Renuka Devi, A. Raja and K. Srinivasan, *Ultrason. Sonochem.*, 2015, **24**, 107–113.
44 M. Louhi-Kultanen, M. Karjalainen, J. Rantanen, M. Huhtanen and J. Kallas, *Int. J. Pharm.*, 2006, **320**, 23–29.
45 H. U. Rodríguez Vera, F. Baillon, F. Espitalier, P. Accart and O. Louisnard, *Ultrason. Sonochem.*, 2019, **58**, 104671.
46 V. Bhamidi, S. H. Lee, G. He, P. S. Chow, R. B. H. Tan, C. F. Zukoski and P. J. A. Kenis, *Cryst. Growth Des.*, 2015, **15**, 3299–3306.
47 W. El Bazi, C. Porte, I. Mabille and J. L. Havet, *J. Cryst. Growth*, 2017, **475**, 232–238.
48 W. E. Ranz and W. Marshall, *Chem. Eng. Prog.*, 1952, **48**, 141.
49 D. H. Charlesworth and W. R. Marshall, *AIChE J.*, 1960, **6**, 9–23.
50 D. E. Walton, *Drying Technol.*, 2000, **18**, 1943–1986.
51 A. Y. Lee, I. S. Lee and A. S. Myerson, *Chem. Eng. Technol.*, 2006, **29**, 281–285.
52 S. K. P. Poornachary, J. V. Parambil, P. S. Chow, R. B. H. Tan and J. Y. Y. Heng, *Cryst. Growth Des.*, 2013, **13**, 1180–1186.
53 M. Boyes, A. Alieva, J. Tong, V. Nagyte, M. Melle-Franco, T. Vetter and C. Casiraghi, *ACS Nano*, 2020, **14**, 10394–10401.
54 M. Bienfait and R. Kern, *Bull. Soc. Fr. Mineral. Cristallogr.*, 1964, **87**, 604.
55 K. Hasegawa, Y. Abe, A. Fujiwara, Y. Yamamoto and K. Aoki, *Microgravity Sci. Technol.*, 2008, **20**, 261–264.
56 Y. Yamamoto, Y. Abe, A. Fujiwara, K. Hasegawa and K. Aoki, *Microgravity Sci. Technol.*, 2008, **20**, 277–280.
57 K. Hasegawa, Y. Abe and A. Goda, *npj Microgravity*, 2016, **2**, 1–5.

Electronic Supplementary Material (ESI) for CrystEngComm.

Crystallisation of Glycine from Binary Solvent under Acoustic Levitation

Adriana Alieva[1], Matthew Boyes[1], Thomas Vetter[2], Cinzia Casiraghi[1*]

[1] School of Chemistry, University of Manchester, Manchester, UK
[2] School of Chemical Engineering and Analytical Science, University of Manchester, Manchester, UK

* Corresponding author: cinzia.casiraghi@manchester.ac.uk

Supplementary Information

S1. State-of-the-art for crystallisation from acoustic levitation

Reference	Compound Studied	In situ	Ex situ	Main results
[1]	Mannitol	CCD camera	Scanning electron microscopy (SEM)	Development of a mechanistic model to describe the drying behaviour and particle shell formation of drying droplets of multicomponent mixtures.
[2]	Sodium chloride	CCD camera		The salt solution droplets exhibit a two-stage evaporation process, involving water evaporation and salt precipitation. A higher concentration of salt and larger diameter of droplets led to a lower evaporation rate.
[3]	Mannitol, Trehalose, and Catalase	CCD camera	SEM	The morphology of the products from levitation experiments show a strong similarity to the crystals obtained from spray-drying indicating some suitability of the levitator as a model for spray-drying.
[4]	Sodium chloride, Ammonium chloride, Lysozyme, and Proteinase K	CCD cameras	Optical microscopy	Crystals obtained from the acoustically levitated droplets exhibits higher growth rates, larger sizes, better shapes, fewer crystals, as well as fewer twins and shards, compared with the control on a vessel wall.
[5]	Sodium chloride	Energy-dispersive X-ray diffraction (EDXD)		The transformation of sodium chloride to a polycrystalline state was observed.
[6]	Ascorbic acid, Acetylsalycic acid, Apoferritin, and Colloidal gold	Small- and wide angle X-ray scattering (SAXS/WAXS)		Did not provide much insight on the crystallisation process of ascorbic acid and acetylsalycic acid. The correct diffraction peaks of the resulting crystals from both molecules were observed.
[7]	Calcium carbonate ($CaCO_3$)	Wide angle X-ray scattering (WAXS)	Different stages characterized by transmission electron microscopy (TEM) and cryogenic-SEM	Detected the formation of amorphous liquid-like structures at early stage of the crystallization of $CaCO_3$. The primary particles form homogenously within the volume of the droplet and serving as a second step templates for the crystallization of calcite.

			and SEM	
[8]	Caffeine on substrates (glass, polystyrene, and polyester)		Atomic Force Microscopy (AFM) and SEM	• Both crystal modifications (α- and *β*-caffeine) are present
	Caffeine from levitation experiments	WAXS		• Only α –form was obtained Due to the continuous diffusion and mixture process in the acoustic field the continuous growth of germs is inhibited thus the crystallization starts at the entire volume of the levitated droplet simultaneously.
[9]	Nifedipine in different solvents	XRD and Raman spectroscopy	Raman spectroscopy	Detected intermediate forms depending on the solvent used. The metastable β-form is favoured when the formation of H bonds between solvent and solute is possible and the glassy form is built whenever formation of H bonds is not an option. Both intermediate phases lead to the formation of the α-form.
[10]	ROY(5-methyl-2-[(2-nitrophenyl)amino]-3-thiophenecarbonitrile) in different solvents	WAXS and Raman		Different intermediate forms and polymorphs of ROY were observed depending on the solvent used. Thus they suggest that the crystallization of a specific polymorph can be attributed to nearest neighbour interactions and intermolecular attractive forces between solvent and analyte.
[11]	Paracetamol (acetaminophen)	WAXS and Raman		Based on the choice of the solvent selective crystallisation of both forms of paracetamol (the monoclinic form I and the metastable form II) was achieved. Two different amorphous stages were identified: which transforms to different polymorphs at later stages.

S2. Acoustic Levitation Setup

Figure S2 shows a schematic representation of the acoustic levitation set-up used for our crystallisation studies. The system consists of an ultrasonic droplet levitator operating at 100 kHz (Tec5, Germany), a CCD camera (Allied Vision Manta G505B), backlight illumination and a controlled evaporator unit (Bronkhorst, CEM202A). The emitter and the reflector are encased in a chamber which is surrounded by a heating jacket to achieve environmental control. The heating jacket is connected to a water bath (Ministat 230, Huber, Germany) allowing the flow of temperature regulated water around the levitation chamber. Conditioned N_2 gas is introduced to the chamber at a controlled gas flow rate, temperature and humidity. The temperature and relative humidity within the levitation chamber were monitored with the use of an iButton temperature and humidity sensor (Thermochron). The flow rate of N_2 gas was set high enough to maintain the environmental control within the chamber without agitating the levitating droplet. The inner diameter of the chamber is 70 mm, with two sealable access windows of diameter of 25 mm, which allow imaging and droplet suspension in the acoustic field. A droplet was injected in the levitator using a Hamilton 1800 syringe. All levitation experiments were captured with a CCD camera.

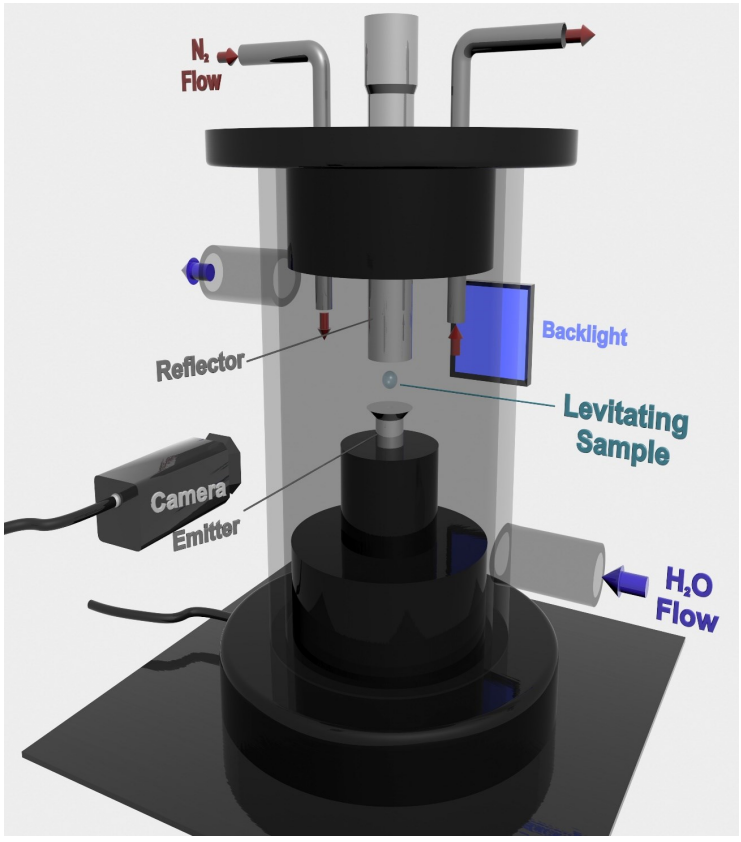

Figure S2. Schematic representation of the acoustic levitation setup.

S3. Evaporation profiles of glycine microdroplets from H_2O:IPA solvent system

Figure S3 shows the evaporation profiles of glycine microdroplets from H_2O:IPA solvent system. It can be clearly seen that both evaporation profiles of the binary solvent mixture for crystals obtained as spherical and non-spherical follow a similar trend.

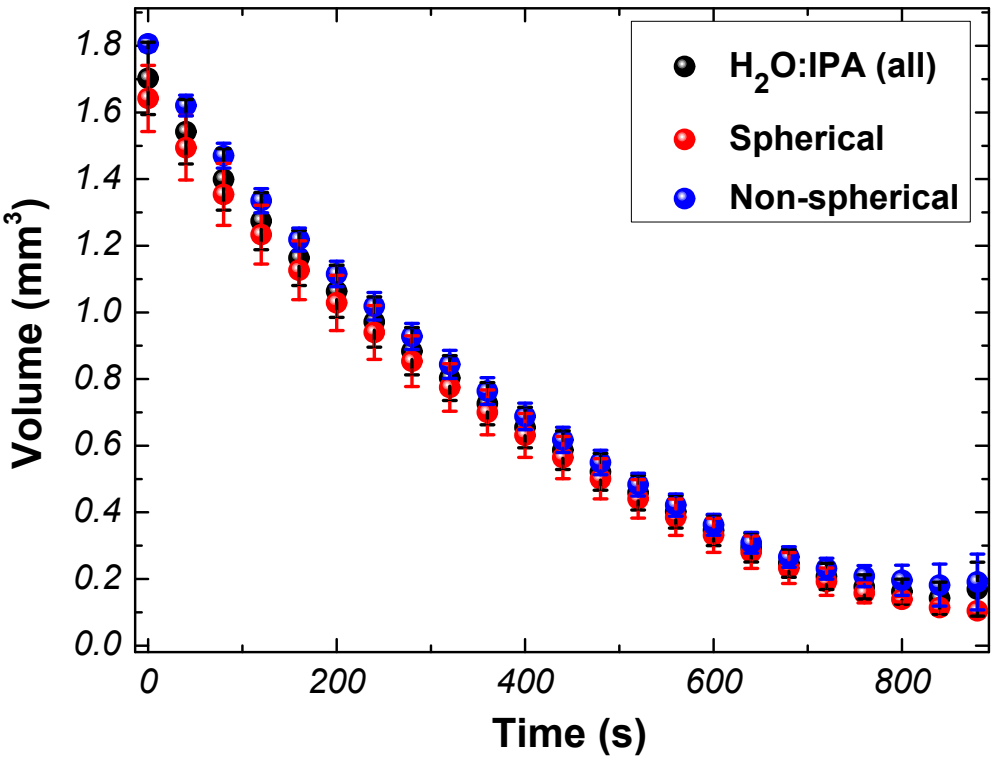

Figure S3. Evaporation profiles of glycine microdroplets from H_2O:IPA solvent system

S4. Characterisation protocol for polymorph screening

Figure S4 shows a schematic of the characterisation protocol developed for polymorph screening of glycine samples based on Raman spectroscopy. The procedure can be summarised as follows:

i) Mounting a glycine sphere on a substrate

ii) Taking Raman measurements from the outside of the sphere

iii) Cutting the sample into half using Laser Cutter

iv) Taking Raman measurements from the inner part of the sphere

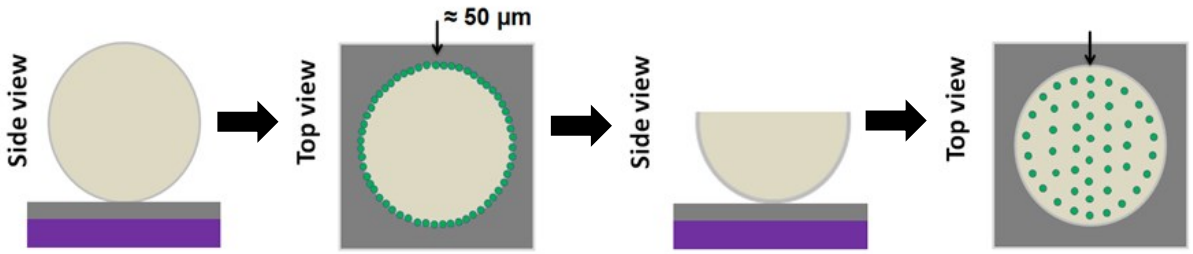

Figure S4. Schematic of the characterisation protocol for the polymorph screening of glycine samples.

S5. Raman spectrum of glycine polymorphs

Figure S5 shows the distinct Raman spectra of the CH region (2900-3050 cm^{-1}) of the three polymorphs of glycine. These peaks represent the symmetric (lower shift) and asymmetric (higher shift) stretches of the C-H bonds. The positions of these modes are distinct for each polymorph, which were found to be at 2972-3007 cm^{-1} for α-form, at 2953-3008 cm^{-1} for β-form and at 2962- 3000 cm^{-1} for γ-form.

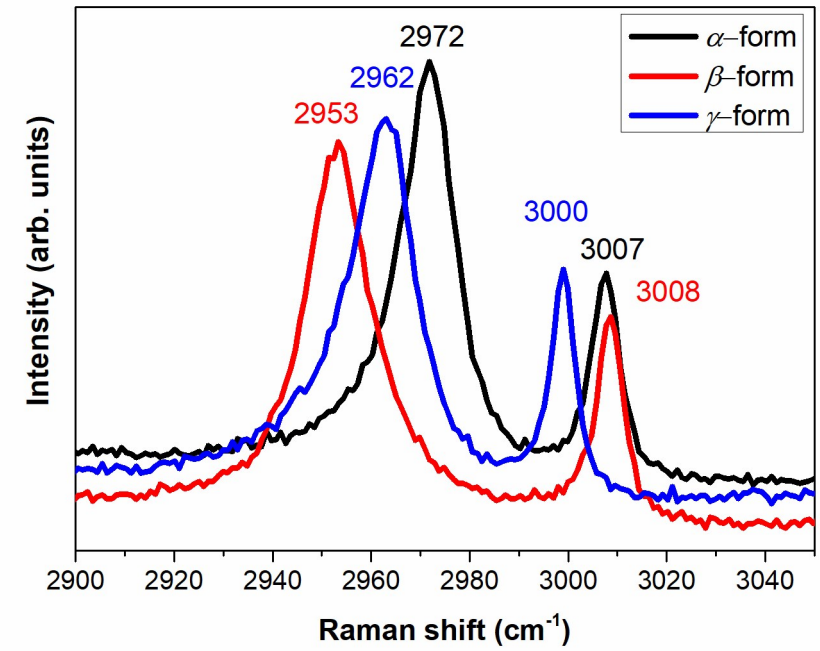

Figure S5. Raman spectra of glycine polymorphs.

S6. Fitting results of polymorphs obtained from different solvent systems

The fitting results for the position and Full Widths at Half Maximum (FWHM) of symmetric CH stretch (ν_s(CH)) and asymmetric CH stretch (ν_{as}(CH)) of Raman measurements taken from different regions of glycine crystals are shown in Table S1.

Table S1. Fitting results of the CH stretching modes of glycine crystals obtained from different solvent systems

Sample	**ν_s(CH)**		**ν_{as}(CH)**	
	Position (cm^{-1})	**FWHM (cm^{-1})**	**Position (cm^{-1})**	**FWHM (cm^{-1})**
H_2O out	2972	13	3008	5.7
H_2O centre	2971.68	12.8	3007	5.2
H_2O:IPA out	2971.60	12.8	3007	5.1
H_2O:IPA centre	2971.63	12.7	3007	5

References

[1] T. Abdullahi, Hassan; Burcham, Christopher; Vetter, "A mechanistic model to predict droplet drying history and particle shell formation in multicomponent systems," *Chem. Eng. Sci.*, vol. 224, 2020.

[2] Y. Maruyama and K. Hasegawa, "Evaporation and drying kinetics of water-NaCl droplets via acoustic levitation," *RSC Adv.*, vol. 10, no. 4, pp. 1870–1877, Jan. 2020, doi: 10.1039/c9ra09395h.

[3] H. Schiffter and G. Lee, "Single-droplet evaporation kinetics and particle formation in an acoustic levitator. Part 2: Drying kinetics and particle formation from microdroplets of aqueous mannitol, trehalose, or catalase," *J. Pharm. Sci.*, vol. 96, no. 9, pp. 2284–2295, 2007, doi: 10.1002/jps.20858.

[4] H.-L. Cao *et al.*, "Rapid crystallization from acoustically levitated droplets," *J. Acoust. Soc. Am.*, vol. 131, no. 4, pp. 3164–3172, 2012, doi: 10.1121/1.3688494.

[5] J. Leiterer, W. Leitenberger, F. Emmerling, A. F. Thünemann, and U. Panne, "The use of an acoustic levitator to follow crystallization in small droplets by energydispersive X-ray diffraction," *J. Appl. Crystallogr.*, vol. 39, no. 5, pp. 771–773, 2006, doi: 10.1107/S0021889806024915.

[6] J. Leiterer, F. Delißen, F. Emmerling, A. F. Thünemann, and U. Panne, "Structure analysis using acoustically levitated droplets," *Anal. Bioanal. Chem.*, vol. 391, no. 4, pp. 1221–1228, 2008, doi: 10.1007/s00216-008-2011-2.

[7] S. E. Wolf, J. Leiterer, M. Kappl, F. Emmerling, and W. Tremel, "Early homogenous amorphous precursor stages of calcium carbonate and subsequent crystal growth in levitated droplets," *J. Am. Chem. Soc.*, vol. 130, no. 37, pp. 12342–12347, 2008, doi: 10.1021/ja800984y.

[8] J. Leiterer, F. Emmerling, U. Panne, W. Christen, and K. Rademann, "Tracing coffee tabletop traces," *Langmuir*, vol. 24, no. 15, pp. 7970–7978, 2008, doi: 10.1021/la800768v.

[9] M. Klimakow *et al.*, "Combined synchrotron XRD/Raman measurements: In situ identification of polymorphic transitions during crystallization processes," *Langmuir*, vol. 26, no. 13, pp. 11233–11237, 2010, doi: 10.1021/la100540q.

[10] T. Gnutzmann, Y. Nguyen Thi, K. Rademann, and F. Emmerling, "Solvent-triggered crystallization of polymorphs studied in situ," *Cryst. Growth Des.*, vol. 14, no. 12, pp. 6445–6450, 2014, doi: 10.1021/cg501287v.

[11] Y. Nguyen Thi, K. Rademann, and F. Emmerling, "Direct evidence of polyamorphism in paracetamol," *CrystEngComm*, vol. 17, no. 47, pp. 9029–9036, 2015, doi: 10.1039/c5ce01583a.

Chapter 7: Enhanced Liquid Phase Exfoliation of Graphene in Water using an Insoluble Bis-Pyrene Stabiliser

My contribution: I prepared some of the graphene dispersions and performed the subsequent zeta potential measurements of those dispersions. I prepared the sample used for the DOSY NMR experiment and wrote all the NMR sections of the manuscript.

Enhanced Liquid Phase Exfoliation of Graphene in Water Using an Insoluble Bis-Pyrene Stabiliser

View Article Online
DOI: 10.1039/C9FD00114J

Yuyoung Shin[1], , Xavier Just-Baringo[1], Matthew Boyes[1]Adyasha Panigrahi[1], Marco Zarattini[1], Yingxian Chen[2], Xinyun Liu[3], Gareth Morris,[1] Eric Prestat[3,4], Kostas Kostarelos[2], Sandra Vranic[2], Igor Larrosa*[1], Cinzia Casiraghi*[1]

[1]*Department of Chemistry, University of Manchester, Oxford Road, Manchester, M13 9PL*
[2]*Nanomedicine Lab, National Graphene Institute and Faculty of Biology, Medicine & Health, AV Hill Building, University of Manchester, Manchester, M13 9PT*
[3]*Department of Materials, University of Manchester, Oxford Road, Manchester, M13 9PL*
[4]*SuperSTEM Laboratory, SciTech Daresbury Campus, Daresbury, WA4 4AD, UK*

Abstract:

Stabilisers, such as surfactants, polymers and polyaromatic molecules, offer an effective way to produce graphene dispersions in water by Liquid Phase Exfoliation (LPE), without degrading the properties of graphene. In particular, pyrene derivatives provide better exfoliation efficiency than traditional surfactants and polymers.

A stabiliser is expected to be relatively soluble in order to disperse hydrophobic graphene in water. Here, we show that exfoliation can also be achieved with insoluble pyrene stabilisers if appropriately designed. In particular, bis-pyrene stabilisers (BPSs) functionalised with pyrrolidine provide higher exfoliation efficiency and percentage of single layers, as compared to traditional pyrene derivatives, under the same experimental conditions. This is attributed to the enhanced interactions between BPS and graphene, provided by the presence of two pyrene binding groups. This approach is therefore attractive not only to produce highly concentrated graphene, but also to use graphene to disperse insoluble molecules in water. The enhanced adsorption of BPS on graphene, however, is reflected in higher toxicity towards human epithelial bronchial immortalized cells, limiting the use of this material for biomedical applications.

Introduction

Graphene, a single layer of graphite, shows great potential for numerous applications due to its outstanding properties, including extreme mechanical strength and exceptionally high electronic and thermal conductivity.[1] Out of all graphene's synthesis techniques, Liquid-Phase Exfoliation (LPE)[2] allows for mass-scalable, cost-effective and versatile production of graphene formulations suitable for a wide range of practical uses, ranging from composites to biomedical applications.[1,3–5]

Liquid Phase Exfoliation relies on the use of solvents with surface tension comparable to that of graphene.[2] Thus, *N*-methyl-2-pyrrolidone (NMP) is typically the solvent of choice.[2] However, its toxicity, high cost and boiling point do not make it an ideal solvent. Water is a low cost and friendly solvent, required in many applications. However, in order to effectively exfoliate graphite in water, the graphene surface needs to be altered, either covalently or non-covalently.[6–8] The use of stabilisers offers an effective method to functionalise the material without introducing defects, hence maintaining the intrinsic properties of graphene, while allowing dispersability in water.[9–11] Different types of stabilisers, including surfactants[9,12–14], polymers[15–17] and polyaromatic molecules[10,18,19] have been investigated.

Stabilisers are typically amphiphilic, *i.e.* they have a hydrophobic binding group, which adsorbs onto the graphene surface through van der Waals interactions, and a hydrophilic group, which prevents re-stacking of exfoliated graphene nanosheets through steric hindrance and/or electrostatic stabilisation.[10,20] Out of all stabilisers, pyrene derivatives have been shown to be very effective at exfoliating graphite, when compared to typical surfactants and polymers, due to the effective adsorption of pyrene on graphene through π - π interactions.[10,11,21–23] In particular, in our group, we have extensively used 1-pyrenesulfonic acid sodium salt (PS1) to obtain biocompatible and inkjet-printable graphene dispersions in water.[4,21,24]

Despite the wide use of pyrene derivatives as stabilisers, the effective mechanisms leading to exfoliation are very poorly understood. Seminal works have shown that not all pyrene derivatives are effective exfoliating agents.[10,11,25] Exfoliation efficiency, as defined by the concentration of graphene, depends strongly on many factors, such as types and number of functional groups, and the charge distribution in the stabiliser, which determinethe thermodynamics of the interaction between the stabiliser and graphene, *e.g.* the adsorption of the pyrene binding group on the graphene surface, the affinity of the functional groups for the solvent medium, and the effectiveness of deterrence of re-stacking of graphene sheets.[9,10,26–28] Since the affinity of the functional groups for the solvent medium of the functional groups is

View Article Online
DOI: 10.1039/C9FD00114J

one of the key parameters, stabilisers with relatively good aqueous solubility have been used up to now.

In this work, we show that pyrene derivatives with extremely low solubility can be exceptionally efficient as exfoliating agents, contradicting the common assumption that an effective stabiliser needs to be soluble in water. A bis-pyrene stabiliser (BPS), functionalized with a pyrrolidine central group (**Scheme 1),** was designed and synthetized *ad hoc* for this study. Its exfoliation efficiency was compared to that of two pyrene derivatives with the same functional group: one with longer linking chains between the pyrene binding groups and the functional group (LBPS) and the other with a mono-pyrene binding group (MPS) (**Scheme 1**). BPS has been found to be insoluble in aqueous media, *i.e.* the aqueous solubility of BPS is under the detection limit of NMR. Despite this the BPS molecule showed exfoliation efficiency up to 3-5 times higher than that obtained with PS1 or MPS. Furthermore, the graphene dispersion prepared with BPS showed a higher percentage of single layer graphene (SLG), compared to PS1. The enhanced exfoliation efficiency of BPS, compared to the other stabilisers, is attributed to the higher interaction strength between BPS and graphene, driven by stronger π-π interactions due to the presence of two pyrene binding groups in BPS, and the insolubility of BPS in water (as confirmed by ^{1}H NMR). Finally, cytotoxicity studies on the graphene dispersions prepared with BPS show the toxicity of graphene to be dependent on the initial BPS concentration, whereas the graphene dispersion prepared with MPS showed no cytotoxic effect. Since the sizes of the nanosheets prepared with BPS and MPS are comparable, the difference in toxicity is attributed to the presence of two pyrene binding groups in BPS, which may affect how these molecules assemble on graphene, in particular at high BPS concentrations.

Methods

Materials

Preparations of pyrene derivatives

The details of the synthesis routes for the pyrene stabilisers and all characterisation methods used for identification of the structure and purity of the compounds are given in the Supplementary Information.

Preparations of graphene dispersions

Natural graphite crystals were provided by Graphexel Ltd. Graphene dispersions were prepared by LPE in water following the protocol developed in previous works.[4,21,29] In detail, 300 mg of graphite and varying amount of stabilisers wereadded to 100 mL of de-ionized (DI) water. The

mixture was then sonicated at 600W for 7 days using a Hilsonic bath sonicator. Afterwards, un-exfoliated graphite was removed by two-step centrifugation (Sigma 1-14k refrigerated centrifuge) at 3500 rpm (903 g) for 20 min. After each centrifugation step, the supernatant containing graphene in water was collected. For cytotoxicity studies, the graphene dispersions prepared were further centrifuged at 15000 rpm (16 600 g) for 60 min to increase the concentration further by collecting the sediment and re-dispersing in a smaller volume of DI water. In the case of the graphene dispersions prepared with BPS, the supernatant was also collected for characterisation. In the case of the graphene dispersions prepared with MPS, the second centrifugation step was repeated twice to remove excess pyrene from the solution.

Characterization

UV-Vis Spectroscopy

The concentration of graphene dispersed in the solution was determined using UV-Vis spectroscopy. The UV-Vis spectrum of graphene appears flat and featureless in the visible-IR region,[2] so the absorption is measured at 660 nm for estimation of the graphene nanosheet concentration using the Beer-Lambert law. Despite the extensive work done towards accurately estimating the absorption coefficient, this is still the subject of considerable debate.[30] In this study, an absorption coefficient of 2460 L/g m was used for estimating the graphene concentration.[9,12,31] A Perkin-Elmer l-900 UV-Vis-NIR spectrophotometer was used to acquire the spectra.

Zeta Potential Measurements

Electrophoretic mobility (μ) was measured using a ZetaSizer Nano ZS (Malvern Instruments, UK) after dilution of samples with water in the folded capillary cells (Malvern Instruments, UK). Default instrument settings for water-based system and automatic analysis were used for all measurements, which were performed at 25 ˚C and at the natural pH. The equipment software automatically converted the mobility μ to zeta potential (ζ) values by Henry's equation: $\mu = 2\varepsilon\zeta F(\kappa a)/3\eta$ where ε is dielectric constant, η is the solution viscosity and $F(\kappa a)$ is Henry's function, approximated to the value of 1.5 using the Smoluchowski approximation for polar media, valid for dispersed particles of any shape including plate-like particles.[32]All values for samples are mean ± standard deviation (SD), calculated from triplicate measurements.

Atomic Force Microscopy (AFM)

A Bruker Atomic Force Microscope (MultiMode 8) in Peak Force Tapping mode, equipped with ScanAsyst-Air tips, was used to determine the lateral size distribution of the flakes. The sample was prepared by drop casting the solution on a clean silicon substrate; areas of 10 to 400 μm^2 were scanned and typically 200 or more flakes were selected for lateral size analysis. Lateral dimension and thickness distributions of graphene nanosheets were carried out using Gwyddion scanning probe microscopy data processing software.

Transmission Electron Microscopy (TEM)

TEM imaging was performed using a FEI Talos 200X operating at an acceleration voltage of 200 kV, and TEM images were acquired using a FEI CETA CMOS (complementary metal-oxide semiconductor) camera. TEM samples were prepared by dip coating the graphene dispersions either on a lacey carbon copper grid or on a 3 nm ultrathin carbon film supported on lacey carbon copper grid. Measurements of the numbers of layers were performed by High Resolution TEM (HRTEM) imaging of free-standing graphene flakes on the lacey carbon film. The graphene dispersion deposited on ultrathin carbon film was used for the measurement of the lateral size of the graphene flakes.

Raman Spectroscopy

Raman measurements were performed using a Renishaw Invia Raman spectrometer equipped with a 514.5 nm excitation line and 2.0 mW laser power. Graphene dispersions were drop-cast onto silicon substrates and measurements were performed on isolated and individual flakes. The Raman spectra were taken with a 100× NA0.85 objective lens and 2400 grooves/mm grating. Typically, 30-50 flakes were measured for each sample. The Raman peaks were fitted with a Lorentzian lineshape. The Raman analysis was performed using a qualitative protocol developed for graphene produced by LPE in our group.[13,26,27,33,34] In detail, the shape of the 2D peak is used for determination of the thickness distribution. The 2D peak is fitted with a single Lorentzian lineshape, and by evaluating the fit residual (R^2), the spectrum is attributed to a single-layer graphene (SLG), or few-layer sheets (FLG), or to graphitic material (>10 layers with AB stacking) in the following way. A single symmetric 2D peak with $R^2 > 0.987$ is attributed to the spectrum of a SLG; a single asymmetric peak with $R^2 < 0.987$ is attributed to FLG; and graphitic material is identified by its characteristic peak shape, characterized by a low-wavenumber shoulder.

Nuclear Magnetic Resonance

All nuclear magnetic resonance (NMR) spectra reported were acquired at a nominal temperature of 25 ˚C using a VNMRS 500 spectrometer operating at 499.826 MHz for ^{1}H. The standard ^{1}H spectrum was acquired in 1.3 h using 90˚ pulses, a spectral width of 10 kHz, 32768

complex data points, and a recycle time of 3.4 s. The diffusion-ordered spectroscopy (DOSY) data were acquired in a total time of 11 h using the Oneshot pulse sequence[35], with a spectral width of 19.8 kHz, a recycle delay of 5 s, and 32768 complex data points, and processed with the manufacturer's VnmrJ software. The Oneshot pulse sequence used a total diffusion-encoding gradient pulse duration of 2 ms (*i.e.* two encoding and two decoding pulses, each of 1 ms duration), a diffusion time of 0.1 s, and 8 diffusion-encoding gradient amplitudes ranging from nominal values of 6 to 54 G/cm in equal increments of gradient squared. The graphene dispersion used for the DOSY experiment was produced via the same LPE process as the rest of this study. Exfoliation of 60 mg of graphite with 12 mg of the BPS in 20 mL of D_2O allowed the production of a dispersion with a final concentration of 0.8 mg/mL.

Cell culture

Human epithelial bronchial immortalized cells (BEAS-2B, CRL-9609, ATCC, LGC standards, UK) were maintained in RPMI-1640 cell culture medium (Sigma-Aldrich), supplemented with 10% foetal bovine serum (FBS) (Gibco, Thermo Fisher Scientific), 1000 units penicillin, and 1 mg/mL streptomycin (Sigma-Aldrich) at 37 ^oC in a humidified 5% CO_2 incubator. Cells were subcultured when reaching 80% confluence, with 0.05% trypsin-EDTA (Sigma-Aldrich), and 10% FBS was used to stop the activity of trypsin-EDTA.

Treatment of the cells

BEAS-2B cells were seeded in P12-well plates (Corning, Costar, Sigma-Aldrich) in complete RPMI medium at 37^oC in a humidified 5% CO_2 incubator for 24 h. After 24 h, BEAS-2B cells reached confluence of ~80 % and were treated with the graphene dispersions prepared with BPS at 0.2 mg/mL, BPS at 0.6 mg/mL, BPS at 1.0 mg/mL and MPS at 0.4 mg/mL (25, 50, 75 and 100 µg/mL, 1 mL/well) in serum-free RPMI medium for 4 h. Following 4 h of incubation, FBS (100 µL/well) was added and the cells were further incubated for additional 20 h. BEAS-2B cells were washed (RPMI w FBS, 1 mL/well) before analysis with a ZEISS Primovert microscope.

Results and discussion

Synthesis of pyrene derivatives

In a general synthetic approach, the stabilisers were synthesised via alkylation of pyrrolidine **2a-b** using the parent (1-pyrenyl)boromoalkane **1a-b** for MPS or two consecutive alkylations for BPS and LBPS.

View Article Online
DOI: 10.1039/C9FD00114J

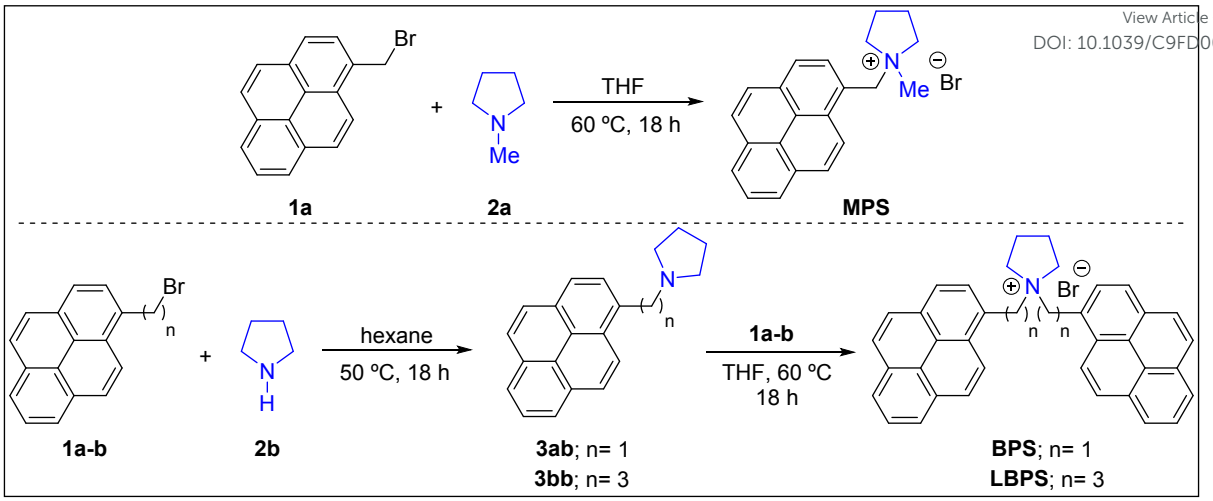

Scheme 1 General schematic plan for synthesis of the pyrene stabilisers

Amination of (1-pyrenyl)bromoalkane: To a vial charged with a stirring suspension of (1-pyrenyl)bromoalkane **1a-b** (1.0 equiv) in dry hexane (1.20 mL) at 0 ˚C was added secondary amine substrate (4.0 equiv). The reaction mixture was stirred at 50 ºC for 18 h. The crude product was cooled down to room temperature and dissolved in CH_2Cl_2 (50 mL) and washed with saturated aqueous $NaHCO_3$. The aqueous layer was extracted with CH_2Cl_2 (2 × 50 mL) and the combined organic fractions were dried ($MgSO_4$) and concentrated under vacuum to afford the corresponding amine products **3ab-bb**.

Preparation of BPS: The crude secondary amines **3ab**/**3bb** or *N*-methylpyrrolidine **2a** were stirred with (1-pyrenyl)bromoalkane **1a-b** in THF at 60 ˚C for 18 h. After this time, the reaction mixture was cooled to room temperature and the precipitate was filtered under vacuum, washed with THF and then Et_2O to afford the desired pyrene stabiliser BPS, LBPS or MPS.

Liquid-Phase Exfoliation

To compare the exfoliation efficiency of BPS, MPS and LBPS, the graphene dispersions were prepared with the same initial stabiliser concentration (0.4 mg/mL). **Figure 1(a)** shows that a graphene concentration of 0.72 mg/mL was achieved by BPS, against 0.28 mg/mL obtained with MPS and 0.06 mg/mL with LBPS. The higher exfoliation efficiency of BPS compared to MPS is attributed to the presence of two pyrene binding groups, which improves the π-π interactions between the molecules and graphene, and also affects the solubility of BPS in water (details in SI), driving the BPS molecules to minimize their interaction with water by adsorbing on graphene. It is interesting to note that the concentration obtained with MPS is comparable to that obtained by PS1 (**Figure 1(a)**), possibly because the two molecules have relatively good

solubility (details in SI) and a similar structure. Remarkably, LBPS, which also has two pyrene binding groups and is also insoluble in water, showed almost negligible exfoliation efficiency (**Figure 1 (a)**). This could be attributed to the different ways that these molecules are expected to assemble on graphene. The long chain connecting the pyrene binding groups in LBPS gives rise to some conformational freedom for the two pyrene binding groups, which may result in disruption of the controlled adsorption of the LBPS molecules due to possible interaction between the two pyrene bases. In the case of BPS, due to the relatively short carbon linking chain between the pyrene binding group and the functional group, the BPS molecule is more rigid, allowing more controlled assembly of BPS on graphene as well as adsorption of both the pyrene binding groups, exposing the charged functional group towards the water solvent. Alternatively, the poorer exfoliation efficiency of MPS could be attributed to intramolecular π-π stacking of the molecules in solution.

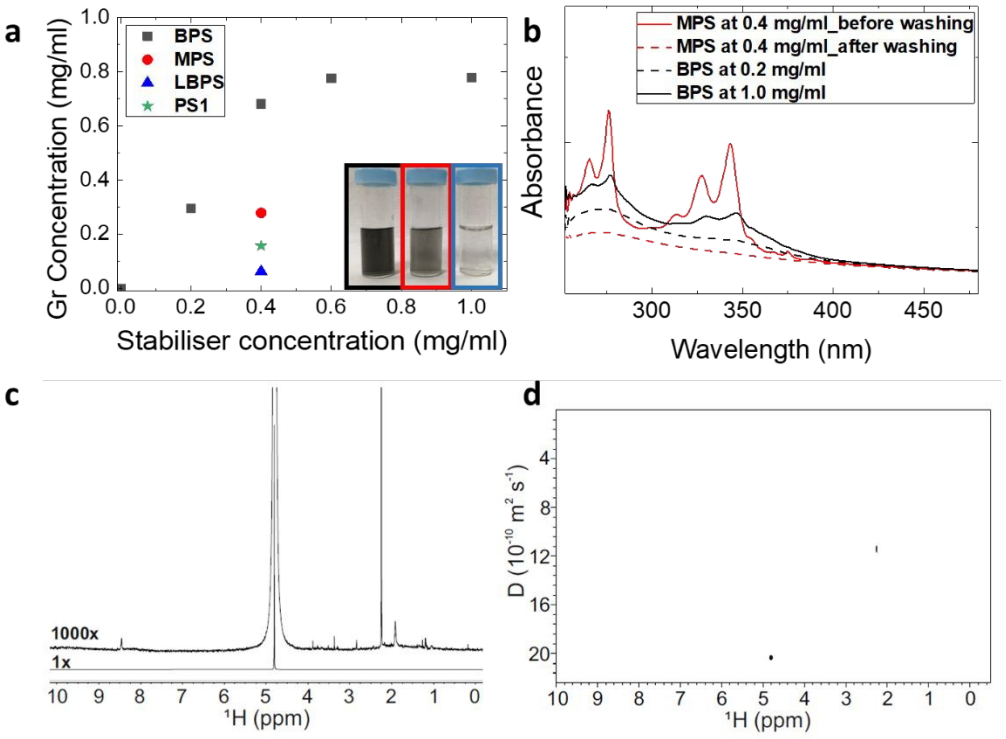

Figure 1 (a) Graphene concentrations obtained for different graphene dispersions. inset: photographs of graphene dispersions prepared with different stabilisers, from left to right, BPS, MPS and LBPS at 0.4 mg/mL, all diluted by factor of 10. **(b)** UV-vis spectra of selected graphene dispersions with different pyrene concentrations. **(c)** Standard ^{1}H spectrum of a graphene dispersion that was produced with an initial BPS concentration of 0.6 mg/mL in D_2O

at 1x and 1000x magnifications. **(d)** 2D DOSY spectrum of a graphene dispersion that was produced with an initial BPS concentration of 0.6 mg/mL in D_2O.

View Article Online
DOI: 10.1039/C9FD00114J

The stability of graphene dispersions was estimated by measuring the zeta potential at ambient conditions. Typically, aqueous suspensions with $|\zeta| > 30$ mV are regarded as stable suspensions.[28] The zeta potential of all the dispersions prepared in this study are between 30 and 50 mV, indicating very good stability (**Table 1** and **Figure S2**).

The enhanced exfoliation efficiency of BPS is attributed to the ability of these molecules to adsorb better on graphene. This is also supported by the observed trend of increasing concentration of the exfoliated graphene with increasing initial BPS concentration, reaching saturation above 0.4 mg/mL of BPS (**Figure 1 (a) and Figure S1**). UV-vis spectroscopy, in particular, shows clear BPS residual peaks, **Figure 1 (b)**. It is interesting to compare the spectrum obtained with BPS and MPS. Note that for better comparison of the intensities of the absorbance peaks of pyrene in the region between 250 nm and 400 nm, the spectra have been normalised against graphene absorbance at 660 nm. The prominent pyrene absorption peak in the dispersions obtained by MPS can easily be removed by a washing step (see Method), leaving no residual pyrene peaks in the UV-Vis spectrum after washing. In the case of BPS, however, there was no noticeable change of absorbance in that region after the washing step (**Figure S3**). As BPS is insoluble, this signal can only be attributed to the BPS adsorbed on the nanosheets. Furthermore, as shown in **Figure 1(b)**, an increase in pyrene absorbance is observed with increasing initial PBS concentration, which should be attributed to the increased amount of BPS molecules adsorbed on the graphene surface.

In order to confirm that all BPS molecules are adsorbed on graphene, we performed 1D and DOSY ^{1}H NMR experiments. DOSY uses measurements of diffusion to enable the separation of the NMR signals of different components in a mixture, and can be used to probe interactions between components.[36,37] Initially, a standard ^{1}H spectrum of a graphene dispersion with a BPS concentration of 0.6 mg/mL was collected, shown in **Figure 1(c)**. This spectrum is dominated by the 0.2% of protons present in the D_2O used and no pyrene aromatic signals are seen. The DOSY spectrum of **Figure 1(d)** shows only the signals of rapidly diffusing water and trace acetone. No free BPS is detected, indicating that the pyrene present is tightly bound to the graphene nanosheets, which tumble slowly in solution, and hence shows rapid spin-spin relaxation. A wide ^{1}H spectrum (**Figure S4**) confirmed that most of the ^{1}H signal intensity comes from very broad signals.

Characterisation of the exfoliated graphene nanosheets

Three graphene dispersions (BPS at 0.4 mg/mL, BPS at 0.6 mg/mL and MPS at 0.4 mg/mL) were chosen for further characterisation of the exfoliated graphene flakes by Raman spectroscopy, AFM and TEM. Supernatants collected for the two BPS dispersions were also characterised for comparison. Note that higher exfoliation yield is not necessarily an indication of a higher percentage of single layers, hence further characterisation is mandatory. The results are summarised in **Table 1**.

	BPS at 0.4 mg/mL	**BPS at 0.6 mg/mL**	**MPS at 0.4 mg/mL**
Concentration of dispersion (*mg/mL*)	0.72	0.78	0.28
Concentration of supernatant (*mg/mL*)	0.06	0.06	/
Zeta potential of dispersion (*mV*)	40	38	39
Zeta potential of supernatant (*mV*)	47	40	/
%SLG of dispersion	~58%	~44%	16%
%SLG of supernatant	~90%	~97%	/
Av. flake size of dispersion (*nm*)	124	121	230
Av. flake size of supernatant (*nm*)	44	50	/

Table 1 Summary of the properties of the selected graphene dispersions and related supernatants.

Raman spectroscopy is the most commonly used characterization tool for graphene.[38] The Raman spectrum of graphene is characterized by the G, D and 2D peaks, lying at ~1580 cm^{-1}, ~1350 cm^{-1}, and 2680 cm^{-1}, respectively. In the case of graphene produced by LPE, which typically has size smaller than 500 nm, the D peak is activated by the edges of the nanosheets[39], thus the intensity ratio between D and G peaks, I(D)/I(G), changes with the size of the flakes.[13,26,27,33] The 2D peak shape is typically used to identify single layer graphene.[40] However, this identification method cannot be applied with the same accuracy to graphene produced by LPE, as the shape of the 2D peak is affected by edge effects, solvent or stabiliser doping and/or re-stacking of flakes.[21,41] Here we performed a qualitative thickness analysis using a protocol developed and tested in our group, based on Lorentzian fitting of the 2D peak (details in the Methods section).[13,26,27,33,34] **Figure 2 (a)** shows representative graphene Raman spectra obtained from the BPS at 0.6 mg/mL dispersion and supernatant. The Raman analysis shows that BPS is highly efficient at exfoliating graphene: both the BPS dispersions had a SLG percentage between 40 and 60%, compared to 16% measured for the MPS dispersion. Thus, BPS gives high exfoliation yield, as well as a high percentage of single and few layers,

compared to traditional pyrene derivatives. Moreover, **Figure 2 (a)** shows that the flakes in the supernatant are characterised by higher R^2 value as well as higher I(D)/I(G). Thus, the supernatant is expected to contain thinner flakes, mostly single-layers and of smaller size, compared to the dispersion. This is confirmed by AFM, **Figure 2 (c) and (d).** These figures show the lateral size distribution for the dispersion and supernatant of BPS at 0.6 mg/mL (AFM images used for statistical analysis and the distribution histograms for the other samples are shown in the SI). AFM results show that the average flake size of the two BPS dispersions is centered at ~125 nm, slightly smaller than that of the flakes in the MPS dispersion, which is peaked at ~230 nm, in agreement with previous studies reporting graphene dispersions prepared with pyrene derivatives.[4,11,21,29] The average flake size of the two supernatant dispersions obtained with BPS was about ~50 nm, which is expected, as smaller and thinner flakes are likely to be found in the supernatant. Note that with traditional pyrene derivatives, the concentration of graphene in the supernatant is too small, typically below 0.01 mg/mL, for further use; in contrast, LPE with BPS offers a very simple way to achieve concentrated and enriched graphene dispersions, although of much reduced flake size.

Thickness distributions obtained by AFM (**Figure S5** and **S6**) confirm the Raman analysis, showing that BPS dispersions contain a higher number of thinner flakes than dispersions made with MPS. However, the thickness distribution obtained by AFM should be viewed with caution as the adsorption of stabilisers and solvent molecules on the surface of graphene flakes leads to higher thicknesses than those theoretically expected.[21,42,43] Because of this, the BPS at 0.6 mg/mL sample was further characterised by TEM. **Figure 3 (a)** shows the lateral size distribution histogram obtained from TEM analysis, which is in good agreement with that obtained from AFM (**Figure 2(c)**).

Figure 3(b) shows the thickness distribution histogram, collected for statistical analysis of more than 200 individual flakes: the dispersion is mostly composed of thin (< 10 layers) flakes. It should be noted that the discrepancy between the SLG percentages estimated by Raman and by TEM analysis is attributable to the different sample preparation: the Raman sample was prepared by drop casting on silicon wafer whereas TEM sample was prepared by dip-coating on lacy carbon grid. However, despite the discrepancy, both techniques show that the graphene dispersion prepared with BPS is well exfoliated, mostly containing thin layers, as further confirmed in **Figure 3(c)** and **(d)**.

Biocompatibility study

Previous work from our group[4] has shown that graphene flakes prepared by LPE with PS1 are highly biocompatible, with no cytotoxicity observed for concentrations up to 100 μg/mL. It is, however, unclear if and how the cytotoxicity is related to the type of pyrene derivative used. Thus, here we compare the cytotoxicity of the dispersions obtained with MPS and BPS, which have the same functional group, but different numbers of pyrene binding groups. As the nanosheets of the graphene dispersions produced by BPS and MPS have comparable size, the comparison of cytotoxicy between the two samples allows the effect of the stabiliser, which determines the surface chemistry, on cellular interactions to be determined.

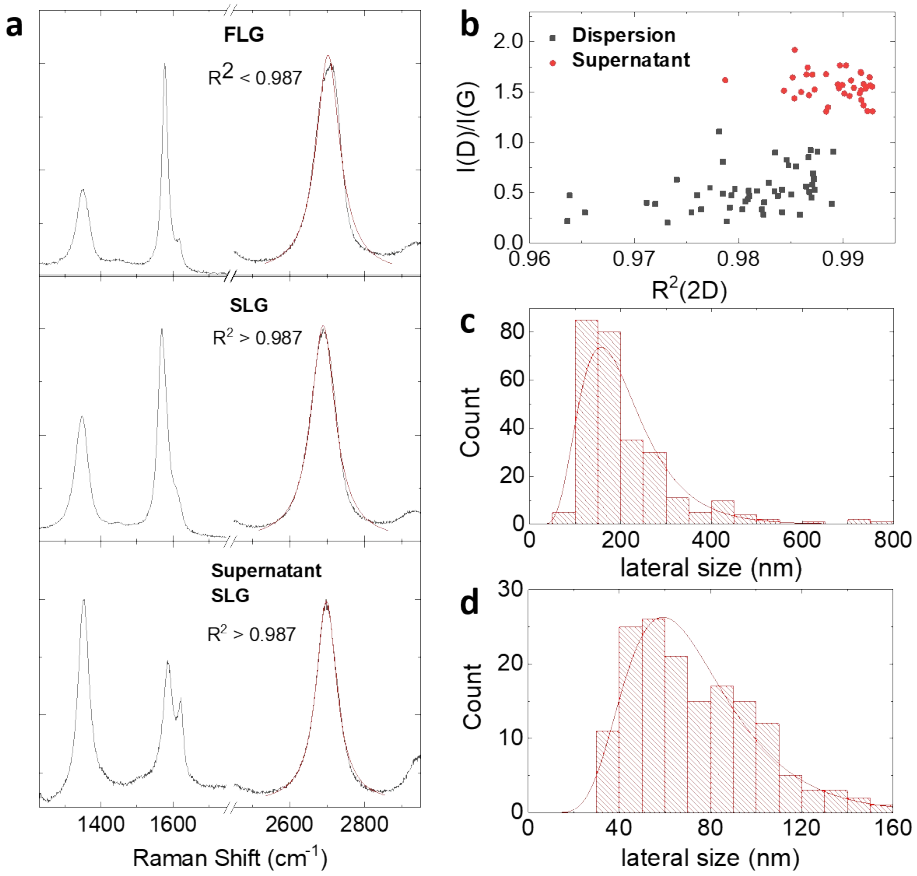

Figure 2 Characterisation of graphene dispersion prepared with BPS at 0.6 mg/mL. **(a)** Representative Raman spectra taken from the dispersion and the supernatant of BPS at 0.6 mg/mL. The fit of the 2D peak is also shown (red line) **(b)** I(D)/I(G) vs fit residual of the 2D peak plot for both dispersions and supernatant samples. **(c)** and **(d)** Lateral size distribution histograms measured by AFM for dispersion and supernatant samples, respectively.

View Article Online
DOI: 10.1039/C9FD00114J

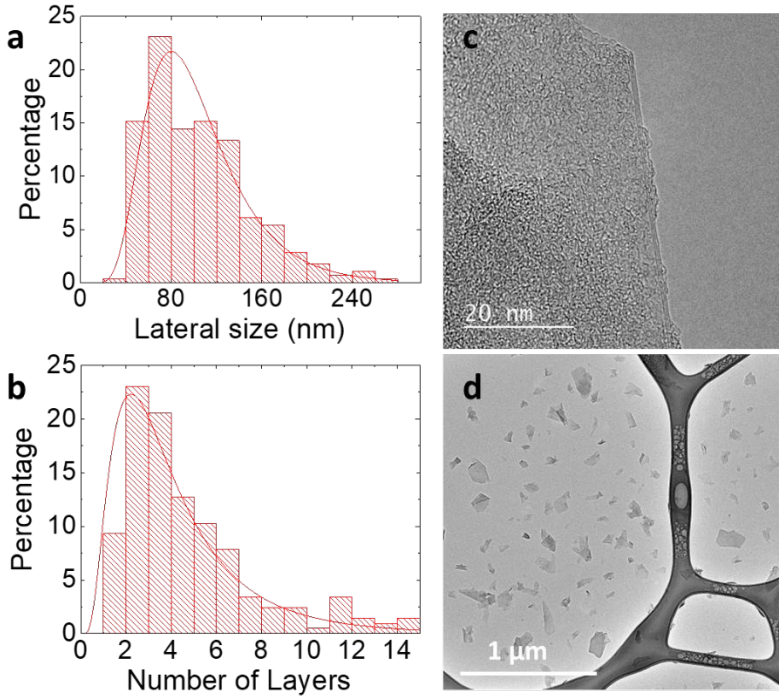

Figure 3 TEM characterisation of graphene dispersion prepared with BPS at 0.6 mg/mL: **(a)** lateral size and **(b)** thickness distribution, **(c)** HRTEM image of a three-layer-thick graphene flake and **(d)** overview TEM image of graphene flakes.

To establish a cytotoxicity profile, optical microscopy was used with BEAS-2B cell lines as an immortalised *in vitro* model for four different graphene dispersions prepared in this study: three graphene dispersions prepared with BPS (BPS at 0.2 mg/mL, BPS at 0.6 mg/mL, BPS at 1.0 mg/mL to determine the effect of BPS concentration), and one graphene dispersion prepared with MPS (MPS at 0.4 mg/mL). Cells were exposed to increasing concentrations of graphene, from 25 µg/mL to 100 µg/mL. As a control, untreated cellswere also observed (**Figure 4, top left panel**)

Figure 4 shows the optical images of the cells exposed to graphene flakes and morphological changes/cellular detachment, as indicators of cell death. **Figure 4** clearly shows that the cytotoxicity of graphene flakes increases with increasing concentration of BPS. No noticeable changes in cell morphology was observed for BPS at 0.2 mg/mL at any of graphene concentrations used. However, for BPS at 0.6 mg/mL, at 25 µg/mL the appearance of the vesicles indicated cellular stress and lysosomal swelling. Dose dependent toxic effects on the cells were also observed, as at 75 µg/mL, rounding of the cells is apparent, indicating apoptotic cell death as well as detachment of dead cells from the support. As expected, highly stressed cells were observed using BPS at 1.0 mg/mL even at the lowest concentration of 25 µg/mL

(high numbers of vesicles appearing in the cells), while cell death and detachment from the support occurred at 50 µg/mL BPS at 1.0 mg/mL.

View Article Online
DOI: 10.1039/C9FD00114J

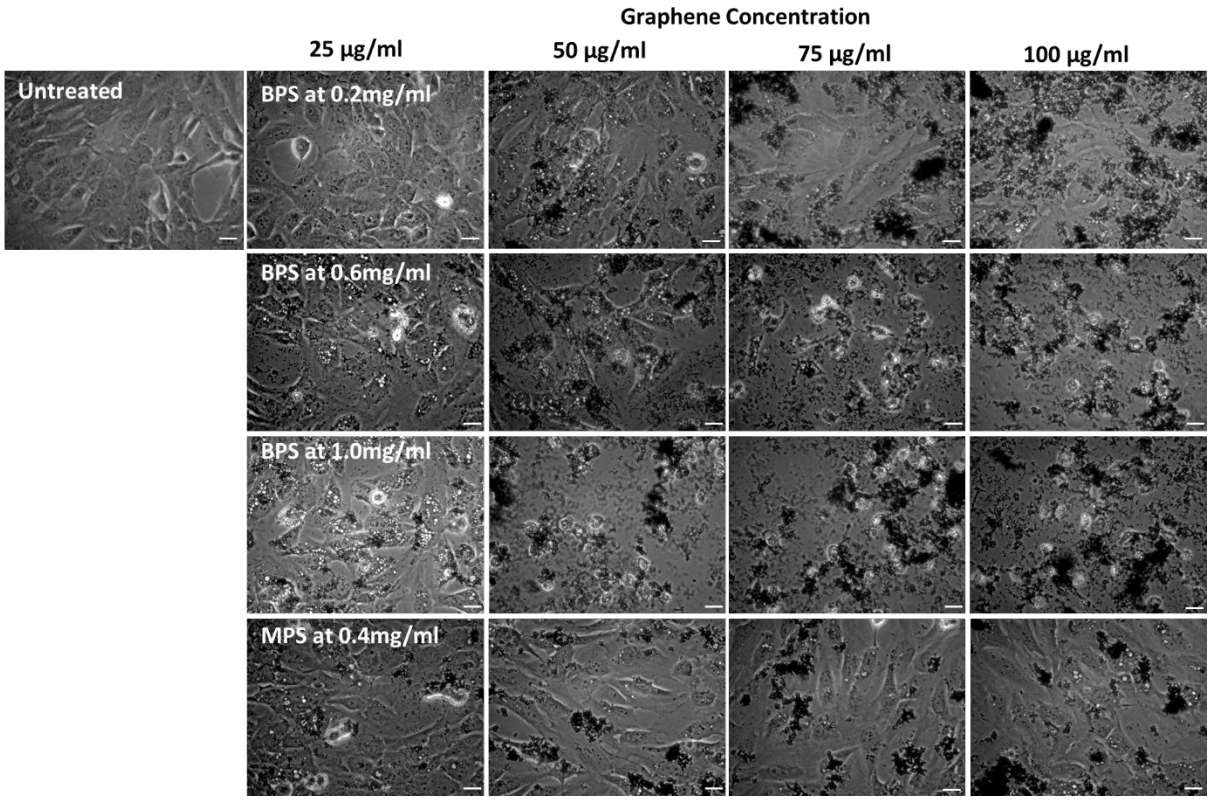

Figure 4 Optical images of BEAS-2B cells, exposed to 4 different graphene dispersions, BPS at 0.2 mg/mL, BPS at 0.6 mg/mL, BPS at 1.0 mg/mL, MPS at 0.4 mg/mL, at 4 different concentrations, 25 µg/mL, 50 µg/mL, 75 µg/mL, and 100 µg/mL. Cells were observed for morphological changes and loss of viability indicated by detachment from the support, in comparison to untreated cells. Scale bar is 10 µm.

On the other hand, cells exposed to MPS at 0.4 mg/mL showed no evident morphological changes or detachment from the support, with few vesicles appearing inside the cells, demonstrating good biocompatibility at high graphene concentration (100 µg/mL) after 24 h of treatment.

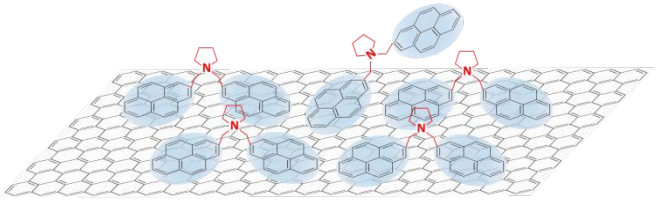

Figure 5 Possible adsorption of BPS at high concentration, giving rise to higher graphene cytotoxicity, compared to MPS.

These results clearly demonstrate the cytotoxic effect of BPS. The simplest explanation is to attribute the higher cytotoxicity to the higher number of molecules adsorbed (Figure 1b). However, it is interesting to note that BPS and MPS are characterised by the same functional group interacting with the cells, but graphene produced by MPS does not show any cytotoxicity even at high concentrations. Thus, a more complex scenario may be possible. In the case of soluble MPS, not all stabiliser is adsorbed on graphene, and the free MPS molecules in water are removed during the washing steps. In the case of the insoluble BPS, the stabiliser needs to be adsorbed on graphene. However, after a certain BPS concentration, the graphene surface could reach complete coverage. As these molecules are insoluble, they will still want to interact with graphene and therefore may accommodate on its surface by adopting a frustrated configuration, in which only one pyrene binding group is adsorbed on graphene. As the other pyrene group is now exposed to the water, this reflects in an effective increase in concentration of pyrene accessible to cells in solution at high BPS concentrations (**Figure 5**), giving rise to a higher cytotoxic effect, compared to the case of MPS molecules. However, this would not affect graphene concentration, as there are enough BPS molecules completely adsrobed on graphene, by providing electrostatic stabilization. Alternatively, the molecules may start interacting with each other, forming large aggregates on graphene, which may affect the cytotoxicity. Further study is required to fully understand the exact mechanism of the increased cytotoxicity observed with BPS molecules.

Conclusion

In summary, we have demonstrated the use of an insoluble stabiliser to achieve highly concentrated aqueous graphene dispersions, mostly containing single or few layer flakes. Although their use in biomedical applications is limited by their reduced biocompatibility, these graphene dispersions are still suitable for many applications, where water is the preferred solvent. Our work also shows that LPE of graphene can be used to disperse insoluble molecules in water, as graphene and the hydrophobic side of the molecules self- assemble together to minimize interactions with water molecules, similarly to micellization

Acknowledgements

This work was supported by the EPSRC in the framework of the project 2D Health (EP/P00119X/1). MB acknowledges financial support by the European Research Council (ERC) in the framework of the European Union's Horizon 2020 research and innovation program under the grant agreement No. 648471. MZ acknowledges the Hewlett-Packard

Company for financial support in the framework of the Graphene NowNano Doctoral Training Center.

DOI: 10.1039/C9FD00114J

Contribution statement

CC, IL, and KK conceived and supervised the project. YY and MB performed the exfoliation experiments and related data analysis. AP and XJ-B made the pyrene derivatives and performed their characterization. YC and SV performed the biological studies and related data analysis. XL and EP performed the electron microscopy measurements and related data analysis. GM performed DOSY NMR and related data analysis. MZ performed AFM measurements and related data analysis. The manuscript was written with contributions from all authors.

References

1. Novoselov, K. S. *et al.* A roadmap for graphene. *Nature* **490**, 192–200 (2012).
2. Hernandez, Y. *et al.* High-yield production of graphene by liquid-phase exfoliation of graphite. *Nat. Nanotechnol.* **3**, 563–568 (2008).
3. Nicolosi, V., Chhowalla, M., Kanatzidis, M. G., Strano, M. S. & Coleman, J. N. Liquid Exfoliation of Layered Materials. *Science.* **340**, 1226419–1226419 (2013).
4. McManus, D. *et al.* Water-based and biocompatible 2D crystal inks for all-inkjet-printed heterostructures. *Nat. Nanotechnol.* **12**, 1–19 (2017).
5. Coleman, J. N. Liquid exfoliation of defect-free graphene. *Acc. Chem. Res.* **46**, 14–22 (2013).
6. Ferrari, A. C. *et al.* Science and technology roadmap for graphene, related two-dimensional crystals, and hybrid systems. *Nanoscale* **7**, 4598–4810 (2015).
7. Ciesielski, A. & Samorì, P. Supramolecular Approaches to Graphene: From Self-Assembly to Molecule-Assisted Liquid-Phase Exfoliation. *Adv. Mater.* **28**, 6030–6051 (2016).
8. Loh, K. P., Bao, Q., Eda, G. & Chhowalla, M. Graphene oxide as a chemically tunable platform for optical applications. *Nat. Chem.* **2**, 1015–1024 (2010).
9. Lotya, M. *et al.* Liquid phase production of graphene by exfoliation of graphite in surfactant/water solutions. *J. Am. Chem. Soc.* **131**, 3611–3620 (2009).
10. Parviz, D. *et al.* Dispersions of non-covalently functionalized graphene with minimal stabilizer. *ACS Nano* **6**, 8857–8867 (2012).
11. Schlierf, A. *et al.* Nanoscale insight into the exfoliation mechanism of graphene with organic dyes: effect of charge, dipole and molecular structure. *Nanoscale* **5**, 4205 (2013).
12. Lotya, M., King, P. J., Khan, U., De, S. & Coleman, J. N. High-concentration, surfactant-stabilized graphene dispersions. *ACS Nano* **4**, 3155–3162 (2010).
13. Haar, S. *et al.* Enhancing the Liquid-Phase Exfoliation of Graphene in Organic Solvents upon Addition of n-Octylbenzene. *Sci. Rep.* **5**, 16684 (2015).
14. Hernandez, Y., Lotya, M., Rickard, D., Bergin, S. D. & Coleman, J. N. Measurement of multicomponent solubility parameters for graphene facilitates solvent discovery. *Langmuir* **26**, 3208–3213 (2010).
15. Villar-Rodil, S., Paredes, J. I., Martínez-Alonso, A. & Tascón, J. M. D. Preparation of graphene dispersions and graphene-polymer composites in organic media. *J. Mater. Chem.* **19**, 3591 (2009).
16. May, P., Khan, U., Hughes, J. M. & Coleman, J. N. Role of solubility parameters in understanding the steric stabilization of exfoliated two-dimensional nanosheets by adsorbed polymers. *J. Phys. Chem. C* **116**, 11393–11400 (2012).
17. Xu, L. *et al.* Production of high-concentration graphene dispersions in low-boiling-point organic solvents by liquid-phase noncovalent exfoliation of graphite with a hyperbranched polyethylene and formation of graphene/ethylene copolymer composites. *J. Phys. Chem. C* **117**, 10730–10742 (2013).
18. Ghosh, A., Rao, K. V., George, S. J. & Rao, C. N. R. Noncovalent Functionalization, Exfoliation, and Solubilization of Graphene in Water by Employing a Fluorescent Coronene Carboxylate. *Chem. - A Eur. J.* **16**, 2700–2704 (2010).
19. Englert, J. M. *et al.* Soluble Graphene: Generation of Aqueous Graphene Solutions Aided by a Perylenebisimide-Based Bolaamphiphile. *Adv. Mater.* **21**, 4265–4269 (2009).
20. Amiri, A., Naraghi, M., Ahmadi, G., Soleymaniha, M. & Shanbedi, M. A review on liquid-phase exfoliation for scalable production of pure graphene, wrinkled, crumpled

and functionalized graphene and challenges. *FlatChem* **8**, 40–71 (2018).
21. Yang, H. *et al.* A simple method for graphene production based on exfoliation of graphite in water using 1-pyrenesulfonic acid sodium salt. *Carbon.* **53**, 357–365 (2013).
22. Lee, D. W., Kim, T. & Lee, M. An amphiphilic pyrene sheet for selective functionalization of graphene. *Chem. Commun.* **47**, 8259–8261 (2011).
23. Zhang, M. *et al.* Production of graphene sheets by direct dispersion with aromatic healing agents. *Small* **6**, 1100–1107 (2010).
24. Yang, H. *et al.* Dielectric nanosheets made by liquid-phase exfoliation in water and their use in graphene-based electronics. *2D Mater.* **1**, 011012 (2014).
25. Heard, K. W. J. *et al.* Initial Studies Directed toward the Rational Design of Aqueous Graphene Dispersants. *ACS Omega* **4**, 1969–1981 (2019).
26. Conti, S. *et al.* Perchlorination of Coronene Enhances its Propensity for Self-Assembly on Graphene. *ChemPhysChem* **17**, 352–357 (2016).
27. Haar, S. *et al.* A supramolecular strategy to leverage the liquid-phase exfoliation of graphene in the presence of surfactants: Unraveling the role of the length of fatty acids. *Small* **11**, 1691–1702 (2015).
28. Smith, R. J., Lotya, M. & Coleman, J. N. The importance of repulsive potential barriers for the dispersion of graphene using surfactants. *New J. Phys.* **12**, (2010).
29. Shin, Y. *et al.* Charge-tunable graphene dispersions in water made with amphoteric pyrene derivatives. *Mol. Syst. Des. Eng.* (2019). doi:10.1039/C9ME00024K
30. Bonaccorso, F. *et al.* Production and processing of graphene and 2d crystals. *Mater. Today* **15**, 564–589 (2012).
31. Khan, U., O'Neill, A., Lotya, M., De, S. & Coleman, J. N. High-concentration solvent exfoliation of graphene. *Small* **6**, 864–871 (2010).
32. Hunter, R. J. *Zeta potential in colloid science : principles and applications*. *Colloid science* **2**, (Academic Press, 1981).
33. Ciesielski, A. *et al.* Harnessing the Liquid-Phase Exfoliation of Graphene Using Aliphatic Compounds: A Supramolecular Approach. *Angew. Chemie Int. Ed.* **53**, 10355–10361 (2014).
34. Shin, Y. *et al.* Synthesis and characterization of composite membranes made of graphene and polymers of intrinsic microporosity. *Carbon N. Y.* **102**, 357–366 (2016).
35. Pelta, M. D., Morris, G. A., Stchedroff, M. J. & Hammond, S. J. A one-shot sequence for high-resolution diffusion-ordered spectroscopy. *Magn. Reson. Chem.* **40**, S147–S152 (2002).
36. Johnson, C. S. Diffusion ordered nuclear magnetic resonance spectroscopy: principles and applications. *Prog. Nucl. Magn. Reson. Spectrosc.* **34**, 203–256 (1999).
37. Bichenkova, E. V *et al.* NMR detects molecular interactions of graphene with aromatic and aliphatic hydrocarbons in water. *2D Mater.* **5**, 15003 (2017).
38. Jorio, A., Saito, R., Dresselhaus, G. & Dresselhaus, M. S. *Raman Spectroscopy in Graphene Related Systems*. *Raman Spectroscopy in Graphene Related Systems* (2011). doi:10.1002/9783527632695
39. Casiraghi, C. *et al.* Raman spectroscopy of graphene edges. *Nano Lett.* **9**, 1433–1441 (2009).
40. Ferrari, A. C. *et al.* Raman spectrum of graphene and graphene layers. *Phys. Rev. Lett.* **97**, 1–4 (2006).
41. Carozo, V. *et al.* Resonance effects on the Raman spectra of graphene superlattices. *Phys. Rev. B - Condens. Matter Mater. Phys.* **88**, 1–10 (2013).
42. Paton, K. R. *et al.* Scalable production of large quantities of defect-free few-layer graphene by shear exfoliation in liquids. *Nat. Mater.* **13**, 624–630 (2014).

43. Backes, C. *et al.* Guidelines for Exfoliation, Characterization and Processing of Layered Materials Produced by Liquid Exfoliation. *Chem. Mater.* **29**, 243–255 (2017).

View Article Online
DOI: 10.1039/C9FD00114J

Supporting Information

Enhanced Liquid Phase Exfoliation of Graphene in Water Using an Insoluble Bis-Pyrene Stabiliser

Yuyoung Shin[1], Xavier Just-Baringo[1], Matthew Boyes[1], Adyasha Panigrahi[1], Marco Zarattini[1], Yingxian Chen[2], Xinyun Liu[3], Gareth Morris,[1] Eric Prestat[3,4], Kostas Kostarelos[2], Sandra Vranic[2], Igor Larrosa*[1], Cinzia Casiraghi*[1]

[1]*Department of Chemistry, University of Manchester, Oxford Road, Manchester, M13 9PL*
2Nanomedicine Lab, National Graphene Institute and Faculty of Biology, Medicine & Health, AV Hill Building, University of Manchester, Manchester, M13 9PT
[3]*Department of Materials, University of Manchester, Oxford Road, Manchester, M13 9PL*
[4]*SuperSTEM Laboratory, SciTech Daresbury Campus, Daresbury, WA4 4AD, UK*

Table of Contents

S1. Synthesis and Characterisation of Pyrene-Based Stabilisers

S1.1. General Information

THF was dried using a PureSolv solvent purification system. All other solvents and reagents used were purchased from commercial suppliers and used without further purification. ^{1}H-NMR spectra were obtained at room temperature on a Bruker 400 MHz or 500 MHz spectrometer. ^{13}C-NMR spectra were obtained at 100 or 125 MHz, respectively. All NMR spectra were processed using *MestReNova* NMR software. Chemical shifts are reported in parts per million (ppm) and coupling constants (*J*) reported in Hz. Splitting patterns are reported as follows: singlet (s), doublet (d), triplet (t), quadruplet (q), quintet (quint). Infra-red spectra were recorded as evaporated films or neat using FT/IR spectrometers. Melting points were measured on solids as obtained after chromatography. Mass spectra were obtained using positive or negative electrospray (ESI), atmospheric pressure chemical ionization (APCI) or atmospheric solids analysis probe (ASAP).

S1.2. Aqueous solubility determination

To a vial charged with **BPS** and fitted with a stirring bar was added D_2O (0.5 mL) prior to sealing it under air. The resulting suspension was sonicated for ten minutes and then stirred at room temperature for 72 h. The suspension was allowed to settle and the supernatant was filtered through cotton. The concentration of the saturated solution was determined by ^{1}H-NMR using nitromethane as an internal standard. The solubility of pyrene-based stabilisers **BPS** and **LBPS** in water was below the limit of detection while the solubility of 1-methyl-1-(pyren-1-ylmethyl)pyrrolidinium bromide **MPS** was found to be 11.4 mg/mL.

S1.3. Synthesis and Characterization

S1.3.1 Spectroscopic and Analytical Data

N-(1-Pyrenylmethyl)pyrrolidine (3ab)

To a vial charged with a stirring suspension of 1-bromomethylpyrene[1] (3.50 g, 11.9 mmol) in dry hexane (12.0 mL) at 0 ˚C was added pyrrolidine (4.0 mL, 47.4 mmol). The stirring mixture was allowed to warm to room temperature and after 21 h the precipitate was filtered under vacuum, dissolved in CH_2Cl_2 (50 mL) and washed with saturated aqueous $NaHCO_3$. The aqueous layer was extracted with CH_2Cl_2 (2 × 50 mL) and the combined organic fractions were dried ($MgSO_4$) and concentrated under vacuum. The title product was obtained as an off-white solid (2.83 g, 84%), **mp**: 97 – 100 ºC. **^{1}H-NMR** (400 MHz, $CDCl_3$) δ 8.51 (d, *J* = 9.2 Hz, 1 H), 8.24 - 8.12 (m, 4 H), 8.11 - 8.04 (m, 3 H), 8.01 (t, *J* = 7.6 Hz, 1 H), 4.42 (bs, 2 H), 2.73 (bs, 4 H), 1.85 (bs, 4 H); **^{13}C-NMR** (125 MHz, $CDCl_3$) δ 133.4, 131.3, 130.9, 130.5, 129.5, 127.6, 127.4, 127.2, 126.9, 125.8, 124.9 (2C), 124.9, 124.8, 124.5, 123.9, 58.4, 54.4, 23.6; **IR** ν_{max} (neat/cm^{-1}): 2922, 2797, 1456, 1344, 1113, 848; **HRMS** calcd for $C_{21}H_{20}N$ $[M+H]^+$: 286.1590, found 286.1578.

1-(3-(Pyren-1-yl)propyl)pyrrolidine (3bb)

To a vial charged with a stirring suspension of 1-(1-pyrenyl)-3-bromopropane[1] (400 mg, 1.24 mmol) in dry hexane (1.20 mL) at 0 ˚C was added pyrrolidine (413 μL, 4.95 mmol). The mixture was stirred at 50 ºC. After 18 h the crude was cooled down to room temperature and dissolved in CH_2Cl_2 (50 mL) and washed with saturated aqueous $NaHCO_3$. The aqueous layer was extracted with CH_2Cl_2 (2 × 50 mL) and the combined organic fractions were dried ($MgSO_4$) and concentrated under vacuum. The title product was obtained as an orange oil (389 mg, >99%), **^{1}H-NMR** (500 MHz, $CDCl_3$) δ δ 8.31 (d, *J* = 9.2 Hz, 1H), 8.16 (dd, *J* = 7.7, 4.6 Hz, 2H), 8.10 (t, *J* = 8.0 Hz, 2H), 8.04 - 7.97 (m, 3H), 7.89 (d, *J* = 7.6 Hz, 1H), 3.40 (t, *J* = 7.8 Hz, 2H), 2.62 (t, *J* = 7.6 Hz, 2H), 2.53 (bs, 4H), 2.10 (quint, *J* = 7.8 Hz, 2H), 1.80 (bs, 4H).; **^{13}C-NMR** (125 MHz, $CDCl_3$) δ 136.8, 131.6, 131.1, 129.9, 128.8, 127.6, 127.3, 127.3, 126.7, 125.9, 125.2, 125.1, 124.9 (2C), 124.8, 123.6, 56.4, 54.4, 31.6, 31.3, 23.6.; **IR** ν_{max} (neat/cm^{-1}): 2937, 904, 846, 723; **HRMS** calcd for $C_{23}H_{24}N$ $[M+H]^+$: 314.1908, found 314.1889.

1-Methyl-1-(pyren-1-ylmethyl)pyrrolidinium bromide (MPS)

A solution of 1-bromomethylpyrene[2] **1a** (148 mg, 0.5 mmol) and *N*-methylpyrrolidine **2a** (53 μL, 0.5 mmol) in THF (1.3 mL) was stirred in a vial sealed under air at 60 ˚C. After 18 h the mixture was allowed to cool to room temperature and the precipitate was filtered under vacuum, washed with THF and then Et_2O. The title product was obtained as a white solid (190 mg, >99%), **mp**: decomposes above 200 ºC. **^{1}H-NMR** (500 MHz, MeOD-d_4) δ 8.58 (d, *J* = 9.2 Hz, 1H), 8.34 - 8.31 (m, 4H), 8.24 (d, *J* = 8.5 Hz, 2H), 8.16 (d, *J* = 8.8 Hz, 1H), 8.12 (t, *J* = 7.6 Hz, 1H), 5.40 (s, 2H), 3.86 - 3.81 (m, 2H), 3.62 - 3.58 (m, 2H), 3.07 (s, 3H), 2.31 - 2.25 (m, 4H); **^{13}C-NMR** (126 MHz, MeOD-d_4) δ 134.6, 133.0, 132.6, 132.5, 131.7, 130.7, 130.3, 128.2, 127.8, 127.6, 127.3, 126.1, 126.0, 125.4, 123.5, 122.5, 68.8, 64.4, 26.5, 22.0; **IR** ν_{max}

(neat/cm^{-1}): 2972, 1587, 1460, 1404, 1240, 1177, 1058, 919; **HRMS** calcd for $C_{22}H_{22}N$ $[M]^+$: 300.1746, found 300.1733.

N,*N*-Di(1-pyrenylmethyl)pyrrolidinium bromide (pyrene tweezer-1) (BPS)

A solution of 1-bromomethylpyrene[1] (432 mg, 1.46 mmol) and 1-(pyren-1-ylmethyl)pyrrolidine **3ab** (418 mg, 1.46 mmol) in THF (4.3 mL) was stirred in a vial sealed under air at 60 ˚C. After 18 h the mixture was allowed to cool to room temperature and the precipitate was filtered under vacuum, washed with THF and then Et_2O. The title product was obtained as an off-white solid (759 mg, 90%), **mp**: decomposes above 165 ºC. **^{1}H-NMR** (500 MHz, MeOD-d_4) δ 8.37 - 8.33 (m, 6 H), 8.31 - 8.14 (m, 10 H), 8.10 (t, *J* = 7.8 Hz, 2 H), 5.55 (s, 4 H), 3.79 (bs, 4 H),2.17 (bs, 4 H); ^{13}C-NMR (125 MHz, MeOD-d_4) δ 134.8, 133.5, 133.2, 132.6, 131.6, 131.0, 130.5, 128.2, 127.9, 127.8, 127.4, 126.2, 126.1, 125.4, 123.0, 121.7, 61.7, 59.6, 21.9,; **IR** ν_{max} (neat/cm^{-1}): 2964, 1462, 1351, 1235, 1186, 1064, 853; **HRMS** calcd for $C_{38}H_{30}N$ $[M]^+$: 500.2373, found 500.2357.

1,1-Bis(3-(pyren-2-yl)propyl)pyrrolidin-1-ium bromide (pyrene tweezer-2) (LBPS)

A solution of 1-(1-pyrenyl)-3-bromopropane[2] (368 mg, 1.14 mmol) and 1-(3-(pyren-1-yl)propyl)pyrrolidine **3bb** (382 mg, 1.22 mmol) in THF (3.4 mL) was stirred in a vial sealed under air at 60 ˚C. After 18 h the mixture was allowed to cool to room temperature and the precipitate was filtered under vacuum, washed with THF and then Et_2O. The title product was obtained as an off-white solid (198 mg, 27%), **mp**: 235 ºC. **^{1}H-NMR** (500 MHz, MeOD-d_4) δ 8.17 - 8.14 (m, 4H), 8.09 (d, *J* = 7.7 Hz, 2H), 8.00 - 7.94 (m, 6H), 7.89 (d, *J* = 8.9 Hz, 2H), 7.79 (d, *J* = 7.8 Hz, 2H), 7.54 (d, *J* = 7.8 Hz, 2H), 3.50 (t, *J* = 7.2 Hz, 4H), 3.39 - 3.34 (m, 4H), 3.24 (t, *J* = 7.4 Hz, 4H), 2.15 (bs, 4H), 2.04 - 1.96 (m, 4H); **^{13}C-NMR** (125 MHz, DMSO-d_6) δ 134.8, 130.9, 130.3, 129.5, 128.1, 127.5, 127.4, 127.3, 126.7, 126.2, 125.1, 124.9, 124.9, 124.2, 124.1, 123.2, 62.54, 58.4, 29.0, 25.0, 21.5; **IR** ν_{max} (neat/cm^{-1}): 3419, 3044, 2941, 1602, 1586, 1461, 1184, 1085 862; **HRMS** calcd for $C_{42}H_{38}N$ $[M]^+$: 556.2998, found 556.2981.

S1.3.2 NMR Spectra

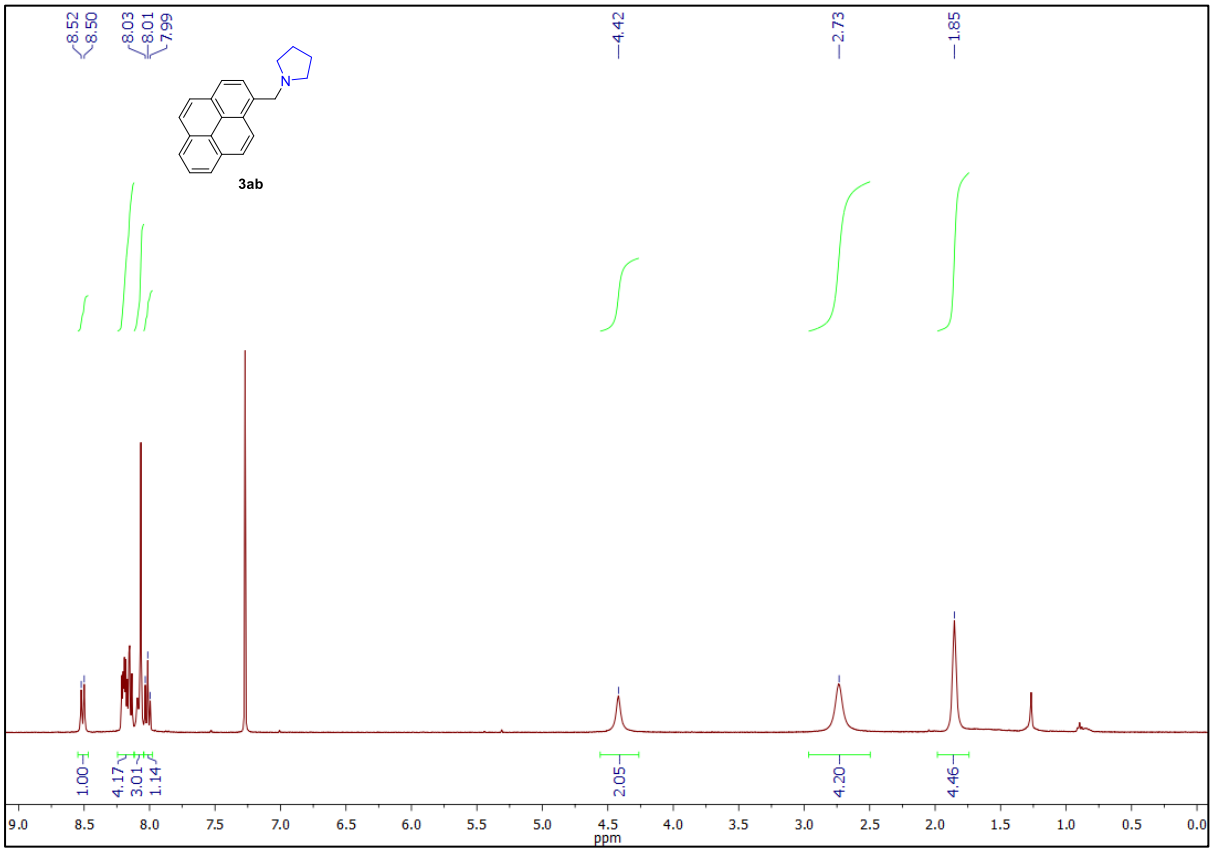

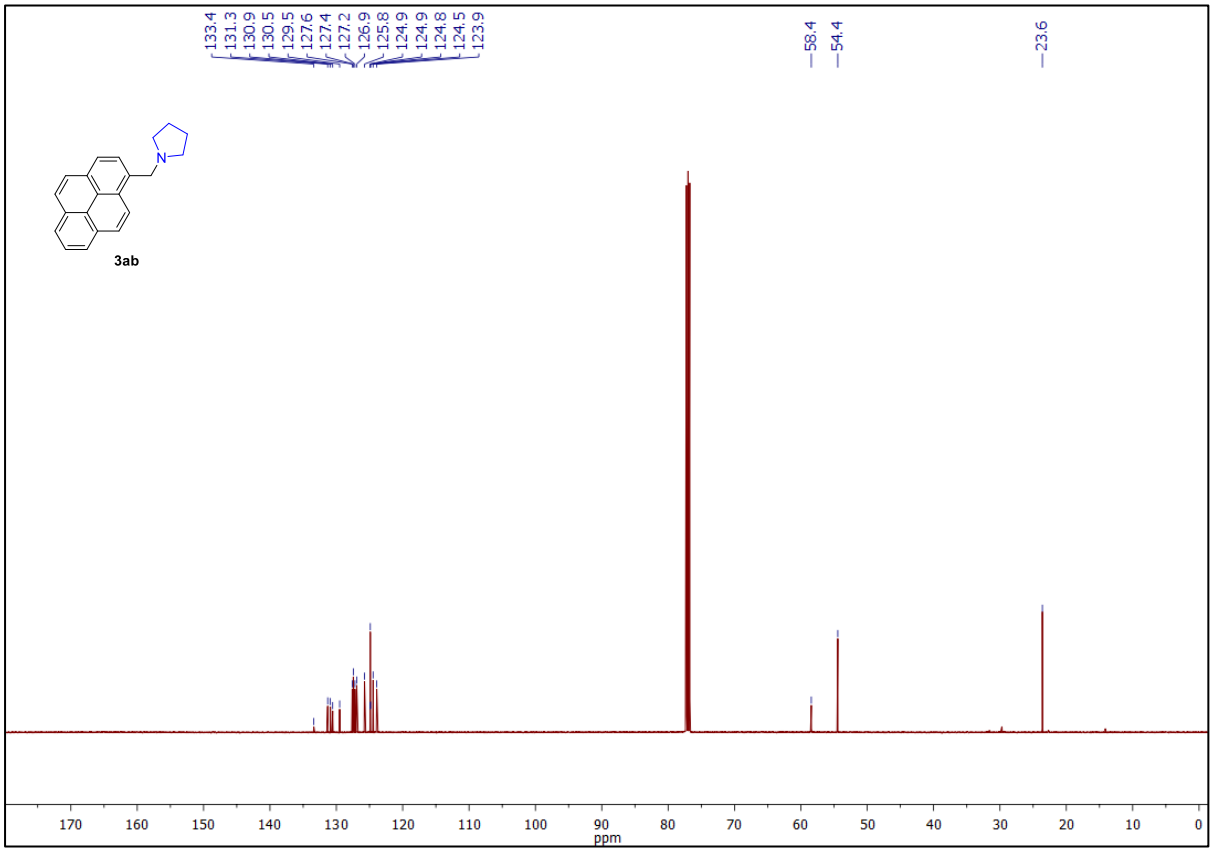

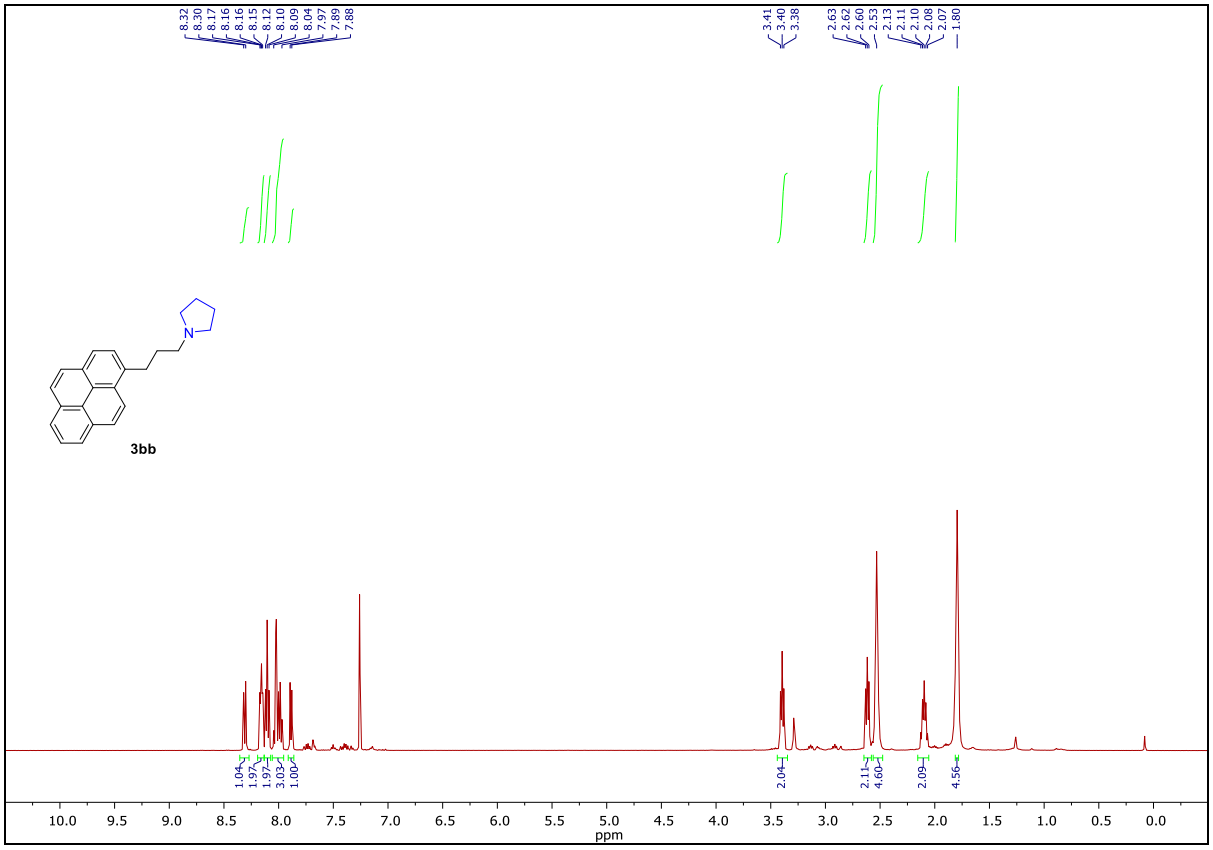
8.32
8.30
8.17
8.16
8.16
8.15
8.12
8.10
8.09
8.04
7.97
7.89
7.88
3.41
3.40
3.38
2.63
2.62
2.60
2.53
2.13
2.11
2.10
2.08
2.07
1.80
3bb
1.04
1.97
1.97
3.03
1.00
2.04
2.11
4.60
2.09
4.56
10.0 9.5 9.0 8.5 8.0 7.5 7.0 6.5 6.0 5.5 5.0 4.5 4.0 3.5 3.0 2.5 2.0 1.5 1.0 0.5 0.0
ppm

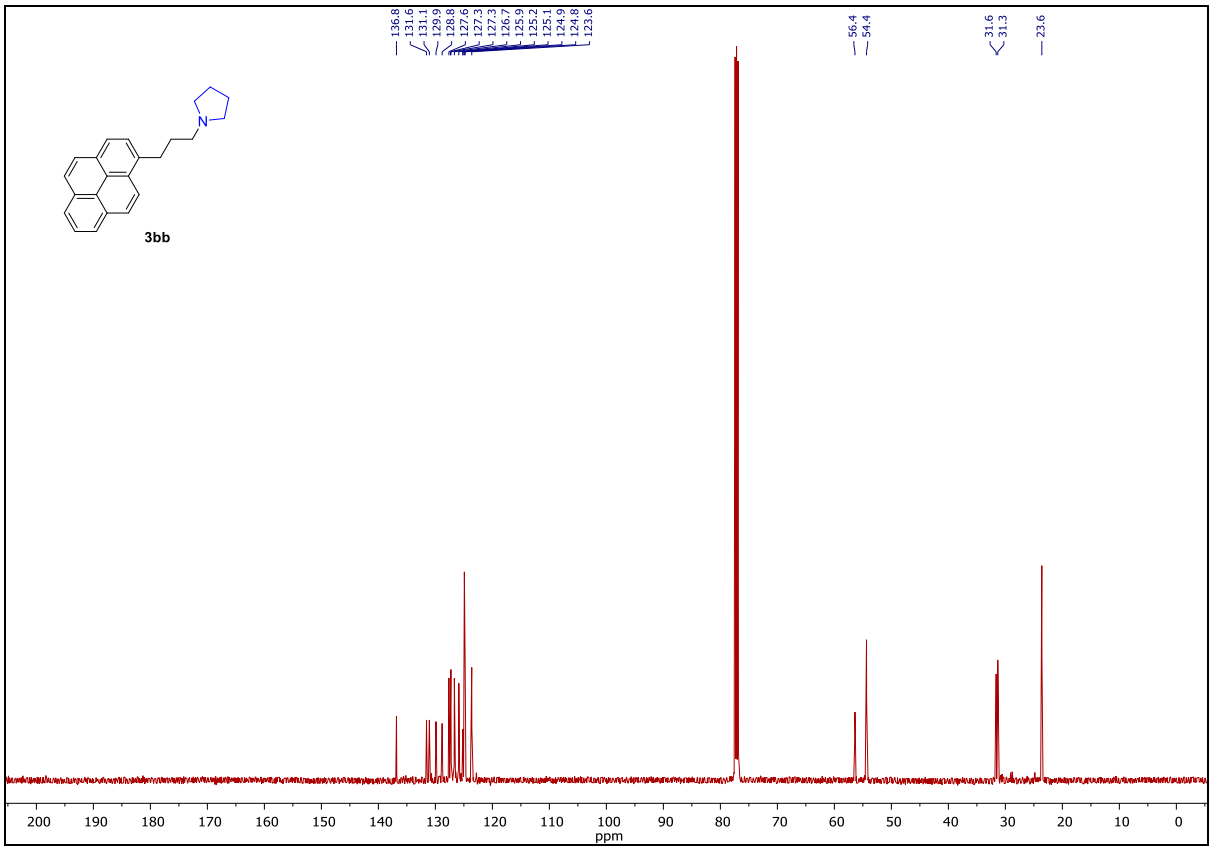
136.8
131.6
131.1
129.9
128.8
127.6
127.3
127.3
126.7
125.9
125.2
125.1
124.9
124.8
123.6
56.4
54.4
31.6
31.3
23.6
3bb
200 190 180 170 160 150 140 130 120 110 100 90 80 70 60 50 40 30 20 10 0
ppm

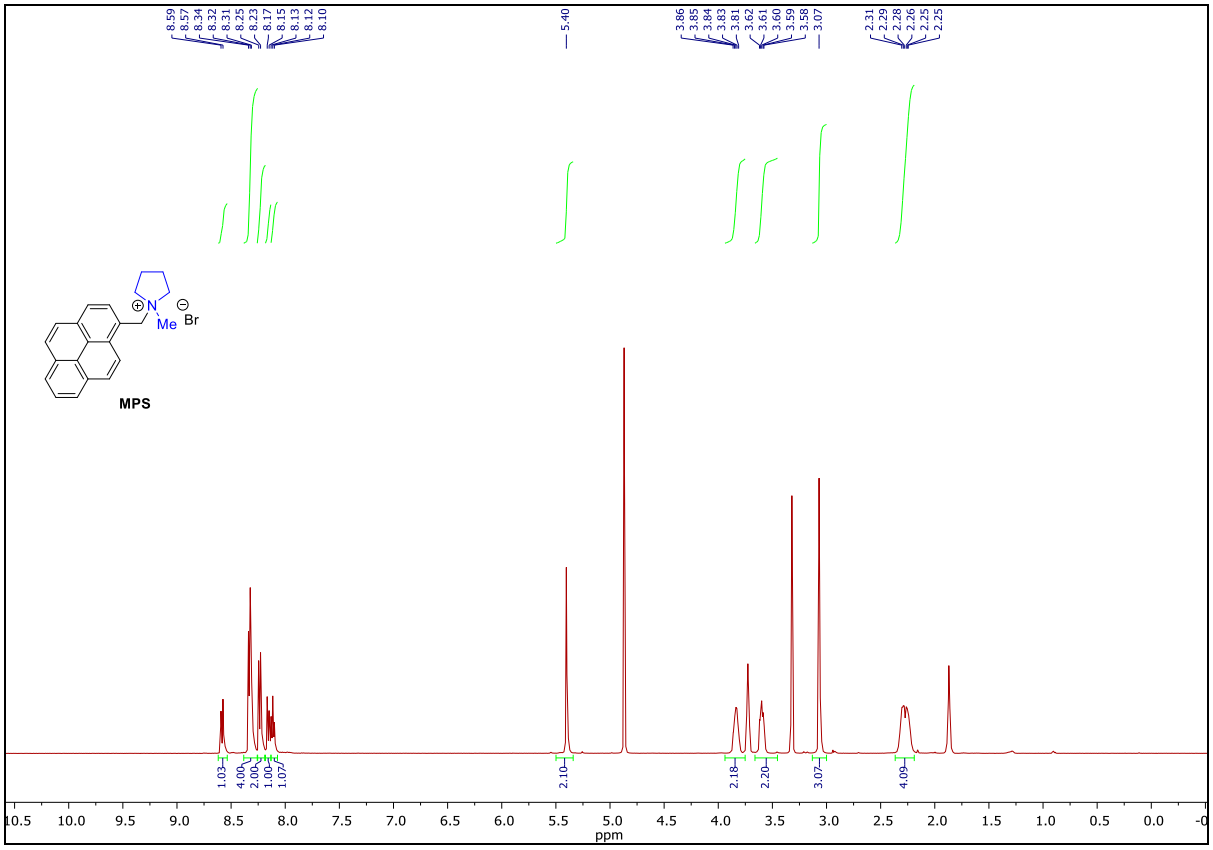
MPS
ppm

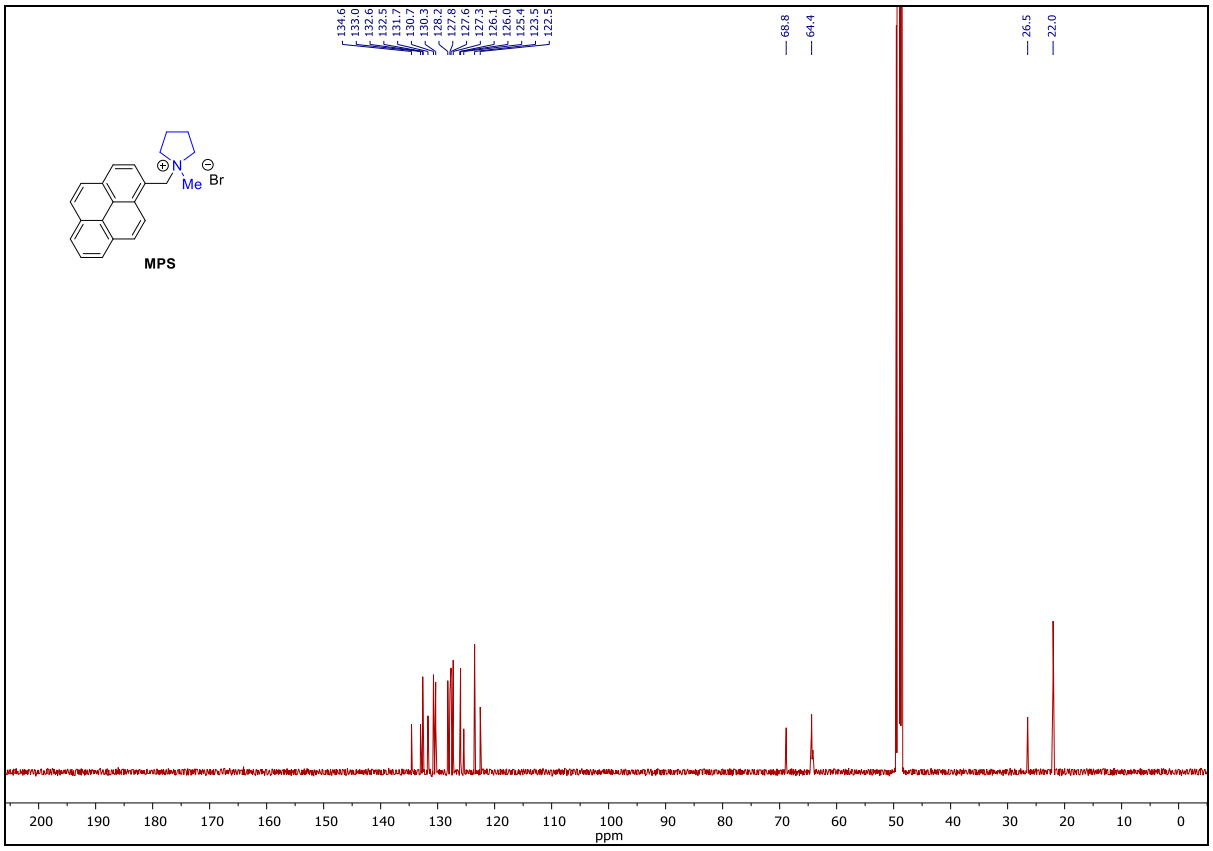
MPS
ppm

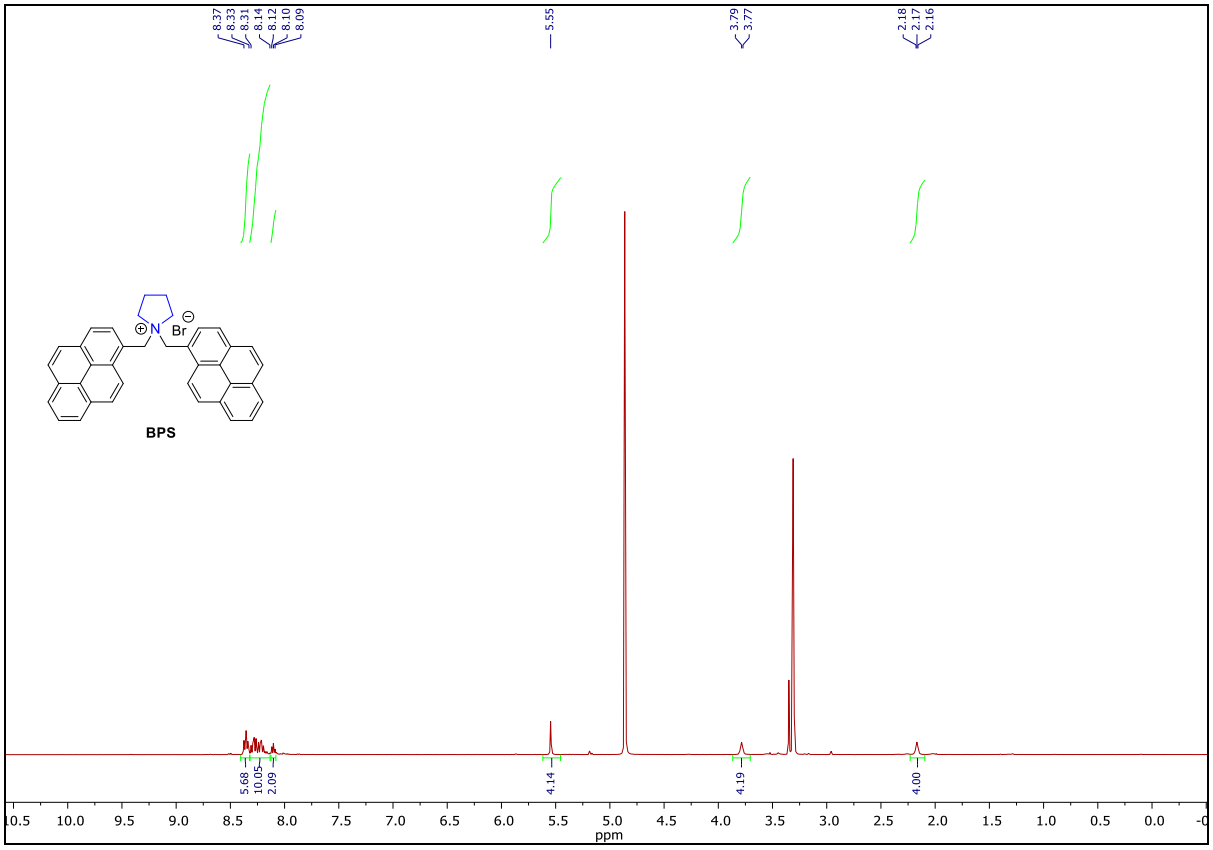
8.37
8.33
8.31
8.14
8.12
8.10
8.09
5.55
3.79
3.77
2.18
2.17
2.16
Br
BPS
5.68
10.05
2.09
4.14
4.19
4.00
ppm

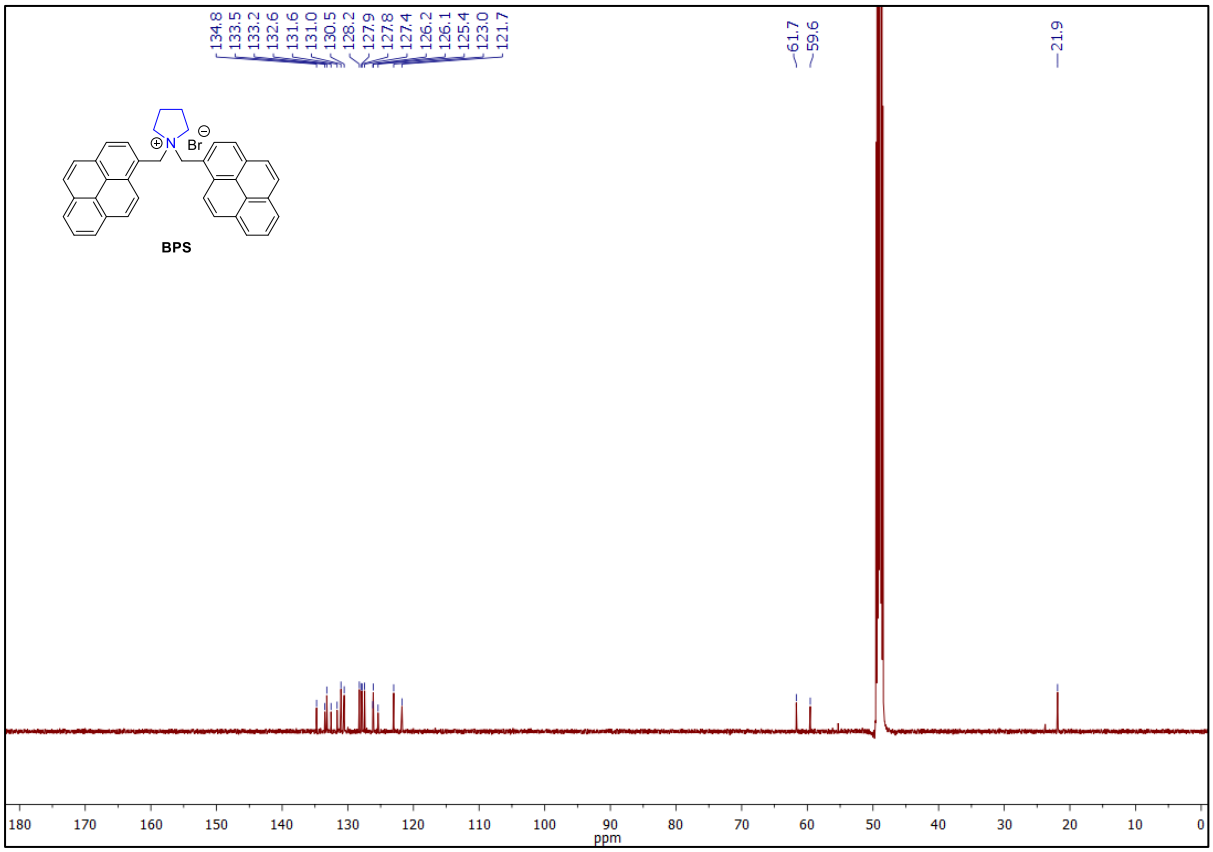
134.8
133.5
133.2
132.6
131.6
131.0
130.5
128.2
127.9
127.8
127.4
126.2
126.1
125.4
123.0
121.7
61.7
59.6
21.9
Br
BPS
ppm

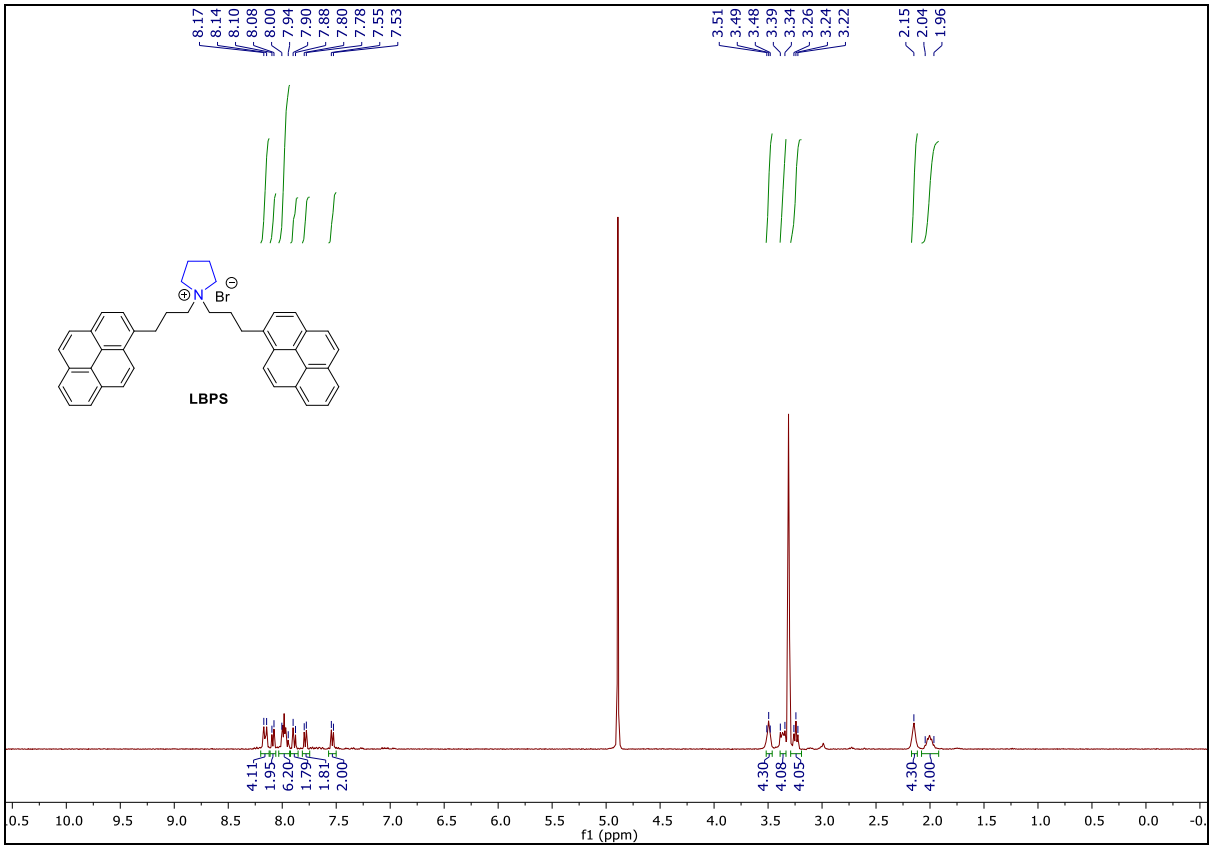
8.17
8.14
8.10
8.08
8.00
7.94
7.90
7.88
7.80
7.78
7.55
7.53
3.51
3.49
3.48
3.39
3.34
3.26
3.24
3.22
2.15
2.04
1.96
Br
LBPS
4.11
1.95
6.20
1.79
1.81
2.00
4.30
4.08
4.05
4.30
4.00
f1 (ppm)

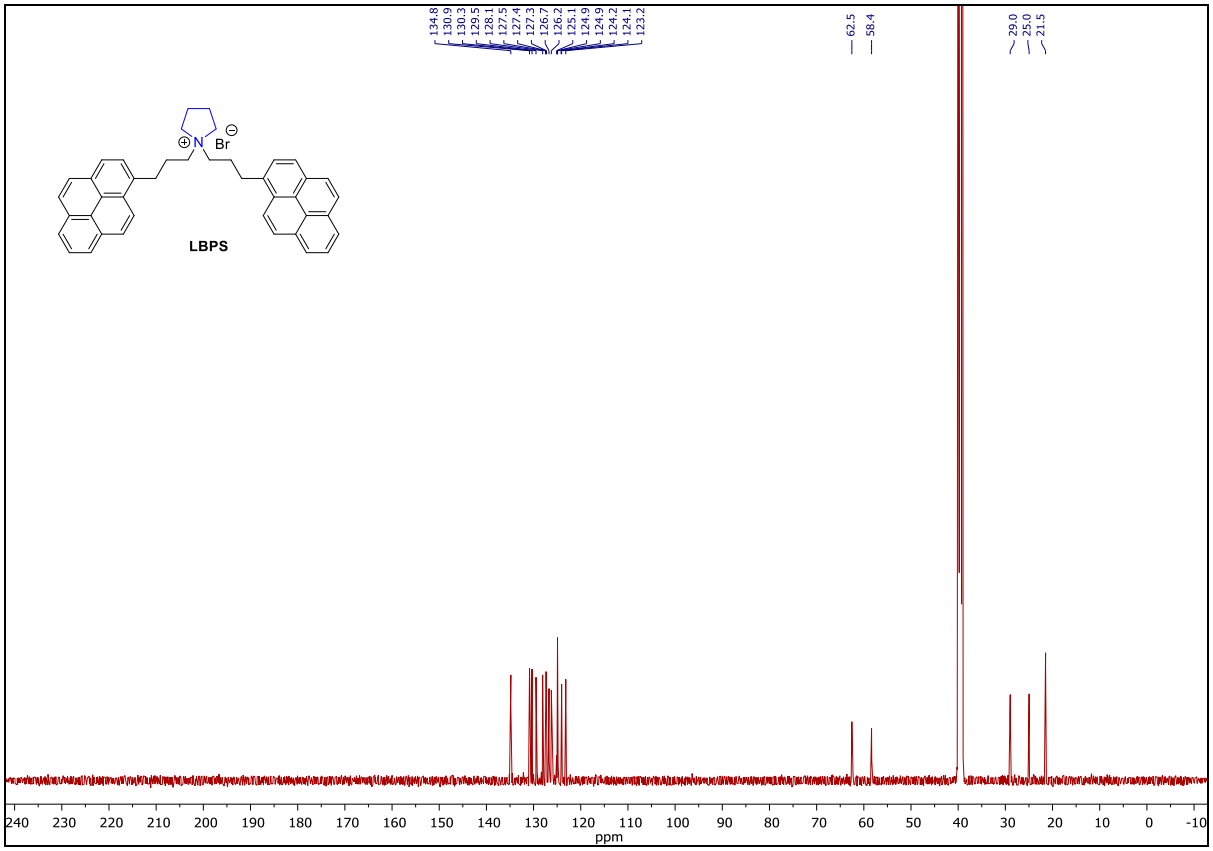
134.8
130.9
130.3
129.5
128.1
127.5
127.4
127.3
126.7
126.2
125.1
124.9
124.9
124.2
124.1
123.2
62.5
58.4
29.0
25.0
21.5
Br
LBPS
ppm

S2. Characterisation of Graphene Dispersions

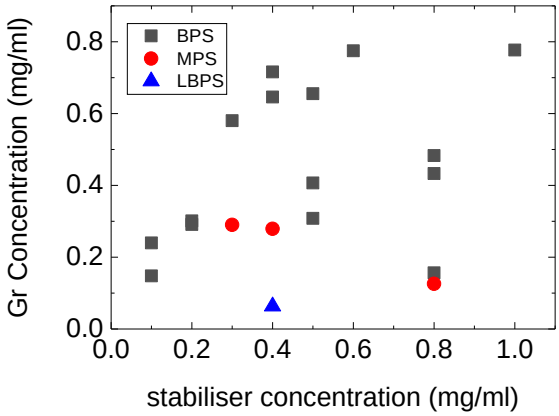

Figure S1 Graphene concentrations obtained for different graphene dispersions.

Due to the nature of bath sonication, there is batch to batch variance of exfoliation efficiency observed for LPE graphene dispersions. However, despite the varying final concentration of graphene dispersions prepared, there is a trend of increasing final graphene dispsersion concentration observed with increasing initial BPS concentration.

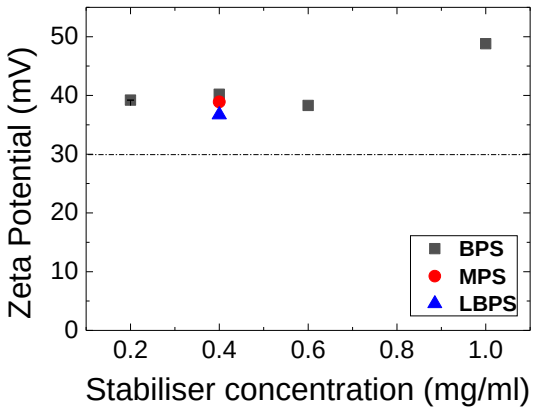

Figure S2 Zeta Potential measured for the graphene dispersions. A guidance line at 30 mV was added to show stability of the dispersions.

The colloidal stability of the produced graphene dispersions was studied by measuring zeta potential. All the graphene dispersions prepared with the pyrene stabilisers in this study shows zeta potential values higher than 30 mV, demonstrating their excellent colloidal stability.

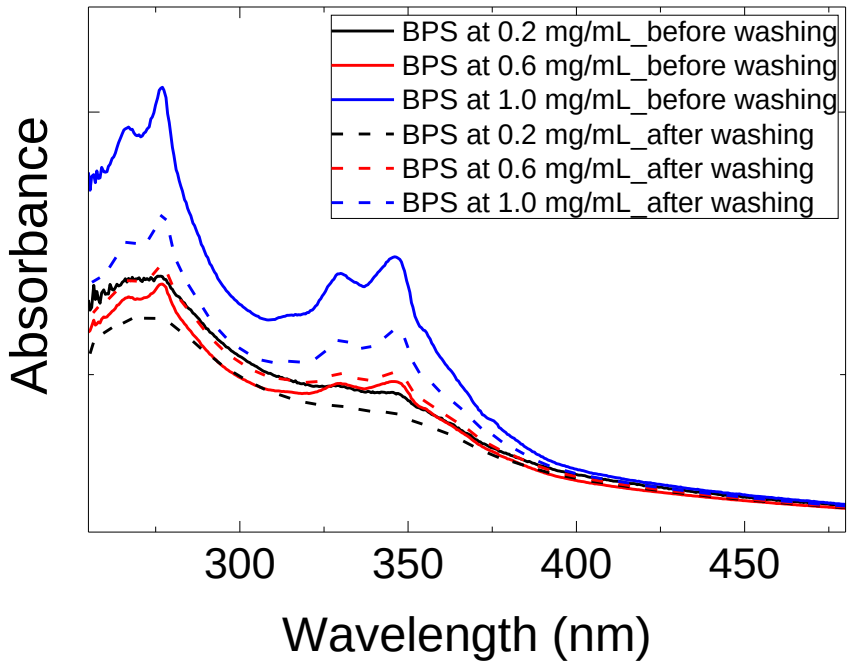

Figure S3 UV-vis spectra of graphene dispersions prepared with BPS stabilisers at different concentrations, before and after washing step.

Because of the insolubility of the BPS molecules in water, washing step using centrifugation, exchanging supernatant solution with DI water does not change the concentration of pyrene present in the final graphene solution even after the washing step. In case of MPS, which is soluble in water, the pyrene peaks observed below 400 nm are significantly reduced after the washing step.

S3. Wide ^{1}H spectrum

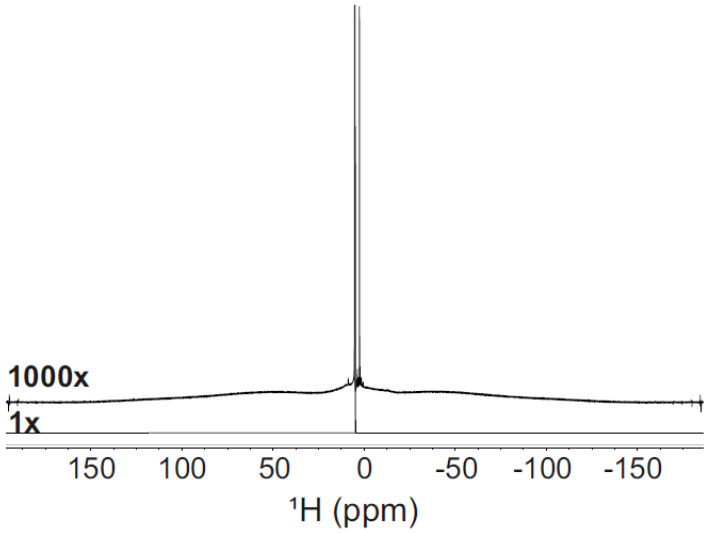

Figure S4 Wide ^{1}H spectrum of a graphene dispersion, of concentration 0.8 mg/mL, with BPS at 0.6 mg/mL in D_2O at 1x and 1000x zoom.

This wide ^{1}H spectrum was acquired in 4.3 h using 19° pulses, a spectral width of 192.3 kHz, 256000 complex data points, and a recycle time of 0.77 s. It confirms that most of the proton signal intensity seen in the standard ^{1}H and DOSY spectra (main text, **Figure 1(c)** and **(d)**, respectively) comes from very broad signals.

S4. AFM Analysis

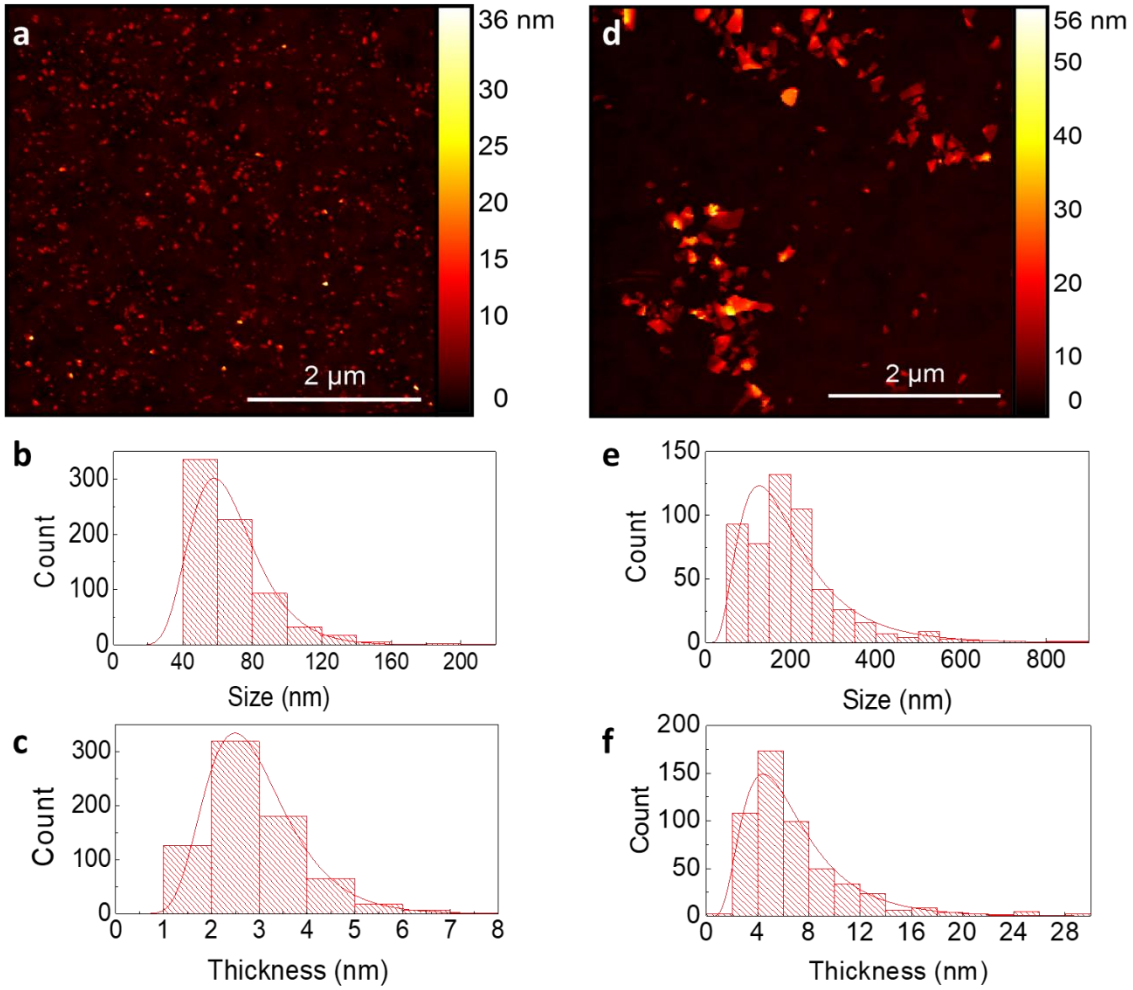

Figure S5 AFM analysis of graphene nanosheets for sample with BPS at 0.4 mg/mL. **(a)** AFM image, **(b)** lateral size and **(c)** thickness distribution for supernatant and **(d)** AFM image, **(e)** lateral size and **(f)** thickness distribution for the dispersion.

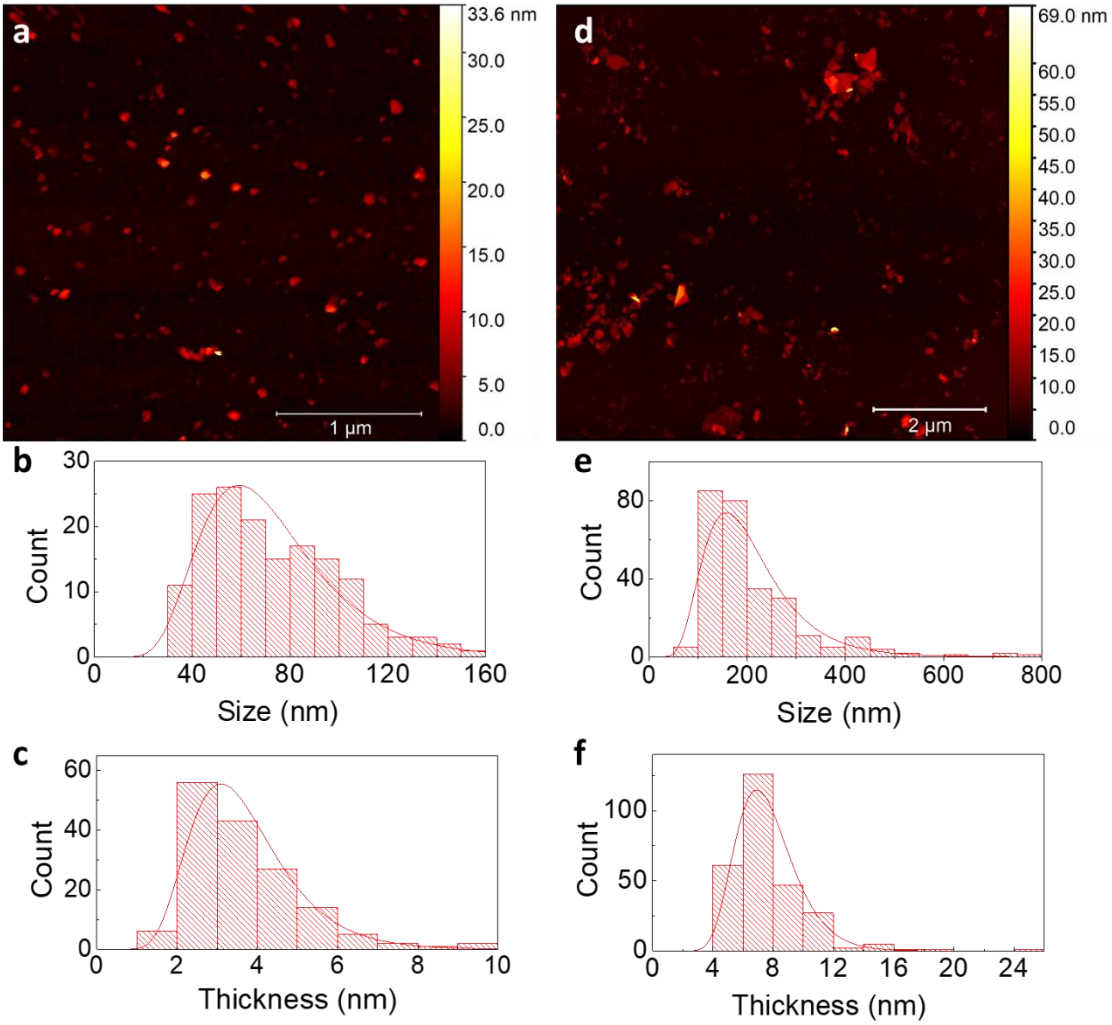

Figure S6 AFM analysis of graphene nanosheets for sample with BPS at 0.6 mg/mL. **(a)** AFM image, **(b)** lateral size and **(c)** thickness distribution for supernatant and **(d)** AFM image, **(e)** lateral size and **(f)** thickness distribution for the dispersion.

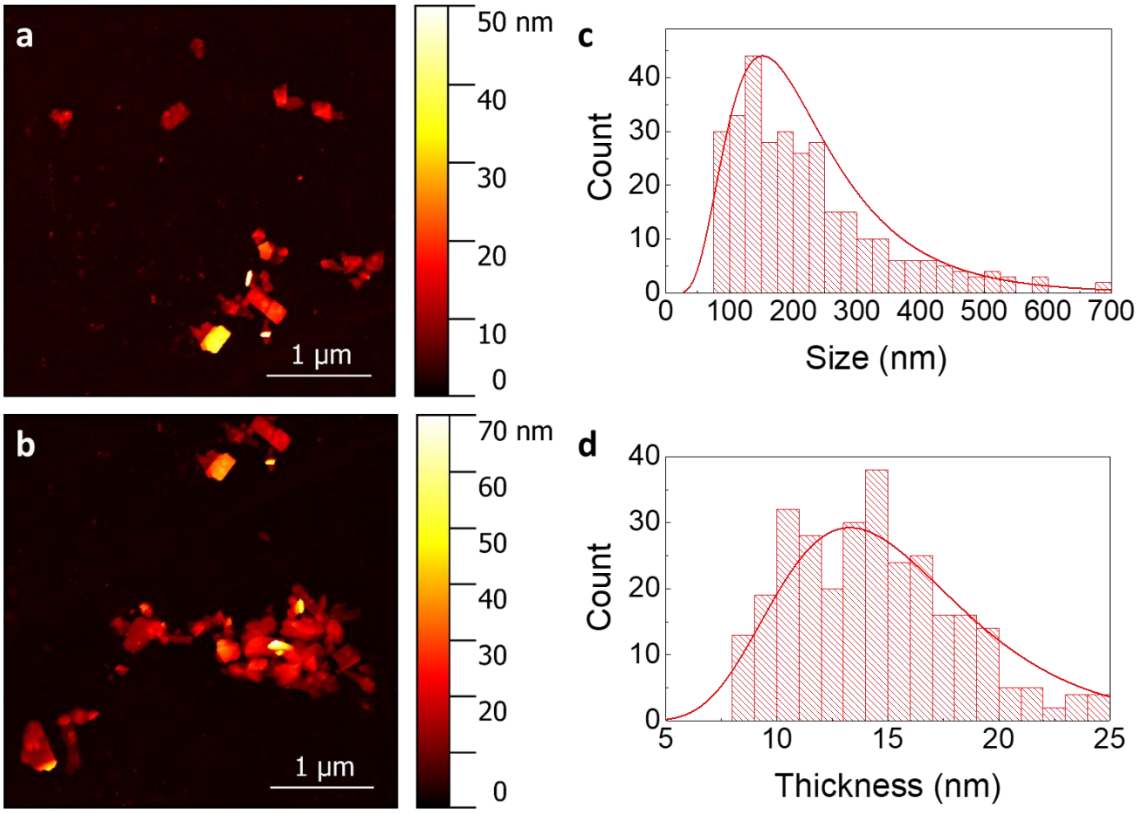

Figure S7 AFM analysis of graphene nanosheets for sample with MPS at 0.4 mg/mL. **(a-b)** AFM images, **(c)** lateral size and **(d)** thickness distribution for the dispersion.

AFM is one of the most popular method for characterisation of the lateral size and thickness distribution of the exfoliated graphene nanosheets. For statistical analysis, AFM images of large area (typically between 25 and 100 μm^2 size) with more than two hundreds of individual flakes were used, or in some cases, several images were used together. Only individual flakes were counted towards statistics and aggregated nanosheets were excluded. The AFM sample is prepared by drop casting dilute (conc. = ~5 μg/mL) graphene dispersion on clean silicon wafer. The distribution histograms for each samples are shown together in each figures (**Figure S4 – S6**).

References

1. Nishimura, T. *et al.* A simple visual sensor with the potential for determining the concentration of fluoride in water at environmentally significant levels. *Chem. Commun.* **49**, 478–480 (2013).

2. Moon, S. J., Park, S. H., Jaworski, J. & Jung, J. H. Pyrene-imidazolium complexed graphene for the selective fluorescent detection of G-quadruplex forming DNA. *Chem. Commun.* **49**, 11698–11700 (2013).

Part III: Conclusions and Future Work

Chapter 8: Conclusions

In this project, an investigation on the crystallisation of glycine molecules from microdroplet solutions with graphene templates and from acoustic levitation was conducted. As well as this, the unusual evaporation behaviour of graphene dispersions was observed, and a novel insoluble stabiliser was used to successfully exfoliate graphene in water. The main results of the experimental findings are summarised as follows:

Chapter 4 investigated the heterogenous nucleation of glycine *via* the use of graphene templates. Using various graphene-based templates ranging from pristine CVD graphene to highly oxidised GO, allowed us to gain insights into the intermolecular interactions between glycine and graphene that promoted a selective polymorphic outcome. Raman spectroscopy was employed to investigate the polymorphism at the contact region of the crystallising droplet, revealing that graphene, either used as a substrate or as an additive, suppresses the formation of the least stable β-form and selectively promoting the α-form. This selectivity was more pronounced for the additive-templated crystallisation experiments, where there was close to complete suppression of the β-form. The use of different graphene types that had varying oxygen content, as well as complementary computer modelling, attributed the selectivity of the α-form to the presence of the oxygen-containing functional groups on the graphene surface, which facilitated the greater stabilisation of the α-form compared to the β-form. It was observed during this study that there exists an optimal oxygen content of the graphene to achieve selectivity. Polymorph selectivity was only found to happen when ECE graphene was used, which has been characterised to have ~15 wt% oxygen. When CVD graphene was used, no templating effect was observed. Conversely, when GO was used, dendritic crystallisation and undesired incorporation of the GO into the crystals occurred which originated from the hydrophilic nature of GO. Consequently, this work suggests that an additive-driven crystal engineering pathway employing *ad hoc* designed graphene additives of tuned surface properties could be exploited for polymorph selectivity.

Chapter 5 shows the results obtained from the acoustic levitation of graphene dispersions. It was observed that certain experiment conditions led to the formation of a liquid marble, with a graphene shell preventing the evaporation of the liquid core. The concentration of graphene and the initial solvent composition appeared to play a vital role in the drying dynamics of the graphene droplets. When the initial volume ratio of water-to-IPA was not 1:1, the graphene

droplets evaporated the same as the graphene-free solvent systems, independent of the concentration of graphene. However, when the initial ratio was equal, a distinct change in the evaporation behaviours was observed when the concentration of graphene passed a given threshold. If the concentration was above this value, then the droplets evaporated completely leaving behind an aggregate of graphitic material. Below the threshold resulted in the eventual lack of continuous evaporation of the solvent and a stable soft matter entity was formed. This difference was hypothesised to be due to the movement of graphene in the droplets. In both cases (above and below the threshold concentration), the graphene would flow towards the surface of the droplet and form a crust. At high concentrations however, there would be significantly more aggregation of the material, resulting in bulkier particles at the surface and a less efficient packing arrangement. Consequently, the solvent could still evaporate through the porous crust, until the droplet buckles under the excess of graphene at the surface. On the other hand, the lower concentrations allowed for the formation of a less porous shell which prevented the evaporation of the solvent, giving rise to the extended droplet lifetimes observed. This work sets up the potential for the use of graphene in the manufacturing of liquid marbles, which would extend the list of potential graphene applications into the soft matter field of research.

Chapter 6 contains an investigation of potential homogeneous nucleation of glycine using acoustic levitation. Two different solvent systems were used in the crystallisation of glycine, either a purely aqueous solution or a binary solvent mixture of water and isopropyl alcohol (IPA). The kinetics of the crystallisation (*i.e.* evaporation profiles and induction times) were followed by recording the levitation process. The presence of IPA enhanced the generation of supersaturation and induced nucleation sooner compared with the pure water solutions. The morphology of the crystals was also affected by the addition of IPA. Two different morphologies were obtained from the mixed solvent system (*i.e.* spherical agglomerates made up of small crystallites, and non-spherical agglomerates made up of larger needle-like crystals), whilst the pure water system only produced the spherical agglomerates. This split was attributed to an increase in glycine's metastable zone width. The internal morphology of the spherical agglomerates was further investigated by precisely opening them with a laser cutter. SEM images show both outer and inner regions of the agglomerates possess a certain directionality, possibly alluding to growth from the external crust region to the centre. A detailed Raman spectroscopy analysis was conducted on the spherical agglomerates to determine polymorphic outcomes, revealing that all the crystals were found to be exclusively

of the α-form, regardless of where the measurement was taken or the solvent system used. The selective crystallisation of the α-form from these levitated microdroplets was attributed to the influence of the acoustic waves, which suppressed the formation of the β-form even in regions of higher supersaturation, *i.e.* liquid-air contact region.

Chapter 7 reports the use of a novel pyrene-based stabiliser (BPS) to enhance the exfoliation of graphene in water *via* LPE. In contrast to previous studies, this pyrene derivative is insoluble in water. Remarkably, the concentrations were even higher than those reported with traditional, water-soluble pyrene derivatives. A combination of Raman spectroscopy and AFM showed that the produced graphene flakes were mostly single to few-layers thick as well as being over 100 nm in lateral size. A range of comparable stabilisers were used in this study (*e.g.* a mono-substituted variant and a variant with a longer chain between the pyrene groups and the central connector). The standard BPS was found to be the most efficient of the stabilisers. Dose-escalated cytotoxicity studies were conducted, showing that unfortunately, these dispersions have reduced biocompatibility when compared to dispersions produced using traditional water-soluble pyrene stabilisers. This was attributed to the insoluble nature of the stabiliser, which led to the hypothesis that, unlike soluble stabilisers, it had a greater affinity to adsorb onto the graphene rather than be in solution, meaning the graphene flakes effectively contained a higher concentration of the stabiliser, making them cytotoxic. Conversely, this work also shows the potential for stabiliser assisted LPE of graphene to be used as a process to disperse insoluble molecules in water.

8.1 Future Work

Further research can be conducted to further the conclusions drawn from the work presented in this thesis. Some potential avenues for future work are detailed below.

Chapter 4 demonstrated nearly complete selectivity of the metastable α-form of glycine through the use of graphene that possessed oxygen-containing functional groups. It also demonstrated that it was necessary for a certain content of oxygen be present on the graphene flakes to facilitate the selectivity. Therefore, further investigation into the use of functionalised graphene could be carried out. It has been previously shown that CVD graphene can be readily functionalised with varying concentrations of oxygen groups using plasma,[314] thereby allowing a greater tunability of the oxygen content on graphene, which can then be used for further graphene-based templated crystallisation experiments. This would allow for a precise definition of the oxygen-content range required for polymorph selectivity.

As well oxygen groups, graphene can be functionalised with a range of different functionalities. This has a clear advantage as specific interactions can be probed using a wide range of functionalities. Exposing graphene to a hydrogen plasma, the reduced analogue of graphene will be produced, graphane.[8] Fluorine can also functionalise graphene.[315] The ability to covalently modify graphene gives rise to the possibility of controlling its properties. For example, a high fluorine coverage will cause graphene to become superhydrophobic. Changing the functionality on graphene means that the interactions between graphene and a crystallising solute will be altered, thus influencing the crystallisation outcome.

The ECE process allows for a one-pot functionalisation process. The anodic process showcased in this thesis decorates the graphene flakes with oxygen-containing groups, but it is possible to functionalise the flakes with other functional groups during the ECE process by adding a diazonium salt to the electrolyte during electrolysis.[316] The diazonium salt would allow for a large variety of different functional groups to be grafted to the graphene flakes. Care would have to be taken with this method though, as the diazonium ions that are formed during the electrochemical process could act as oxygen scavengers, which would result in a lower oxidised, thus a less water dispersible, graphene flake. Using a sufficiently large functional group could direct the templating process during crystallisation away from the graphene basal plane, thereby removing a steric hinderance component from the templating effect.

The graphene produced *via* the ECE process have a lateral flake size of between 5-10 μm. As Using these flakes allowed for nearly exclusive selectivity of the α-glycine form. If the amount of interactions between graphene and glycine could be increased, then it is likely to generate only the α-form. However, this was shown in **Chapter 4** to not be the case through the use of GO, so another route to increase the potential amount of interactions is needed. If the flake size is reduced, then the effective concentration of graphene would increase, which would have a proportional effect on the amount of intermolecular interactions possible between graphene and glycine. Size reduction (down to sub-micron sizes) could be achieved through the use of a tip sonicator once the ECE graphene dispersions were prepared as detailed in **Chapter 4**. As a tip sonicator is typically more powerful than a bath sonicator, the graphene flakes would be subjected to a higher amount of energy, which would fragment them to a greater degree.[75]

An obvious extension to the work shown in **Chapter 4** is through the investigation of graphene's ability to template different compounds of greater industrial relevance. One example could be D-mannitol which is a common pharmaceutical excipient that also exhibits polymorphism. Like glycine, mannitol's polymorphs commonly crystallise concomitantly due

to competing thermodynamic and kinetic factors.[317,318] A previous study using inkjet printing reported the formation of the stable *β*-form upon crystallisation of *p*L droplets, whilst larger droplets (of the magnitude of *n*L) produced a mixture of the less stable *α*- and *γ*-forms.[138] The same study also performed crystallisation *via* spray drying using even larger volumes (*μ*L) which again yielded the *β*-form, whilst the presence of additives resulted in the formation of the *α*-form, suggesting that surface-induced polymorph selectivity exists for mannitol. Therefore, tailor-made graphene templates that possess different functionalities could be utilised in the crystallisation of mannitol to help understand the clearly complex crystallisation mechanism that mannitol has. Finally, the crystallising molecule does not just have to interact with graphene through hydrogen bonding but can interact through other intermolecular interactions. This could be achieved using aromatic compounds, which would likely tend to favour π-π stacking interactions with graphene's basal plane. Example compounds such as paracetamol or aspirin could be used to investigate these interactions.

Concerning **Chapter 5** the next step would be to develop a computation model to describe the levitating droplets (similar to ones detailed in Section 3.2.2) to reproduce the results obtained at the higher and lower graphene concentrations. The model associated to the evaporative process should take into account the unique properties of graphene when it is dispersed in solution, such as re-aggregation rates and flake distribution within the droplet. Additionally, the acoustic levitation system could be altered to allow for additional *in situ* measurements of the levitating droplets, like the ones detailed in Section 3.2.1. Specifically, coupling to Raman spectroscopy makes the most sense as it is extensively used in the characterisation of graphene so could be used to track any changes in the properties of graphene induced by acoustic levitation that results in the unusual drying behaviours. Finally, graphene produced by other methods (*i.e.* LPE) or that have different surface properties (*e.g.* varying oxygen content or different functionalities) could be acoustically levitated to assess whether the unusual drying behaviour is exclusive to this particular ECE graphene or if it is more universal to graphene itself.

A follow up to **Chapter 6** would be to investigate more solvent systems than those reported to elucidate the impact of solvent and the ultrasonic waves on the crystallisation of glycine, such as other ratios of water and IPA, and even other organic solvents typically used in the crystallisation of glycine, like methanol or ethanol. Further to this, crystallisation experiments using the levitator could expand to the use of graphene additives, as conducted in **Chapter 4**. However, it should be noted that glycine is not the ideal system for this set of experiments:

taking into account that both the homogeneous crystallisations presented in **Chapter 6** and the heterogeneous crystallisations presented in **Chapter 4** both produced the α-form of glycine. Thus, it is not expected to reveal much about the influence of graphene on the polymorphism of glycine. Yet, this study could be utilised to explore the polymorphism of other molecules that potentially have more complex polymorphic characteristics, such as mannitol.[295]

Crystallisation can also be influenced by the presence of an electric field.[214,319,320] It is generally understood that the electric field induces dipole alignment of the solute which enhances nucleation rates by lowering the energy barrier to nucleation. Graphene can be readily coupled to an electrode and an electric field can be generated. This would allow for the exploration of the electrostatic interactions between graphene and a crystallising molecule. Whilst glycine would fit as a model molecule for proof-of-concept purposes, crystallising molecules of technological interest (*e.g.* organic semiconductors) would be of significant interest where molecular alignment is a crucial parameter to device performance.

As mentioned in **Chapter 2**, spatial confinement is an effective method to template the crystallisation of organic molecules. Confining the process switches it from a kinetically controlled process, where the least stable polymorphs form initially in accordance with Oswald's Law, to a thermodynamically controlled one. There are many examples of confining crystallisation (see Section 2.4), but utilising graphene in these experiments has not yet been explored. Crystallisation can be forced to occur within a graphene membrane; by filtering a solution through the membrane, the solute molecules should collect within the pores and achieve supersaturation. The membrane could then be dispersed so the collection of the crystals can occur. This also offers the opportunity to induce secondary nucleation as the loaded membrane could be immersed in a solution that has the same solute dissolved in it. Recently, our group has reported the use of a gas-blow coater to deposit organic semiconductors on substrates with controlled morphologies.[321] This technique could easily induce spatial confinement through the controlled application of gas pressures and blade movement speed. This type of planar confinement could be compared to the confinement achieved through microemulsions, which is an example of curved confinement.

In summary, this project has developed a simple and reproducible droplet-based investigation setup that allowed for a robust investigation on the crystallisation of glycine, as well as the evaporation behaviour of graphene dispersions. The know-how obtained from the studies of this thesis can be extended to the study of the crystallisation of different organic molecules, the

further alteration of graphene's surface properties through functionalisation, or towards molecules of more technological interest (*e.g.* pharmaceuticals).

References

1. Novoselov, K. S. S. *et al.* Electric Field Effect in Atomically Thin Carbon Films. *Science* **306**, 666–669 (2004).
2. Novoselov, K. S. *et al.* Two-dimensional atomic crystals. *Proc. Natl. Acad. Sci. U. S. A.* **102**, 10451–10453 (2005).
3. Geim, A. K. Status and Prospects. *Science* **324**, 1530–1534 (2009).
4. Geim, A. K. & Grigorieva, I. V. Van der Waals heterostructures. *Nature* **499**, 419–425 (2013).
5. Geim, A. K. & Novoselov, K. S. The rise of graphene. *Nat. Mater.* **6**, 183–191 (2007).
6. Novoselov, K. S. *et al.* A roadmap for graphene. *Nature* **490**, 192–200 (2012).
7. Ferrari, A. C. *et al.* Science and technology roadmap for graphene, related two-dimensional crystals, and hybrid systems. *Nanoscale* **7**, 4598–4810 (2015).
8. Elias, D. C. *et al.* Control of graphene's properties by reversible hydrogenation: evidence for graphane. *Science* **323**, 610–3 (2009).
9. Castro Neto, A. H., Guinea, F., Peres, N. M. R., Novoselov, K. S. & Geim, A. K. The electronic properties of graphene. *Rev. Mod. Phys.* **81**, 109–162 (2009).
10. Huang, Y. *et al.* Universal mechanical exfoliation of large-area 2D crystals. *Nat. Commun.* **11**, 2453 (2020).
11. Jorio, A., Saito, R., Dresselhaus, G. & Dresselhaus, M. S. *Raman Spectroscopy in Graphene Related Systems*. *Raman Spectroscopy in Graphene Related Systems* (2011). doi:10.1002/9783527632695
12. Charlier, J.-C., Eklund, P. C., Zhu, J. & Ferrari, A. C. Electron and Phonon Properties of Graphene: Their Relationship with Carbon Nanotubes BT - Carbon Nanotubes: Advanced Topics in the Synthesis, Structure, Properties and Applications. *Carbon Nanotub.* **111**, 673–709 (2008).
13. Kumar, C. S. S. R. *Raman spectroscopy for nanomaterials characterization*. *Raman Spectroscopy for Nanomaterials Characterization* **9783642206**, (2012).
14. Du, X., Skachko, I., Barker, A. & Andrei, E. Y. Approaching ballistic transport in suspended graphene. *Nat. Nanotechnol.* **3**, 491–495 (2008).
15. Nair, R. R. *et al.* Fine structure constant defines visual transparency of graphene. *Science* **320**, 1308 (2008).
16. Blake, P. *et al.* Making graphene visible. *Appl. Phys. Lett.* **91**, (2007).
17. Lee, C., Wei, X., Kysar, J. W. & Hone, J. Measurement of the Elastic Properties and

Intrinsic Strength of Monolayer Graphene. *Science* **321**, 385 LP – 388 (2008).

18. Bae, S. *et al.* Roll-to-roll production of 30-inch graphene films for transparent electrodes. *Nat. Nanotechnol.* **5**, 574–578 (2010).
19. Balandin, A. A. Thermal properties of graphene and nanostructured carbon materials. *Nat. Mater.* **10**, 569 (2011).
20. Moser, J., Barreiro, A. & Bachtold, A. Current-induced cleaning of graphene. *Appl. Phys. Lett.* **91**, 163513 (2007).
21. Bunch, J. S. *et al.* Impermeable atomic membranes from graphene sheets. *Nano Lett.* **8**, 2458–2462 (2008).
22. Schedin, F. *et al.* Detection of individual gas molecules adsorbed on graphene. *Nat. Mater.* **6**, 652–655 (2007).
23. Emtsev, K. V *et al.* Towards wafer-size graphene layers by atmospheric pressure graphitization of silicon carbide. *Nat. Mater.* **8**, 203–207 (2009).
24. Li, X. *et al.* Large area synthesis of high quality and uniform graphene films on copper foils. *Science* **324**, 1312–1314 (2009).
25. Kim, K. S. *et al.* Large-scale pattern growth of graphene films for stretchable transparent electrodes. *Nature* **457**, 706–710 (2009).
26. Hernandez, Y. *et al.* High-yield production of graphene by liquid-phase exfoliation of graphite. *Nat. Nanotechnol.* **3**, 563–568 (2008).
27. Cui, X., Zhang, C., Hao, R. & Hou, Y. Liquid-phase exfoliation, functionalization and applications of graphene. *Nanoscale* **3**, 2118–2126 (2011).
28. Backes, C. *et al.* Equipartition of Energy Defines the Size–Thickness Relationship in Liquid-Exfoliated Nanosheets. *ACS Nano* **13**, 7050–7061 (2019).
29. Furtado, C. A. *et al.* Debundling and Dissolution of Single-Walled Carbon Nanotubes in Amide Solvents. *J. Am. Chem. Soc.* **126**, 6095–6105 (2004).
30. Giordani, S. *et al.* Debundling of Single-Walled Nanotubes by Dilution: Observation of Large Populations of Individual Nanotubes in Amide Solvent Dispersions. *J. Phys. Chem. B* **110**, 15708–15718 (2006).
31. Hasan, T. *et al.* Stabilization and "Debundling" of Single-Wall Carbon Nanotube Dispersions in N-Methyl-2-pyrrolidone (NMP) by Polyvinylpyrrolidone (PVP). *J. Phys. Chem. C* **111**, 12594–12602 (2007).
32. Landi, B. J., Ruf, H. J., Worman, J. J. & Raffaelle, R. P. Effects of Alkyl Amide Solvents on the Dispersion of Single-Wall Carbon Nanotubes. *J. Phys. Chem. B* **108**,

17089–17095 (2004).

33. Nicolosi, V., Chhowalla, M., Kanatzidis, M. G., Strano, M. S. & Coleman, J. N. Liquid Exfoliation of Layered Materials. *Science* **340**, 1226419–1226419 (2013).
34. Hernandez, Y., Lotya, M., Rickard, D., Bergin, S. D. & Coleman, J. N. Measurement of multicomponent solubility parameters for graphene facilitates solvent discovery. *Langmuir* **26**, 3208–3213 (2010).
35. Ciesielski, A. & Samorì, P. Supramolecular Approaches to Graphene: From Self-Assembly to Molecule-Assisted Liquid-Phase Exfoliation. *Advanced Materials* **28**, 6030–6051 (2016).
36. Loh, K. P., Bao, Q., Eda, G. & Chhowalla, M. Graphene oxide as a chemically tunable platform for optical applications. *Nat. Chem.* **2**, 1015–1024 (2010).
37. Hummers, W. S. & Offeman, R. E. Preparation of Graphitic Oxide. *J. Am. Chem. Soc.* **80**, 1339–1339 (1958).
38. Aboutalebi, S. H., Gudarzi, M. M., Zheng, Q. B. & Kim, J. K. Spontaneous formation of liquid crystal in ultra large graphene oxide dispersions. *Adv. Funct. Mater.* **21**, 2978–2988 (2011).
39. Gudarzi, M. M., Moghadam, M. H. M. & Sharif, F. Spontaneous exfoliation of graphite oxide in polar aprotic solvents as the route to produce graphene oxide - Organic solvents liquid crystals. *Carbon N. Y.* **64**, 403–415 (2013).
40. Morimoto, N., Kubo, T. & Nishina, Y. Tailoring the Oxygen Content of Graphite and Reduced Graphene Oxide for Specific Applications. *Sci. Rep.* **6**, 21715 (2016).
41. Stankovich, S. *et al.* Graphene-based composite materials. *Nature* **442**, 282–286 (2006).
42. Gao, W. The chemistry of graphene oxide. *Graphene Oxide Reduct. Recipes, Spectrosc. Appl.* **39**, 61–95 (2015).
43. Collins, W. R., Lewandowski, W., Schmois, E., Walish, J. & Swager, T. M. Claisen rearrangement of graphite oxide: A route to covalently functionalized graphenes. *Angew. Chemie - Int. Ed.* **50**, 8848–8852 (2011).
44. He, H., Klinowski, J., Forster, M. & Lerf, A. A new structural model for graphite oxide. *Chem. Phys. Lett.* **287**, 53–56 (1998).
45. Dreyer, D. R., Park, S., Bielawski, C. W. & Ruoff, R. S. The chemistry of graphene oxide. *Chem. Soc. Rev.* **39**, 228–240 (2010).
46. Pacilé, D. *et al.* Electronic properties and atomic structure of graphene oxide

membranes. *Carbon N. Y.* **49**, 966–972 (2011).

47. Parviz, D. *et al.* Dispersions of Non-Covalently Functionalized Graphene with Minimal Stabilizer. *ACS Nano* **6**, 8857–8867 (2012).
48. Amiri, A., Naraghi, M., Ahmadi, G., Soleymaniha, M. & Shanbedi, M. A review on liquid-phase exfoliation for scalable production of pure graphene, wrinkled, crumpled and functionalized graphene and challenges. *FlatChem* **8**, 40–71 (2018).
49. Lotya, M. *et al.* Liquid phase production of graphene by exfoliation of graphite in surfactant/water solutions. *J. Am. Chem. Soc.* **131**, 3611–3620 (2009).
50. Lotya, M., King, P. J., Khan, U., De, S. & Coleman, J. N. High-concentration, surfactant-stabilized graphene dispersions. *ACS Nano* **4**, 3155–3162 (2010).
51. Smith, R. J., Lotya, M. & Coleman, J. N. The importance of repulsive potential barriers for the dispersion of graphene using surfactants. *New J. Phys.* **12**, (2010).
52. Villar-Rodil, S., Paredes, J. I., Martínez-Alonso, A. & Tascón, J. M. D. Preparation of graphene dispersions and graphene-polymer composites in organic media. *J. Mater. Chem.* **19**, 3591 (2009).
53. May, P., Khan, U., Hughes, J. M. & Coleman, J. N. Role of solubility parameters in understanding the steric stabilization of exfoliated two-dimensional nanosheets by adsorbed polymers. *J. Phys. Chem. C* **116**, 11393–11400 (2012).
54. Ghosh, A., Rao, K. V., George, S. J. & Rao, C. N. R. Noncovalent Functionalization, Exfoliation, and Solubilization of Graphene in Water by Employing a Fluorescent Coronene Carboxylate. *Chem. - A Eur. J.* **16**, 2700–2704 (2010).
55. Englert, J. M. *et al.* Soluble Graphene: Generation of Aqueous Graphene Solutions Aided by a Perylenebisimide-Based Bolaamphiphile. *Adv. Mater.* **21**, 4265–4269 (2009).
56. Schlierf, A. *et al.* Nanoscale insight into the exfoliation mechanism of graphene with organic dyes: effect of charge, dipole and molecular structure. *Nanoscale* **5**, 4205 (2013).
57. Yang, H. *et al.* A simple method for graphene production based on exfoliation of graphite in water using 1-pyrenesulfonic acid sodium salt. *Carbon N. Y.* **53**, 357–365 (2013).
58. McManus, D. *et al.* Water-based and biocompatible 2D crystal inks for all-inkjet-printed heterostructures. *Nat. Nanotechnol.* **12**, 343–350 (2017).
59. Ciesielski, A. & Samorì, P. Graphene via sonication assisted liquid-phase exfoliation.

Chem. Soc. Rev. **43**, 381–98 (2014).

60. Shin, Y. *et al.* Stable, concentrated, biocompatible, and defect-free graphene dispersions with positive charge. *Nanoscale* **12**, 12383–12394 (2020).
61. Shin, Y. *et al.* Charge-tunable graphene dispersions in water made with amphoteric pyrene derivatives. *Mol. Syst. Des. Eng.* (2019). doi:10.1039/C9ME00024K
62. Heard, K. W. J. *et al.* Initial Studies Directed toward the Rational Design of Aqueous Graphene Dispersants. *ACS Omega* **4**, 1969–1981 (2019).
63. An, X. *et al.* Stable Aqueous Dispersions of Noncovalently Functionalized Graphene from Graphite and their Multifunctional High-Performance Applications. *Nano Lett.* **10**, 4295–4301 (2010).
64. Abdelkader, A. M., Cooper, A. J., Dryfe, R. A. W. & Kinloch, I. A. How to get between the sheets: a review of recent works on the electrochemical exfoliation of graphene materials from bulk graphite. *Nanoscale* **7**, 6944–6956 (2015).
65. Parvez, K. *et al.* Exfoliation of graphite into graphene in aqueous solutions of inorganic salts. *J. Am. Chem. Soc.* **136**, 6083–6091 (2014).
66. Parvez, K. *et al.* Electrochemically Exfoliated Graphene as Solution-Processable, Highly Conductive Electrodes for Organic Electronics. *ACS Nano* **7**, 3598–3606 (2013).
67. Low, C. T. J., Walsh, F. C., Chakrabarti, M. H., Hashim, M. A. & Hussain, M. A. Electrochemical approaches to the production of graphene flakes and their potential applications. *Carbon N. Y.* **54**, 1–21 (2013).
68. Zhang, W., Zeng, Y., Xiao, N., Hng, H. H. & Yan, Q. One-step electrochemical preparation of graphene-based heterostructures for Li storage. *J. Mater. Chem.* **22**, 8455–8461 (2012).
69. Wang, G. *et al.* Highly efficient and large-scale synthesis of graphene by electrolytic exfoliation. *Carbon N. Y.* **47**, 3242–3246 (2009).
70. Alanyalıoğlu, M., Segura, J. J., Oró-Solè, J. & Casañ-Pastor, N. The synthesis of graphene sheets with controlled thickness and order using surfactant-assisted electrochemical processes. *Carbon N. Y.* **50**, 142–152 (2012).
71. Khanra, P., Kuila, T., Bae, S. H., Kim, N. H. & Lee, J. H. Electrochemically exfoliated graphene using 9-anthracene carboxylic acid for supercapacitor application. *J. Mater. Chem.* **22**, 24403–24410 (2012).
72. Yang, S., Lohe, M. R., Müllen, K. & Feng, X. New-Generation Graphene from

Electrochemical Approaches: Production and Applications. *Adv. Mater.* (2016). doi:10.1002/adma.201505326

73. Marković, Z. M. *et al.* Semi-transparent, conductive thin films of electrochemical exfoliated graphene. *RSC Adv.* **6**, 39275–39283 (2016).
74. Nagyte, V. *et al.* Raman Fingerprints of Graphene Produced by Anodic Electrochemical Exfoliation. *Nano Lett.* **20**, 3411–3419 (2020).
75. Parvez, K., Worsley, R., Alieva, A., Felten, A. & Casiraghi, C. Water-based and inkjet printable inks made by electrochemically exfoliated graphene. *Carbon N. Y.* **149**, 213–221 (2019).
76. Schmelzer, E. J. W. P. *Nucleation Theory and Applications*. *Wiley-VCH* (2005).
77. Cubillas, P. & Anderson, M. W. Synthesis Mechanism: Crystal Growth and Nucleation. in *Zeolites and Catalysis: Synthesis, Reactions and Applications* **1**, 1–55 (2010).
78. Mullin, J. W. *Crystallization*. (Butterworth-Heinemann, 2001).
79. Kashchiev, D. *Nucleation*. (Butterworth-Heinemann, 2000).
80. Gibbs, J. W. *The Collected Works*. (1948).
81. Young, S. W. Mechanical stimulus to crystallization in supercooled liquids. *J. Am. Chem. Soc.* **33**, 148–162 (1911).
82. Berkeley, T. E. of. Solubility and supersolubility from the osmotic standpoint. *Philos. Mag.* **24**, 867–869 (1912).
83. Davey, R. & Garside, J. *From molecules to crystallizers*. (Oxford University Press, 2000).
84. Markov, I. V. *Crystal Growth for Beginners*. (WORLD SCIENTIFIC, 2003).
85. Shi, D. *et al.* Low trap-state density and long carrier diffusion in organolead trihalide perovskite single crystals. *Science* **347**, 519–522 (2015).
86. Minemawari, H. *et al.* Inkjet printing of single-crystal films. *Nature* **475**, 364–367 (2011).
87. Volmer, M. & Weber, A. Keimbildung in übersättigten Gebilden. *Zeitschrift für Phys. Chemie* **119U**, 277–301 (1926).
88. Young, T. An essay on cohesion of fluids. *Philos. Trans. te R. Soc. London* (1805).
89. Volmer, M. Kinetics of Phase Formation. *Dresden: Steinkopff* 232 (1939).
90. Knezic, D., Zaccaro, J. & Myerson, A. S. Nucleation Induction Time in Levitated Droplets. *J. Phys. Chem. B* **108**, 10672–10677 (2004).

91. Rodríguez-Hornedo, N. & Murphy, D. Significance of controlling crystallization mechanisms and kinetics in pharmaceutical systems. *Journal of Pharmaceutical Sciences* **88**, 651–660 (1999).
92. Swanson, S. E. Relation of nucleation and crystal-growth rate to the development of granitic textures. *Am. Mineral.* **62**, 966–978 (1977).
93. Xiao, Y., Tang, S. K., Hao, H., Davey, R. J. & Vetter, T. Quantifying the Inherent Uncertainty Associated with Nucleation Rates Estimated from Induction Time Data Measured in Small Volumes. *Cryst. Growth Des.* **17**, 2852–2863 (2017).
94. Jiang, S. & Ter Horst, J. H. Crystal nucleation rates from probability distributions of induction times. *Cryst. Growth Des.* **11**, 256–261 (2011).
95. Kulkarni, S. A., Kadam, S. S., Meekes, H., Stankiewicz, A. I. & ter Horst, J. H. Crystal Nucleation Kinetics from Induction Times and Metastable Zone Widths. *Cryst. Growth Des.* **13**, 2435–2440 (2013).
96. Wagner, P. E. & Strey, R. Homogeneous nucleation rates of water vapor measured in a two-piston expansion chamber. *J. Phys. Chem.* **85**, 2694–2698 (1981).
97. Wright, D., Caldwell, R. & El-Shall, M. S. Vapor phase homogeneous nucleation of acetonitrile: the effect of dipole—dipole interaction. *Chem. Phys. Lett.* **176**, 46–54 (1991).
98. Wright, D. & El-Shall, M. S. Reply to the Comment on the homogeneous nucleation of CH3CN and the scaling law for onset supersaturation ratios. *Chem. Phys. Lett.* **189**, 103–104 (1992).
99. Hale, B. N. Application of a scaled homogeneous nucleation-rate formalism to experimental data at T<<Tc. *Phys. Rev. A* **33**, 4156–4163 (1986).
100. Greenwood, G. W., Greer, A. L., Herlach, D. M., Kelton, K. F. & Oxtoby, D. W. Crystal nucleation in simple and complex fluids. *Philos. Trans. R. Soc. London. Ser. A Math. Phys. Eng. Sci.* **361**, 419–428 (2003).
101. Erdemir, D., Lee, A. Y. & Myerson, A. S. Nucleation of Crystals from Solution: Classical and Two-Step Models. *Acc. Chem. Res.* **42**, 621–629 (2009).
102. Vekilov, P. G. Dense Liquid Precursor for the Nucleation of Ordered Solid Phases from Solution. *Cryst. Growth Des.* **4**, 671–685 (2004).
103. Schüth, F. Nucleation and crystallization of solids from solution. *Curr. Opin. Solid State Mater. Sci.* **5**, 389–395 (2001).
104. Davey, R. J., Schroeder, S. L. M. & ter Horst, J. H. Nucleation of Organic Crystals-A

Molecular Perspective. *Angew. Chemie Int. Ed.* **52**, 2166–2179 (2013).

105. Pan, W., Kolomeisky, A. B. & Vekilov, P. G. Nucleation of ordered solid phases of proteins via a disordered high-density state: Phenomenological approach. *J. Chem. Phys.* **122**, 174905 (2005).
106. Kashchiev, D., Vekilov, P. G. & Kolomeisky, A. B. Kinetics of two-step nucleation of crystals. *J. Chem. Phys.* **122**, 244706 (2005).
107. Vekilov, P. G. The two-step mechanism of nucleation of crystals in solution. *Nanoscale* **2**, 2346–2357 (2010).
108. Gebauer, D., Völkel, A. & Cölfen, H. Stable Prenucleation Calcium Carbonate Clusters. *Science* **322**, 1819–1822 (2008).
109. Gebauer, D., Kellermeier, M., Gale, J. D., Bergström, L. & Cölfen, H. Pre-nucleation clusters as solute precursors in crystallisation. *Chem. Soc. Rev.* **43**, 2348–2371 (2014).
110. Sosso, G. C. *et al.* Crystal Nucleation in Liquids: Open Questions and Future Challenges in Molecular Dynamics Simulations. *Chem. Rev.* **116**, 7078–7116 (2016).
111. Bonnett, P. E., Carpenter, K. J., Dawson, S. & Davey, R. J. Solution crystallisation via a submerged liquid–liquid phase boundary: oiling out. *Chem. Commun.* **6**, 698–699 (2003).
112. Dey, A. *et al.* The role of prenucleation clusters in surface-induced calcium phosphate crystallization. *Nat. Mater.* **9**, 1010–1014 (2010).
113. Kellermeier, M. *et al.* Colloidal Stabilization of Calcium Carbonate Prenucleation Clusters with Silica. *Adv. Funct. Mater.* **22**, 4301–4311 (2012).
114. Baumgartner, J. *et al.* Nucleation and growth of magnetite from solution. *Nat. Mater.* **12**, 310–314 (2013).
115. Sorell, L. S. & Myerson, A. S. Diffusivity of urea in concentrated, saturated and supersaturated solutions. *AIChE J.* **28**, 772–779 (1982).
116. Meng, C. K. & Fenn, J. B. Formation of charged clusters during electrospray ionization of organic solute species. *Org. Mass Spectrom.* **26**, 542–549 (1991).
117. Takats, Z., Nanita, S. C., Cooks, R. G., Schlosser, G. & Vekey, K. Amino Acid Clusters Formed by Sonic Spray Ionization. *Anal. Chem.* **75**, 1514–1523 (2003).
118. Parveen, S., Davey, R. J., Dent, G. & Pritchard, R. G. Linking solution chemistry to crystal nucleation: the case of tetrolic acid. *Chem. Commun.* **12**, 1531–1533 (2005).
119. Hamad, S., Hughes, C. E., Catlow, C. R. A. & Harris, K. D. M. Clustering of Glycine Molecules in Aqueous Solution Studied by Molecular Dynamics Simulation. *J. Phys.*

Chem. B **112**, 7280–7288 (2008).

120. Kleber, W. Verma, Ajit Ram and P. Krishna Polymorphism and polytypism in crystals. John Wiley and Sons, Inc. New York-London-Sydney 1966. XIX+3415. *Krist. und Tech.* **1**, 665–666 (1966).
121. Liebig, J. & Wohler, F. Untersuchungen iiber das Radical der Benzoesaure. *Pharm Anntiinflam* **249**, 514 (1832).
122. Bernstein, J. *Polymorphism in Molecular Crystals*. (Oxford University Press, 2010).
123. Bučar, D.-K., Lancaster, R. W. & Bernstein, J. Disappearing Polymorphs Revisited. *Angew. Chemie Int. Ed.* **54**, 6972–6993 (2015).
124. Cruz-Cabeza, A. J., Reutzel-Edens, S. M. & Bernstein, J. Facts and fictions about polymorphism. *Chem. Soc. Rev.* **44**, 8619–8635 (2015).
125. Nyman, J. & Day, G. M. Static and lattice vibrational energy differences between polymorphs. *CrystEngComm* **17**, 5154–5165 (2015).
126. Beran, G. J. O. Modeling Polymorphic Molecular Crystals with Electronic Structure Theory. *Chem. Rev.* **116**, 5567–5613 (2016).
127. Bernstein, J., Davey, R. J. & Henck, J.-O. Concomitant Polymorphs. *Angew. Chemie Int. Ed.* **38**, 3440–3461 (1999).
128. Ostwald, W. Studien uber die Bildung und Umwaldlung fester Korper. *Phys. Chem.* **22**, 289–330 (1897).
129. Van Santen, R. A. The Ostwald Step Rule. *J. Phys. Chem* **88**, 5768–5769 (1984).
130. Burley, J. C., Duer, M. J., Stein, R. S. & Vrcelj, R. M. Enforcing Ostwald's rule of stages: Isolation of paracetamol forms III and II. *Eur. J. Pharm. Sci.* **31**, 271–276 (2007).
131. Black, J. *et al.* Crystal nucleation and growth in a polymorphic system: Ostwald's Rule, p-aminobenzoic acid and nucleation transition states. *CrystEngComm* **20**, 768–776 (2018).
132. Hamilton, B. D., Hillmyer, M. A. & Ward, M. D. Glycine Polymorphism in Nanoscale Crystallization Chambers. *Cryst. Growth Des.* **8**, 3368–3375 (2008).
133. Lee, E. H. A practical guide to pharmaceutical polymorph screening & selection. *Asian J. Pharm. Sci.* **9**, 163–175 (2014).
134. Gracin, S. & Rasmuson, Å. C. Polymorphism and Crystallization of p-Aminobenzoic Acid. *Cryst. Growth Des.* **4**, 1013–1023 (2004).
135. Khoshkhoo, S. & Anwar, J. Crystallization of polymorphs: the effect of solvent. *J.*

Phys. D. Appl. Phys. **26**, B90–B93 (1993).

136. Zhou, G. X. *et al.* Direct Design of Pharmaceutical Antisolvent Crystallization through Concentration Control. *Cryst. Growth Des.* **6**, 892–898 (2006).
137. Buanz, A. B. M. & Gaisford, S. Formation of Highly Metastable β Glycine by Confinement in Inkjet Printed Droplets. *Cryst. Growth Des.* **17**, 1245–1250 (2017).
138. Buanz, A., Gurung, M. & Gaisford, S. Crystallisation in printed droplets: understanding crystallisation of d-mannitol polymorphs. *CrystEngComm* **21**, 2212–2219 (2019).
139. Ha, J.-M., Wolf, J. H., Hillmyer, M. A. & Ward, M. D. Polymorph Selectivity under Nanoscopic Confinement. *J. Am. Chem. Soc.* **126**, 3382–3383 (2004).
140. Jiang, Q. & Ward, M. D. Crystallization under nanoscale confinement. *Chem. Soc. Rev.* **43**, 2066–2079 (2014).
141. Cooper, S., Cook, O. & Loines, N. Crystallization in Microemulsions: A Generic Route to Thermodynamic Control and the Estimation of Critical Nucleus Size. in *Crystallization - Science and Technology* (ed. Cook, O.) Ch. 5 (InTech, 2012). doi:10.5772/47977
142. Bryant, G. W., Hallett, J. & Mason, B. J. The epitaxial growth of ice on single-crystalline substrates. *J. Phys. Chem. Solids* **12**, 189-IN18 (1960).
143. Souda, R., Aizawa, T., Sugiyama, N. & Takeguchi, M. Structure Analysis of Water Ice Crystallites on NaCl(001), KCl(001), and CaF2(111) by Reflection High-Energy Electron Diffraction. *J. Phys. Chem. C* **124**, 15180–15187 (2020).
144. MCPHERSON, A. & SHLICHTA, P. Heterogeneous and Epitaxial Nucleation of Protein Crystals on Mineral Surfaces. *Science* **239**, 385 LP – 387 (1988).
145. Meyer zu Heringdorf, F.-J., Reuter, M. C. & Tromp, R. M. Growth dynamics of pentacene thin films. *Nature* **412**, 517–520 (2001).
146. Cartier, L. *et al.* Epitaxial crystallization and crystalline polymorphism of polylactides. *Polymer (Guildf).* **41**, 8909–8919 (2000).
147. Travaille, A. M. *et al.* Highly Oriented Self-Assembled Monolayers as Templates for Epitaxial Calcite Growth. *J. Am. Chem. Soc.* **125**, 11571–11577 (2003).
148. Cheng, J. Y., Ross, C. A., Smith, H. I. & Thomas, E. L. Templated Self-Assembly of Block Copolymers: Top-Down Helps Bottom-Up. *Adv. Mater.* **18**, 2505–2521 (2006).
149. Wang, L. *et al.* Synthesis of Honeycomb-Structured Beryllium Oxide via Graphene Liquid Cells. *Angew. Chemie Int. Ed.* **59**, 15734–15740 (2020).

150. Canselier, J. P. THE EFFECTS OF SURFACTANTS ON CRYSTALLIZATION PHENOMENA. *J. Dispers. Sci. Technol.* **14**, 625–644 (1993).
151. Weissbuch, I., Lahav, M. & Leiserowitz, L. Toward Stereochemical Control, Monitoring, and Understanding of Crystal Nucleation. *Cryst. Growth Des.* **3**, 125–150 (2003).
152. Pons Siepermann, C. A. & Myerson, A. S. Inhibition of Nucleation Using a Dilute, Weakly Hydrogen-Bonding Molecular Additive. *Cryst. Growth Des.* **18**, 3584–3595 (2018).
153. Dobberschütz, S. *et al.* The mechanisms of crystal growth inhibition by organic and inorganic inhibitors. *Nat. Commun.* **9**, 1578 (2018).
154. Torbeev, V. Y., Shavit, E., Weissbuch, I., Leiserowitz, L. & Lahav, M. Control of Crystal Polymorphism by Tuning the Structure of Auxiliary Molecules as Nucleation Inhibitors. The β-Polymorph of Glycine Grown in Aqueous Solutions. *Cryst. Growth Des.* **5**, 2190–2196 (2005).
155. Dowling, R. *et al.* Acceleration of crystal growth rates: an unexpected effect of tailor-made additives. *Chem. Commun.* **46**, 5924 (2010).
156. Titiz-Sargut, S. & Ulrich, J. Influence of Additives on the Width of the Metastable Zone. *Cryst. Growth Des.* **2**, 371–374 (2002).
157. Hrkovac, M., Prlic Kardum, J., Schuster, A. & Ulrich, J. Influence of Additives on Glycine Crystal Characteristics. *Chem. Eng. Technol.* **34**, 611–618 (2011).
158. Prasad, K. V. R., Ristic, R. I., Sheen, D. B. & Sherwood, J. N. Crystallization of paracetamol from solution in the presence and absence of impurity. *Int. J. Pharm.* **215**, 29–44 (2001).
159. Rodríguez-Spong, B., Price, C. P., Jayasankar, A., Matzger, A. J. & Rodríguez-Hornedo, N. General principles of pharmaceutical solid polymorphism: A supramolecular perspective. *Adv. Drug Deliv. Rev.* **56**, 241–274 (2004).
160. Losev, E. A., Mikhailenko, M. A., Achkasov, A. F. & Boldyreva, E. V. The effect of carboxylic acids on glycine polymorphism, salt and co-crystal formation. A comparison of different crystallisation techniques. *New J. Chem.* **37**, 1973–1981 (2013).
161. Lee, E. H., Boerrigter, S. X. M., Rumondor, A. C. F., Chamarthy, S. P. & Byrn, S. R. Formation and Solid-State Characterization of a Salt-Induced Metastable Polymorph of Flufenamic Acid. *Cryst. Growth Des.* **8**, 91–97 (2008).

162. Yang, X., Lu, J., Wang, X.-J. & Ching, C.-B. Effect of sodium chloride on the nucleation and polymorphic transformation of glycine. *J. Cryst. Growth* **310**, 604–611 (2008).
163. Van Driessche, A. E. S. *et al.* Molecular nucleation mechanisms and control strategies for crystal polymorph selection. *Nature* **556**, 89–94 (2018).
164. Han, G., Chow, P. S. & Tan, R. B. H. Salt-dependent growth kinetics in glycine polymorphic crystallization. *CrystEngComm* **18**, 462–470 (2016).
165. Schreiber, R. E. *et al.* Real-time molecular scale observation of crystal formation. *Nat. Chem.* **9**, 369–373 (2017).
166. Carter, P. W. & Ward, M. D. Topographically directed nucleation of organic crystals on molecular single-crystal substrates. *J. Am. Chem. Soc.* **115**, 11521–11535 (1993).
167. Bonafede, S. J. & Ward, M. D. Selective Nucleation and Growth of an Organic Polymorph by Ledge-Directed Epitaxy on a Molecular Crystal Substrate. *J. Am. Chem. Soc.* **117**, 7853–7861 (1995).
168. Stojaković, J., Baftizadeh, F., Bellucci, M. A., Myerson, A. S. & Trout, B. L. Angle-Directed Nucleation of Paracetamol on Biocompatible Nanoimprinted Polymers. *Cryst. Growth Des.* **17**, 2955–2963 (2017).
169. Di Profio, G., Fontananova, E., Curcio, E. & Drioli, E. From Tailored Supports to Controlled Nucleation: Exploring Material Chemistry, Surface Nanostructure, and Wetting Regime Effects in Heterogeneous Nucleation of Organic Molecules. *Cryst. Growth Des.* **12**, 3749–3757 (2012).
170. Nordquist, K. A., Schaab, K. M., Sha, J. & Bond, A. H. Crystal Nucleation Using Surface-Energy-Modified Glass Substrates. *Cryst. Growth Des.* **17**, 4049–4055 (2017).
171. Chadwick, K., Myerson, A. & Trout, B. Polymorphic control by heterogeneous nucleation - A new method for selecting crystalline substrates. *CrystEngComm* **13**, 6625–6627 (2011).
172. de Poel, W. *et al.* Surfaces with Controllable Topography and Chemistry Used as a Template for Protein Crystallization. *Cryst. Growth Des.* (2018). doi:10.1021/acs.cgd.7b01174
173. Seyedhosseini, E. *et al.* Growth and nonlinear optical properties of β-glycine crystals grown on pt substrates. *Cryst. Growth Des.* **14**, 2831–2837 (2014).
174. Hiremath, R., Basile, J. A., Varney, S. W. & Swift, J. A. Controlling Molecular Crystal Polymorphism with Self-Assembled Monolayer Templates. *J. Am. Chem. Soc.* **127**,

18321–18327 (2005).

175. Capacci-Daniel, C., Gaskell, K. J. & Swift, J. A. Nucleation and Growth of Metastable Polymorphs on Siloxane Monolayer Templates. *Cryst. Growth Des.* **10**, 952–962 (2010).

176. Solomos, M. A., Capacci-Daniel, C., Rubinson, J. F. & Swift, J. A. Polymorph Selection via Sublimation onto Siloxane Templates. *Cryst. Growth Des.* **18**, 6965–6972 (2018).

177. Cox, J. R., Ferris, L. A. & Thalladi, V. R. Selective Growth of a Stable Drug Polymorph by Suppressing the Nucleation of Corresponding Metastable Polymorphs. *Angew. Chemie Int. Ed.* **46**, 4333–4336 (2007).

178. Yang, X., Sarma, B. & Myerson, A. S. Polymorph Control of Micro/Nano-Sized Mefenamic Acid Crystals on Patterned Self-Assembled Monolayer Islands. *Cryst. Growth Des.* **12**, 5521–5528 (2012).

179. Dressler, D. H. & Mastai, Y. Controlling Polymorphism by Crystallization on Self-Assembled Multilayers. *Cryst. Growth Des.* **7**, 847–850 (2007).

180. Jiang, Q., Hu, C. & Ward, M. D. Stereochemical Control of Polymorph Transitions in Nanoscale Reactors. *J. Am. Chem. Soc.* **135**, 2144–2147 (2013).

181. Foster, J. A. *et al.* Anion-switchable supramolecular gels for controlling pharmaceutical crystal growth. *Nat. Chem.* **2**, 1037–1043 (2010).

182. Foster, J. A. *et al.* Pharmaceutical polymorph control in a drug-mimetic supramolecular gel. *Chem. Sci.* **8**, 78–84 (2017).

183. Diao, Y., Harada, T., Myerson, A. S., Alan Hatton, T. & Trout, B. L. The role of nanopore shape in surface-induced crystallization. *Nat. Mater.* **10**, 867–871 (2011).

184. Hamilton, B. D., Ha, J.-M., Hillmyer, M. A. & Ward, M. D. Manipulating Crystal Growth and Polymorphism by Confinement in Nanoscale Crystallization Chambers. *Acc. Chem. Res.* **45**, 414–423 (2012).

185. Nicholson, C. E., Chen, C., Mendis, B. & Cooper, S. J. Stable Polymorphs Crystallized Directly under Thermodynamic Control in Three-Dimensional Nanoconfinement: A Generic Methodology. *Cryst. Growth Des.* **11**, 363–366 (2011).

186. Nicholson, C. E. & Cooper, S. J. Crystallization of Mefenamic Acid from Dimethylformamide Microemulsions: Obtaining Thermodynamic Control through 3D Nanoconfinement. *CRYSTALS* **1**, 195–205 (2011).

187. Hilden, J. L. *et al.* Capillary Precipitation of a Highly Polymorphic Organic

Compound. *Cryst. Growth Des.* **3**, 921–926 (2003).

188. Diao, Y., Myerson, A. S., Hatton, T. A. & Trout, B. L. Surface design for controlled crystallization: The role of surface chemistry and nanoscale pores in heterogeneous nucleation. *Langmuir* **27**, 5324–5334 (2011).
189. Belenguer, A. M., Lampronti, G. I., Cruz-Cabeza, A. J., Hunter, C. A. & Sanders, J. K. M. Solvation and surface effects on polymorph stabilities at the nanoscale. *Chem. Sci.* **72**, 171–179 (2016).
190. Chen, C., Cook, O., Nicholson, C. E. & Cooper, S. J. Leapfrogging Ostwald's Rule of Stages: Crystallization of Stable γ-Glycine Directly from Microemulsions. *Cryst. Growth Des.* **11**, 2228–2237 (2011).
191. Ding, Y. & Krogh-Jespersen, K. The 1:1 glycine zwitterion-water complex: An ab initio electronic structure study. *J. Comput. Chem.* **17**, 338–349 (1996).
192. Balabin, R. M. The First Step in Glycine Solvation: The Glycine−Water Complex. *J. Phys. Chem. B* **114**, 15075–15078 (2010).
193. Perlovich, G. L., Hansen, L. K. & Bauer-Brandl, A. The Polymorphism of Glycine. Thermochemical and structural aspects. *J. Therm. Anal. Calorim.* **66**, 699–715 (2001).
194. Dawson, A. *et al.* Effect of high pressure on the crystal structures of polymorphs of glycine. *Cryst. Growth Des.* **5**, 1415–1427 (2005).
195. Boldyreva, E. V, Ahsbahs, H. & Weber, H.-P. A comparative study of pressure-induced lattice strain of α- and γ-polymorphs of glycine. *Zeitschrift für Krist. - Cryst. Mater.* **218**, 231–236 (2003).
196. Moggach, S. A., Marshall, W. G., Rogers, D. M. & Parsons, S. How focussing on hydrogen bonding interactions in amino acids can miss the bigger picture: a high-pressure neutron powder diffraction study of ε-glycine. *CrystEngComm* **17**, 5315–5328 (2015).
197. Goryainov, S. V, Boldyreva, E. V & Kolesnik, E. N. Raman observation of a new (ζ) polymorph of glycine? *Chem. Phys. Lett.* **419**, 496–500 (2006).
198. Boldyreva, E. V. *et al.* Polymorphism of glycine: Thermodynamic aspects. Part I - Relative stability of the polymorphs. *J. Therm. Anal. Calorim.* **73**, 409–418 (2003).
199. Boldyreva, E. V. *et al.* Polymorphism of glycine: Thermodynamic aspects. Part II - Polymorphic transitions. *J. Therm. Anal. Calorim.* **73**, 419–428 (2003).
200. Bordallo, H. N., Boldyreva, E. V, Buchsteiner, A., Koza, M. M. & Landsgesell, S. Structure−Property Relationships in the Crystals of the Smallest Amino Acid: An

Incoherent Inelastic Neutron Scattering Study of the Glycine Polymorphs. *J. Phys. Chem. B* **112**, 8748–8759 (2008).

201. Marsh, R. E. A refinement of the crystal structure of glycine. *Acta Crystallogr.* **11**, 654–663 (1958).
202. Drebushchak, T. N., Boldyreva, E. V & Shutova, E. S. β-Glycine. *Acta Crystallogr. Sect. E* **58**, o634–o636 (2002).
203. Iitaka, Y. The crystal structure of γ-glycine. *Acta Crystallogr.* **14**, 1–10 (1961).
204. Albrecht, G. & Corey, R. B. The Crystal Structure of Glycine. *J. Am. Chem. Soc.* **61**, 1087–1103 (1939).
205. Pilling, S. *et al.* The influence of crystallinity degree on the glycine decomposition induced by 1 MeV proton bombardment in space analog conditions. *Astrobiology* **13**, 79–91 (2013).
206. Iitaka, Y. The Crystal Structure of beta-Glycine. *Acta. Cryst.* **13**, 35–45 (1960).
207. Guerin, S. *et al.* Control of piezoelectricity in amino acids by supramolecular packing. *Nat. Mater.* **17**, 180–186 (2018).
208. Di Profio, G., Tucci, S., Curcio, E. & Drioli, E. Selective Glycine Polymorph Crystallization by Using Microporous Membranes. *Cryst. Growth Des.* **7**, 526–530 (2007).
209. Gnanasambandam, S. & Rajagopalan, R. Growth morphology of α-glycine crystals in solution environments: an extended interface structure analysis. *CrystEngComm* **12**, 1740–1749 (2010).
210. Ferrari, E. S., Davey, R. J., Cross, W. I., Gillon, A. L. & Towler, C. S. Crystallization in Polymorphic Systems: The Solution-Mediated Transformation of β to α Glycine. *Cryst. Growth Des.* **3**, 53–60 (2003).
211. Trauffer, D. I., Maassel, A. K. & Snyder, R. C. Non-Needle-like Morphology of β-Glycine Particles Formed from Water Solutions via Monodisperse Droplet Evaporation. *Cryst. Growth Des.* **16**, 1917–1922 (2016).
212. Han, G., Poornachary, S. K., Chow, P. S. & Tan, R. B. H. Understanding Growth Morphology Changes of γ-Glycine and dl-Alanine Polar Crystals in Pure Aqueous Solutions. *Cryst. Growth Des.* **10**, 4883–4889 (2010).
213. Chongprasert, S., Knopp, S. A. & Nail, S. L. Characterization of Frozen Solutions of Glycine. *J. Pharm. Sci.* **90**, 1720–1728 (2001).
214. Aber, J. E., Arnold, S., Garetz, B. A. & Myerson, A. S. Strong dc Electric Field

Applied to Supersaturated Aqueous Glycine Solution Induces Nucleation of the γ Polymorph. *Phys. Rev. Lett.* **94**, 145503 (2005).

215. Bernal, J. D. Short notifications and notes - The crystal structure of the natural amino acids and related compounds. *Zeitschrift Fur Krist.* **78**, 363–369 (1931).
216. Garetz, B. A., Matic, J. & Myerson, A. S. Polarization Switching of Crystal Structure in the Nonphotochemical Light-Induced Nucleation of Supersaturated Aqueous Glycine Solutions. *Phys. Rev. Lett.* **89**, 175501 (2002).
217. Matsumoto, M., Wada, Y. & Onoe, K. Change in glycine polymorphs induced by minute-bubble injection during antisolvent crystallisation. *Adv. Powder Technol.* **26**, 415–421 (2015).
218. Weissbuch, I., Torbeev, V. Y., Leiserowitz, L. & Lahav, M. Solvent Effect on Crystal Polymorphism: Why Addition of Methanol or Ethanol to Aqueous Solutions Induces the Precipitation of the Least Stable β Form of Glycine. *Angew. Chemie Int. Ed.* **44**, 3226–3229 (2005).
219. Tang, W. *et al.* Glycine's pH-dependent polymorphism: A perspective from self-association in solution. *Cryst. Growth Des.* **17**, 5028–5033 (2017).
220. Little, L. J., Sear, R. P. & Keddie, J. L. Does the γ Polymorph of Glycine Nucleate Faster? A Quantitative Study of Nucleation from Aqueous Solution. *Cryst. Growth Des.* **15**, 5345–5354 (2015).
221. Lee, A. Y., Lee, I. S., Dette, S. S., Boerner, J. & Myerson, A. S. Crystallization on Confined Engineered Surfaces: A Method to Control Crystal Size and Generate Different Polymorphs. *J. Am. Chem. Soc.* **127**, 14982–14983 (2005).
222. Lewis, I. R. & Edwards, H. *Handbook of Raman Spectroscopy*. *Handbook of Raman Spectroscopy* (Marcel Dekker, 2001). doi:10.1201/9781420029253
223. Atkins, P. & Paula, J. De. Atkins' Physical chemistry 8th edition. *Chemistry* (2009).
224. Kim, K., Centrone, A., Hatton, T. A. & Myerson, A. S. Polymorphism control of nanosized glycine crystals on engineered surfaces. *CrystEngComm* **13**, 1127–1131 (2011).
225. Lee, A. Y., Lee, I. S. & Myerson, A. S. Factors Affecting the Polymorphic Outcome of Glycine Crystals Constrained on Patterned Substrates. *Chem. Eng. Technol.* **29**, 281–285 (2006).
226. Zhu, G., Zhu, X., Fan, Q. & Wan, X. Raman spectra of amino acids and their aqueous solutions. *Spectrochim. Acta Part A Mol. Biomol. Spectrosc.* **78**, 1187–1195 (2011).

227. Lee, I. S., Lee, A. Y. & Myerson, A. S. Concomitant Polymorphism in Confined Environment. *Pharm. Res.* **25**, 960–968 (2008).
228. Singh, A., Lee, I. S. & Myerson, A. S. Concomitant Crystallization of ROY on Patterned Substrates: Using a High Throughput Method to Improve the Chances of Crystallization of Different Polymorphs. *Cryst. Growth Des.* **9**, 1182–1185 (2009).
229. Earnshaw, S. On the Nature of the Molecular Forces which regulate the Constitution of the Luminiferous Ether. *Trans. Cambridge Philos. Soc.* **7**, 97–112 (1842).
230. Brandt, E. H. Levitation in Physics. *Science* **243**, 349–355 (1989).
231. Braunbeck, W. Free diamagnetic levitation of bodies in the magnetic field. *Z. Phys.* **112**, 753–763 (1939).
232. Mirica, K. A., Shevkoplyas, S. S., Phillips, S. T., Gupta, M. & Whitesides, G. M. Measuring densities of solids and liquids using magnetic levitation: fundamentals. *J. Am. Chem. Soc.* **131**, 10049–10058 (2009).
233. Berry, M. V & Geim, A. K. Of flying frogs and levitrons. *Eur. J. Phys.* **18**, 307–313 (1997).
234. Geim, A. K., Simon, M. D., Boamfa, M. I. & Heflinger, L. O. Magnet levitation at your fingertips. *Nature* **400**, 323–324 (1999).
235. Okress, E. C., Wroughton, D. M., Comenetz, G., Brace, P. H. & Kelly, J. C. R. Electromagnetic Levitation of Solid and Molten Metals. *J. Appl. Phys.* **23**, 545–552 (1952).
236. Kelton, K. F. *et al.* First X-Ray Scattering Studies on Electrostatically Levitated Metallic Liquids: Demonstrated Influence of Local Icosahedral Order on the Nucleation Barrier. *Phys. Rev. Lett.* **90**, 195504 (2003).
237. Barnes, M. D., Ng, K. C., Whitten, W. B. & Ramsey, J. M. Detection of single Rhodamine 6G molecules in levitated microdroplets. *Anal. Chem.* **65**, 2360–2365 (1993).
238. Whitten, W. B., Ramsey, J. M., Arnold, S. & Bronk, B. V. Single-molecule detection limits in levitated microdroplets. *Anal. Chem.* **63**, 1027–1031 (1991).
239. Ng, K. C., Whitten, W. B., Arnold, S. & Ramsey, J. M. Digital chemical analysis of dilute microdroplets. *Anal. Chem.* **64**, 2914–2919 (1992).
240. Lierke, E. G. Comparative Considerations of Aerodynamic, Acoustic and Electrostatic Single-Drop Levitation-Systems. *Forsch. im Ingenieurwes. - Eng. Res.* **61**, 201–216 (1995).

241. Roosen, G. La lévitation optique de sphères. *Can. J. Phys.* **57**, 1260–1279 (1979).
242. Ashkin, A. Acceleration and Trapping of Particles by Radiation Pressure. *Phys. Rev. Lett.* **24**, 156–159 (1970).
243. Hoffmann, G. G., Lentz, E. & Schrader, B. Simple device for the generation and optical levitation of single aerosol particles. *Rev. Sci. Instrum.* **64**, 823–824 (1993).
244. Bücks, K. & Müller, H. Über einige Beobachtungen an schwingenden Piezoquarzen und ihrem Schallfeld. *Zeitschrift für Phys.* **84**, 75–86 (1933).
245. Hanson, A. R., Domich, E. G. & Adams, H. S. Acoustical Liquid Drop Holder. *Rev. Sci. Instrum.* **35**, 1031–1034 (1964).
246. Apfel, R. E. A Novel Technique for Measuring the Strength of Liquids. *J. Acoust. Soc. Am.* **49**, 145–155 (1971).
247. Trinh, E. H. Compact acoustic levitation device for studies in fluid dynamics and material science in the laboratory and microgravity. *Rev. Sci. Instrum.* **56**, 2059–2065 (1985).
248. Brenn, G., Deviprasath, L. J., Durst, F. & Fink, C. Evaporation of acoustically levitated multi-component liquid droplets. *Int. J. Heat Mass Transf.* **50**, 5073–5086 (2007).
249. Santesson, S. & Nilsson, S. Airborne chemistry: Acoustic levitation in chemical analysis. *Analytical and Bioanalytical Chemistry* **378**, 1704–1709 (2004).
250. Ashkin, A. Applications of Laser Radiation Pressure. *Science* **210**, 1081 LP – 1088 (1980).
251. Zhao, H., Sadhal, S. S. & Trinh, E. H. Singular perturbation analysis of an acoustically levitated sphere: Flow about the velocity node. *J. Acoust. Soc. Am.* **106**, 589–595 (1999).
252. Oran, W. A., Berge, L. H. & Parker, H. W. Parametric study of an acoustic levitation system. *Rev. Sci. Instrum.* **51**, 626–631 (1980).
253. Xie, W. J. & Wei, B. Parametric study of single-axis acoustic levitation. *Appl. Phys. Lett.* **79**, 881–883 (2001).
254. Lierke, E. G. Acoustic Levitation - a Comprehensive Survey of Principles and Applications. *ACUSTICA* **82**, 220–237 (1996).
255. Andrade, M. A. B., Pérez, N. & Adamowski, J. C. Review of Progress in Acoustic Levitation. *Brazilian J. Phys.* **48**, 190–213 (2018).
256. Zang, D. *Acoustic Levitation - From Physics to Applications*. (Springer Singapore,

2020).

257. Gorkov, L. P. Forces Acting on a Small Particle in an Acoustic Field within an Ideal Fluid. *Dokl. Akad. Nauk SSSR* **140**, 88 (1961).
258. Zang, D. *et al.* Acoustic levitation of liquid drops: Dynamics, manipulation and phase transitions. *Adv. Colloid Interface Sci.* **243**, 77–85 (2017).
259. Watanabe, A., Hasegawa, K. & Abe, Y. Contactless Fluid Manipulation in Air : Droplet Coalescence and Active Mixing by Acoustic Levitation. *Sci. Rep.* **8**, 10221 (2018).
260. Geng, D. L., Xie, W. J., Yan, N. & Wei, B. Vertical vibration and shape oscillation of acoustically levitated water drops. *Appl. Phys. Lett.* **105**, 104101 (2014).
261. Trinh, E. H. & Hsu, C. Equilibrium shapes of acoustically levitated drops. *J. Acoust. Soc. Am.* **79**, 1335–1338 (1986).
262. Yamamoto, Y., Abe, Y., Fujiwara, A., Hasegawa, K. & Aoki, K. Internal Flow of Acoustically Levitated Droplet. *Microgravity Sci. Technol.* **20**, 277 (2008).
263. Yan, Z. L., Xie, W. J. & Wei, B. Vortex flow in acoustically levitated drops. *Phys. Lett. A* **375**, 3306–3309 (2011).
264. Hasegawa, K., Abe, Y., Fujiwara, A., Yamamoto, Y. & Aoki, K. External Flow of an Acoustically Levitated Droplet. *Microgravity Sci. Technol.* **20**, 261 (2008).
265. Shi, Q. *et al.* A General Approach to Free-Standing Nanoassemblies via Acoustic Levitation Self-Assembly. *ACS Nano* **13**, 5243–5250 (2019).
266. Weber, R. J. K. *et al.* Acoustic levitation: recent developments and emerging opportunities in biomaterials research. *Eur. Biophys. J.* **41**, 397–403 (2012).
267. Puskar, L. *et al.* Raman acoustic levitation spectroscopy of red blood cells and Plasmodium falciparum trophozoites. *Lab Chip* **7**, 1125–1131 (2007).
268. Sundvik, M., Nieminen, H. J., Salmi, A., Panula, P. & Hæggström, E. Effects of acoustic levitation on the development of zebrafish, Danio rerio, embryos. *Sci. Rep.* **5**, 13596 (2015).
269. Xie, W. J., Cao, C. D., Lü, Y. J., Hong, Z. Y. & Wei, B. Acoustic method for levitation of small living animals. *Appl. Phys. Lett.* **89**, 214102 (2006).
270. Chainani, E. T., Ngo, K. T. & Scheeline, A. Electrochemistry in an Acoustically Levitated Drop. *Anal. Chem.* **85**, 2500–2506 (2013).
271. Leiterer, J. *et al.* Acoustically Levitated Droplets. *Ann. N. Y. Acad. Sci.* **1130**, 78–84 (2008).

272. Xie, W. J. & Wei, B. Dependence of acoustic levitation capabilities on geometric parameters. *Phys. Rev. E* **66**, 26605 (2002).
273. Zang, D. *et al.* Switchable Opening and Closing of a Liquid Marble via Ultrasonic Levitation. *Langmuir* **31**, 11502–11507 (2015).
274. Priego-Capote, F. & de Castro, L. Ultrasound-assisted levitation: Lab-on-a-drop. *TrAC Trends Anal. Chem.* **25**, 856–867 (2006).
275. Trinh, E. & Wang, T. G. Large-amplitude free and driven drop-shape oscillations: experimental observations. *J. Fluid Mech.* **122**, 315–338 (1982).
276. Tian, Y., Holt, R. G. & Apfel, R. E. A new method for measuring liquid surface tension with acoustic levitation. *Rev. Sci. Instrum.* **66**, 3349–3354 (1995).
277. Trinh, E. H., Marston, P. L. & Robey, J. L. Acoustic measurement of the surface tension of levitated drops. *J. Colloid Interface Sci.* **124**, 95–103 (1988).
278. Tian, Y., Holt, R. G. & Apfel, R. E. Investigation of Liquid Surface Rheology of Surfactant Solutions by Droplet Shape Oscillations: Experiments. *J. Colloid Interface Sci.* **187**, 1–10 (1997).
279. Hu, H. & Larson, R. G. Evaporation of a sessile droplet on a substrate. *J. Phys. Chem. B* **106**, 1334–1344 (2002).
280. Guéna, G., Poulard, C., Voué, M., De Coninck, J. & Cazabat, A. M. Evaporation of sessile liquid droplets. *Colloids Surfaces A Physicochem. Eng. Asp.* **291**, 191–196 (2006).
281. Erbil, H. Y. Evaporation of pure liquid sessile and spherical suspended drops: A review. *Adv. Colloid Interface Sci.* **170**, 67–86 (2012).
282. Ooi, C. H. *et al.* Evaporation of Ethanol–Water Binary Mixture Sessile Liquid Marbles. *Langmuir* **32**, 6097–6104 (2016).
283. Picknett, R. G. & Bexon, R. The evaporation of sessile or pendant drops in still air. *J. Colloid Interface Sci.* **61**, 336–350 (1977).
284. Li, Y. *et al.* Evaporation-Triggered Segregation of Sessile Binary Droplets. *Phys. Rev. Lett.* **120**, 224501 (2018).
285. Barash, L. Y., Bigioni, T. P., Vinokur, V. M. & Shchur, L. N. Evaporation and fluid dynamics of a sessile drop of capillary size. *Phys. Rev. E - Stat. Nonlinear, Soft Matter Phys.* **79**, (2009).
286. Carrithers, A. D. *et al.* Multiscale Self-Assembly of Distinctive Weblike Structures from Evaporated Drops of Dilute American Whiskeys. *ACS Nano* **14**, 5417–5425

(2020).

287. Rigas, G.-P. *et al.* Spray printing of organic semiconducting single crystals. *Nat. Commun.* **7**, 13531 (2016).
288. Paudel, A., Worku, Z. A., Meeus, J., Guns, S. & Van den Mooter, G. Manufacturing of solid dispersions of poorly water soluble drugs by spray drying: Formulation and process considerations. *Int. J. Pharm.* **453**, 253–284 (2013).
289. Davis, M. & Walker, G. Recent strategies in spray drying for the enhanced bioavailability of poorly water-soluble drugs. *J. Control. Release* **269**, 110–127 (2018).
290. Jermain, S. V, Brough, C. & Williams, R. O. Amorphous solid dispersions and nanocrystal technologies for poorly water-soluble drug delivery – An update. *Int. J. Pharm.* **535**, 379–392 (2018).
291. Yarin, A. L., Brenn, G., Kastner, O., Rensink, D. & Tropea, C. Evaporation of acoustically levitated droplets. *J. Fluid Mech.* **399**, 151–204 (1999).
292. Yarin, A. L., Brenn, G., Kastner, O. & Tropea, C. Drying of acoustically levitated droplets of liquid–solid suspensions: Evaporation and crust formation. *Phys. Fluids* **14**, 2289 (2002).
293. Yarin, A. L., Brenn, G. & Rensink, D. Evaporation of acoustically levitated droplets of binary liquid mixtures. *Int. J. Heat Fluid Flow* **23**, 471–486 (2002).
294. Niimura, Y. & Hasegawa, K. Evaporation of droplet in mid-air: Pure and binary droplets in single-axis acoustic levitator. *PLoS One* **14**, e0212074 (2019).
295. Schiffter, H. & Lee, G. Single-droplet evaporation kinetics and particle formation in an acoustic levitator. Part 2: Drying kinetics and particle formation from microdroplets of aqueous mannitol, trehalose, or catalase. *J. Pharm. Sci.* **96**, 2284–2295 (2007).
296. Duranty, E. R., McCardle, H., Reichert, W. M. & Davis, J. H. Acoustic levitation and infrared thermography: a sound approach to studying droplet evaporation. *Chem. Commun.* **56**, 4224–4227 (2020).
297. Abdullahi, H., Burcham, C. L. & Vetter, T. A mechanistic model to predict droplet drying history and particle shell formation in multicomponent systems. *Chem. Eng. Sci.* **224**, 115713 (2020).
298. Maruyama, Y. & Hasegawa, K. Evaporation and drying kinetics of water-NaCl droplets via acoustic levitation. *RSC Adv.* **10**, 1870–1877 (2020).
299. Combe, N. A. & Donaldson, D. J. Water Evaporation from Acoustically Levitated

Aqueous Solution Droplets. *J. Phys. Chem. A* **121**, 7197–7204 (2017).

300. Frohn, A. & Roth, N. *Dynamics of Droplets*. (Springer Berlin Heidelberg, 2000).
301. Vehring, R., Foss, W. R. & Lechuga-Ballesteros, D. Particle formation in spray drying. *J. Aerosol Sci.* **38**, 728–746 (2007).
302. Gregson, F. K. A., Robinson, J. F., Miles, R. E. H., Royall, C. P. & Reid, J. P. Drying Kinetics of Salt Solution Droplets: Water Evaporation Rates and Crystallization. *J. Phys. Chem. B* **123**, 266–276 (2019).
303. Walton, D. E. & Mumford, C. J. Spray Dried Products—Characterization of Particle Morphology. *Chem. Eng. Res. Des.* **77**, 21–38 (1999).
304. Walton, D. E. THE MORPHOLOGY OF SPRAY-DRIED PARTICLES A QUALITATIVE VIEW. *Dry. Technol.* **18**, 1943–1986 (2000).
305. Cao, H.-L. *et al.* Rapid crystallization from acoustically levitated droplets. *J. Acoust. Soc. Am.* **131**, 3164–3172 (2012).
306. Wolf, S. E. *et al.* Strong Stabilization of Amorphous Calcium Carbonate Emulsion by Ovalbumin : Gaining Insight into the Mechanism of ' Polymer-Induced Liquid Precursor ' Processes. *J. Am. Chem. Soc.* **133**, 12642–12649 (2011).
307. Leiterer, J., Emmerling, F., Panne, U., Christen, W. & Rademann, K. Tracing Coffee Tabletop Traces. *Langmuir* **24**, 7970–7978 (2008).
308. Leiterer, J., Delißen, F., Emmerling, F., Thünemann, A. F. & Panne, U. Structure analysis using acoustically levitated droplets. *Anal. Bioanal. Chem.* **391**, 1221–1228 (2008).
309. Tuckermann, R., Puskar, L., Zavabeti, M., Sekine, R. & McNaughton, D. Chemical analysis of acoustically levitated drops by Raman spectroscopy . *Anal. Bioanal. Chem.* **394**, 1433–1441 (2009).
310. Gnutzmann, T., Nguyen Thi, Y., Rademann, K. & Emmerling, F. Solvent-triggered crystallization of polymorphs studied in situ. *Cryst. Growth Des.* **14**, 6445–6450 (2014).
311. Wolf, S. E., Leiterer, J., Kappl, M., Emmerling, F. & Tremel, W. Early Homogenous Amorphous Precursor Stages of Calcium Carbonate and Subsequent Crystal Growth in Levitated Droplets. *J. Am. Chem. Soc.* **130**, 12342–12347 (2008).
312. Nguyen Thi, Y., Rademann, K. & Emmerling, F. Direct evidence of polyamorphism in paracetamol. *CrystEngComm* **17**, 9029–9036 (2015).
313. Klimakow, M. *et al.* Combined Synchrotron XRD/Raman Measurements: In Situ

Identification of Polymorphic Transitions during Crystallization Processes. *Langmuir* **26**, 11233–11237 (2010).

314. Felten, A. *et al.* Single- and double-sided chemical functionalization of bilayer graphene. *Small* **9**, 631–639 (2013).
315. Nair, R. R. *et al.* Fluorographene: A two-dimensional counterpart of Teflon. *Small* **6**, 2877–2884 (2010).
316. Ossonon, B. D. & Bélanger, D. Functionalization of graphene sheets by the diazonium chemistry during electrochemical exfoliation of graphite. *Carbon N. Y.* **111**, 83–93 (2017).
317. Cornel, J., Kidambi, P. & Mazzotti, M. Precipitation and Transformation of the Three Polymorphs of d-Mannitol. *Ind. Eng. Chem. Res.* **49**, 5854–5862 (2010).
318. Braun, D. E. *et al.* Simultaneous quantitative analysis of ternary mixtures of d-mannitol polymorphs by FT-Raman spectroscopy and multivariate calibration models. *Int. J. Pharm.* **385**, 29–36 (2010).
319. Wang, M. *et al.* Pulsed electric fields induce modulation of protein liquid–liquid phase separation. *Soft Matter* **16**, 8547–8553 (2020).
320. Al-Ani, A. J., Herdes, C., Wilson, C. C. & Castro-Dominguez, B. Engineering a New Access Route to Metastable Polymorphs with Electrical Confinement. *Cryst. Growth Des.* **20**, 1451–1457 (2020).
321. Tong, J., Doumbia, A., Alieva, A., Turner, M. L. & Casiraghi, C. Gas Blow Coating: A Deposition Technique To Control the Crystal Morphology in Thin Films of Organic Semiconductors. *ACS Omega* **4**, 11657–11662 (2019).